

## Stellingen

behorende bij het proefschrift

### **New Inorganic Scintillators and Storage Phosphors for Detection of Thermal Neutrons.**

1. Bij het optimaliseren van de DQE van een image plate detector moet niet alleen het neutronenabsorptierendement en de efficiëntie van de opslagfosfor in het omzetten van secundaire straling in fotostimuleerbare centra beschouwd worden, maar zeker ook de variantie in het aantal gecreëerde fotostimuleerbare centra.  
*Hoofdstuk 7 van dit proefschrift.*
2. Het is een misverstand om te veronderstellen dat de DQE van een image plate niet meer toe kan nemen wanneer voor het gemiddeld aantal fotoelektronen  $N_{phe}$  dat per invallend neutron geproduceerd wordt geldt:  $N_{phe} > 1$ .  
*M. Thoms, M.S. Lehmann, C. Wilkinson, Nucl. Instr. and Meth. 384 (1996) 457.*
3. Het onderzoek aan opslagfosforen en in mindere mate ook aan scintillatoren is gebaat bij een meer gedetailleerde chemische analyse van de aanwezige onzuiverheden in de materialen dan tot nu toe het geval is.
4. Zolang thermoluminescentie gloeicurves niet worden gecorrigeerd voor de temperatuurafhankelijke quenching van de luminescentie, is het doen van een analyse aan zo'n gloeicurve door beschouwing van gloeipiekparameters als de aktivatie-energie en de frequentiefactor, zinloos.  
*Zie bijv. Y.S. Horowitz, D. Yossian, Rad. Prot. Dosimetry 60(1) (1995) 1.*
5. Op grond van het argument dat Nederland geen enkel Europees fysisch instituut binnen haar grenzen heeft dat beschikt over een deeltjesversneller, is ons land een goede kandidaat voor de huisvesting van de toekomstige 'European Spallation Source' (ESS). Om hier nog een argument aan toe te voegen moet Nederland zich sterk profileren op het gebied van neutronen-gerelateerd onderzoek, hetgeen ook het doen van méér onderzoek op dit gebied inhoudt.
6. 'Foto-gestimuleerde luminescentie'<sup>a</sup> en 'dolfijn-gestimuleerde luminescentie'<sup>b</sup> hebben minder met elkaar te maken dan op grond van de begrippen verwacht mag worden.  
<sup>a</sup> *dit proefschrift*  
<sup>b</sup> *Nature 39 (1998) 731.*
7. De florerende fazantenkolonie rondom het Interfacultair Reactor Instituut te Delft bewijst dat kernreactoren en het milieu elkaar niet op alle fronten bijten. De direkte omgeving van een kernreactor kan uitstekend fungeren als stiltegebied.
8. De veelgehoorde reactie "Nu ga je dus werken" aan het adres van jonge doctors impliceert dat zij niet moeten verwachten na hun promotie nog veel te leren.

9. De voortschrijdende natuurwetenschap doet de kennis over de natuur toenemen. De duur van natuurwetenschappelijke opleidingen neemt echter niet toe. Derhalve zijn klachten over het dalende niveau van juist afgestudeerde natuurwetenschappers terecht.
10. De termen 'modernisme' en 'postmodernisme' suggereren dat het einde der tijden nabij is.

# Theses

belonging to the dissertation

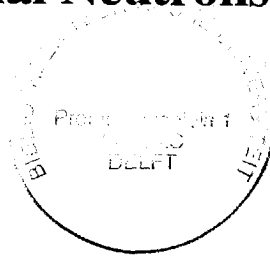
## **New Inorganic Scintillators and Storage Phosphors for Detection of Thermal Neutrons.**

1. When optimising the DQE of an thermal neutron image plate detector one must not only consider the neutron absorption efficiency and the efficiency of the storage phosphor in converting secondary radiation into photostimulable centres, but also the variance of the number of photostimulable centres created.  
*Chapter 7 of this dissertation.*
2. It is a misunderstanding to suppose that the DQE of an image plate can not increase anymore when for the average number of photoelectrons  $N_{phe}$  which is produced per incident neutron applies:  $N_{phe} > 1$ .  
*M. Thoms, M.S. Lehmann, C. Wilkinson, Nucl. Instr. and Meth. 384 (1996) 457.*
3. The research on storage phosphors and to a lesser extent also on scintillators is would be helped by a more detailed chemical analysis of the impurities which are present in the materials.
4. When thermoluminescence glow curves are not corrected for the temperature-dependent quenching of the luminescence, the analysis of such a glow curve by considering the glow curve parameters as the activation energy and the frequency factor, does not make sense.  
*Zie bijv. Y.S. Horowitz, D. Yossian, Rad. Prot. Dosimetry 60(1) (1995) 1.*
5. The Netherlands is a good candidate for accommodating the future 'European Spallation Source' (ESS), since this country does not accommodate any European physical institute which has a particle accelerator. In order to add a second argument the Netherlands must present itself strongly on the field of neutron related research, which implies that it should increase the research activity in this field
6. 'Photostimulated luminescence'<sup>a</sup> and 'dolphin stimulated luminescence'<sup>b</sup> are not so similar as one may expect when considering both terms.  
<sup>a</sup> *dit proefschrift*  
<sup>b</sup> *Nature 39 (1998) 731.*
7. The flourishing colony of pheasants at the surroundings of the Interfaculty Reactor Institute at Delft proves that nuclear reactors and the environment are not entirely incompatible. The direct surroundings of a nuclear reactor can very well serve as a 'quiet area'.
8. The remark "So now you are going to work", often made to young doctors, implies that these should not expect to learn a lot anymore after their promotion.

9. The advancing science increases our knowledge about nature. However, the duration of scientific education does not increase. Therefore, complaints about the lowering education level of graduates are correct.
10. The terms 'modernism' en 'postmodernism' suggest that the end of times is near.

TR 3252

**New Inorganic Scintillators and  
Storage Phosphors  
for  
Detection of Thermal Neutrons**



**Nieuwe Anorganische Scintillatoren en Opslagfosforen  
voor  
Detectie van Thermische Neutronen**

**Cover:**

*Inset: Adapted fragment of the painting 'The Alchemist' (1771) by the English painter Joseph Wright (1734-1797). The fictitious scenery shows the alchemist Henning Brand discovering phosphor. Actually, Brand was looking for the philosopher's stone. He tried to find it by distillation of human urine. The non-evaporating part appeared to be white phosphor which illuminated in the dark.*

Photograph: Derby Museum and Art Gallery, Derby, England. With permission.

*Background: Adapted photograph of the boron-rich mountains surrounding Death Valley, California. During the 1880s large-scale mining of borax took place here, as boron and its compounds are used for many more purposes than only absorption or detection of neutrons. Nowadays, minerals containing boron are still mined in the southwestern United States although not in Death Valley. Those minerals are very rare in the earth's crust. Deposits mined in this area constitute about fifty percent of the world's supply of boron. There even exists a small town named 'Boron'.*

Photograph: M. Knitel

Cover advice: Van der Wegen/Kramer Artworks.

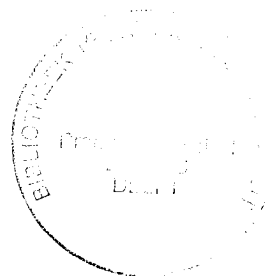


The research described in this thesis was performed in the Radiation Technology Group of the Interfaculty Reactor Institute, Delft University of Technology, Mekelweg 15, 2629 JB Delft, The Netherlands.

This research has been financially supported by the Netherlands Technology Foundation (STW).

**New Inorganic Scintillators and Storage  
Phosphors  
for  
Detection of Thermal Neutrons**

**PROEFSCHRIFT**



ter verkrijging van de graad van doctor  
aan de Technische Universiteit Delft,  
op gezag van de Rector Magnificus prof. ir. K. F. Wakker,  
in het openbaar te verdedigen ten overstaan van een commissie,  
door het College voor Promoties aangewezen,

op vrijdag 11 december 1998 te 10:30 uur

door

**Mathijs Johan KNITEL**

doctorandus in de natuurkunde,  
geboren te Eindhoven

Dit proefschrift is goedgekeurd door de promotor:

Prof. dr. ir. C. W. E. van Eijk

Samenstelling promotiecommissie:

Rector Magnificus, voorzitter

Prof. dr. ir. C. W. E. van Eijk, Technische Universiteit Delft, promotor

Prof. dr. ir. A. H. M. Verkooijen, Technische Universiteit Delft

Prof. dr. ir. F. Tuinstra, Technische Universiteit Delft

Prof. dr. A. Meijerink, Universiteit van Utrecht

Prof. dr. H. Postma, Technische Universiteit Delft

Dr. P. Dorenbos, Technische Universiteit Delft

P.J.R. Leblans dr. Sc., Agfa-Gevaert N.V.

*Published and distributed by:*

Delft University Press

Mekelweg 4

2628 CD Delft

The Netherlands

Telephone: +31 15 2783254

Fax: +31 15 2781661

E-mail: dup@dup.tudelft.nl

Knitel, Mathijs

ISBN 90-407-1775-3 / CIP

NUGI: 812

Subject headings: radiation detectors / neutron detectors / scintillators  
storage phosphors / image plates.

Copyright ©1998 by M.J. Knitel.

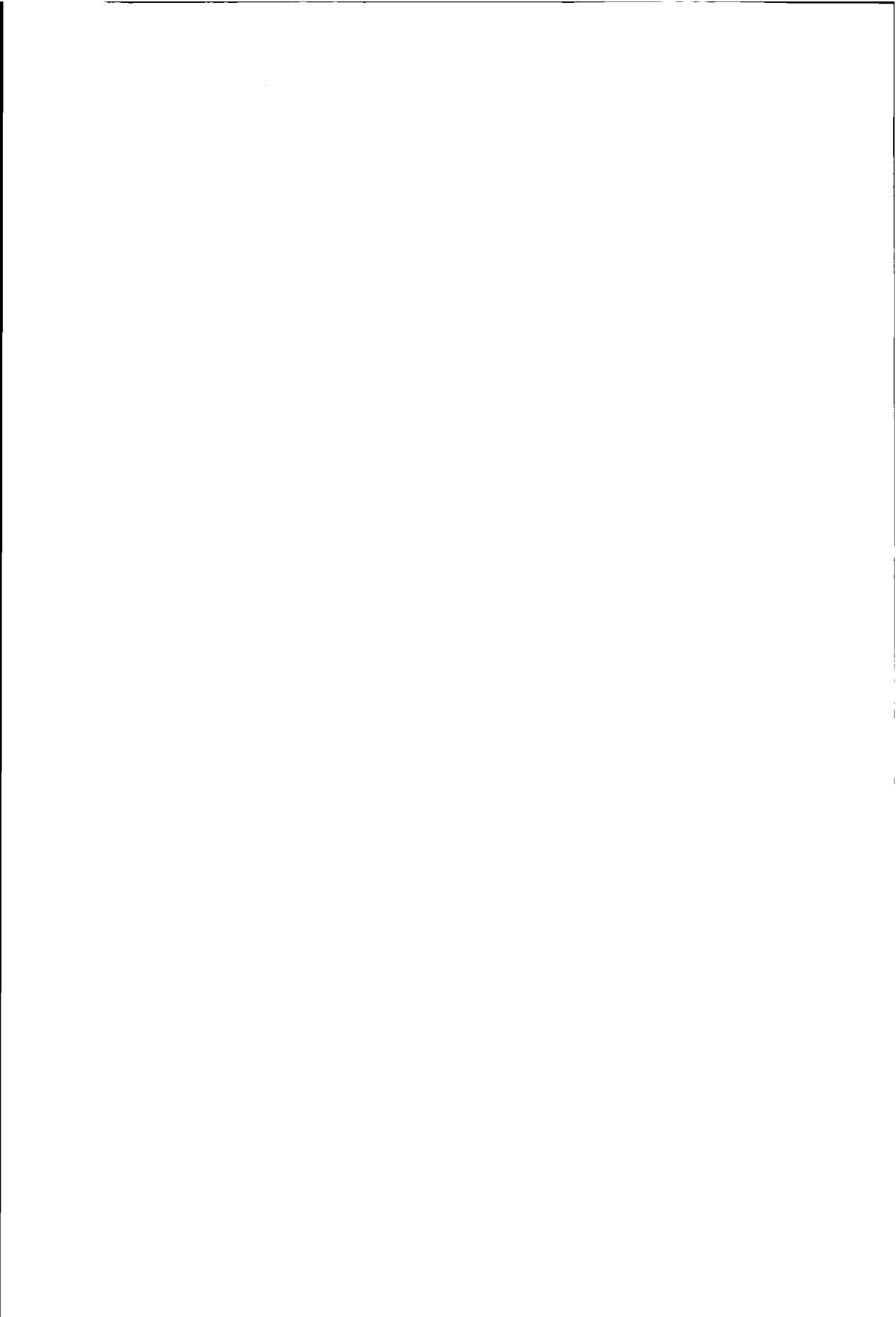
All rights reserved. No part of the material protected by this copyright notice may be reproduced or utilized in any form or by any means, electronic or mechanical, including photocopying, recording or by any information storage and retrieval system, without permission from the publisher: Delft University Press.

Printed in the Netherlands.



*For a successful technology,  
reality must take precedence  
over public relations,  
for Nature cannot be fooled.*

*Richard P. Feynman*



# Contents

<b>1</b>	<b>Introduction</b>	<b>1</b>
<b>2</b>	<b>Thermal neutron detection methods</b>	<b>5</b>
2.1	Introduction . . . . .	5
2.2	Neutron capture reactions . . . . .	5
2.2.1	The $^3\text{He}$ reaction . . . . .	6
2.2.2	The $^6\text{Li}$ reaction . . . . .	7
2.2.3	The $^{10}\text{B}$ reaction . . . . .	7
2.2.4	The $^{155}\text{Gd}$ and $^{157}\text{Gd}$ reactions . . . . .	8
2.2.5	The $^{235}\text{U}$ and $^{239}\text{Pu}$ reactions . . . . .	10
2.2.6	The DQE of a detector . . . . .	10
2.3	Counting detectors . . . . .	12
2.3.1	Gas proportional counters . . . . .	12
2.3.2	Scintillators: traditional materials . . . . .	15
2.3.3	Scintillators: Fibre coupled systems, Anger cameras and other systems . . . . .	18
2.3.4	Foil detectors . . . . .	20
2.3.5	Semiconductors . . . . .	22
2.4	Integrating detectors . . . . .	23
2.4.1	Photographic techniques . . . . .	23
2.4.2	Image plates . . . . .	24
2.4.3	CCD based detectors . . . . .	26
2.5	Conclusion . . . . .	27
<b>3</b>	<b>Selection of materials</b>	<b>29</b>
3.1	Introduction . . . . .	29
3.2	Neutron sensitivity . . . . .	30
3.3	Gamma sensitivity . . . . .	32
3.4	Scintillators . . . . .	33
3.4.1	Scintillation decay time . . . . .	34
3.5	Storage phosphors . . . . .	35
3.5.1	Luminescence decay time . . . . .	36

3.5.2	The case BaFBr:Eu <sup>2+</sup> . . . . .	36
3.5.3	Other storage phosphors . . . . .	38
3.6	Conclusions . . . . .	39
3.6.1	Scintillators . . . . .	39
3.6.2	Storage phosphors . . . . .	40
<b>4</b>	<b>LiBaF<sub>3</sub>, a thermal neutron scintillator with optimal n-γ discrimination</b>	<b>41</b>
4.1	Introduction . . . . .	41
4.2	Experimental . . . . .	41
4.3	Results I: Scintillation properties . . . . .	43
4.4	Results II: n-γ discrimination . . . . .	46
4.4.1	Experimental method and setup . . . . .	46
4.4.2	n-γ discrimination in a mixed radiation field . . . . .	47
4.4.3	Gamma sensitivity and intrinsic radioactivity . . . . .	48
4.5	Discussion . . . . .	51
4.6	Conclusion and Outlook . . . . .	52
<b>5</b>	<b>Scintillation and storage properties of LiYSiO<sub>4</sub>:Ce<sup>3+</sup> and LiLuSiO<sub>4</sub>:Ce<sup>3+</sup></b>	<b>55</b>
5.1	Introduction . . . . .	55
5.2	Experimental . . . . .	56
5.2.1	Sample preparation . . . . .	56
5.2.2	Optical measurements . . . . .	56
5.2.3	Irradiation facilities . . . . .	60
5.3	Applicability as scintillator/storage phosphor . . . . .	62
5.3.1	Excitation/emission and scintillation . . . . .	62
5.3.2	Optical stimulation . . . . .	65
5.3.3	Discussion . . . . .	68
5.4	Thermoluminescence . . . . .	71
5.4.1	Results . . . . .	71
5.4.2	Discussion . . . . .	74
5.5	Summary and Conclusion . . . . .	76
<b>6</b>	<b>Photoluminescence, scintillation and thermoluminescence in several Ce<sup>3+</sup> or Eu<sup>2+</sup> activated borates</b>	<b>77</b>
6.1	Introduction . . . . .	77
6.2	Experimental . . . . .	78
6.2.1	Sample preparation . . . . .	78
6.2.2	Luminescence and light yield measurements . . . . .	80
6.3	Results . . . . .	80
6.3.1	Excitation/emission measurements . . . . .	80
6.3.2	X-ray induced emission and scintillation light yields . . . . .	86

6.3.3	Thermoluminescence . . . . .	88
6.4	Discussion . . . . .	89
6.5	Summary and Conclusion . . . . .	91
<b>7</b>	<b>The feasibility of the storage phosphors <math>M_2B_5O_9X:Eu^{2+}</math> (<math>M=Ca,Sr,Ba</math>; <math>X=Cl,Br</math>) in thermal neutron image plates</b>	<b>93</b>
7.1	Introduction . . . . .	93
7.2	The DQE of a thermal neutron image plate . . . . .	94
7.2.1	Image plate based on $BaFBr:Eu^{2+} \cdot Gd_2O_3$ (IP-Gd) . . . . .	96
7.2.2	Image plate based on a haloborate (IP-B) . . . . .	106
7.3	Experimental . . . . .	110
7.3.1	Samples . . . . .	110
7.3.2	Irradiation facilities and optical measurements . . . . .	110
7.4	Results . . . . .	111
7.5	Discussion . . . . .	116
7.6	Summary and Conclusion . . . . .	117
<b>8</b>	<b>On the trapping and recombination of charge carriers in <math>Sr_2B_5O_9Br:Eu^{2+}</math></b>	<b>119</b>
8.1	Introduction . . . . .	119
8.2	Methods of experiments and calculations . . . . .	121
8.2.1	Samples . . . . .	121
8.2.2	Irradiation facilities . . . . .	121
8.2.3	Excitation, emission and stimulation measurements . . . . .	121
8.2.4	TL and EPR measurements . . . . .	122
8.2.5	Theoretical calculations . . . . .	122
8.3	Results . . . . .	123
8.3.1	Spectroscopic properties of the Eu dopant ions . . . . .	123
8.3.2	Radiation induced absorption and stimulation bands . . . . .	125
8.3.3	TL and its relation to photostimulated luminescence (PSL) . . . . .	127
8.3.4	Filling of traps by illumination with UV light . . . . .	130
8.3.5	EPR measurements . . . . .	133
8.3.6	Photon yield of X-ray induced scintillation and thermoluminescence . . . . .	136
8.3.7	Time dependence of the recombination luminescence . . . . .	139
8.4	Discussion . . . . .	143
8.4.1	Role of the $Eu^{2+}$ and $Eu^{3+}$ ions . . . . .	143
8.4.2	Nature of the traps . . . . .	146
8.4.3	Recombination . . . . .	146
8.5	Summary and Outlook . . . . .	147
	<b>Summary</b>	<b>151</b>

<b>Bibliography</b>	<b>155</b>
<b>List of Abbreviations</b>	<b>169</b>
<b>Publications</b>	<b>171</b>
<b>Samenvatting</b>	<b>173</b>
<b>Nawoord</b>	<b>179</b>
<b>Curriculum Vitae</b>	<b>181</b>

# 1

## Introduction

Since the first neutron diffraction experiments in 1946 the neutron has become one of the key microscopic probes of condensed matter research. However, neutrons are also an expensive probe and in Europe the neutron sources are consistently oversubscribed. One does not solely want to wait for new sources that have been planned for the future. A European network has been established in 1992 with the aim to improve neutron instrumentation, thus contributing to a more efficient use of the current neutron sources. One of the central issues of the program is the development of better and low cost neutron detectors. In order not to 'waste' neutrons high detection efficiencies and the coverage of large solid angles are the first requirements.

Another European initiative is the proposal for a new neutron facility, the European Spallation Source (ESS) [1]. The ESS should be available for science in 2010. It should have an average neutron flux roughly equivalent to that of the High Flux Reactor at ILL, but the peak flux will be 40 times greater than this average. The argument for building this facility is not only that more neutron beams become available. Neutron scattering is still a very intensity limited technique. Higher (peak) intensities will allow for higher spatial and temporal resolutions, and the study of smaller samples, more subtle effects and more complex systems. The use of higher intensities does also have implications for the requirements on the detectors.

The work to be presented here is aimed to contribute to the improvement of the neutron detector technology. The focus is on inorganic crystalline scintillator and storage phosphor materials. New materials have been studied and their potential for application in detectors has been considered.

Storage phosphors have in common with scintillators that they convert ionising radiation into visible light. But instead of responding directly they store part of the absorbed ionisation energy. Free electrons and holes created by radiation absorption do not rapidly recombine, but are separately trapped at impurities or defect sites in the material. By optical stimulation the trapped charge is liberated. Next the recombination of the electrons and holes can occur radiatively, similarly to scintillators.

Scintillators are already used in radiation technology for many decades. The interest in storage phosphors actually started only in 1983 with the introduction of a new two-dimensional

X-ray detector in the field of medical diagnostics [2]. This detector was called 'image plate' (IP) and was based on the storage phosphor material  $\text{BaFBr:Eu}^{2+}$ .

Figure 1.1 shows a schematic of an IP.

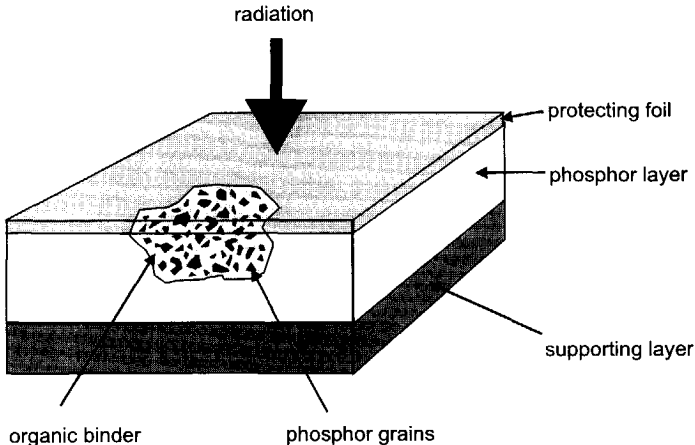


**Figure 1.1:** Construction of an image plate.

Crystalline powder of the storage phosphor is mixed with an organic binder material and deposited on a supporting layer. The mixture is covered with a protecting foil. During the experiment the IP is exposed to ionising radiation and electrons and holes are trapped. Next the readout procedure takes place as indicated in figure 1.2.

The IP is optically stimulated pixel-by-pixel by means of a laser beam. The photons emitted during stimulation are detected by a photomultiplier tube (PMT). The number of photons detected during stimulation of a pixel is a measure for the amount of radiation absorbed in that pixel. Stepping from one pixel to another occurs by moving the laser beam and/or the plate. Thus a complete image can be reconstructed.

Since the introduction the interest in storage phosphors has greatly increased and the X-ray IP has found application in many fields [3–5]. The first neutron-sensitive IP followed in 1992 [6] and the first workshop on Neutron Image Plates was held in 1996 at Brookhaven National Laboratory.

This thesis has been organised as follows. In chapter 2 the neutron detection technology is reviewed and the qualities of scintillator based detectors and IPs are compared with those of other detector systems. Also the demands and possibilities for improvements are mentioned. In chapter 3 is argued which materials should be examined to find a scintillator or storage phosphor which could improve this class of neutron detectors. It will become clear why the compounds that are discussed in the chapters 4–8 were chosen as subjects of research. Chapter 4 deals with



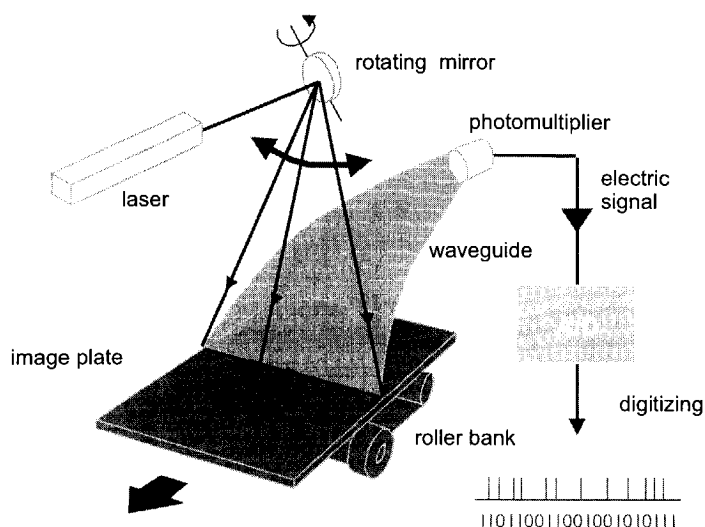
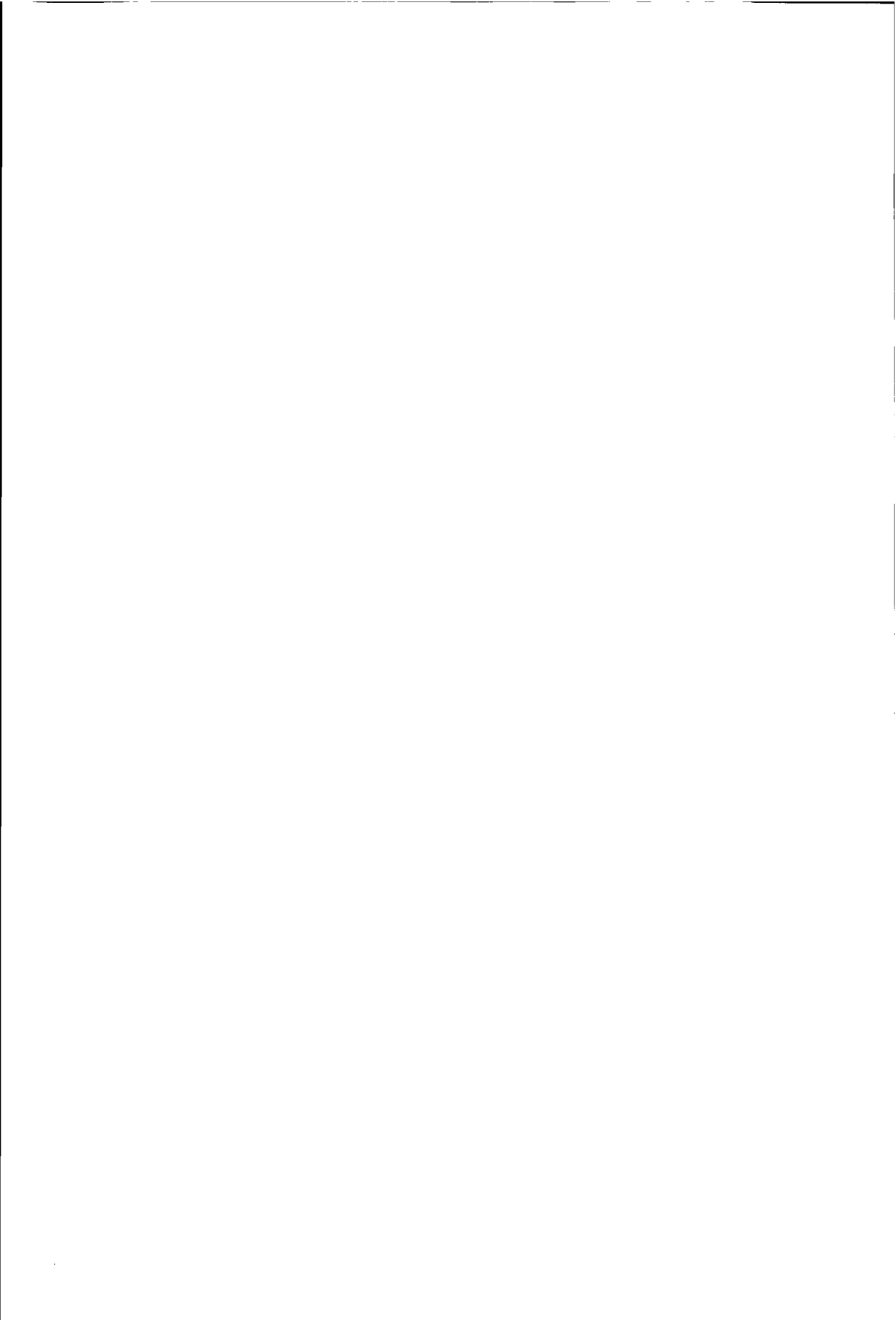


**Figure 1.2:** Sketch of a setup for reading out an image plate. This example shows the setup as constructed by Agfa-Gevaert [7].

the scintillator properties of  $\text{LiBaF}_3$  and it is shown that with this compound very efficient  $n\text{-}\gamma$  discrimination is possible. In chapter 5 the scintillation and storage properties of  $\text{Ce}^{3+}$  activated  $\text{LiYSiO}_4$  and  $\text{LiLuSiO}_4$  are presented. In particular the scintillation properties are promising. A class of  $\text{Ce}^{3+}$  activated borate materials is discussed in chapter 6. Since it appeared already soon that the storage properties of these materials are poor, attention is mainly focussed on the scintillation qualities. The next chapters deal purely with storage phosphors. Chapter 7 starts with a theoretical analysis together with computer simulations to compare the DQE of an IP based on a boron loaded storage phosphor (IP-B) with that of an IP containing the  $\text{BaFBr:Eu}^{2+}\cdot\text{Gd}_2\text{O}_3$  mixture (IP-Gd). For calculating the DQE of the IP-B the attractive storage phosphor materials  $\text{M}_2\text{B}_5\text{O}_9\text{X:Eu}^{2+}$  ( $\text{M}=\text{Ca},\text{Sr},\text{Ba}$ ;  $\text{X}=\text{Cl},\text{Br}$ ) were taken as example. Their storage phosphor qualities were also examined experimentally. One of these materials,  $\text{Sr}_2\text{B}_5\text{O}_9\text{Br:Eu}^{2+}$ , is subject of chapter 8. Its interesting macroscopic properties were enough reason to try to answer some questions on a microscopic level. How charge traps are created, which defects and impurities play a role in the trapping and how recombination of detrapped charge occurs are the topics of discussion.



## 2

# Thermal neutron detection methods

## 2.1 Introduction

In this chapter the status of thermal neutron detection technology will be briefly reviewed. The purpose is not to provide the reader with the completest possible knowledge of the field, but to indicate the unique position of scintillator and storage phosphor based detectors in the total spectrum of detectors. In addition the possibilities for improvements will be pointed out.

A distinction is made between so-called *counting detectors* and *integrating detectors*, as scintillators belong to the former and image plates (IPs) to the latter. A broad overview of neutron detection technology until 1982 was given by Convert and Forsyth [8] and more recently the topic was discussed by Fraser [9] and Rausch [10]. For other literature, see [11–13].

## 2.2 Neutron capture reactions

Most radiation detectors rely on the creation of free charge carriers. Since neutrons are uncharged, free charge carriers can only be created either by direct collisions with nuclei which are subsequently displaced or by utilisation of nuclear reactions. In case of thermal neutrons there is not sufficient energy available to accomplish displacements by collisions so only the second option remains. The nuclear reactions of importance are those with a high neutron capture cross section in order to limit the neutron-absorbing volume of the detector.

Table 2.1 lists the most interesting neutron capture reactions. Reactions in which the energy is released as kinetic energy to particles, the (n,p), (n, $\alpha$ ) and (n,fission) reactions, should be distinguished from the (n, $\gamma$ ) reactions. The former give rise to ionisations within several micrometers of the point of interaction. The (n,p) and (n, $\alpha$ ) reactions have in common that the reaction products are ejected collinearly, as required by conservation of momentum. The (n, $\gamma$ ) reactions listed have a high probability of internal conversion. The conversion electrons (ce's) ejected are much easier stopped than the gamma rays and provide more accurate spatial information about the point of interaction. An example of a material not meeting the latter requirement is  $^{113}\text{Cd}$ . Its

**Table 2.1:** The thermal neutron capture reactions utilised for detection of slow neutrons.

${}^3\text{He} + {}^1_0\text{n}$	$\longrightarrow$	${}^3\text{H} + {}^1_1\text{p} + 0.77 \text{ MeV}$		
${}^6\text{Li} + {}^1_0\text{n}$	$\longrightarrow$	${}^3\text{H} + {}^4_2\text{He} + 4.79 \text{ MeV}$		
${}^{10}\text{B} + {}^1_0\text{n}$	$\longrightarrow$	${}^7\text{Li} + {}^4_2\text{He} + 2.78 \text{ MeV}$	(7%)	
		$\longrightarrow$	${}^7\text{Li}^* + {}^4_2\text{He} + 2.30 \text{ MeV}$	(93%)
		$\quad \quad \quad \longmapsto$	${}^7\text{Li} + {}^4_2\text{He} + \gamma (0.48 \text{ MeV})$	
${}^{155}\text{Gd} + {}^1_0\text{n}$	$\longrightarrow$	${}^{156}\text{Gd}^*$		
		$\longrightarrow$	${}^{156}\text{Gd} + (\gamma\text{'s} + \text{ce}\text{'s}; 7.9 \text{ MeV})$	
${}^{157}\text{Gd} + {}^1_0\text{n}$	$\longrightarrow$	${}^{158}\text{Gd}^*$		
		$\longrightarrow$	${}^{158}\text{Gd} + (\gamma\text{'s} + \text{ce}\text{'s}; 8.5 \text{ MeV})$	
${}^{235}\text{U} + {}^1_0\text{n}$	$\longrightarrow$	fission fragments + $\sim 80 \text{ MeV}$		
${}^{239}\text{Pu} + {}^1_0\text{n}$	$\longrightarrow$	fission fragments + $\sim 80 \text{ MeV}$		

high neutron capture cross section is well-known (see figure 2.1) but the probability of internal conversion is only 4% of that of  ${}^{155}\text{Gd}$  and  ${}^{157}\text{Gd}$ .

In table 2.2 the reaction cross sections  $\sigma_n$  and individual particle energies of the reactions are given, together with the natural abundances and prices of the enriched isotopes. The cross sections are listed for  $1.8 \text{ \AA}$  (25 meV) neutrons.

In addition, figure 2.1 shows the dependence of the cross sections on the neutron energy  $E_n$ . The cross sections of  ${}^3\text{He}$ ,  ${}^6\text{Li}$  and  ${}^{10}\text{B}$  are inversely proportional to  $\sqrt{E_n}$ . For the detector application this means that the neutron absorption probability varies smoothly and in a known manner, a feature which is very useful in some experiments. The cross sections for the other reactions show a more complex energy dependent structure.

### 2.2.1 The ${}^3\text{He}$ reaction

The first isotope in table 2.1,  ${}^3\text{He}$ , is widely used in proportional gas chambers. The advantages are the high capture cross section and the low atomic number ( $Z = 2$ ) which guarantees a low gamma sensitivity of the detector. A disadvantage is the long range of the reaction products in the gas, which negatively affects the spatial resolution. The ranges amount to 6 cm for the proton and 2.5 cm for the triton in pure He gas at 1 bar at room temperature. By using a 'stopping gas', consisting of more heavy molecules like  $\text{CF}_4$ , and by increasing the pressure the ranges

can be significantly reduced. In 3 bars partial  $\text{CF}_4$  pressure the range is 1.5 mm and 0.5 mm, respectively for p and  $^3\text{H}$ .

### 2.2.2 The $^6\text{Li}$ reaction

The converter  $^6\text{Li}$  is used in scintillator materials, either as a dopant or as a constituent of the host crystal. It is also available as a metal foil and used in combination with proportional chambers. Its advantage is the high amount of energy released in the reaction. However, the reaction cross section is relatively low. The ranges of the triton and the alpha particles in solid matter are 40-150  $\mu\text{m}$  and 5-10  $\mu\text{m}$  respectively.

### 2.2.3 The $^{10}\text{B}$ reaction

$^{10}\text{B}$  is used in proportional gas chambers as  $\text{BF}_3$ , in solid state detectors as dopant, and as metal converter foil. In the  $\text{BF}_3$  medium at room temperature and 1 bar, the ranges of the reaction products are 3.8 mm for the alpha particle and about 2 mm for the Li particle. Note that these ranges are an order of magnitude shorter than those mentioned for 1 bar  $^3\text{He}$ .

In case of solid state detectors there are some interesting advantages. The neutron capture cross section is some four times higher than that of  $^6\text{Li}$ , and the available amount of reaction energy is still amply sufficient to generate a detectable signal. The 480 keV gamma ray, that is emitted in 93% of the cases, can be utilised as a coincidence signal to reduce the effects of ambient gamma background. On the other hand it can be disturbing if coincident registration is not possible, e.g. in position-sensitive detectors. The range of the reaction products in solid

**Table 2.2:** The neutron capture reaction cross sections at a neutron wavelength of 1.8 Å ( $\equiv$  25 meV), the energy of the useful reaction products and relevant data concerning the isotopes.

reaction	$\sigma_n$ [barns]	particle energy [MeV]	natural abundance	enrich- ment	price (USD)
$^3\text{He}(n,p)$	5333	p 0.57 $^3\text{H}$ 0.2	0.00014% <sup>a</sup>		90 $\text{dm}^{-3}$
$^6\text{Li}(n,\alpha)$	940	$\alpha$ 2.05 $^3\text{H}$ 2.74	7.5%	95%	1.5 $\text{g}^{-1}$ $^6\text{Li}$ metal
$^{10}\text{B}(n,\alpha)$	3837	$\alpha$ 1.47 $^7\text{Li}$ 0.83	19.8%	99%	12 $\text{g}^{-1}$ $^{10}\text{B}_2\text{O}_3$
$^{155}\text{Gd}(n,\gamma)$	60900	ce's 0.039-0.25	14.8%		
$^{157}\text{Gd}(n,\gamma)$	254000	ce's 0.029-0.23	15.7%	86%	8000 $\text{g}^{-1}$ $^{157}\text{Gd}_2\text{O}_3$
$^{\text{nat}}\text{Gd}(n,\gamma)$	48890	"	100%		1.5 $\text{g}^{-1}$ $^{\text{nat}}\text{Gd}_2\text{O}_3$
$^{235}\text{U}(n,\text{fission})$	583 <sup>b</sup>	$\sim$ 80 total	0.72%		
$^{239}\text{Pu}(n,\text{fission})$	748 <sup>b</sup>	$\sim$ 80 total	0		

<sup>a</sup>In fact,  $^3\text{He}$  is obtained as a product from nuclear industry

<sup>b</sup>fission only

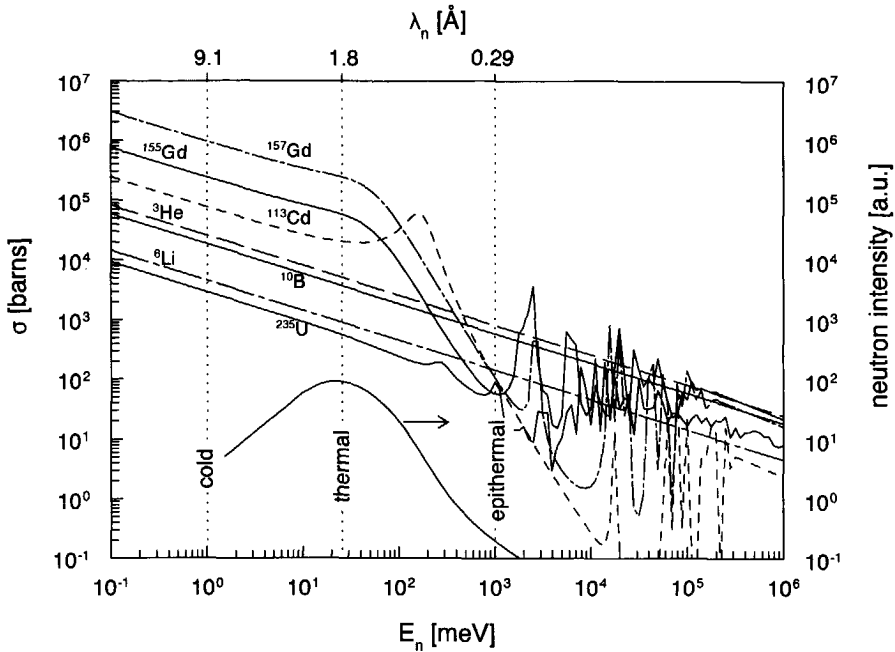


**Figure 2.1:** The cross sections for the most important neutron capture reactions versus the neutron energy. The lowest curve shows a typical spectrum of moderated neutrons at a nuclear reactor. Definitions of cold, thermal and epithermal neutrons are indicated.

matter is 3-7  $\mu\text{m}$  for the alpha particle and even less for  $^7\text{Li}$  nuclei. These numbers are smaller than those of the  $^6\text{Li}$  reaction, which can result in a better spatial resolution in some situations. However, short ranges imply relatively dense ionisation tracks. In scintillators, and probably also in storage phosphors, dense tracks reduce the efficiency of converting ionisation energy into photons. The latter will be discussed in more detail in the next chapter.

#### 2.2.4 The $^{155}\text{Gd}$ and $^{157}\text{Gd}$ reactions

Interesting are also the  $^{155}\text{Gd}$  and  $^{157}\text{Gd}$  isotopes because of their very high neutron capture cross sections. In enriched form these isotopes are expensive. However, due to these isotopes  $^{\text{nat}}\text{Gd}$  has the highest capture cross section of all natural elements. Note that the cross section declines rapidly in the epithermal region, see figure 2.1. When combining the natural abundances of  $^{155}\text{Gd}$  and  $^{157}\text{Gd}$  with the reaction cross sections it is found that in  $^{\text{nat}}\text{Gd}$ ,  $^{155}\text{Gd}$  captures 18.43% of the neutrons and  $^{157}\text{Gd}$  81.56%.

Very thin ( $\mu\text{m}$ ) foils of  $^{\text{nat}}\text{Gd}$  are sufficient for absorption of almost 100% of the thermal neutrons. The foils can be used in combination with low-pressure gas counters or semiconductor

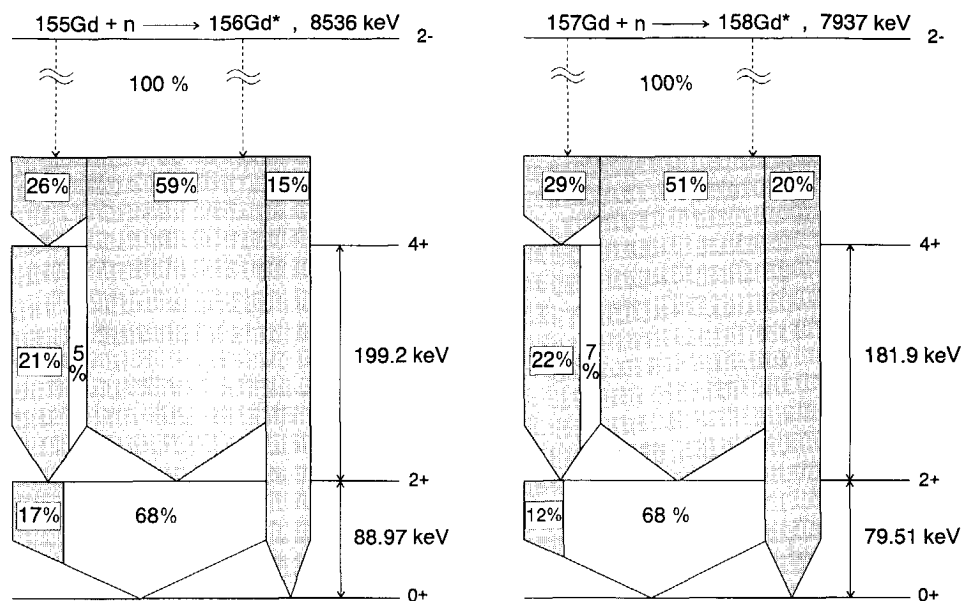


**Figure 2.2:** Simplified scheme of the decay from the lowest excited states of  $^{156}\text{Gd}$  and  $^{158}\text{Gd}$  that can be occupied after neutron capture by  $^{155}\text{Gd}$  and  $^{157}\text{Gd}$  respectively [10]. The white areas indicate decay by emission of a conversion electron, the dark areas by emission of a gamma ray.

based detectors to detect the secondary radiation. An important limitation is that the amount of energy given to conversion electrons is only some 50 keV on the average. This means for example, that Gd based scintillators will always have a low light output per absorbed neutron. Another disadvantage is the high atomic number ( $Z = 64$ ), implying a high gamma sensitivity per unit of mass.

Gadolinium is still an attractive converter in, for instance, the storage phosphor based image plate (IP) application (section 2.4.2), where the use of thin layers (100-300  $\mu\text{m}$ ) of detector material is indispensable. Therefore, the reaction products must be considered in more detail. The highly complicated scheme of decay transitions of the  $\text{Gd}^*$  nuclei has been studied and documented by Bäcklin *et al.* [14] and Greenwood *et al.* [15]. Initially the  $\text{Gd}^*$  nuclei are in a state energetically about 8 MeV above the ground state, corresponding with the binding energy of the captured neutron. The cascade of transitions that follows is mainly accompanied by emission of high-energy gamma rays ( $>200$  keV). For the transitions originating from the two lowest excited states of Gd, the energy released is less than 200 keV. From the neutron detection point of view, these transitions are most interesting.

In figure 2.2, a strongly simplified scheme of the population probabilities of the two lowest

excited states and the possible transition processes to the ground state are given, for both  $^{156}\text{Gd}$  and  $^{158}\text{Gd}$ . The figure shows that in respectively 15% and 20% of the  $\text{Gd}^*$  decay processes the two lowest states above the ground state (2+ and 4+) are not populated at all. So in  $^{\text{nat}}\text{Gd}$ , this number is 19%. If the lowest states do become populated, energy is not only released by means of gamma ray emission, but also emission of conversion electrons is possible. In  $^{\text{nat}}\text{Gd}$  the probability is about 70% that one or more conversion electrons are emitted.<sup>1</sup> Figure 2.2 does not indicate that the ejection of a conversion electron is followed by the emission of Auger electrons and/or characteristic X-rays. The energy of these electrons/X-rays depends on the atomic shell the conversion electron is ejected from.

### 2.2.5 The $^{235}\text{U}$ and $^{239}\text{Pu}$ reactions

The final basis for thermal neutron detection is provided by the fission of  $^{235}\text{U}$  or  $^{239}\text{Pu}$ . Although the reaction energy is very high, the relatively low cross sections, the (too) small ranges of the reaction products in solid matter and the difficulties concerning the enrichment of these isotopes make that they are relatively little used in practice. Flux monitoring by using U foil suspended in a gas chamber is reported by Mori *et al.* [17].

### 2.2.6 The DQE of a detector

For comparison of the detectors to be described below, the quantities characterising a detector should be well defined. One of the most important quantities is the probability that a neutron incident on a detector is registered. Before giving an accurate definition for this quantity, the distinction between a *counting detector* and an *integrating detector* should be clear.

A counting detector registers each neutron capture event individually, and timing information is in principle available. A scintillator is an example of a counting detector. An integrating detector adds up more detection events before giving an output signal, and thus does not provide timing information about a single event. An IP is an example of an integrating detector.

In the literature the neutron detection probability is termed 'detection efficiency' or 'quantum efficiency' (QE). Here 'detection efficiency' (DE) will be used:

$$\text{DE} = \frac{\text{Number of registered neutrons}}{\text{Number of incident neutrons}} \quad (2.1)$$

In the case of a counting detector this is an adequate quantity. Generally, the fact that the pulse height of the electric signal generated by a detection event varies from neutron to neutron is no problem as long as it passes a certain threshold or fits in a certain pulse height 'window'. Therefore the fraction of registered neutrons does often not differ very much from the fraction that is absorbed. In a scintillator based detector for example, the difference will be due to a small

<sup>1</sup>Recently, a controversy has risen about these numbers and the interpretation of experimental data. Gebauer *et al.* [16] state that in 87.3% of the cases one or more conversion electrons are released. However, there are strong arguments to suppose that this number can never be larger than 76%.



number of absorptions on the very edge of the scintillator crystal, generating substantially less photons because of quenching effects and secondary radiation escaping the crystal.

For an integrating detector the situation is more complicated. The number of neutrons registered by the detector can only be determined by taking the integral signal they generated and dividing it by the average signal that is expected for a single neutron. The signal of a single event, contributing to the integral signal, is susceptible to statistical and other variations, as is the case for counting detectors. Consequently the number of registered neutrons can not be deduced from the integral signal without consideration of a number indicating the variance of the number of neutrons. This variance is very important because the larger it is, the lower the detector quality. The problem is that the variance can not be taken into account in expression (2.1).

Rose [18] proposed in 1946 the concept that is usually termed the 'detective quantum efficiency' (DQE) but is also sometimes called the '(noise-)equivalent quantum efficiency', and that is applicable to any detector. For a detector input signal that varies only because of quantum noise it is defined as:

$$\text{DQE} = \frac{\left(\frac{\langle S_o \rangle}{\sigma_o}\right)^2}{\left(\frac{\langle S_i \rangle}{\sigma_i}\right)^2} = \frac{\nu_i}{\nu_o} \quad (2.2)$$

where  $\langle S \rangle$  is the mean integral signal,  $\sigma$  is the standard deviation or noise in this signal and the subscripts  $i$  and  $o$  refer to the input and output respectively. Equivalently, the DQE can be written as the ratio of the relative variances  $\nu$  in the input and output signal.

Taking the IP detector as an example,  $S_i$  is the number of neutrons incident on one pixel.  $S_o$  is the integral of the photomultiplier tube (PMT) current generated during the detection of the photostimulated luminescence of the pixel. The mean value of both can be determined by averaging the signals of many pixels that were exposed to the same radiation intensity or by many times repeating the experiment on one and the same pixel. Variations in the output signal are in the first place caused by statistical variation in the number of incident neutrons. Secondly by the variations in the number of created photostimulable centres per neutron and the number of photons detected by the PMT per photostimulable centre. For a perfect detector the DQE is unity and the image quality is only governed by the signal-to-noise ratio of the neutrons incident on each detector pixel.

The DQE can also be determined for a counting detector. Suppose that  $N$  Poisson distributed neutrons are incident on the detector such that  $DE \cdot N$  neutrons are counted. Then with equation (2.2) follows:

$$\text{DQE} = \frac{\left(\frac{DE \cdot N}{\sqrt{DE \cdot N}}\right)^2}{\left(\frac{N}{\sqrt{N}}\right)^2} = DE \quad (2.3)$$

which indicates that the DQE is in fact a more fundamental description of the same detector

quality.

It is important to note that for position-sensitive detectors the DQE is related to the spatial resolution. This is explained in detail in [19] and is only briefly mentioned here. For an input signal that modulates sinusoidally in one spatial dimension,  $1 + \langle S_i \rangle \cos(2\pi ux)$ , with  $u$  the so-called spatial frequency [19], the amplitude and the standard deviation of the output signal,  $\langle S_o \rangle / \sigma_o$ , depend on  $u$  according to:

$$\frac{\langle S_o \rangle}{\sigma_o} = \frac{\langle S_o(0) \rangle \text{MTF}(u)}{\sigma_o(u)}. \quad (2.4)$$

Here,  $\langle S_o(0) \rangle$  is the signal at zero spatial frequency and MTF is the so-called modulation transfer function [19]. The MTF is characteristic for the spatial resolution of the detector. By definition it equals 1 for  $u = 0$  and normally decreases to 0 for  $u \rightarrow \infty$ . However,  $\lim_{u \rightarrow \infty} \sigma_o(u) \neq 0$  and thus the DQE will decrease with increasing  $u$ . A detailed analysis of the MTF of the IP is given by Hillen *et al.* [20].

In the next sections different detectors will be discussed and compared, with an emphasis on position-sensitive systems. The separation between counting detectors and integrating detectors is used, since it fits well in the context of this thesis. The characteristic data of the detectors is obtained from literature. On basis of equation (2.3), 'DQE' is used in the tables 2.3 and 2.6 for all cases where the 'detection efficiency' or 'quantum efficiency' was used in the literature source.

## 2.3 Counting detectors

### 2.3.1 Gas proportional counters

Gas proportional counters are the most classical and widespread thermal neutron detectors. Both  $^{10}\text{BF}_3$  and  $^3\text{He}$  filled cells are used.  $^3\text{He}$  has the advantage of the higher capture cross section (table 2.2) and a higher grade of chemical inertness. The inertness enables the use of pressures up to 20 bars to enhance the quantum efficiency whereas for  $^{10}\text{BF}_3$  maximal some 3 bars can be applied. With  $^{10}\text{BF}_3$  still the highest resolutions can be obtained. Since the cost of  $^3\text{He}$  has dropped considerably over the last 20 years  $^3\text{He}$  detectors have become much more popular and  $^{10}\text{BF}_3$  detectors find only applications in some cold neutron experiments.

Even for a high-pressure chamber a neutron path length in the cm range is required to obtain a high absorption probability. With this neutron path length parallax errors in the determination of the event position can not be neglected. By increasing the sample-to-detector distance the parallax can be reduced, but this also reduces the solid angle covered by the detector. A long neutron path length in the detector is also at the expense of an accurate timing of the absorption event, which is necessary for so-called time-of-flight (TOF) experiments [12].

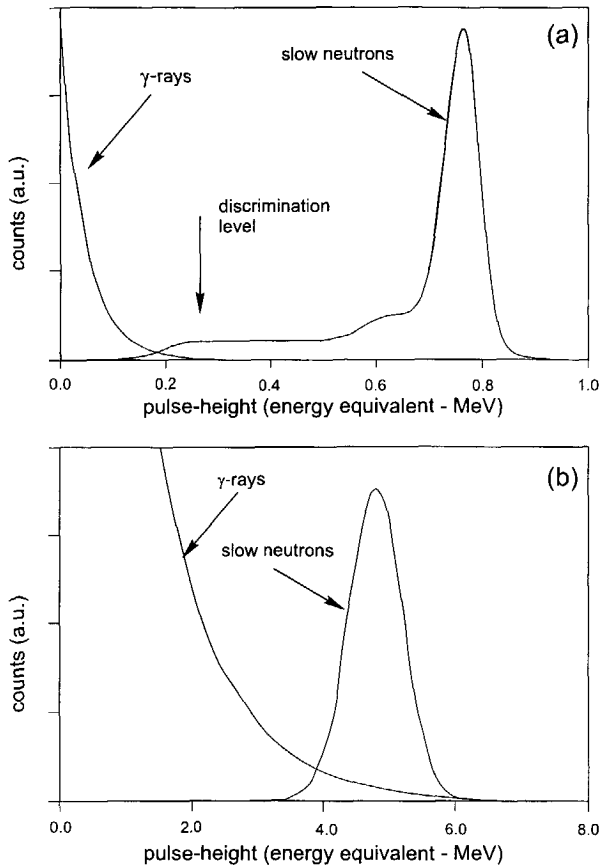


**Figure 2.3:** Typical pulse height spectra of (a) a  $^3\text{He}$  filled proportional counter and (b) a  $^6\text{Li}$  glass scintillator + photomultiplier. The x-axis is calibrated with the neutron peak by attributing the neutron reaction energy (0.77 MeV in (a), 4.78 MeV in (b)) to the peak maximum. Details on actual pulse height spectra will depend on specific detector geometries, materials, and operating conditions.

Since the energy needed to produce an electron-hole pair in neutron detecting gases is typically 30-35 eV, about 20,000(70,000) e-h hole pairs are produced when a neutron is absorbed in  $^3\text{He}(^{10}\text{BF}_3)$ . Then the statistical (Poisson) variation will be less than 1%. However, in proportional counters other contributions to the statistical broadening are more important [13], like the variations in the multiplication process. This results in a FWHM of the neutron peak in the pulse height spectrum of 10-15%, see figure 2.3(a). The tail on the left side of the neutron peak originates from energy loss during the gas ionisation process due to charged particles striking the

**Table 2.3:** Typical specifications of two gas based and two scintillator based counting detectors. The data of the gas detectors was obtained from [8], that of the fibre coupled system from [43] and that of the Anger camera from [51] and [8].

	gas detectors		scintillator detectors	
	MWPC BF <sub>3</sub> (1.5 bars)	banana <sup>3</sup> He (10 bars)	Fibre coupled <sup>6</sup> LiF/ZnS:Ag <sup>+</sup>	Anger camera <sup>6</sup> Li glass
thickness	1.5 cm	4.2 cm	0.4 mm	1 mm
DQE	60% @ 8 Å	80% @ 0.5 Å	50% @ 1.0 Å	82% 1.8 Å
pulse pair resolution	2-6 μs	2-6 μs	2.5 μs	300 ns
spatial resolution	2.5 mm	4 mm	3 mm	2 mm
γ-sensitivity <sup>a</sup>	~ 10 <sup>-7</sup>	~ 10 <sup>-8</sup>	<10 <sup>-7</sup>	2·10 <sup>-4</sup>
application <sup>b</sup>	SANS (2D)	PD (1D)	PD, CD	TOFPD (TOF)SANS PD, CD

<sup>a</sup>The probability that a 1.2 MeV gamma ray incident on the detector is registered as a neutron.

<sup>b</sup>SANS: small-angle scattering; PD: powder diffractometry; CD: single crystal diffractometry

detector wall.

Spatial resolution is obtained by construction of a multi-element array [21] or by using a multiwire proportional chamber (MWPC). The latter exists with 1D resolution capacity, like the so-called banana types [22], but also 2D MWPCs are widely used [23]. With MWPCs usually higher resolutions are obtained, but multi-element arrays allow higher pressures.

In table 2.3 the relevant data are listed for two typical position-sensitive gas proportional counters. The counting rates are limited by the collection time of the ions and the slow electronics of the charge sensitive amplifier. The spatial resolution is limited by the distance between the electrode wires. Because of mechanical reasons there is a minimum separation distance required. However, the fundamental limit of the resolution is determined by the range of the secondary particles. More particularly, by the asymmetry in the ionisation cloud around the point of reaction [8], which is due to the different ranges of the secondary particles. This implies that the resolution can not be much lower than 1 mm [11]. The data given in table 2.3 must be compared with similar data from scintillator based detectors to be discussed below.

Recent developments are the so-called microstrip [24,25] and microgap chambers [26]. The anodes and cathodes of a conventional multiwire proportional chamber are replaced by metallic strips, which are positioned on a glass substrate by means of photolithography. Shorter anode-anode and anode-cathode distances are possible, which leads to significant improvement of the count rate (factor >10) and a spatial resolution determined by the fundamental limit.

The advantages and disadvantages of gas proportional counters can be summarised as follows (+:good, o:average, -:negative):

- + High detection efficiency possible.
- + Low gamma sensitivity.
- + Low intrinsic background.
- + High stability.
- + Well developed technology.
- o Banana types combine a high detection efficiency over a large area with a moderate resolution (3-6 mm) at the expense of count rate and timing accuracy.
- o 2D multiwire chambers combine a relatively high resolution (2 mm) with a moderate timing accuracy at the expense of detection efficiency and count rate.
- o Multi-element arrays combine a high detection efficiency over a large area with a high count rate, at the expense resolution (5-10 mm) and timing accuracy.
- Choice of geometry limited.
- Often expensive.

### 2.3.2 Scintillators: traditional materials

Densities of crystalline (or glass) materials are roughly three orders of magnitude higher than those of gases. This implies that the stopping power of solid state scintillators are much higher and neutron path lengths of several mm are sufficient for a high absorption probability.

Before discussing scintillator based detector systems the known scintillator materials suited for slow neutron detection and their properties will be given. In table 2.4 the most important materials are mentioned. The  ${}^6\text{Li}$  based materials are by far most popular. They will be discussed in more detail below.

#### Ce-activated ${}^6\text{Li}$ -glass

The first neutron glass scintillator was reported 40 years ago by Ginther [28], containing  ${}^{10}\text{B}$  as the converter constituent and Ce as activator. In 1960 he also reported about Li based glass [29]. Two years later Bollinger *et al.* reported about a group B and Li containing glasses from which they concluded that the Li-containing series gives roughly an order of magnitude higher light output [30]. The present glass scintillators were developed by Anderson [31]. He reported for the first time about the use of 96% enriched  ${}^6\text{Li}$ . The glasses consist of  $\text{LiO}_2$ ,  $\text{MgO}$ ,  $\text{AlO}_2$ , and  $\text{CeO}_2$ . The highest light output was found for a  $\text{CeO}_2$  content of 6.5% by weight.

The whole series of commercially available glasses (NE-series, from the company Nuclear Enterprises [42]) has been examined in detail by Spowart *et al.* [32–34] with respect to light output, decay time and influence of temperature. It was found that too high a Li content quenches the

**Table 2.4:** Characteristics of solid state scintillator materials. The data of the  ${}^6\text{Li}$  containing materials was obtained from [11], that of  $\text{Gd}_2\text{SiO}_5:\text{Ce}^{3+}$  from [44].

material	conc. Li [ $\text{cm}^{-3}$ ]	light output pho/neutron	decay time [ns]	$\lambda_{em}$ [nm]	$\gamma$ -equiv. energy <sup>a</sup> [MeV]
${}^6\text{Li}$ -glass: $\text{Ce}^{3+b}$	$\sim 2.0 \cdot 10^{22}$	6000-7000	75	395	1.6
${}^6\text{Li}:\text{Eu}^{2+}$	$1.83 \cdot 10^{23}$	51000	$1.4 \cdot 10^3$	470	4.1
${}^6\text{LiF}/\text{ZnS}:\text{Ag}^{+c}$	$1.18 \cdot 10^{22}$	160000	$1 \cdot 10^3$	450	see text
${}^6\text{Li}$ glass: $\text{Tb}^{3+}$	$3.0 \cdot 10^{22}$	45000	$3 \cdot 10^6$	550	
$\text{Gd}_2\text{SiO}_5:\text{Ce}^{3+}$	-	800	56/600	430	0.077

<sup>a</sup>The energy of a gamma quantum that, when fully absorbed, induces a scintillation pulse with equal pulse height as a neutron-induced pulse.

<sup>b</sup>Data representative for NE905, NE908, NE912 and dependent on exact glass composition [42]; According to [27] the light outputs are much lower: 2000-3000 pho/neutron.

<sup>c</sup>Powdered crystal mixture in a plastic binder, similar to NE422 or NE426 [42].

light output and a good compromise is found at a  ${}^6\text{Li}$  content of 7% by weight (like e.g. NE905, see table 2.4). In figure 2.3(b) a typical pulse height spectrum of a Li-glass/PMT combination is given which shows the overlap between the gamma and neutron spectra. A neutron-induced scintillation pulse has the same pulse height as a pulse induced by a 1.6 MeV gamma ray (table 2.4). Hence, n- $\gamma$  discrimination based on pulse height has limited effect. The possibility of pulse shape discrimination has also been examined [35, 36]. Unfortunately the decay time of scintillation pulses induced by gamma rays differs only 6-10% from those induced by neutrons. The FWHM of the neutron peak is usually 10-20%.

With the current status of this technology the favourable features of the glasses are the short decay time and the versatility in possible thicknesses and sizes at low cost. Important disadvantages are the relatively low light output and the high gamma sensitivity.

### ${}^6\text{Li}:\text{Eu}^{2+}$

${}^6\text{Li}:\text{Eu}^{2+}$  is the only well-known inorganic thermal neutron scintillator that is available as a single crystal. Efficient scintillation in LiI was first recognised by Hofstadter *et al.* [37] who activated it with  $\text{TI}^+$ . Later Schenck *et al.* [38] reported it to be even more efficient when doped with  $\text{Eu}^{2+}$ . It combines a high light yield with a neutron stopping power that exceeds that of the others by far (table 2.4). The gamma equivalent energy has the high value of 4.1 MeV. This is much higher than that of a glass scintillator and facilitates the discrimination against gamma rays on basis of pulse height.  ${}^6\text{Li}:\text{Eu}^{2+}$  is commercially available with 95% enriched  ${}^6\text{Li}$ .

There are also some important drawbacks of this material. At first there is the rather long decay time of  $1.4 \mu\text{s}$ . Secondly, the gamma equivalent energy may be favourable, but simultaneously the gamma absorption probability is high. Obviously, Iodide with  $Z = 53$  that makes

up 95 mass percent of this compound, is responsible for this. Other practical problems are its high hygroscopicity which necessitates sealing of the scintillator, and its high refractive index of 1.96, which makes optical coupling difficult. Furthermore it should be stored in the dark since illumination of daylight causes the formation of colour centres.

These practical problems make this crystal only a best choice for specific experimental conditions:

(a) At spallation sources (with relatively many epithermal neutrons) when a high detection efficiency is important. Kurz *et al.* have demonstrated that by electronically shaping a pulse pair resolution of less than 150 ns can be obtained [39].

(b) For high spatial resolution (<0.5 mm) experiments. The maximal resolution is directly connected with the light output as will be pointed out later.

### ${}^6\text{LiF/ZnS:Ag}^+$

Mixing of converter and scintillator material in the form of crystalline grains of several  $\mu\text{m}$  should allow a much greater flexibility in the choice of the scintillator compounds. But in practice it is difficult to match the refraction indices of the compounds so that such mixtures are usually not very transparent for their own scintillation light. This is also the case for the  ${}^6\text{LiF/ZnS:Ag}^+$  mixture pressed together with an organic binder, that was already tested in the early 50's [40]. Also  ${}^{10}\text{B}$  and  ${}^{235}\text{U}$  were tried as converters by many researchers [41], but the shorter range of the reaction products appeared to affect the light output negatively. Today the commercially available plates consist of a 0.4 mm thick layer deposited on a 1 mm thick Al layer [42]. The neutron path length being short implies that short sample to detector distances can be used without causing a significant parallax error. However, the short path length also implies that the neutron absorption probability is only 28% at 1.8 Å. Stacking of plates or tilting the plate with respect to the average neutron beam direction are both utilised to improve the detection efficiency [43]. This is attended by an increase of parallax.

The highly efficient scintillator guarantees an exceptional high maximum light output per neutron absorbed, but still the self-absorption is responsible for a long tail of the neutron 'peak' in the pulse height spectrum that goes down to 0 photons per neutron. Therefore the definition of the gamma equivalent energy does not apply for this detector. Important are also the relatively low gamma sensitivity of the plate and its rather long decay time of 1  $\mu\text{s}$ .

### $\text{Gd}_2\text{SiO}_5:\text{Ce}^{3+}$ and $\text{Gd}_2\text{O}_2\text{S:Tb}^{3+}$

$\text{Gd}_2\text{SiO}_5:\text{Ce}^{3+}$  has been examined by Reeder [44]. Despite the complexity of secondary radiation, the pulse height spectrum recorded in a neutron field shows a particular peak at 77 keV which, according to the author, could be used for neutron counting. However, only a small fraction of the neutron absorptions will contribute to this peak and gamma discrimination will remain difficult.

$\text{Gd}_2\text{O}_2\text{S:Tb}^{3+}$  has been reported to be used in a neutron imaging device that was originally

designed for X-ray imaging [45]. It is thought to be useful for real-time radiography. No specifications were given. However, the response time of the Tb luminescence centre is at ms level.

### Liquid, plastic, or gas scintillators

Those scintillators are rarely used for thermal neutron detection. Liquid and plastic scintillators consisting of organic materials have a very short decay time in common and find applications in fast neutron experiments. Attempts to introduce thermal neutron converters have been unsuccessful so far because of poor light output [39]. The inert gases and N<sub>2</sub> are known to scintillate. For the operation of a detector based on a <sup>3</sup>HeXe gas mixture, see [46].

### 2.3.3 Scintillators: Fibre coupled systems, Anger cameras and other systems

Two detectors that are based on inorganic scintillators are mentioned here.

The first is a so-called fibre-optic encoded scintillation counter, first demonstrated by Davidson *et al.* [47]. The principle of fibre-coupling is sketched in a simple form in figure 2.4. The light produced by neutron capture in any scintillator element is divided among three fibre-optic channels, which are then coupled to a unique combination of three PMTs. This way the ratio between the number of PMTs and the number of elements is reduced.

The specifications of this detector type are included in table 2.3, to compare them with those of gas based counters. The data is given for the <sup>6</sup>LiF/ZnS:Ag<sup>+</sup> based fibre coupled system operational at ISIS [43]. Summarising, this system as well as other <sup>6</sup>LiF/ZnS:Ag<sup>+</sup> based scintillator detectors have the following advantages and disadvantages:

- + Low gamma sensitivity.
- + Small parallax errors.
- + Low intrinsic detector background.
- + Easy to cover large, continuous areas.
- o Moderate resolution.
- Relatively low detection efficiency (20-50% @ 1.8Å) because limited thickness.
- Low maximum count rate.

Applications are found in crystal and powder diffractometry.

The second detector to be mentioned is the Anger camera which is sketched in figure 2.5. This detector became an attractive option for neutron detection by the work of Strauss [48]. More recent developments are reported by Kurz *et al.* and Heiderich *et al.* [49,50].



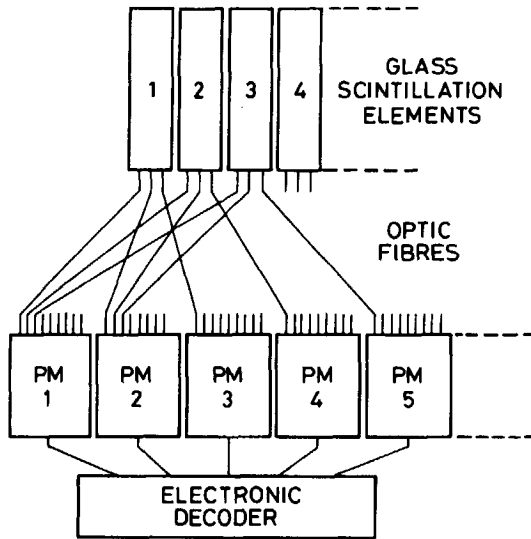


Figure 2.4: Principle of the fibre-optic coding of a discrete element scintillation detector [8].

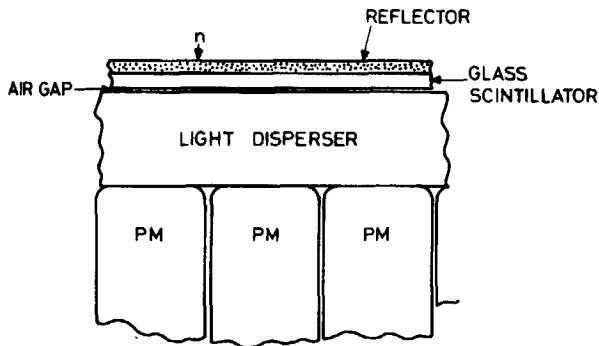


Figure 2.5: Schematic of the construction of a neutron Anger camera [8].

It consists of a single sheet of scintillator material, a light disperser and a set of photomultipliers. Each PMT sees a certain part of the scintillation event and by a 'point of gravity calculation' the location of the event can be reconstructed. The purpose of the air-gap is that total internal

reflection restricts the cone of light to a  $\sim 45^\circ$  forward angle, i.e. to just a few PMTs around the event centre. The characteristic data of the Anger camera are given in table 2.3. They represent the  $^6\text{Li}$  glass based type as presented in [50, 51]. The pulse pair resolution of the Anger camera of some 300 ns is longer than the scintillator decay time of 75 ns, which is due to the readout electronics. Still, it is better than that of other detectors. Its spatial resolution is inverse proportional to  $\sqrt{N}$ , with  $N$  the number of photons emitted by the scintillator per neutron absorbed [52]. Kurz *et al.* have demonstrated that using  $\text{LiI:Eu}^{2+}$  instead of glass improved the resolution to 0.5 mm [39], at the expense of pulse pair resolution and other qualities.

$^6\text{Li}$  glass is also used in fibre-coupled systems, giving properties comparable to those of the Anger camera. The properties of the Anger camera and other Ce-activated  $^6\text{Li}$  glass based detectors can be generalised as follows:

- + Relatively high count rates possible.
- + High neutron sensitivity possible, also for epithermal neutrons for large areas.
- + Small parallax errors.
- + Good detection timing ( $1 \mu\text{s}$ ) because of thin layers.
- + Lower cost than  $^3\text{He}$  detectors.
- o Resolution comparable with that of gaseous systems but improvement is possible.
- Relatively high gamma sensitivity.
- Some intrinsic background due to radioactive Ce-isotopes.

To improve the resolution without loss of the other qualities there are two possibilities. The first is to use PMTs with a smaller diameter. To improve the resolution with a factor of 2 requires 3 times more PMTs and preamplifiers which highly raises the costs. The second is to find a more efficient scintillator. Probably this would also result in a reduction of the gamma sensitivity. Applications of Anger cameras are already found at pulsed neutron sources, high neutron intensity experiments, TOF experiments and/or experiments with  $< 1 \text{ \AA}$  neutrons.

An interesting development is the combination of  $^6\text{Li}$  glass with a microchannel plate (MCP, an image intensifying device) as first proposed by Schrack [53] in 1984. Recently, such a detector with a spatial resolution of no more than  $40 \mu\text{m}$  and a gamma sensitivity of  $4 \cdot 10^{-6}$  at 662 keV has been presented [10]. An important drawback is the limited detection area that can be covered.

### 2.3.4 Foil detectors

If the neutron converter comes in the form of a foil, the charged particles created by neutron capture have a chance to escape from the converter and enter a charged particle detector like a gas

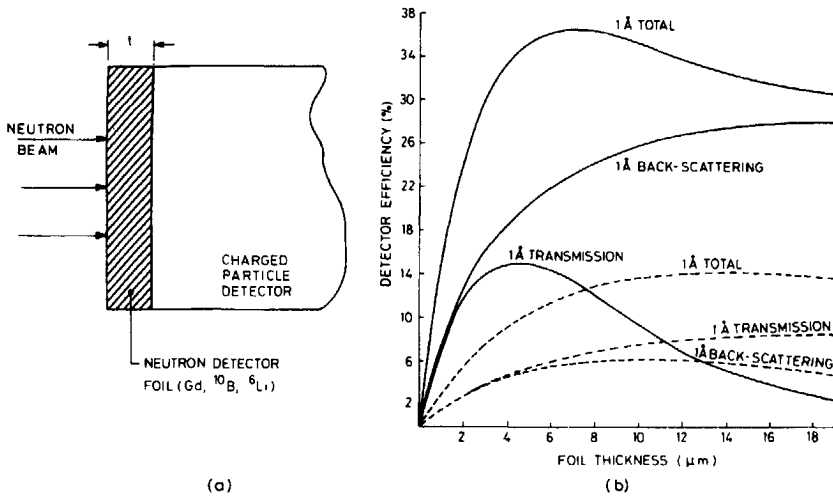


**Figure 2.6:** (a) Foil-converter detector in transmission geometry. (b) The efficiencies of  $^{157}\text{Gd}$  (solid lines) and  $^{\text{nat}}\text{Gd}$  foils (broken lines) for  $1 \text{ \AA}$  neutrons, as a function of thickness and detection geometry [8].

**Table 2.5:** Optimum thickness  $d_{\text{opt}}$  and quantum efficiencies for neutron absorbing foils. The quantum efficiency is defined as the probability that a  $1.8 \text{ \AA}$  neutron is captured and the secondary particle with the longest range can enter the detection volume.

material	particle	range [ $\mu\text{m}$ ]	$d_{\text{opt}}$ [ $\mu\text{m}$ ]	quantum eff. [%]
$^6\text{Li}$	p	120	97	$\sim 10$
$^{10}\text{B}$	$\alpha$	3.8	3.5	$\sim 4$
$^{157}\text{Gd}$	ce's	$\sim 8\text{-}80 \mu\text{m}$	4	$\sim 20$
$^{235}\text{U}$	fission	$\sim 8$	7.9	$\sim 0.6$

detector, semiconductor, or MCP. Foils can be used in transmission geometry (see figure 2.6(a)), backscatter geometry, or both. The neutron absorption probability increases with increasing foil thickness  $d$ , but the probability for the secondary particles to escape decreases. In a transmission geometry this means that a compromise has to be found. Table 2.5 lists the optimum foil thicknesses,  $d_{\text{opt}}$ , and maximum neutron quantum efficiencies for foils made of elemental (enriched) Li, B, Gd or U.

The foils have rather low capture probabilities. Foils in backscatter geometries give similar results except for the  $^{157}\text{Gd}$  foil which has an maximum efficiency of  $\sim 30\%$ . The detection

efficiency of a Gd foil detector versus the foil thickness is depicted in figure 2.6(b). The figure shows that when the charged particle detector is sandwiched by Gd foil, maximum detection efficiency of  $\approx 40\%$  can be obtained.

In particular for detectors employing  ${}^6\text{Li}$  or  ${}^{10}\text{B}$ , very broad neutron peaks in the pulse height spectra can be expected, because of the large spread in the energy of the particles escaping the foil.

Recently, Dangendorf *et al.* [54] presented a composite Gd/CsI foil/MWPC system that allows very high count rates ( $> 1 \text{ Mhz s}^{-1} \text{ mm}^{-1}$ ), good resolution ( $< 0.5 \text{ mm}$ ) and excellent timing accuracy (100 ns). The detection efficiency amounts 8% at 1 Å. Fraser *et al.* [55] presented a Gd foil/MCP system with good resolution (1.8 mm and potentially even  $< 0.5 \text{ mm}$ ) and a detection efficiency of 3.3% at 1 Å. A combination of a  ${}^6\text{LiF}$  layer on a silicon semiconductor has been examined by Schelten *et al.* [56]. A spatial resolution of 1.25 mm and a gamma sensitivity below  $10^{-6}$  is combined with a detection efficiency of 5% at 1.8 Å. Petrillo *et al.* [57] state that with a silicon pixel detector which is on both sides coated with Gd, a resolution of 40  $\mu\text{m}$ , a detection efficiency of 40% at 2 Å, and a count rate higher than 1 Mhz can be obtained. The value for the detection efficiency seems to be optimistic.

The properties of foil based counting detectors are obviously system dependent but can be summarised as follows:

- + High resolution possible.
- + Good timing accuracy possible.
- + Easy to cover large, continuous areas
- Low detection efficiency.
- Discrimination against gamma rays often difficult.

Counting detectors using a foil are applied in cold neutron experiments, TOF experiments, and radiography.

### 2.3.5 Semiconductors

Semiconductor detectors have proved to be successful for detection of X-rays and charged particles, because of their high energy resolution and the possibilities of spatial resolution provided by the semiconductor processing techniques [13]. Apart from the previously discussed combination with a foil, their application in slow neutron detection is yet unsuccessful, because direct detection of the neutron in the semiconductor bulk material is inefficient. Both B and Li are commonly used as dopants in Si detectors but their presence is only some  $10^{17} \text{ cm}^{-3}$ . A breakthrough in the direct detection of thermal neutrons in semiconductors awaits the development of another semiconductor material which can incorporate large amounts of Li or B in its active region. A study like presented by Kumashiro *et al.* [58] on the relatively unknown semiconductor material BP is therefore interesting.

**Table 2.6:** Characteristic data of three integrating detection systems. The data of the film/converter was obtained from [8], the data of the IP and the CCD system was obtained from [10].

	film + converter	IP (BaFBr:Eu <sup>2+</sup> ·Gd <sub>2</sub> O <sub>3</sub> )	CCD <sup>6</sup> LiF/ZnS:Ag <sup>+</sup>
thickness	<1 mm	150-300 μm	400 μm
DQE (@ 1.8 Å)	unknown	≤23%	≤12%
spatial resolution	20-100 μm	140 μm	300 μm <sup>a</sup>
dynamic range	0.3-1·10 <sup>2</sup>	10 <sup>5b</sup>	8·10 <sup>3</sup>
γ-sensitivity <sup>c</sup>	low	6·10 <sup>-3</sup>	5·10 <sup>-4</sup>
application <sup>d</sup>	SANS, CD	RD, SANS, PD, CD	RD, SANS

<sup>a</sup>When the light collecting lens is chosen such that an area 63×63 mm<sup>2</sup> of the total scintillator screen is used. If the entire screen of 280×280 mm<sup>2</sup> is used the resolution is worse.

<sup>b</sup>This is the dynamic range of the storage phosphor material. The dynamic range of the system presented in [10] is smaller due to the PMTs used. By using modern PMTs the entire range can be employed.

<sup>c</sup>Measured at 662 keV.

<sup>d</sup>see footnote table 2.4; RD: radiography.

## 2.4 Integrating detectors

By definition integrating detectors do not provide timing information of the detection of single neutrons. They are therefore unsuitable for time-of-flight experiments and less favourable for spallation sources. On the other hand, they do not have a limitation concerning the count rate. Moreover, the systems that will be discussed have in common that the spatial resolution is high, there is virtually no parallax and the covering of large detector areas is easy.

### 2.4.1 Photographic techniques

Photographic film has been used for neutron diffraction experiments since 1948 [59] and is still regarded as the standard high resolution imaging detector. The film consists of ~5 μm silver halide grains that determine the intrinsic resolution of such detector. It is blackened by the secondary radiation of a converter foil. When quantitative results are required the blackening, which is expressed in the so-called optical density, can be read-out and digitised with an optical scanner. The intrinsic resolution is best approached when Gd foil is used as converter: 20 μm is possible. As an alternative converter a <sup>6</sup>LiF/ZnS:Ag<sup>+</sup> screen can be used which simultaneously acts as intensifier. Hohlwein describes a system where a film is sandwiched between two such screens [60] and reports a resolution of 100 μm. In table 2.6 typical data is given for the most important features of this detector.

An important disadvantage of film is that in the optical density versus neutron-dose curve a

small linear regime is rapidly followed by a saturating regime. This explains the small dynamic range given in table 2.6. The DQE is unknown but the neutron absorption efficiency is  $2 \times 27\%$  at 1.7 Å. Hohlwein has shown that about 2000 neutrons/mm<sup>2</sup> are necessary to obtain an optical density located in the centre of the dynamic range. This suggests that only a few neutrons per  $100 \times 100 \mu\text{m}$  pixel are necessary for a useful signal.

The characteristics are summarised as follows:

- + Low gamma sensitivity.
- + Low cost and maintenance, no electronics required.
- o DQE unknown.
- Small dynamic range.
- Hard to get accurate quantitative results.
- Measurement results not instantaneously available.

### 2.4.2 Image plates

As indicated in chapter 1 this detector type is rather new and subject of development. Using the X-ray storage phosphor material BaFBr:Eu<sup>2+</sup>, different concepts for a neutron-sensitive IP have been tested. Reported in literature are BaFBr:Eu<sup>2+</sup> powder deposited on Gd foil in a backscatter geometry [6, 61, 62], a powder mixture of LiF [63, 64] or Li<sub>2</sub>CO<sub>3</sub> [64] and BaFBr:Eu<sup>2+</sup>, and a mixture of Gd<sub>2</sub>O<sub>3</sub> with BaFBr:Eu<sup>2+</sup> [6, 62–65]. Best result with respect to the DQE and the spatial resolution have been achieved using the latter concept. The option of reading out the plate on the side opposite to the irradiation side has been examined, with negative result [66].

The current detector properties have been best specified by Rausch and are indicated in table 2.6 for comparison with the film based detector. Apart from the efficiency of the storage phosphor BaFBr:Eu<sup>2+</sup> in converting ionisations into photostimulable centres, the DQE of the IP depends on the volume ratio between BaFBr:Eu<sup>2+</sup> grains, Gd<sub>2</sub>O<sub>3</sub> grains and the binder material and on the packing density of the grains. The spatial resolution is determined by the scattering of the stimulating laser light at the grain/binder boundaries. This in turn depends on the size of the grains, their packing density, the plate thickness, and the difference between the refraction index of the powder grains and the binder. Some of these aspects will be discussed in more detail in chapter 7.

The rather high gamma sensitivity is caused by the presence of Ba and Gd, both elements with a high atomic number. Another problem that can occur if the dynamic range of the plate is fully employed, is the activation of Br, Ba and Eu isotopes during irradiation. Beta and gamma rays emitted from activated nuclei create a 'ghost' picture as a signature from previous irradiations, in addition to the current picture.

It is also inherent to this phosphor material that the stored information fades away. Due to fading, the PSL signal decreases to 60% of its initial value in the first 10 minutes after irradiation. Then, fading slows down. After 1.5 hours the PSL signal 50% of its initial signal.

Finally it is noted that time is needed to perform a readout scan and to erase the information that is left, before the detector is operational again. Von Seggern [67] reports a total time of about 40 s for a plate of 20×30 cm.

The qualities and drawbacks of this detector can be summarised as follows:

- + Relatively high DQE.
- + High resolution (although inferior to film/converter).
- + Large dynamic range.
- + Easy to cover large, continuous areas.
- + Low intrinsic background.
- Relatively high gamma sensitivity.
- Ghost picture, although in most cases not disturbing.
- Readout and 'reset' time needed between to measurements.
- Stored information fades away.
- Rather complicated system compared to the other integrating detectors.

Within the concept described here, research is continuing to optimise the IP by varying the weight percentage of  $Gd_2O_3$ , the plate thickness and the packing density of the grains. Recently, a DQE of 40% at 2.1 Å has been measured by Wilkinson [68]. Furthermore it has been proposed to remove the  $^{79}Br$  isotope in order to reduce the effect of ghost images in case a high dynamic range is required. Crawford [69] has incorporated Gd in the storage phosphor by preparation of  $Ba_{0.78}Gd_{0.1}K_{0.1}Eu_{0.02}FBr$ . Unfortunately, the sensitivity of this material was reduced to 60% of the original material.

For the given storage phosphor/converter combination there are no possibilities for significant reduction of the gamma sensitivity. Therefore Von Seggern [67] proposed to test other storage phosphors with a lower effective  $Z$  like  $SrFBr:X$ ,  $KCl:X$ ,  $KBr:X$ ,  $RbCl:X$  and  $RbBr:X$  ( $X=Eu, Ce$ ). In this thesis it will be pointed out that also boron based materials are interesting (see chapter 7) and several materials have been examined.

The neutron IPs have already found application in many experiments where time information is not needed like in radiography and tomography experiments [65], Laue scattering of biological macromolecules [70], and single crystal and powder diffraction [71].

### 2.4.3 CCD based detectors

The last detector system that will be discussed here has been introduced first by Chernyshov *et al.* in 1986 [72]. This detector consists basically of a scintillating screen ( ${}^6\text{LiF/ZnS:Ag}^+$ ) which is imaged by a demagnifying lens onto a charge coupled device (CCD), as sketched in figure 2.7. The CCD integrates the charge that is created during the illumination by the scintillator. The size of the CCD and the demagnification factor of the lens determine the size of the active area of the detector and, to a certain extent, its spatial resolution.

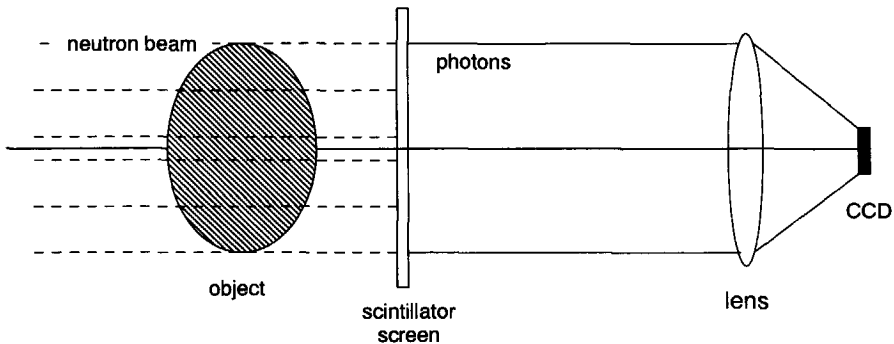


**Figure 2.7:** Schematic representation of a radiographic measurement with a scintillator/CCD detector.

Recently, Rausch [10] has reported about a system consisting of a  $28 \times 28 \text{ cm}^2$  screen that is projected onto a Peltier cooled CCD of  $512 \times 512$  pixels of  $19 \times 19 \mu\text{m}^2$ . The properties of this system are listed in table 2.6. The DQE is limited by the neutron absorption efficiency of the  ${}^6\text{LiF/ZnS:Ag}^+$  screen and by the dark current of the CCD, relative to the current (indirectly) generated by the neutrons. The latter could be much higher if the wavelength of the photons emitted by the scintillator would match the red-sensitive CCD better.

The current advantages and disadvantages of this detector are:

- + Large continuous area possible.
- + Simple construction.
- o Moderate gamma sensitivity, but better than that of IP.
- o Rather good spatial resolution, but worse than that of IP.
- Dark current of the CCD lowers DQE with increasing active detection area and decreasing neutron intensity.
- Cooling necessary to reduce dark current.



Also for this detector there are important prospects for improvement. CCD sensors with significantly lower dark currents per pixel are being developed and moreover CCDs with a sensitivity that is stretched towards the blue spectral range. On the other hand, it is proposed to use the Tb-doped glass scintillator (see table 2.4) or ZnS:Cu<sup>+</sup>, which both emit at longer wavelengths than ZnS:Ag<sup>+</sup> [10]. Also CCDs with smaller pixels become available which can improve the resolution of this detector.

## 2.5 Conclusion

Scintillation technology offers the opportunity to exploit a set of characteristics different from those available with gas technology. <sup>6</sup>Li loaded ZnS:Ag<sup>+</sup> screens are cost effective detectors, with flexible geometry and insignificant parallax. The spatial and pulse pair resolution, gamma sensitivity and detector background are comparable with some gas detectors. <sup>6</sup>Li loaded glass scintillators have a high pulse pair resolution, low parallax and high detection efficiency. These qualities are combined with a spatial resolution that is comparable with gas detectors, but the number of background and gamma induced counts is higher. Other scintillation detectors are less important.

None of the known scintillators combines a high light yield with a short decay time (< 100 ns) and a low intrinsic background. The short decay time, allowing high count rates, becomes a more important requirement considering the high intensity ESS source proposed (chapter 1). As indicated by Johnson [73], it is likely that in some experiments dead times of no more than 10-50 ns are required. A higher light yield can give rise to better spatial resolution, for example in Anger cameras, and also to a better gamma discrimination. If such a scintillator is found, detectors with a unique and rather complete combination of qualities become available.

The integrating detectors discussed have in common that their spatial resolution is higher than that of counting detectors and the count rate they allow is unlimited. The position of the image plates in this class is unique. Compared to film based techniques they show a much higher dynamic range and easy readout. Compared to CCD detectors they show a higher resolution which, in addition, is independent of the active area. Also the DQE of the IP is highest.

The most profound limitation is its high gamma sensitivity. To lower this sensitivity other storage phosphor materials should be examined. When using other materials, further improvement of the DQE is perhaps also possible.

# 3

## Selection of materials

### 3.1 Introduction

The materials that will be discussed in the following chapters were obviously not randomly chosen. But until today, the essential question 'What exactly makes a scintillator/storage phosphor efficient in converting ionisations into light?' has not been answered for any material. This implies that a certain degree of trial and error can not be avoided. However, some simple detector requirements limit the choice of materials considerably. Moreover, variations on a group of materials that has yielded good results before importantly increases the chance of success.

General selection criteria that apply both to scintillator and storage phosphor materials are:

- Neutron sensitivity
- Gamma sensitivity
- Decay time
- Emission wavelength (350-800 nm to match sensitivity of PMT or photodiode)
- Hygroscopicity

A low gamma sensitivity is required, as unwanted gamma radiation is in general present at neutron sources. In the following sections it will be discussed in general which materials provide a high neutron sensitivity and a low gamma sensitivity. Then, the discussion is confined to scintillators. Additional scintillator specific criteria will be given and it will be pointed out which materials can in principle have a short scintillation decay time.

Next, storage phosphors are discussed. Additional selection criteria which apply specifically to storage phosphors will be mentioned. The implications of the decay time requirement, being less stringent than for scintillators, will be briefly discussed. Then, the physics of the most well-known phosphor  $\text{BaFBr:Eu}^{2+}$  will be reviewed to provide an idea of defects which can act

as electron or hole traps. Also some other efficient (but neutron insensitive) storage phosphor materials will be mentioned.

Finally, some indications for materials that should be examined are given, both for scintillators and storage phosphors.

### 3.2 Neutron sensitivity

Because of the high neutron capture reaction energies the selection of materials is limited to Li or B containing compounds. This choice will be clarified below (see also chapter 7).

When a neutron traverses a distance  $d$  through a Li or B containing scintillator or storage phosphor medium, the probability  $P$  that it is captured amounts to:

$$P = 1 - e^{-\mu_n d} \quad (3.1)$$

where  $\mu_n$  is the linear attenuation coefficient. This coefficient equals to

$$\mu_n = N\sigma_n \quad (3.2)$$

with  $N$  the number of interaction centres,  ${}^6\text{Li}$  or  ${}^{10}\text{B}$  nuclei, per unit of volume and  $\sigma_n$  reaction cross section per  ${}^6\text{Li}$  or  ${}^{10}\text{B}$  nucleus<sup>1</sup>. For  $N$  applies:

$$N = \frac{\rho N_A W}{A} \quad (3.3)$$

with  $\rho$  the material density,  $N_A$  the number of Avogadro,  $A$  the molar  ${}^6\text{Li}$  or  ${}^{10}\text{B}$  mass and  $W$  the weight fraction of  ${}^6\text{Li}$  or  ${}^{10}\text{B}$  in the material.

So,  $\mu_n$  expresses the neutron capture cross section *per unit of material volume* and is proportional to the material density  $\rho$ . A high value for  $\rho$  seems attractive for a high neutron sensitivity but also the gamma sensitivity is proportional to  $\rho$ . Hence, when comparing different materials it is better to use the neutron and gamma sensitivity *per unit of mass*. For the neutron sensitivity follows:

$$\mu_n/\rho = \frac{N_A \sigma_n W}{A} \quad (3.4)$$

which is termed the mass attenuation coefficient in units of  $\text{cm}^2/\text{g}^{-1}$ . Apart from the converter isotope  ${}^6\text{Li}$  or  ${}^{10}\text{B}$ ,  $W$  is the only variable.

Which of the  ${}^6\text{Li}$  or  ${}^{10}\text{B}$  is preferred? As mentioned in chapter 2, it was found that for neutron sensitive glass scintillators the light yield of Li containing glasses is about an order of magnitude higher than that of B containing glasses. The reaction energies however, do only

<sup>1</sup>In fact  $\sigma_n$  is the neutron interaction cross section and  $\sigma_n = \sigma_{capt} + \sigma_{scat}$  where  $\sigma_{capt}$  is the neutron capture cross section and  $\sigma_{scat}$  is the scattering cross section. At the derivation of the equations (3.1) and (3.2) it is assumed that  $\sigma_{capt} \gg \sigma_{scat}$  such that  $\sigma_n = \sigma_{capt}$ .

differ by a factor of 1.72 (table 2.1). It is well-known that the light yield is not only related to the ionisation energy available, but also to the density of the ionisation track. In other words, the particle that creates the ionisations is important. Often, the efficiency of a scintillator in converting ionisation energy into photons decreases with increasing ionisation density. Thus a lower efficiency is expected for the ionisations caused by  $^{10}\text{B}$  capture reaction products when compared to those caused by the  $^6\text{Li}$  reaction products. It can be expected that the ionisation density is also important for the conversion efficiency of a storage phosphor.

It is this quenching effect that has confined the search for  $^{10}\text{B}$  loaded thermal neutron scintillators. Large quenching does not only imply a low light yield. It also implies a low gamma equivalent energy which complicates neutron-gamma discrimination. However, the amount of quenching is strongly dependent on the scintillator material, as illustrated in table 3.1.

**Table 3.1:** The experimentally determined light yield per unit of absorbed alpha particle energy,  $L_\alpha$ , relative to the light yield per unit of absorbed gamma ray energy,  $L_\gamma$ , for some well known scintillators. The energies of the alpha particles  $E_\alpha$  used in the experiment are also given. The gamma rays originated in all cases from  $^{137}\text{Cs}$  (662 keV).

compound	$E_\alpha$ [MeV]	$L_\alpha/L_\gamma$	ref.
CsI:Tl <sup>+</sup>	2.0	0.5	[74]
NaI:Tl <sup>+</sup>	5.3	0.5	[75]
LiI:Eu <sup>2+</sup>	2.1	0.19	[76]
LiF:Eu <sup>2+</sup>	5.3	0.95	[77]
BaF <sub>2</sub>	5.41	0.35	[78]
Lu <sub>2</sub> SiO <sub>5</sub> :Ce <sup>3+</sup>	4.17	0.14	[79]
Y <sub>3</sub> Al <sub>5</sub> O <sub>12</sub> :Ce <sup>3+</sup>	3.94	0.3	[80]
Bi <sub>4</sub> Ge <sub>3</sub> O <sub>12</sub>	5.3	0.15	[77]
CdWO <sub>4</sub>	5.3	0.075	[77]
GS20 glass <sup>a</sup>	5.49	0.23	[42]
NE102 plastic	5.3	0.084	[75]

<sup>a</sup>Equal to NE905

The table gives the experimentally determined ratio  $L_\alpha/L_\gamma$  for some known scintillators, where  $L_\alpha$  is the light yield per unit of energy deposited by an alpha particle, and  $L_\gamma$  is the light yield per unit of energy deposited by gamma rays. The energies of the alpha particles and gamma rays employed are also given because of the non-proportional response of scintillators which particularly applies for low energy alpha particles. The strong dependence of  $L_\alpha/L_\gamma$  on the scintillating medium is clear. It varies between 0.075 for CdWO<sub>4</sub> and 0.95 for LiF:Eu<sup>2+</sup>. It is to be expected that the gamma equivalent energy (defined in table 2.4) of most B containing scintillators  $\lesssim 1$  MeV and consequently n- $\gamma$  discrimination based on pulse height is not very

effective.

In conclusion, for scintillators the Li containing materials have the best prospects for high light yield and a high gamma equivalent energy. But B containing materials are still worth examining. The problem of the 'low' gamma equivalent energy can be partly resolved by using enriched  $^{10}\text{B}$ . Then a single-crystal thickness of 200-500  $\mu\text{m}$  is sufficient for absorption of more than 90% of the neutrons while the gamma sensitivity is low. Note also that according to table 3.1, the reaction products of the  $^{10}\text{B}(n,\alpha)$  reaction would still generate a light yield of 30,000-50,000 photons in  $\text{NaI:Tl}^+$  or  $\text{CsI:Tl}^+$ .

For storage phosphors the situation is different. As long as powder layers of storage phosphor material are used in an IP, the layer can not be thicker than several hundreds of  $\mu\text{m}$ . Thicker layers are not transparent for stimulating and emitted photons. A Li containing powder layer of this thickness will not show a high neutron absorption probability. Although a B containing layer will have a lower absorption probability than a Gd containing layer, the difference does not have to be so large. For instance, the thermal neutron absorption probability in a 300  $\mu\text{m}$  powder layer of  $\text{YBO}_3$  (95% enriched  $^{10}\text{B}$ ) with a packing density of 60%, is still 70%. Boron containing compounds should therefore not be excluded a priori when searching for neutron sensitive storage phosphors.

### 3.3 Gamma sensitivity

An equation similar to (3.4) applies for  $\mu_p/\rho$  the mass attenuation coefficient for high energy photons. But in this case all elements in a compound can have a significant contribution to  $\mu_p/\rho$ . The contribution  $(\mu_p/\rho)_i$  from element  $i$  with weight fraction  $W_i$  to  $\mu_p/\rho$  amounts to:

$$(\mu_p/\rho)_i = \frac{N_A \sigma_{p_i} W_i}{A_i} \quad (3.5)$$

where  $A_i$  is the mass number of element  $i$  and  $\sigma_{p_i}$  is the total photon interaction cross section per atom of element  $i$ .

For a photon energy of 50 keV - 10 MeV the photoelectric effect, Compton effect and pair production are the main effects responsible for interaction [81] and thus they contribute to  $\sigma_{p_i}$ . In all cases the contribution is proportional with  $Z_i^m$  where  $Z_i$  is the atomic number of element  $i$ . The power  $m$  depends on the type of interaction. Taking the photoelectric effect as an example,  $m = 4 - 5$  [81], dependent on the photon energy. For  $(\mu_p/\rho)_i^{phot}$ , the contribution of the photoeffect to  $(\mu_p/\rho)_i$ , can be written:

$$(\mu_p/\rho)_i^{phot} \propto \frac{N_A W_i Z_i^{4-5}}{A_i} \propto N_A W_i Z_i^{3-4} \quad (3.6)$$

where it is used that  $Z_i/A_i = 0.45 \pm 0.05$  for all elements except H. The dependence of  $\mu_p/\rho$  on the atomic number  $Z$  and the photon energy  $E_p$  is summarised in table 3.2 for the different interaction mechanisms.

**Table 3.2:** Dependence of the mass attenuation coefficient  $\mu_p/\rho$  for a high energy photon traversing a medium, on the photon energy  $E_p$  and the medium atomic number  $Z$ . The dependence is splitted up into the main interaction mechanisms contributing to  $\mu_p/\rho$ .

Dependence	on $E_p$	on $Z$
Photoelectric effect	$E_p^{-3}$	$Z^3 - Z^4$
Compton effect	$E_p^{-0.5} - E_p^{-1}$	$\sim Z^0$
Pair production	$E_p^1 - \ln(E_p)$	$Z$

The contribution of the Compton effect to  $\mu_p/\rho$  is almost independent of  $Z$  and consequently it is roughly the same for all materials (which do not contain H). Compton scattering is always dominant as the primary interaction for gamma energies between 1 and 5 MeV. This is also the range in which the gamma equivalent energy of a good neutron scintillator is located and therefore these gammas are most difficult to discriminate from neutrons.

Still the photoelectric effect is very important for absorbing Compton scattered photons. It is often involved in events where the full gamma energy is absorbed. The gamma sensitivity of different compounds varies mainly due to a different  $(\mu_p/\rho)_i^{phot}$ . So when comparing  $(\mu_p/\rho)_i^{phot}$  for different compounds it is clear from (3.6) that  $\sum_i W_i Z_i^{3-4}$  is the relevant parameter. Therefore the effective atomic number for the photo-effect,  $Z_{eff}$ , has been defined:

$$Z_{eff} = \sqrt[4]{\sum_i W_i Z_i^4}. \quad (3.7)$$

which will be used in this thesis. A low  $Z_{eff}$  is desirable for a neutron scintillator or storage phosphor. A low  $Z_{eff}$  is also beneficial for the insensitivity of high energy gammas ( $>5$  MeV), when the pair production becomes relevant.

## 3.4 Scintillators

In addition to the selection criteria mentioned in section 3.1 the following aspects are specifically important for scintillator crystals:

- Light yield (photons emitted per absorbed neutron)
- Index of refraction
- Crystal growth
- Crystal ruggedness

Additional information can be found in [82]. Of all the criteria, the scintillator decay time and light yield are decisive in a first selection.

### 3.4.1 Scintillation decay time

Scintillation is observed in hundreds of inorganic compounds. Also the variety of compounds is large: efficient scintillation is found in alkali halides, alkaline earth halides, sulphides, simple oxides and oxide systems like silicates, germanates, tungstates and aluminates. Some materials show intrinsic scintillation, others when they are activated with a luminescence impurity ion. In addition to the materials listed in table 3.1, the 'classical' scintillators  $\text{CaF}_2:\text{Eu}^{2+}$  [83],  $\text{ZnS}:\text{Ag}^+$  [84] and commercially available  $\text{Gd}_2\text{O}_2\text{S}:\text{Pr}^{3+}$  [85] can be mentioned.

In most scintillators, the last stage of scintillation, the luminescence, is well-understood and the various luminescence mechanisms can be easily classified. Only a few types of luminescence can show a decay time shorter than 100 ns:

- Core valence luminescence (CVL). This is a form of intrinsic host lattice luminescence. It involves electronic transitions between states of the upper core band and the valence band of the compound (see also chapter 4). These transitions offer a very short subnanosecond decay time but the scintillation light yield has never observed to be more than 2500 photons per MeV of absorbed gamma energy [86], being less than 7% of that of  $\text{NaI}:\text{Tl}^+$ .
- Excitonic luminescence. Fast excitonic luminescence can be a very efficient process below some 100 K, for instance in alkali halides and alkaline earth halides. But it is almost always quenched at RT. However, there are some exceptions.  $\text{Y}_3\text{Al}_5\text{O}_{12}$  exhibits exciton luminescence with a decay time  $\tau = 100$  ns, and a scintillation light yield of 27% relative to  $\text{NaI}:\text{Tl}^+$  [87]. The iodides  $\text{CsI}$  and  $\text{CdI}_2$  show excitonic-like luminescence at RT with decay times of  $10 + 36$  ns and 4 ns respectively [88, 89]. The scintillation light yields are not very high: about 6% and 1% relative to  $\text{NaI}:\text{Tl}^+$ .
- '5d-4f luminescence'. With this luminescence is meant the emission of photons by the class of rare-earth ions, connected with an electronic transition between an excited state belonging to a  $5d4f^{n-1}$  configuration and the ground state belonging to a  $4f^n$  configuration of the outer electrons. Contrary to, for example, the radiative transitions in the so-called  $ns^2$  ions like  $\text{Tl}^+$ ,  $\text{In}^+$  and  $\text{Bi}^{3+}$ , this transition is dipole allowed. For those rare-earth ions with a less than half-filled 4f shell ( $1 < n < 7$ , the series Ce-Eu in the periodic system) the transition is also spin allowed. In particular these dipole - and spin allowed transitions give rise to a relatively short luminescence decay time. The 5d-4f luminescence has by far the most potentiality for new fast neutron scintillators and is further specified next.

The decay times of the 5d-4f luminescence in triply ionised rare-earth ions vary between 20-80 ns for  $\text{Ce}^{3+}$  (in its ground state the number of electrons  $n$  in the 4f shell equals 1), 10-30 ns for  $\text{Pr}^{3+}$  ( $n=2$ ) and  $\leq 15$  ns for  $\text{Nd}^{3+}$  ( $n=3$ ). The energy gap between the ground state and the excited state increases with increasing  $n$ . For  $n > 3$  it usually exceeds the forbidden gap between the valence band and conduction band. With increasing  $n$  the probability also increases that the excited state belonging to the  $5d4f^{n-1}$  configuration is energetically positioned just above

excited states belonging to the  $4f^n$  configuration. Then nonradiative transitions from the former to the latter states can occur. Hence, with increasing  $n$  a radiative  $5d-4f$  transition becomes less probable. For  $Ce^{3+}$  the energy gap is smallest and therefore  $Ce^{3+}$  luminescence has been observed in the widest range of materials. The maximum of the  $Ce^{3+}$  emission band depends on the host lattice and varies between 282 nm in  $LaF_3$  [90] and about 700 nm in  $Y_2O_2S$  [91]. Fast  $Pr^{3+}$  luminescence has been mainly observed in wide bandgap materials like oxides and fluorides and ranges from 210 to 310 nm [92].  $Nd^{3+}$  is known to luminesce in several fluorides around 180 nm [92].

Most rare-earths have their highest stability in a compound when they are triply ionised. However,  $Eu^{2+}$ ,  $Sm^{2+}$ ,  $Yb^{2+}$  and  $Tm^{2+}$  can also be incorporated as stable impurities [77]. Also in these ions  $5d-4f$  luminescence is possible. But it is too slow for the scintillator application and often quenched at RT.

It is clear that the search for neutron scintillators should focus on  $Ce^{3+}$  activated lattices in the first place. Materials that could show both CVL and  $Ce^{3+}$  luminescence are most interesting (chapter 4).

### 3.5 Storage phosphors

For storage phosphors the following selection criteria should be added to the list give above:

- PSL yield/conversion efficiency
- Stimulation energy
- Dynamic range
- Rate of fading of stored information
- Stimulation wavelength

The PSL yield is defined as the number of photons emitted under photostimulation per incident neutron. For X-ray storage phosphors a similar quantity called the conversion efficiency (CE) was defined, being the photon energy emitted under photostimulation per unit of X-ray exposure and per unit of IP area, expressed in  $pJ/mm^2/mR$ . The stimulation energy (SE) is defined as the amount of laser energy needed per unit of IP area to reduce the PSL signal to  $1/e$  times the initial signal. The SE is expressed in  $\mu J/mm^2$ . Sometimes the 'PSL sensitivity' is used additionally, defined as the ratio  $(CE)/(SE)$  [93]. This is a measure for the number of photons emitted per stimulating photon, per unit of X-ray exposure.

Fading of stored information should be slow compared to the time needed for the exposure of the IP during experiment and readout. Efficient photostimulation should be possible with photons which are spectrally well-separated from the emission wavelength. Stimulation in the red or infrared region is preferred, enabling the use of a HeNe laser or solid-state laser.



### 3.5.1 Luminescence decay time

The luminescence decay time is also important for the IP application. If the optical stimulation of the trapped charge is a fast process it is the decay time which limits the readout speed of the IP. Therefore this decay time should preferably be no longer than 1  $\mu\text{s}$ . Considering the rare-earth ions this implies that next to  $\text{Ce}^{3+}$  (and  $\text{Pr}^{3+}$  and  $\text{Nd}^{3+}$ ) also  $\text{Eu}^{2+}$  can be used. Like  $\text{Ce}^{3+}$ ,  $\text{Eu}^{2+}$  luminesces in a wide range of materials with the emission maximum varying between 367 nm in  $\text{SrB}_4\text{O}_7:\text{Eu}^{2+}$  [94] and 720 nm in  $\text{CaO}$  [95]. The decay time of the  $4f^65d-4f^7$  transition amounts to 0.6-0.9  $\mu\text{s}$ . Among the divalent ions it is the most stable one and thermal quenching of the luminescence mentioned above occurs at relatively high temperatures, often above RT.

Also the mercury-like ions  $\text{Tl}^+$  and  $\text{In}^+$  are candidates, with decay times between 200 and 700 ns.

### 3.5.2 The case $\text{BaFBr}:\text{Eu}^{2+}$

The  $\text{Eu}^{2+}$  ion does also function as the recombination centre in the well known storage phosphor  $\text{BaFBr}:\text{Eu}^{2+}$ . In this phosphor the laser energy needed to stimulate the trapping centres is so low that in practice the  $\text{Eu}^{2+}$  luminescence decay time is the factor that limits the readout speed [96]. Because of its excellent stimulability and its efficient conversion of ionisations into photostimulable centres  $\text{BaFBr}:\text{Eu}^{2+}$  has been extensively studied. What has been understood today about the physical mechanisms responsible for storage and PSL in this material, is reviewed below.

#### Electron and hole storage centres

Several defects have been identified as electron storage centres, namely  $\text{F}(\text{Br}^-)$  and  $\text{F}(\text{F}^-)$  centres,  $\text{F}_A(\text{F}^-, \text{Eu}^{2+})$  centres and aggregates of two F-centres:  $\text{M}(\text{F}^-)$  and  $\text{M}_A(\text{F}^-, \text{Eu}^{2+})$  [97, 98]. Thoms *et al.* [98] found that the only electron centres that contribute significantly to the PSL process are the  $\text{F}(\text{Br}^-)$  centres, together with yet unidentified centres with a broad stimulation band centered around 400 nm, overlapping the  $\text{Eu}^{2+}$  emission at 390 nm. However, Spaeth *et al.* [99] recently reported that the  $\text{F}(\text{F}^-)$  are also photostimulable.

The nature of the hole centres is less well understood. In the literature there exists some controversy. Takahashi *et al.* [100] have reported an increase of the  $\text{Eu}^{2+}$  luminescence intensity after exposure to radiation implying that  $\text{Eu}^{2+}$  ions have trapped holes. Several authors dispute this model and can not reproduce the experiment. At low temperatures (<120 K) the trapped holes were found in the form of  $\text{Br}_2^- V_k$  centres [101]. When warming up to RT part of the holes recombine radiatively with the F-centres and another part diffuses to oxygen impurities which are unavoidably present. These impurities are located on fluoride sites and are denoted  $\text{O}_F^{2-}$ , becoming  $\text{O}_F^-$  when capturing the hole [102]. At low temperature the  $\text{O}_F^{2-}$  centres are charge compensated locally by  $\text{Br}^-$  vacancies, which may diffuse away above 200 K. Possible other hole sites have not (yet) been identified. It is possible that hole trapping is stabilised by  $\text{Eu}^{2+}$  impurity ions [103]. Also the presence of  $\text{OH}^-$  on several sites [104] and  $\text{H}_F^-$  centres [105] is

reported and their role as hole trap suggested, but more experimental evidence is needed.

### Formation of electron- and hole centres and recombination

There exists no unique proof about the formation of the storage centres upon irradiation. Two models are suggested so far which are based on different initial conditions. On the first model it is assumed that prior to irradiation a large number of  $\text{Br}^-$  vacancies are present which trap the electrons that were liberated under irradiation. The second model proposed by Von Seggern *et al.* [103] is derived from the model proposed by Itoh for alkali halides [106]. Defects are predominantly created during irradiation via highly excited excitons. The deexcitation energy of the excitons is used to displace Br atoms onto interstitial lattice sites. The vacancies created form F-centres with the electrons while the Br atoms are bound by  $\text{Br}^-$  ions to form  $\text{Br}_2^-$  H-centres. The role of the  $\text{O}_F^{2-}$  centres which are present prior to irradiation seems to support the first model.

The first stage of optical stimulation is well understood. The stimulating photons (2.1-2.5 eV) are absorbed by the  $\text{F}(\text{Br}^-)$  centres. Generally spoken, the energy level structure and the electron wave functions of the F-centre are quite similar to those of atomic hydrogen. The transition from the H-like 1s ground state to the 2p excited state is responsible for the absorption. This is followed by an energetic relaxation induced by a spatial relaxation of the surrounding lattice, due to the changed Coulombic interaction with the F-centre. The so-called 'relaxed excited state' (RES) is energetically close to the conduction band, according to [98] about 35 meV below the band edge. Next, there are several opportunities for the trapped electron, as suggested by different experiments [98]:

- (Non)radiative return to the ground state.
- Thermal escape into the conduction band followed by recombination with a trapped hole or retrapping by a Br vacancy.
- Tunnelling to a neighbouring hole centre.

The last two processes can give rise to PSL, although it is not clear how exactly the excitation of  $\text{Eu}^{2+}$ , which must be the last step before luminescence, takes place. Tunnelling requires spatial correlation between electron- and hole centres. Different experiments indicate that at least part of the electron and hole traps is correlated indeed, forming a complex together with  $\text{Eu}^{2+}$  activator ions [98, 101, 102]

An important phenomenon in the recombination process is the effect of replenishment of the PSL. When first the PSL signal of a sample is exhausted by optical stimulation at 10 K, followed by a warming up of the sample to RT and recooling, the PSL signal is restored. This experiment can be repeated several times [101]. Restoration also occurs after complete exhaustion at RT, and waiting for 24 h. The phenomenon is thought to be due to diffusion of electron and/or hole centres towards complexes where the centres and  $\text{Eu}^{2+}$  ions become spatially correlated and at which PSL is possible [102, 107]. This is consistent with the observed mobility of the  $\text{F}(\text{Br}^-)$

**Table 3.3:** The conversion efficiencies (CE) and stimulation energies (SE) of some x-ray storage phosphors relative to BaFBr:Eu<sup>2+</sup>.

Material	CE	SE	ref.
BaFBr:Eu	1	1	
Cs <sub>2</sub> NaYF <sub>6</sub> :Ce <sup>3+</sup>	0.3	4.1	[109]
RbBr:Tl <sup>+</sup>	-	-	[110]
KBr:In <sup>+</sup>	0.1	0.17	[111]
Ba <sub>5</sub> SiO <sub>4</sub> Br <sub>6</sub> :Eu <sup>2+</sup>	1.9	4.1	[112]
LiTaO <sub>3</sub> :Tb <sup>3+</sup>	-	-	[113]
Ba <sub>3</sub> (PO <sub>4</sub> ) <sub>2</sub> :Eu <sup>2+</sup> ,La <sup>3+</sup>	0.2	> 3 · 10 <sup>2</sup>	[114]

centres above 200 K. It is speculated by Harrison *et al.* [107] that here the notable efficiency of BaFBr:Eu<sup>2+</sup> finds its origin. The compound consists of layers of Br<sup>-</sup> and F<sup>-</sup> ions which are separated by the Ba<sup>2+</sup>. Electron centres can migrate over the bromine layers whereas hole centres are present in the fluorine layers, probably migrating as well, until a spatially correlated complex is formed.

### 3.5.3 Other storage phosphors

In many other materials PSL has been reported. Table 3.3 lists some of them, which have been characterised for X-ray imaging and show stimulation energies and conversion efficiencies of the same order of magnitude as BaFBr:Eu<sup>2+</sup>. The values are given relative to those of BaFBr:Eu<sup>2+</sup> since the absolute values reported by the different authors vary. Moreover, the conversion efficiency depends on the X-ray energy used [108]. Therefore the numbers have only an indicative meaning.

Nearly all compounds are halides. In all cases the role of the F-centres as electron traps is mentioned whereas the nature of the hole trap is often unknown. The dipole-allowed 1s-2p transition of the F-centres in alkali halides is known to have a high transition rate. A measure for the transition rate is the oscillation strength [115]. For F-centres, typical values from 0.3 to 0.85 have been reported [115]. In fact one may not expect to obtain higher values. Consequently, relatively low stimulation energies may be expected in halide based compounds.

In first approximation the position of the F-centre (1s-2p) absorption band is determined by the lattice spacing. Empirically the Mollwo-Ivey relation:

$$E_{2p} - E_{1s} = \frac{0.97}{(2a)^{1.77}} \text{ eV} \quad (3.8)$$

has been found for the alkali-halides [116], where  $a$  denotes the distance in nm between the nearest neighbours of the vacancy. It follows that the maximum of the F-centre absorption band shifts to longer wavelengths with increasing  $a$ . The lattice parameter  $a$  depends on the size of

the cations and anions. Absorption bands in the red region are found for alkali halide with large anions ( $I^-$  rather than  $F^-$ ) and large cations ( $Rb^+$  rather than  $Li^+$ ). A similar trend is observed for the alkaline earth fluorides and the mixed alkaline earth halides  $BaFX$  ( $X=Cl, Br, I$ ) [117].

$RbBr:Tl^+$  is given in table 3.3 because it is claimed that it has storage properties comparable to those of  $BaFBr:Eu^{2+}$ . The same applies for the non-halide  $LiTaO_3:Tb^{3+}$ . Only a few other oxidic compounds showing PSL can be found in the literature [118] (see also chapter 5) but the identity of the traps was never studied in great detail.

Another group of materials exhibiting PSL is formed by the infrared stimulable sulphides  $MS$  ( $M=Mg, Ca, Sr, Ba$ ) activated with both  $Ce^{3+}$  and  $Sm^{3+}$  or  $Eu^{2+}$  and  $Sm^{3+}$  [119, 120]. It has been demonstrated that upon UV exposure holes are trapped on  $Ce^{3+}$  (or  $Eu^{2+}$ ) and electrons on  $Sm^{3+}$ . This co-doping technique is known since long [121] and has also been successful in improving the efficiency of compounds already showing PSL. Examples are  $Ba_3(PO_4)_2:Eu^{2+}, La^{3+}$  [114],  $Ba_5SiO_4Br_6:Eu^{2+}, Nb^{5+}$  [122]. In these examples the incorporation of the co-dopant requires charge compensation, which may induce extra lattice vacancies.

## 3.6 Conclusions

The neutron sensitivity of a material must be characterised by its weight fraction  ${}^6Li$  or  ${}^{10}B$ ,  $W_{Li,B}$  as indicated in equation (3.4). The gamma sensitivity must be characterised by the effective atomic number  $Z_{eff}$  according to equation (3.7). Materials with a high  $W_{Li,B}$  and a low  $Z_{eff}$  are desirable.

### 3.6.1 Scintillators

Both Li and B containing hosts are worth studying. It should be possible to activate the host lattice with  $Ce^{3+}$ . This has the following implications for the host lattice material.

a) It should be transparent for the  $Ce^{3+}$  luminescence. Hence the band gap of the material should be wide enough. Incorporation of other ions that are optically active in the  $Ce^{3+}$  emission region, like the transition metals, must be avoided. Host lattice ions with the noble gas configuration are recommended.

b) The lattice must contain a cation that can be substituted by  $Ce^{3+}$ . Considering the periodic table of elements, the interesting ones are those that appear triply ionised in a compound, because then the substitution does not require charge compensation. Moreover, all elements with the atomic number  $Z$  greater than that of Ce ( $Z=58$ ) should be avoided, to retain a low gamma sensitivity. The candidates left are  $Sc^{3+}$ ,  $Y^{3+}$  and  $La^{3+}$ . As far as is known to the author, one has never succeeded in substituting  $Al^{3+}$  by  $Ce^{3+}$ . Apparently the difference in ionic radii is too large. Alternatively, one can think of the divalent cations  $Mg^{2+}$ ,  $Ca^{2+}$ ,  $Sr^{2+}$  and  $Ba^{2+}$ . It is hard to predict how the extra positive charge will be compensated. In  $BaF_2:Ce^{3+}$  there are indications that extra interstitial  $F^-$  ions are incorporated, and that so-called  $Ce_{Ba}^{3+}-F_i^-$  centres are formed. Other experimental observations are attributed to  $Ce_{Ba}^{3+}-O_F^{2-}$  centres, meaning that  $F^-$  ions on

regular sites are replaced by  $O^{2-}$  ions [123]. In  $SrB_4O_7:Ce^{3+}$  two  $Ce^{3+}$  ions replace three  $Ba^{2+}$  ions, resulting in clearly different  $Ce^{3+}$  sites [124]. The  $Mg^{2+}$  ion is small compared to  $Ce^{3+}$ , but efficient  $Ce^{3+}$  luminescence in for instance  $MgS:Ce^{3+}$  [125] and  $Mg_2SiO_4:Ce^{3+}$  [126] is observed.

Additionally, compounds in which CVL is possible next to  $Ce^{3+}$  luminescence are interesting. CVL is observed in wide bandgap compounds (fluorides, chlorides) containing large, monovalent or divalent cations like  $Cs^+$ ,  $Rb^+$ ,  $K^+$  and  $Ba^{2+}$  [86].

### 3.6.2 Storage phosphors

The selection must be confined to boron containing materials. It is unknown in which materials efficient hole trapping can be expected. Halide vacancies have proven to be attractive electron traps in  $BaFBr:Eu^{2+}$  and many other phosphors. Therefore the so-called haloborates are most interesting. These can be activated with  $Eu^{2+}$ ,  $Ce^{3+}$ ,  $Tl^+$ , or  $In^+$ . A list of existing haloborate stoichiometries is given in table 3.4. First candidates are the borates with the larger ( $I^-$ ,  $Br^-$ ) anions.

**Table 3.4:** Haloborate stoichiometries that have been reported in literature. When luminescence of dopants ions in one of these lattices is known, the dopant ion is given. In case of (fast)  $Eu^{2+}$  or  $Ce^{3+}$  luminescence the maximum of the emission band is added. With  $T_q$  the luminescence quenching temperature is denoted. References are giving information about structure, preparation and, if available, luminescence.

compound	dopant	maximum [nm]	ref.
$M_2B_5O_9Cl$ (M=Ca,Sr,Ba)	$Eu^{2+}$	410-450	[127]
$M_2B_5O_9Br$ (M=Ca,Sr,Ba)	$Eu^{2+}$	410-450	[128]
$Ca_2(BO_3)Cl$			[129]
$Ca_5(BO_3)_3F$			[130]
$Sr_5(BO_3)_3Cl$			[131]
$BaBOF_3$			[132]
$BaCaBO_3F$			[133]
$Ba_2Y(BO_3)_2Cl$	$Eu^{2+}$	465,570,low $T_q$	[134]
$Ba_2Y(BO_3)_2Cl$	$Ce^{3+}$	480,low $T_q$	[134]
$Ba_5(B_2O_5)_2F_2$	$Eu^{2+}$		[135]
$Ba_7(BO_3)_3F_5$			[133]
$Mg_3BO_3F_3$	$Eu^{3+}, Sm^{3+}, Pr^{3+}$		[136, 137]
$Mg_3B_7O_{13}X$ (X=F,Cl,Br,I)			[138]
$Mg_5(BO_3)_3F$			[139]
$Li_4B_7O_{12}Cl$			[140]

## 4

# LiBaF<sub>3</sub>, a thermal neutron scintillator with optimal n- $\gamma$ discrimination

## 4.1 Introduction

In this chapter the properties of a potential new thermal neutron detector, the inorganic scintillator LiBaF<sub>3</sub> are presented. This compound exhibits core-valence luminescence (CVL) and incorporation of Ce<sup>3+</sup> activator ions is perhaps possible.

First we report on the general scintillation properties of LiBaF<sub>3</sub>. The scintillation pulses induced by thermal neutrons are compared with those induced by gamma rays. Next, results are presented of a pulse shape discrimination method made possible by the different response of core-valence luminescence and self-trapped-exciton luminescence.

LiBaF<sub>3</sub> has the inverse perovskite structure [141], a density of 5.24 g/cm<sup>3</sup> and an effective atomic number  $Z_{eff}$  of 51. The weight fraction  $W$  of Li atoms is 3.45%. We studied a polished crystal with a diameter of 7 mm and a thickness of 1.75 mm. It contains natural Li.

## 4.2 Experimental

To obtain the emission spectrum, the crystal was continuously irradiated with X-rays from an X-ray tube (copper anode, 35 kV, 25 mA). The X-rays excite the crystal after passing a 0.3 mm beryllium window. The light emitted by the crystal is detected by a combination of a vacuum monochromator (model ARC VM502) and a Thorn EMI photomultiplier tube (PMT). The spectrum was corrected for the transmittance of the monochromator and the quantum efficiency of the PMT. The spectrum is compared with that of a pure BaF<sub>2</sub> single crystal recorded under identical experimental conditions. Because this crystal has a well-determined light yield of 11,000 photons/MeV of absorbed X-ray energy, the light yield of the LiBaF<sub>3</sub> crystal can also be determined by integration of the measured spectrum. Further details on the experimental set-up and the determination of the BaF<sub>2</sub> light yield can be found elsewhere [142].

Scintillation decay curves were measured either by means of the single photon counting technique [143] or by using a LeCroy LS 140 digital oscilloscope. Single photon counting was carried out with the multi-hit method [144] using LeCroy 934 Constant Fraction Discriminators for accurate timing of the start and stop pulses, a LeCroy 4208 Time-to-Digital Converter (TDC) for measurement of the time between start and stop pulses and a LeCroy 222 Gate Generator for definition of the time window after a start pulse. It has experimentally been verified that the time resolution of this system is predominantly determined by the channel width of the TDC which is 1 ns. The multi-hit dead time of the TDC is about 3 ns.

Pulse height spectra were recorded with standard spectroscopic techniques, using gamma or neutron radiation. The scintillation light (SL) yield is determined from these spectra as follows. The ratio of the single electron peak and the photopeak position yields the amount of photoelectrons  $N$  that are released on the PMT cathode due to detection of a scintillation pulse induced by a known amount of radiation energy  $E_r$ . Knowing  $N$ , the SL yield of the crystal can be found with:

$$\text{SL yield} = \frac{N}{\eta \cdot \text{QE} \cdot E_r} \quad (4.1)$$

where  $\eta$  is the collection efficiency of the emitted photons by the PMT and QE is the product of the quantum efficiency of the PMT cathode and the collection efficiency of the first dynode. Since the crystal is wrapped in Teflon (PTFE) foil  $\eta$  has the high value of 90%.

Thermal neutron induced scintillation measurements were carried out with a Pu-Be source surrounded by paraffin and 6 cm of Pb. The decay curve, however, was recorded with a <sup>244</sup>Cm

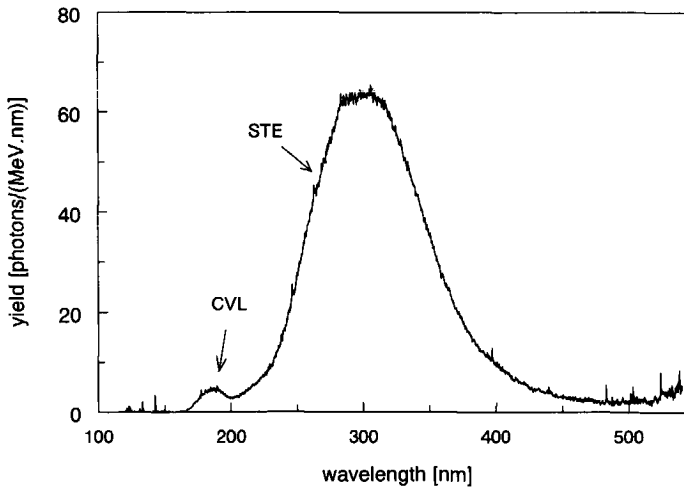


**Figure 4.1:** The X-ray induced emission spectrum of LiBaF<sub>3</sub>. Wavelength resolution 1 nm. A second CVL band is hidden under the broad STE emission band.

alpha source rather than with a Pu-Be neutron source because the Pu-Be source emits gamma rays as well. Using that source would unavoidably result in a contribution from gamma induced scintillation pulses. The alpha particles are supposed to simulate the reaction products of the neutron capture reaction (see table 2.1).

### 4.3 Results I: Scintillation properties

Figure 4.1 shows the emission spectrum of  $\text{LiBaF}_3$  under X-ray excitation. Similarly to the spectrum of pure  $\text{BaF}_2$  [145], two components can be distinguished:

(a) A 100 nm wide band with its emission maximum located near 300 nm. This band is due to self-trapped-exciton (STE) luminescence, as is strongly suggested by the excitation threshold close to the fundamental band gap of  $\approx 10$  eV [146], the width of the band, and the decay time of the emission which is in the  $\mu\text{s}$  regime (see below) [147].

(b) A more narrow band with its emission maximum at 187 nm. This band has been previously studied in  $\text{LiBaF}_3$  [146, 148, 149]. It is generally accepted that it is due to core-valence luminescence (CVL) [150]. A second emission maximum due to the CVL at 225 nm is hidden under the STE band [151].

The top of the STE band has a somewhat 'unnatural' shape. This is caused by the fact that the crystal is contaminated with 10-100 ppm Ce, giving additional weak ( $\approx 150$  ph/MeV) luminescence around 320 nm [152]. We assume that the type of irradiation does not affect the location of the emission maxima. It is noted that the emission spectrum is entirely different from that reported by Lecoq *et al.* [153]. They observe an excitation band peaking at 345 nm which is not sufficient to create an exciton in the matrix. Therefore it seems improbable that their spectrum belongs to the pure, non-irradiated material.

Curve 1 in figure 4.2 shows the scintillation decay curve of the  $\text{LiBaF}_3$  crystal, under excitation with gamma rays from a  $^{60}\text{Co}$  source. The fast component in the first 10 ns of the spectrum is due to the CVL. By fitting a more detailed decay curve measurement (see inset) of this component, a decay time  $\tau = 0.8$  ns was found. The peak at 15 ns after the fast component is due to a PMT afterpulse, which is an experimental artefact. Another short component with a decay time of several tens of ns is observed, which can be ascribed to luminescence of the Ce impurities [152]. The 'slow' exponential-like component with  $\tau \approx 6 \mu\text{s}$  is attributed to the STE luminescence. Furthermore, some emission at millisecond level can be observed on the oscilloscope. We note that the decay times reported are estimated values. A reliable fit of the decay curve could not be made.

Also in figure 4.2, the scintillation decay curve is shown recorded during irradiation with alpha particles from a  $^{244}\text{Cm}$  source, see curve 2. Obviously, the shape of the curve is different from that of curve 1 in the sense that the fast component is absent. We observe only the component  $\tau \approx 6 \mu\text{s}$  and an additional component with  $\tau \approx 32 \mu\text{s}$ . These values are derived from a two-exponential fit of the measured curve. Again, some emission at millisecond level is observed on the oscilloscope. It is not clear why curve 2 does not show the small Ce component observed



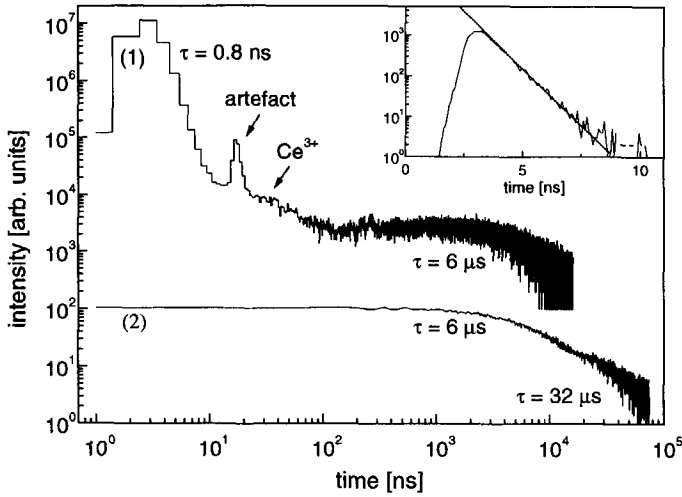


**Figure 4.2:** Curve 1: Decay curve of LiBaF<sub>3</sub> excited with <sup>60</sup>Co gamma rays, obtained with the single photon counting technique. The channel width is 1 ns. Curve 2: Decay curve of LiBaF<sub>3</sub> excited with <sup>244</sup>Cm alpha-particles ( $E_{\alpha} \approx 4.25$  MeV at arrival in the crystal). The spectrum is an average over 1000 events recorded with a LeCroy LS140 digital oscilloscope. Inset: Single photon counting measurement of the fast decay component. Channel width: 0.082 ns.

in curve 1. This is still a subject of study.

Similar decay curves are to be expected under alpha particle excitation or thermal neutron excitation. However, it should be noted that the alphas penetrate only several  $\mu\text{m}$  of the crystal whereas thermal neutrons are absorbed throughout the bulk. Thus, surface effects could cause a difference between the decay curves. This was checked by comparing pulse height spectra as a function of shaping time recorded with both radiation types. Also, individual scintillation events were compared on the digital oscilloscope. No essential difference in the decay pulse form was observed.

To obtain information on the absolute scintillation light yields for each scintillation decay component, pulse height spectra were measured as a function of the shaping time of the spectroscopic amplifier. Shaping times between 1 and 10  $\mu\text{s}$  were used. Figure 4.3 presents two examples of such spectra. Spectrum 1 is recorded under irradiation with 662 keV gammas and spectrum 2 under irradiation with thermal neutrons from the PuBe source. With the maximum shaping time of 10  $\mu\text{s}$  the absolute light yields of the 6  $\mu\text{s}$  component could be determined. But also the content of CVL component in the ns regime can be estimated by extrapolating the measurement results to  $\tau = 0 \mu\text{s}$ . However, as for the alphas, the maximum light yield in this component could be estimated more stringently from the oscilloscope measurements mentioned before. The results are presented in table 4.1.

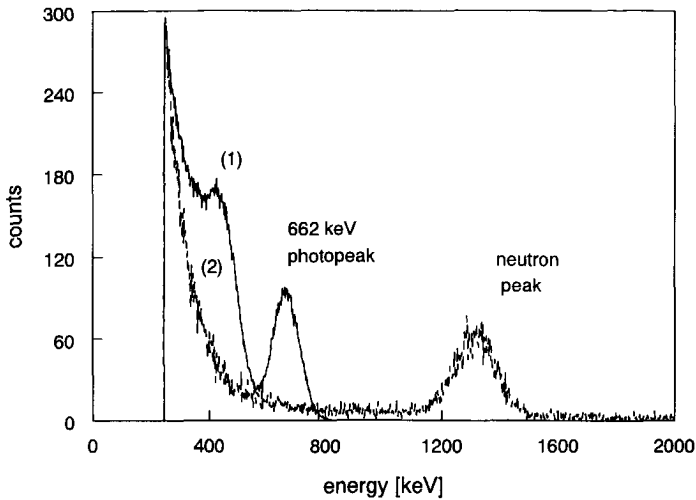


**Figure 4.3:** Pulse height spectra of LiBaF<sub>3</sub> excited with (1) 662 keV  $\gamma$ -rays and (2) thermal neutrons from a PuBe source. Shaping time  $\tau = 10 \mu\text{s}$ . The energy scale on the x-axis refers to the gamma energy.

**Table 4.1:** Estimated light yields of LiBaF<sub>3</sub> upon excitation by 662 keV gamma rays (column 2) and thermal neutrons (column 3). The light yields are given for each decay component in photons created per MeV absorbed gamma-ray energy or in photons per captured neutron. Upon gamma excitation, 4500 ph/MeV are emitted more than 6  $\mu\text{s}$  after excitation. Upon neutron excitation there is slow emission (2100 ph/MeV) with a decay time of 32  $\mu\text{s}$ . The light yield of slower emission components could not be determined.

component	$\gamma$ exc.(ph/MeV)	neutron exc.(ph/neutr.)
0.8 ns	$\leq 1200$	$< 10$
6 $\mu\text{s}$	1600	3500
slower	4500 ( $> 6 \mu\text{s}$ )	2100 (32 $\mu\text{s}$ ), ? ( $> 32 \mu\text{s}$ )

The number of 4500 photons/MeV, representing the light yield of the decay components  $> 6 \mu\text{s}$  is estimated as follows: from figure 4.1 a total light yield of 7300 photons per MeV X-ray energy is measured. This light yield contains *all* decay components. When the light yields of the 0.8 ns and the 8  $\mu\text{s}$  component are subtracted 4500 photons/MeV remain. An alpha-excited emission spectrum could not be measured. Therefore the content of the 32  $\mu\text{s}$  component is determined from the decay curve, by determining its intensity relative to that of the 6  $\mu\text{s}$  component. A reliable estimate of the light yield of the  $> 32 \mu\text{s}$  component(s) could not be given.

Figure 4.3 also learns that the energy resolution of the 662 keV photopeak is  $17 \pm 1\%$ . The

neutron peak appears at a gamma equivalent energy of 1.34 MeV whereas the neutron capture reaction energy is 4.78 MeV. It follows that efficiency of the scintillation process induced by a neutron is 0.28 times that induced by gamma rays (only taking into account the components  $< 10 \mu\text{s}$ ). The resolution of the neutron peak is about 14% which is worse than the 10% measured for glass scintillators [154]. The background counts around the neutron peak (spectrum 2) which are numerous below 500 keV are due to gamma rays emitted by the PuBe source.

In conclusion, the most remarkable scintillation property of LiBaF<sub>3</sub> is the absence of the core-valence luminescence decay component upon alpha/thermal neutron capture. The observation of this phenomena is not new. It has also been reported by Kubota *et al.* [155] comparing scintillation pulses induced by electrons and alpha particles in BaF<sub>2</sub>. From an application point of view it makes the LiBaF<sub>3</sub> crystal very interesting for performing n- $\gamma$  discrimination. In the next section we present a method of pulse shape discrimination against gamma rays. Although pulse shape discrimination is a widely used technique for particle identification, also concerning gammas and slow neutrons [156–158], it is not always as effective as in this case. A similar method as presented here was used by Wisshak *et al.* for BaF<sub>2</sub> to discriminate alpha particles from gammas [159].

## 4.4 Results II: n- $\gamma$ discrimination

### 4.4.1 Experimental method and setup

The method is in fact very simple. A gamma ray gives a relatively high fast response at  $t \approx 0$ . A thermal neutron does not. Thus, to observe neutrons and not gamma rays, signals with a high amplitude at  $t \approx 0$  have to be vetoed.

A block diagram of the experimental arrangement is shown in figure 4.4. The LiBaF<sub>3</sub> crystal is mounted on a Philips XP2020Q photomultiplier tube. A fraction of the PMT anode pulse is sent directly to a charge integrating Q-ADC. The other fraction is used to determine whether an event is probably a neutron scintillation and if so, to open the gate of the Q-ADC. Two discriminators are used to select the events of interest:

- 1) The 'low' discriminator that discriminates scintillation events from noise and single photoelectron signals (the threshold voltage level is only a few times larger than the amplitude of a single photoelectron signal).
- 2) The 'high' discriminator which detects scintillation events that contain a fast component with a relatively high amplitude as indicated in the lower part of figure 4.4. If the amplitude of the fast component exceeds the 'high' threshold level, the coincidence unit is blocked for  $30 \mu\text{s}$  by a veto signal. After this time the signal of the  $6 \mu\text{s}$  tail of the gamma-ray induced event is sufficiently small compared to the lower threshold level to keep the Q-ADC gate closed.

Per accepted event, the gate generator opens the Q-ADC gate for  $2.4 \mu\text{s}$ . By choosing this integration time the thermal neutron peak appears at a convenient location in the pulse height spectra.

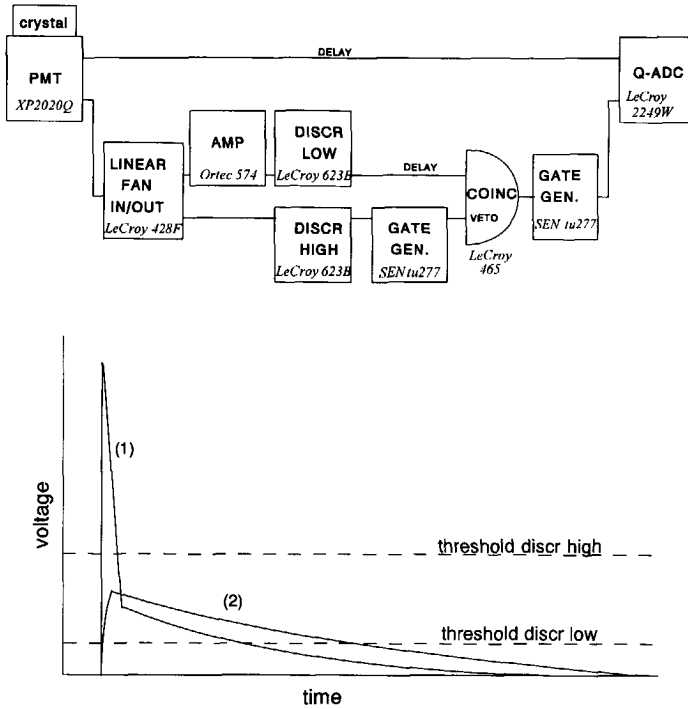


**Figure 4.4:** Block scheme of the experimental set-up used to discriminate gamma rays by evaluating the scintillation pulse shapes. In the lower part of the figure the threshold levels of the discriminators relative to scintillation pulses induced by (1) gamma rays and (2) thermal neutrons are sketched.

The dead time of our detection system is due to the Q-ADC readout, which takes about 1 ms. However, the basic limiting factor is the 30  $\mu$ s veto time required because of the slow scintillator response.

### 4.4.2 n- $\gamma$ discrimination in a mixed radiation field

First, the crystal was exposed to radiation from the Pu-Be source. The shielded source emits a mixed field of thermal neutrons and gamma rays, as was indicated before. Two pulse height spectra were made, see figure 4.5. In one case (spectrum 1) the veto (figure 4.4) was switched off so gamma-ray induced scintillation events were *not* discriminated, in the second case (spectrum 2) the veto was on. Both spectra were measured under identical conditions and are normalised

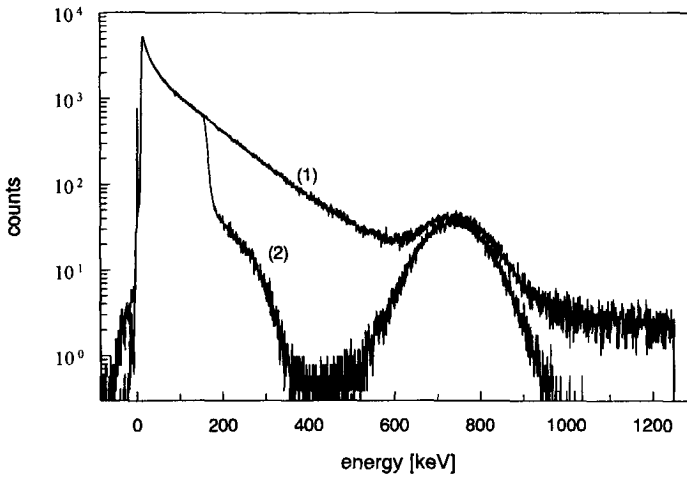


**Figure 4.5:** Pulse height spectra (pulse integration time 2.4  $\mu$ s). Spectrum 1 is the result of a measurement with a Pu-Be source shielded with paraffine and 6 cm of Pb. Spectrum 2 is measured under similar conditions, but with active discrimination against gamma-ray induced scintillation events. The spectra are normalised to an effective counting time of 1 hour.

to an *effective* counting time of 1 hour. So dead time effects are corrected for.

In spectrum 1, the intensity of the gamma-ray contribution in the mixed radiation field decreases with increasing energy. The neutron peak appears at a gamma equivalent energy of 761 keV. Note that this value differs from that obtained with figure 4.3 because of the different measurement technique. Here, only part of the scintillation pulse is integrated.

When we discriminate against the gamma-ray induced scintillation events (spectrum 2), a clear well resolved neutron peak is observed which shows that the new pulse shape discrimination method is quite effective. The FWHM of the neutron peak is about 166 keV. The threshold level of the 'high' discriminator was such that the CVL scintillation pulses caused by low energetic gamma rays (<400 keV) did not reach this level and consequently this radiation was still registered.

When spectrum 2 is subtracted from 1, a smooth spectrum results that is continuously decreasing between 400 and 1200 keV. This shows that the n- $\gamma$  discrimination does not affect the detection efficiency of the thermal neutrons.

### 4.4.3 Gamma sensitivity and intrinsic radioactivity

How effective is our gamma-ray suppression method? To answer this question, we will determine the probability that a gamma quantum incident on the crystal is absorbed, not vetoed by the electronics and will give a count in the pulse height spectrum in the energy region of the neutron

peak. The crystal was exposed to 662 keV gamma quanta from a  $^{137}\text{Cs}$  source. Spectra with and without electronic veto were measured, see figure 4.6. The normalisation procedure of these spectra is similar to that of figure 4.5.

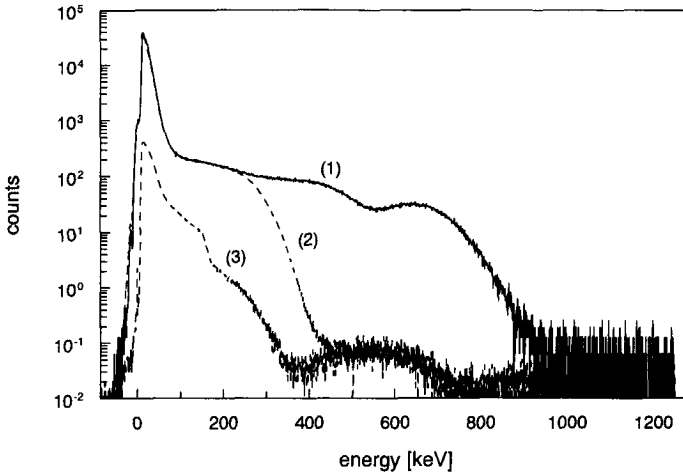


**Figure 4.6:** Pulse height spectra (pulse integration time  $2.4 \mu\text{s}$ ). Spectrum 1 is the result of a measurement with a  $^{137}\text{Cs}$  gamma source. Spectrum 2 is, apart from an active electronic suppression of gamma-ray induced scintillation events, measured under identical conditions. The difference between spectrum 2 and 3 is, that spectrum 3 is measured without the  $^{137}\text{Cs}$  source. The spectra are normalised to an effective counting time of 1 hour.

In spectrum 1, the photopeak of the 662 keV gamma rays is clearly visible. The sharp increase at energies below 100 keV is the very right wing of the single electron spectrum. Also it contains a contribution of gamma rays, or rather free electrons which resulted from their interaction, generating Cerenkov light in the PMT quartz window.

For the measurement of spectrum 2, the threshold level of the 'high' discriminator (fig. 4) was such that all gamma rays having deposited more than 400 keV energy in the crystal were excluded from registration. We note that the minimum threshold level that can be chosen corresponds with 250 keV energy deposited. Despite this measurement condition and the absence of thermal neutrons, spectrum 2 still shows some counts under the photopeak.

If the  $^{137}\text{Cs}$  source is removed and the n- $\gamma$  discrimination condition is maintained spectrum 3 in figure 4.6 results. We see that spectrum 3 has the same structure as spectrum 2 in the range of 450 to 1000 keV. This suggests that the events are caused by intrinsic radioactivity of the crystal. Since the 3 elements in  $\text{LiBaF}_3$  are not radioactive, the activity must be caused by an alpha emitting impurity. This impurity has been identified as  $^{226}\text{Ra}$  (radium is a homologue of barium) [160]. A similar background is observed in  $\text{BaF}_2$  detectors [159] The intrinsic activ-

ity causes  $6.1 \cdot 10^2$  counts/(hour-cm<sup>3</sup>) in the energy range 400-1000 keV. Of this number, 80 counts/(hour-cm<sup>3</sup>) appear in the energy range of the FWHM of the neutron peak.

To draw quantitative conclusions from figure 4.6, we define:

$$N_1 = \sum_{E=568keV}^{756keV} (\text{spectrum 1}) \quad (4.2)$$

$$N_2 = \sum_{E=568keV}^{756keV} (\text{spectrum 2}) \quad (4.3)$$

$$N_3 = \sum_{E=568keV}^{756keV} (\text{spectrum 3}) \quad (4.4)$$

$$\Sigma_1 = \sum_{E=0}^{\infty} (\text{spectrum 1}) \quad (4.5)$$

All numbers are in counts/hour. The energy interval 568-756 keV corresponds with  $[(662 - \frac{1}{2}FWHM) \text{ keV}, (662 + \frac{1}{2}FWHM) \text{ keV}]$  of the photopeak of spectrum 1.

Now we define the (total) absorption probability  $p_\gamma$  of the crystal as:

$$p_\gamma = 1 - e^{-\mu_{tot}d} = \frac{\Sigma_1}{\Phi} \quad (4.6)$$

with  $\mu_{tot}$  the total linear attenuation coefficient for 662 keV gammas,  $d$  the thickness of the crystal and  $\Phi$  is the number of 662 keV gamma quanta incident on the crystal per hour.

Furthermore we define the electronic suppression factor  $s_\gamma$ <sup>1</sup>:

$$s_\gamma = \frac{N_2 - N_3}{N_1 - N_3} \quad (4.7)$$

which expresses the probability that a gamma-ray induced event is *not* vetoed, and the gamma sensitivity  $S_\gamma$  of our detection system as:

$$S_\gamma = \frac{N_2 - N_3}{\Phi} \quad (4.8)$$

With  $S_\gamma$ , we are able to indicate what the contribution of gamma induced counts to the neutron peak in the spectrum will be if the flux of the gamma quanta is known. Note that  $S_\gamma$  is independent of intrinsic radioactivity.

From spectra 1-3 we find:

$$N_1 = (7.1 \pm 0.2) \cdot 10^3 \text{ counts/hour}$$

$$N_2 = 13.36 \pm 0.24 \text{ counts/hour}$$

$$N_3 = 13.01 \pm 0.23 \text{ counts/hour}$$

$$\Sigma_1 = (8.1 \pm 0.1) \cdot 10^4 \text{ counts/hour}$$

<sup>1</sup>It is more proper to call this factor a *electronic transmission* factor but the meaning of this name is less clear.

**Table 4.2:** The absorption probability  $p_\gamma$  ( $p_n$ ), electronic suppression factor  $s_\gamma$  ( $s_n$ ) and the gamma- (neutron-) sensitivity  $S_\gamma$  ( $S_n$ ) for the crystal experimented with, and for a 96%  ${}^6\text{Li}$  enriched crystal.

	crystal experiment d=1.75 mm	enriched crystal d=3 mm, 96% ${}^6\text{Li}$
$\gamma$ rays (662 keV)		
$p_\gamma$	$0.68 \cdot 10^{-1}$	0.11
$s_\gamma$	$\leq 1.0 \cdot 10^{-4}$	$\leq 1.0 \cdot 10^{-4}$
$S_\gamma$	$\leq 5.7 \cdot 10^{-7}$	$\leq 1.0 \cdot 10^{-6}$
thermal neutrons		
$p_n$	0.20	$> 0.99$
$s_n$	1	1
$S_n$	0.15	0.76

We have corrected  $\Sigma_1$  for the contribution of the counts that make up the sharp peak around 40 keV. With the equations (6-8), values for  $p_\gamma$ ,  $s_\gamma$  and  $S_\gamma$  are found.  $S_\gamma$  amounts at most  $5.7 \cdot 10^{-7}$  for the crystal experimented with.

We have defined similar parameters  $p_n$ ,  $s_n$  and  $S_n$  to indicate the sensitivity of the crystal for thermal neutrons. However, for thermal neutrons  $s_n$  and  $S_n$  are not defined on the energy interval of the 662 keV photopeak but on the energy interval of the neutron peak:  $[(761 - \frac{1}{2}\text{FWHM}) \text{ keV}, (761 + \frac{1}{2}\text{FWHM}) \text{ keV}]$ . The values for  $p_n$ ,  $s_n$  and  $S_n$  are determined theoretically with the assumption that thermal-neutron induced pulses are not electronically suppressed ( $s_n = 1$ ).

The results are presented in table 4.2 (column 2).

## 4.5 Discussion

We add some remarks to the results concerning the n- $\gamma$  discrimination.

- 1) We calculated the number  $N_2 - N_3$ . Since the error in this number (0.33) is of the order of the number itself (0.35), we are not able to give a more stringent estimate of the electronic suppression factor  $s_\gamma$  and  $S_\gamma$ . These numbers may very well be a few orders of magnitude smaller.
- 2) We did not have a radioactive source that emits gamma quanta of  $\sim 756$  keV, the gamma equivalent energy of the thermal neutrons. As an alternative, we used 662 keV gammas and defined the gamma sensitivity on the energy range of the 662 keV photopeak and not on the range of the neutron peak, which would be more logical. We do not expect that the difference of definition affects the value of  $S_\gamma$  much. Spectra 2 and 3 in figure 4.6 show a factor of 2 more counts in the range 568-756 keV (the location of the FWHM of the photopeak) than in the range 678-844 keV (the location of the FWHM of the neutron peak). Taking into account remark 1 we



would even be able to estimate a lower gamma sensitivity with the other definition than with the definition actually used.

3) Consider a LiBaF<sub>3</sub> crystal that is enriched to 96% <sup>6</sup>Li. In this case the linear attenuation coefficient  $\mu$  for thermal neutrons equals 16.1 cm<sup>-1</sup>. This implies that we need a thickness of 3 mm to absorb more than 99% of the thermal neutrons. In table 4.2 (column 3), the values  $p_n$ ,  $s_n$  and  $S_n$  for such a crystal are presented. Also, the calculated values for  $p_\gamma$ ,  $s_\gamma$  and  $S_\gamma$  for this crystal are given. The calculations are based on the experimental results of column 2.

Finally, the question remains why CVL is not generated under alpha/neutron excitation. It is not surprising that publications about this consider the high ionisation density at the particle track as the basis of the explanation. Itoh *et al.* [161] propose that the high concentration of free electrons and holes recombine quickly to STEs which absorb the UV light from the CVL process. More recently, Terekhin *et al.* [162] have demonstrated that in BaF<sub>2</sub> the CVL decay curve is a not exponential for 30-90 eV excitation which is a strong indication that quenching plays a role. The observation that at 90 eV the CVL efficiency is lower than at 30 eV is explained as follows. At 90 eV more than 1 (about 3 on the average) electronic excitations can be created, at distances short enough to enable dipole-dipole interactions which should induce radiationless decay [162].

To complete the understanding of the lack of CVL it is necessary to consider not only the density of the excitations, but also the energy distribution. More particularly, it would be interesting if the number of Ba(5p) core holes (in case of LiBaF<sub>3</sub> or BaF<sub>2</sub>) created by a gamma-ray and an alpha particle of equal energy could be compared. This number should be related to the CVL yield. Unfortunately there is no probe available to measure these numbers.

## 4.6 Conclusion and Outlook

The scintillation properties of a single LiBaF<sub>3</sub> crystal were investigated. The photon yield is about 2800 ph/MeV for gamma irradiation and 3500 ph/neutron. The energy resolution for the <sup>6</sup>Li(n, $\alpha$ ) reaction is about 14%. The gamma-ray induced pulses contain a very fast (ns) core-valence luminescence component with a relatively high amplitude whereas the thermal neutron induced pulses do not. Utilizing this property a very simple way of pulse shape discrimination could be applied. The threshold of a discriminator was used as lower level of the high fast scintillation component in order to determine whether a scintillation event was caused by a gamma quantum or not. With this discrimination method the gamma sensitivity of our detector, defined with equation (8), could be reduced to a value of at most  $5.7 \cdot 10^{-7}$ . It might even be much lower. Unfortunately, the crystal shows some intrinsic, presumably alpha, activity. The intrinsic radioactivity causes  $6.1 \cdot 10^2$  scintillation pulses/(hour·cm<sup>3</sup>). About 80 counts/(hour·cm<sup>3</sup>) are added to the thermal neutron peak in our Q-ADC spectrum.

These results are promising and make LiBaF<sub>3</sub> crystals interesting for use in thermal neutron scintillation detectors, the more so as a gamma background suppression of the order  $10^{-6} - 10^{-8}$

can be a stringent requirement at neutron facilities like nuclear reactors and spallation sources.

Future investigations should be directed to the shortening of the scintillation response time. Recently it has been tried to incorporate  $\text{Ce}^{3+}$  activator ions in order to replace the STE recombination channel by that of the faster  $\text{Ce}^{3+}$  5d-4f recombination [152]. Doping of high  $\text{Ce}^{3+}$  concentrations ( $>0.1$  mol%) is difficult, probably because of the required charge compensation. The  $\text{Ce}^{3+}$  light yield under X-ray excitation is limited and the STE component is still present. Using  $\text{Rb}^+$  or  $\text{K}^+$  as a co-dopant enables higher  $\text{Ce}^{3+}$ -dopant concentrations (0.3 mol%) [160]. As a result, the  $\text{Ce}^{3+}$  light yield is not considerably enhanced but the STE decay component is shortened.

Another problem to be encountered is the radiation damage affecting the optical properties of these crystals [163, 164].

## 5

## Scintillation and storage properties of $\text{LiYSiO}_4:\text{Ce}^{3+}$ and $\text{LiLuSiO}_4:\text{Ce}^{3+}$

### 5.1 Introduction

The luminescence of  $\text{Ce}^{3+}$  in silicates have been extensively studied in the past [165–171]. In particular the  $\text{Ce}^{3+}$  activated silicates  $\text{Ln}_2\text{SiO}_5$  ( $\text{Ln}=\text{Y},\text{Lu},\text{Gd}$ ) are well-known because of their fast and efficient scintillation [170]. Storage properties of oxides and oxide systems are rather unknown. However, recently it has been reported that  $\text{Y}_2\text{SiO}_5:\text{Ce}^{3+}$  (YSO:Ce) and YSO:Ce,Sm [172], as well as YSO:Sm,Tb and YSO:Ce,Tb,Zr [173] show efficient conversion of ionisation energy into photostimulable centres. Also the photostimulated luminescence and thermoluminescence of  $\text{Lu}_2\text{SiO}_5:\text{Ce}^{3+}$  has been studied [174, 175].

In this chapter we will report about the scintillation and storage properties of the silicates  $\text{LiYSiO}_4:\text{Ce}^{3+}$  and  $\text{LiLuSiO}_4:\text{Ce}^{3+}$ . The preparation and X-ray diffraction data have been reported in 1967 by Blasse *et al.* [176]. The structure has been unravelled by Nikolskii [177]. These silicates belong to a group of isomorphous compounds with the formula  $\text{ALnBO}_4$  ( $\text{A}=\text{Li},\text{Na}$ ;  $\text{B}=\text{Si},\text{Ge}$ ;  $\text{Ln}=\text{some of the lanthanides, or Y}$ ) having the olivine structure [178]. The  $\text{Ln}^{3+}$  occupies a distorted octahedral site (symmetry C1) with coordination number 6.

It is known that  $\text{Ce}^{3+}$  luminesces in isostructural  $\text{NaGdSiO}_4$  [169]. Of the other  $\text{ALnBO}_4$  compounds with the olivine structure only the  $\text{Eu}^{3+}$  luminescence properties have been studied [179]. The growth of a  $\text{LiYSiO}_4:\text{Ce}^{3+}$  single crystal was reported *et al.* [177]. The crystal densities of  $\text{LiYSiO}_4:\text{Ce}^{3+}$  and  $\text{LiLuSiO}_4:\text{Ce}^{3+}$  amount to 3.79 and 5.61  $\text{g}/\text{cm}^3$ . The effective atomic number  $Z_{eff}$  of  $\text{LiYSiO}_4$  is 32 and that of  $\text{LiLuSiO}_4:\text{Ce}^{3+}$  is 63.4. The weight percentage Li amounts to 3.69% and 2.53% respectively.

In the first part of this chapter we will discuss the applicability of these compounds as (neutron) scintillator or storage phosphor. Most attention will be paid to  $\text{LiYSiO}_4:\text{Ce}^{3+}$ , because of its relatively low  $Z_{eff}$ . The scintillation properties of  $\text{LiLuSiO}_4:\text{Ce}^{3+}$  have been discussed elsewhere [180]. The second part deals with thermoluminescence (TL) measurements  $\text{LiYSiO}_4:\text{Ce}^{3+}$ . It is noted that this is the first chapter in which the characterisation of a storage

phosphor is discussed. Therefore extra attention is paid to the description of the experimental methods to do so.

## 5.2 Experimental

### 5.2.1 Sample preparation

The  $\text{LiY}_{0.98}\text{Ce}_{0.02}\text{SiO}_4$  powder sample was prepared by mixing  $\text{Li}_2\text{CO}_3$ ,  $\text{Y}_2\text{O}_3$ ,  $\text{SiO}_2$  and Ce oxalate and firing the mixture for 8 h at 800 °C in an atmosphere of 75%  $\text{N}_2$  and 25%  $\text{H}_2$ . Subsequently the sample was ground and fired for 8 h at a temperature of 1150 °C.

Three samples of  $\text{LiLuSiO}_4$  were studied. These were all prepared by mixing  $\text{Li}_2\text{CO}_3$ ,  $\text{Lu}_2\text{O}_3$ ,  $\text{SiO}_2$  and  $\text{CeO}_2$  and pressing them into a pill form. One sample,  $\text{LiLu}_{0.99}\text{Ce}_{0.01}\text{SiO}_4$ , was obtained by firing such a pill two times at 1200 °C for 30 h in a reducing atmosphere with intermediate grinding and re-pressing to a pill. The two other samples were prepared by firing the pill for 12 h at 800 °C in air, 15 h at 1000 °C in a reducing atmosphere (99%Ar/1% $\text{H}_2$ ), next 15 h at 1200 °C in air and another 15 h at 1000 °C in the reducing atmosphere. The intention was to prepare one  $\text{LiLuSiO}_4$  and one  $\text{LiLu}_{0.99}\text{Ce}_{0.01}\text{SiO}_4$  sample but the photoluminescence and thermoluminescence measurements revealed that both samples contained detectable amounts of  $\text{Tb}^{3+}$ , introduced by impurities in  $\text{Lu}_2\text{O}_3$ . Therefore these samples will be referred to as  $\text{LiLuSiO}_4:\text{Tb}^{3+}$  and  $\text{LiLuSiO}_4:\text{Ce}^{3+},\text{Tb}^{3+}$ . All samples were checked by X-ray powder diffraction, using  $\text{CuK}\alpha$  radiation. The patterns corresponded with that reported by Blasse *et al.* [179].

For practical reasons the powders were pressed into pills with a diameter of 5 mm. The measured densities of the pills were 2.8  $\text{g/cm}^3$  for  $\text{LiYSiO}_4:\text{Ce}^{3+}$  and 3.8-4.1  $\text{g/cm}^3$  for the  $\text{LiLuSiO}_4$  samples.

### 5.2.2 Optical measurements

Optical measurements were performed with the setup depicted in figure 5.1. The basis of this setup consists of an IBH model 5000U spectrophotometer. Both monochromators have single (1200 grooves/mm) gratings blazed in first order at 340 nm. With this setup the following types of measurements were carried out:

- excitation/emission measurements
- stimulation measurements
- continuous stimulation response measurements

For excitation and emission measurements, a xenon flashlamp is employed as the excitation source. The pulse duration is several  $\mu\text{s}$  and the repetition rate typically 100 Hz. The flashing of the lamp is synchronised with the scanning of the monochromators and the signal conversion

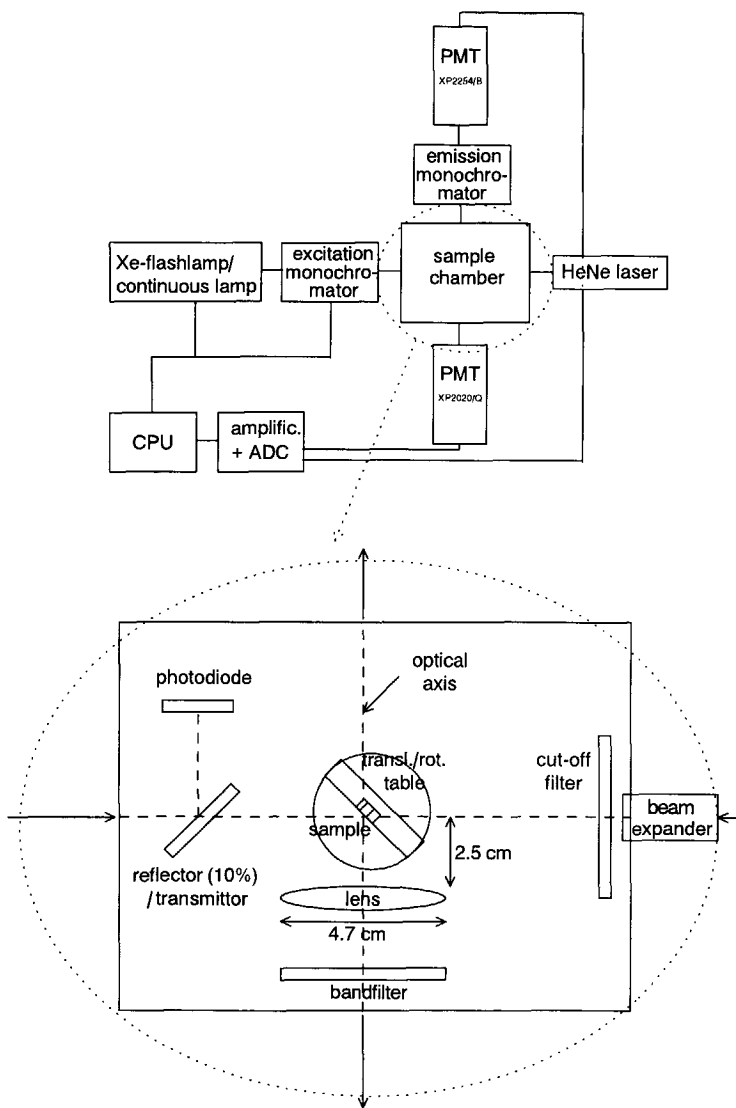


**Figure 5.1:** The experimental setup for performing optical measurements. In the lower part a more detailed sketch of the sample chamber is depicted.

by the ADC. The induced emission pulses are focussed on the emission monochromator and detected with a Philips XP2254/B photomultiplier. The excitation spectra are corrected for the wavelength dependent intensity of the lamp by dividing the spectra by the excitation spectrum of

a sample of sodium salicylate. A flashlamp instead of a continuous lamp is used because a better signal to noise ratio can be obtained. Noise is only picked up for the duration of the lamp flash.

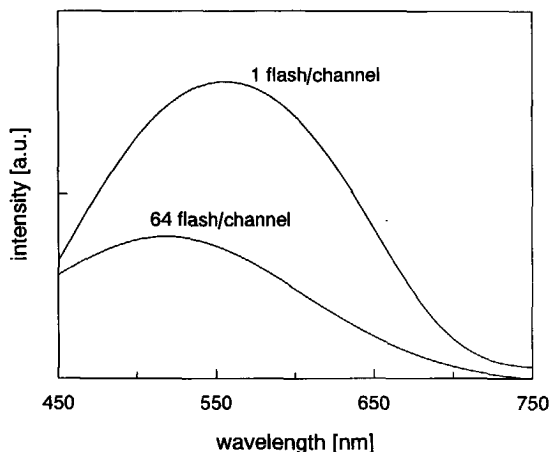


**Figure 5.2:** Two stimulation spectra of  $\text{BaFBr}:\text{Eu}^{2+}$  recorded after the sample was given a dose of 200 Gy from a  $^{60}\text{Co}$  gamma-ray source. One is recorded by flashing the lamp 64 times per monochromator step, the other by flashing only once. In both cases the scanning direction was from 450 nm to 750 nm.

Stimulation spectra are recorded with the same measurement technique. Here another advantage of the flash lamp comes about. For a measurement traps have to be emptied which means that during the measurement the number of stimuable traps changes. That this change can be significant is illustrated in figure 5.2. The figure shows two stimulation spectra of the  $\text{BaFBr}:\text{Eu}^{2+}$  reference sample. For one, 64 times more stimulation energy has been used during the measurement than for the other. In the former measurement a significant part of the stored energy is read out and therefore the spectrum is deformed when compared to the other. By synchronous flashing and measuring, the number of traps that are emptied during the experiment is relatively low.

Recording stimulation spectra generally requires a higher system sensitivity than recording excitation spectra. This is achieved by using another photon detection system. A combination of a lens with a diameter of 4.7 cm and a focal length of 2.5 cm, and behind it a bandpass filter (10 nm bandwidth), are used to separate the stimulation light from the emission light. Detection occurs with a Philips XP2020Q photomultiplier tube. In table 5.1 is indicated how each element contributes to the total photon collection efficiency.

Correction of the stimulation spectra for the lamp occurs differently than correction of the excitation spectra. Since the former range typically from 400 to 800 nm, it is possible to record the lamp spectrum simultaneously using a photodiode.

**Table 5.1:** The photon detection efficiency of the optical system used for stimulation measurements or continuous stimulation response measurements. The efficiency is given for both the  $\text{LiYSiO}_4:\text{Ce}^{3+}$  sample and the  $\text{BaFBr}:\text{Eu}^{2+}$  reference sample.

	$\text{LiYSiO}_4:\text{Ce}^{3+}$	$\text{BaFBr}:\text{Eu}^{2+}$
fractional solid angle lens	0.15	0.15
transmission band pass filter	0.057	0.10
quantum efficiency PMT	0.20	0.20
total detection efficiency	0.0017	0.0030

Determination of the total amount of photostimulable energy stored after exposure of the sample to a known dose of X-rays, alpha particles or neutrons, occurs via continuous stimulation response measurements. For samples that are stimuable in the red a HeNe laser is used. It is combined with a beam expander to obtain a more homogeneously illuminated spot on the sample, and a cut-off filter to block higher order modes from the laser. For the  $\text{LiYSiO}_4:\text{Ce}^{3+}$  and  $\text{LiLuSiO}_4:\text{Ce}^{3+}$  samples the laser wavelength of 632.8 nm was inappropriate and a 150 W continuous xenon lamp was used instead, together with the monochromator selecting a band

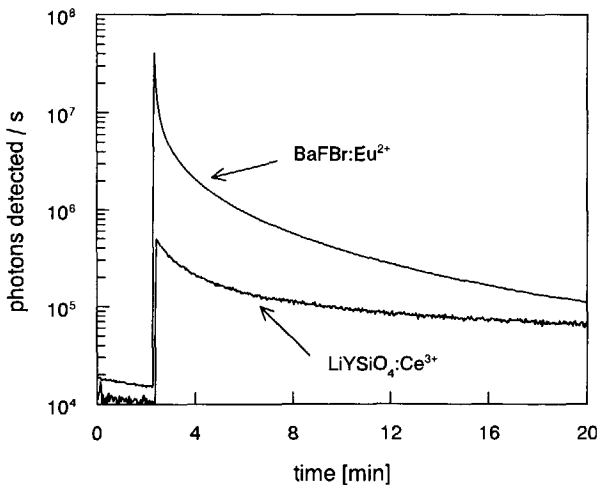


**Figure 5.3:** Measured decay of the PSL intensity of an X-ray irradiated  $\text{LiYSiO}_4:\text{Ce}^{3+}$  sample and the  $\text{BaFBr}:\text{Eu}^{2+}$  reference sample under continuous stimulation with 515 nm light from a xenon lamp. For the emission of the  $\text{LiYSiO}_4:\text{Ce}^{3+}$  sample a Melles Griot 410FS10 band-pass filter was used, for the emission of the  $\text{BaFBr}:\text{Eu}^{2+}$  sample a Melles Griot 390FS10 filter (bandwidth 10 nm).

around 515 nm. Using a diaphragm with  $d = 1$  mm in contact with the sample, an area of  $0.785 \text{ mm}^2$  is stimulated. The photons emitted are detected by the XP2020Q photomultiplier in combination with the optical elements mentioned before. A single photon counting technique is applied to register the photons detected. A similar measurement was carried out with a reference sample. The reference sample used is part of a commercially available image plate from Fuji, type IP-5 HR. It contains a phosphor layer of  $\text{BaFBr}_{0.85}\text{I}_{0.15}$  doped with  $\text{Eu}^{2+}$  ions. It has a density of  $2.67 \text{ g/cm}^3$  and a thickness of  $150 \mu\text{m}$  [181]. For this sample  $Z_{eff} = 50$ . An example of this measurement is given in figure 5.3. The area under the curve represents the total number of photons detected during stimulation. To convert this into a total number of photons emitted it must be divided by the photon detection efficiency of the setup (table 5.1).

For the other measurements other facilities were used. Excitation measurements in the VUV range were performed with the synchrotron at Daresbury Laboratory, United Kingdom. The X-ray induced emission spectra were recorded with a different setup described by Dorenbos *et al.* [142]. The X-ray tube described in the next section was used, without the Al filter. The X-ray spectrum is located between 8 and 35 keV. Powder layers of typically  $100 \mu\text{m}$  were measured in transmission. For these measurements a sample of powdered  $\text{BaF}_2$  was used as a reference sample. As a single crystal,  $\text{BaF}_2$  has a well determined light yield of 11,000 photons per MeV of absorbed X-ray energy [142], almost independent of the energy of the exciting X-rays or gamma quanta. We observed a light yield of about 4800 photons per MeV of absorbed alpha particle energy for  $\text{BaF}_2$  crystals.

The  $\text{BaF}_2$  reference sample has been used as well for the pulse height measurements. This measurement technique was described in chapter 4. The scintillation decay time measurement was carried out with a standard single photon counting technique (chapter 4).

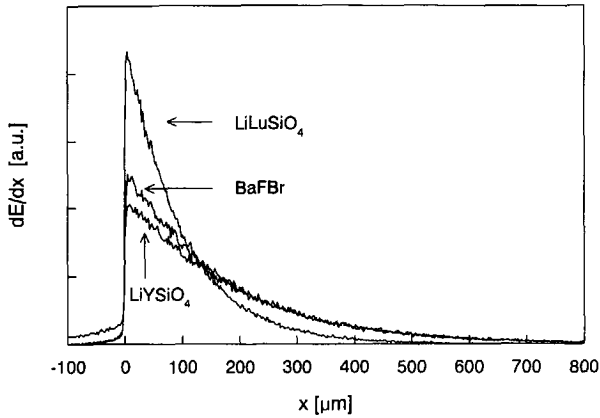
### 5.2.3 Irradiation facilities

The samples have been irradiated with X-rays, alpha particles and thermal neutrons. When determining the number of photons emitted by photostimulation per unit of radiation, it is necessary to know the flux of this radiation incident on the sample.

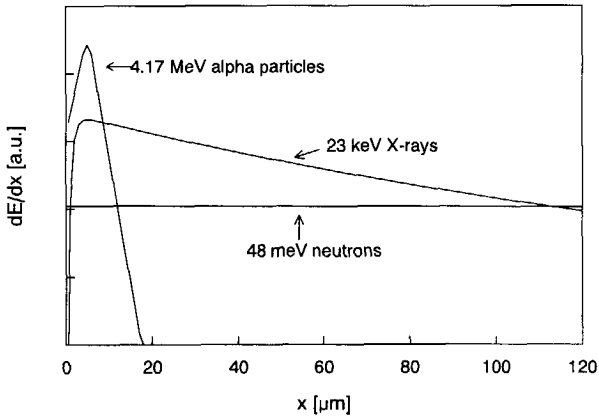
Irradiation with X-rays occurred with a calibrated X-ray tube with a copper anode that operates at 35 kV and 25 mA. To obtain an appropriate exposure rate and a more monochromatic spectrum, a Be-filter ( $d = 0.5$  mm) and an Al filter ( $d = 2$  mm) are placed between the tube and the sample. The energy distribution of the incident X-ray quanta is rather gaussian shaped with an average energy  $\bar{E} = 23$  keV and a standard deviation  $\sigma = 4.5$  keV. The flux at the sample position was determined at  $4 \pm 3 \cdot 10^9$  X-rays/( $\text{cm}^2 \cdot \text{s}$ ) and the exposure rate amounts to  $0.7 \pm 0.5$  R/s.

Figure 5.4 shows the energy absorption profiles of the X-ray radiation in the  $\text{LiYSiO}_4:\text{Ce}^{3+}$  and  $\text{LiLuSiO}_4:\text{Ce}^{3+}$  pills and in the  $\text{BaFBr}:\text{Eu}^{2+}$  sample. Despite the large differences in  $Z_{eff}$  the profiles of  $\text{LiYSiO}_4:\text{Ce}^{3+}$  and  $\text{BaFBr}:\text{Eu}^{2+}$  do not differ very much at this X-ray energy. The stopping power of  $\text{LiLuSiO}_4:\text{Ce}^{3+}$  is substantially better.





**Figure 5.4:** Energy absorption profiles  $dE/dx$  as a function of the depth  $x$  below the pill surface in the  $\text{LiYSiO}_4$  and  $\text{LiLuSiO}_4$  pills and the  $\text{BaFBr:Eu}^{2+}$  sample, when irradiated by 23 keV X-rays. The profiles were calculated using the Monte Carlo code GEANT [182] (see also chapter 7). The pill densities used were  $2.80 \text{ g/cm}^3$  for  $\text{LiYSiO}_4$ ,  $4.00 \text{ g/cm}^3$  for  $\text{LiLuSiO}_4$  and  $2.67 \text{ g/cm}^3$  for  $\text{BaFBr}$ .



**Figure 5.5:** Energy absorption profiles  $dE/dx$  as a function of the depth  $x$  below the pill surface in the  $\text{LiYSiO}_4$  pill, when irradiated with 23 keV X-rays, 48 meV neutrons or 4.17 MeV alpha particles. The X-ray profile was calculated with the Monte Carlo code GEANT [182], the alpha particle profile with the 'home-made' Monte Carlo code 'DOSALPH' [183]. The neutron profile is calculated using equation (3.1). The pill density was taken  $2.8 \text{ g/cm}^3$  and  $\mu_n = 0.41 \text{ cm}^{-1}$ .

For irradiating the sample with neutrons we used the pool-type research reactor at the Interfaculty Reactor Institute at Delft was used. A neutron beam pipe guides the thermalised neutrons out of the pool. A Zn(002) monochromator selects neutrons with an energy of 48 meV, which is close to the average energy of 25 meV for thermal neutrons. The cross section  $\sigma_n$  of  $^6\text{Li}$  for 48 meV neutrons is 660 barns. The neutron flux  $I_0$  is determined by measuring the activity of a gold foil irradiated with the beam and it amounts to  $1.3 \cdot 10^6 \text{ n}/(\text{cm}^2 \cdot \text{s})$ . With equation (3.1) the number of neutrons absorbed by the  $^6\text{Li}$  isotopes per unit of sample area and per unit of time can be calculated. The value for  $\mu_n$  of  $0.41 \text{ cm}^{-1}$  using equation (3.2).

The source used for alpha particle irradiation consists of solid  $^{241}\text{AmO}_2$  deposited on a silver foil with a diameter of 11 mm. It is covered with  $2 \mu\text{m}$  of gold. The source is calibrated and has an activity of 409.6 kBq and the particle fluency over  $2\pi$  is  $2.04 \cdot 10^5 \text{ s}^{-1}$ . Irradiation occurs by positioning the sample in a central position in front of the source at a distance of 2 mm. From a Monte Carlo simulation that takes this geometrical situation into account, follows an average energy of alpha particles impinging on the sample surface of 4.17 MeV and a particle flux at the surface of  $1.4 \cdot 10^5/(\text{cm}^2 \cdot \text{s})$ .

In figure 5.5 the energy absorption profiles in the  $\text{LiYSiO}_4:\text{Ce}^{3+}$  pill for the different radiation types are compared. The absorption probability of the 48 meV neutrons in the pill is 4%. Therefore the neutron absorption profile is almost flat. The average penetration depth of the 4.17 MeV alpha particles in  $\text{LiYSiO}_4:\text{Ce}^{3+}$  is only  $17 \mu\text{m}$  and the energy absorption shows a maximum at  $5 \mu\text{m}$  below the pill surface. The profiles depicted in figure 5.4 and 5.5 will be used later in this chapter.

## 5.3 Applicability as scintillator/storage phosphor

### 5.3.1 Excitation/emission and scintillation

Figure 5.6 shows the excitation and emission spectra of  $\text{LiYSiO}_4:\text{Ce}^{3+}$  recorded at room temperature. The emission (curve (b)) occurs over a broad band with a maximum at 405 nm. It can be ascribed to the transition from the lowest 5d level to the  $^2\text{F}_{5/2}$  and  $^2\text{F}_{7/2}$  levels of the  $4f^1$  configuration of  $\text{Ce}^{3+}$ . The splitting of the 4f levels which should be  $2000 \text{ cm}^{-1}$  [116], can not be resolved.

The excitation spectrum (curve (a)) of the  $\text{Ce}^{3+}$  emission exhibits two main bands at 348 nm and 310 nm and a shoulder at 293 nm. Due to the crystal field interaction the  $\text{Ce}^{3+}$  5d state is expected to be 5-fold splitted. In the inset of figure 5.6 the excitation spectrum recorded in the (V)UV range is plotted. At the long wavelength side the same bands are observed and at 210 nm (see arrow) the spectrum shows another local maximum which could be ascribed to a 4f-5d transition. The weakness of this maximum suggests that this 5d level is positioned in the conduction band making ionisation of the excited  $\text{Ce}^{3+}$  ion highly probable.

It is known that with an increase of the Stokes shift the individual excitation and emission bands broaden and are not resolved anymore. From figure 5.6, the Stokes shift is about 3600

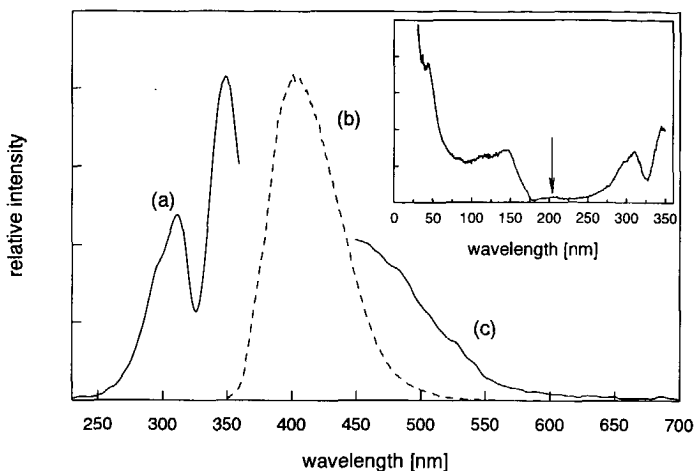


**Figure 5.6:** Excitation spectrum (curve (a)), emission spectrum (curve (b)) and stimulation spectrum (curve (c)) of  $\text{LiYSiO}_4:\text{Ce}^{3+}$  measured at 300 K. The excitation spectrum and the stimulation spectrum are recorded for  $\lambda_{em} = 410$  nm, the emission spectrum is recorded for  $\lambda_{ex} = 330$  nm. The excitation spectrum and the stimulation spectrum were corrected for the wavelength dependent xenon lamp intensity. The excitation spectrum in the inset is recorded using synchrotron radiation.

$\text{cm}^{-1}$ . This is comparable to the Stokes shift of  $3700 \text{ cm}^{-1}$   $\text{YAlO}_3:\text{Ce}^{3+}$  [184]. For this compound, the  $\text{Ce}^{3+}$  emission spectrum measured at RT does not reveal the splitting of the ground state either. The inset of figure 5.6 shows at 175 nm (7.1 eV) the onset of band-to-band transitions. The excitation at shorter wavelength is about equal to that under direct excitation of  $\text{Ce}^{3+}$  at 310 nm. This implies that the transfer of host lattice excitation energy to  $\text{Ce}^{3+}$  is efficient.

For  $\text{LiLuSiO}_4:\text{Ce}^{3+}$  the excitation and emission spectra look very similar to those of figure 5.6 (see also [180]). The broad emission band identically peaks at 405 nm. Excitation maxima are located at 353 nm, 315 nm and below 300 nm and excitation of the host lattice starts at 180 nm (6.9 eV).

In figure 5.7, spectrum (a), the X-ray induced emission spectrum of  $\text{LiYSiO}_4:\text{Ce}^{3+}$  is depicted. The  $\text{Ce}^{3+}$  emission band of figure 5.6 is observed again and apparently no other emission channels are available upon excitation by X-rays. Spectrum (b) is the emission spectrum of  $\text{BaF}_2$  powder. This spectrum is normalised to a total light output of 11,000 photons per MeV of absorbed X-ray energy and spectrum (a) is multiplied with the same normalisation factor. The light yield of a  $\text{LiYSiO}_4:\text{Ce}^{3+}$  single crystal is estimated on  $10^4$  photons/MeV. This is three times less than was measured for  $\text{LiLuSiO}_4:\text{Ce}^{3+}$  [180].

The scintillation decay curve of  $\text{LiYSiO}_4:\text{Ce}^{3+}$  under excitation with gamma quanta from a  $^{60}\text{Co}$  source is shown in figure 5.8, curve (a). The intense very fast component in the first few

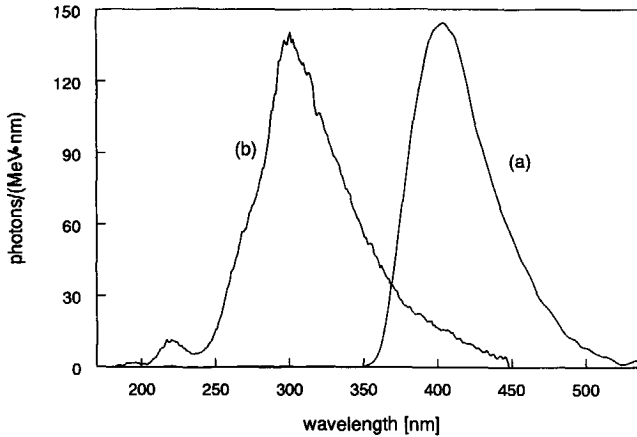


**Figure 5.7:** Prompt emission spectra upon X-ray excitation of  $\text{LiYSiO}_4:\text{Ce}^{3+}$  (curve (a)) and a reference sample of pure  $\text{BaF}_2$  (curve (b)). The spectra were corrected individually for the wavelength dependent detection efficiency of the system and relative to each other for the difference between the two materials in X-ray energy absorption per unit of time. Then spectrum (b) was normalised to a total light output of 11,000 photons per MeV of absorbed X-ray energy and spectrum (a) was multiplied with the same normalisation factor.

ns of the decay curve is due to Cerenkov pulses generated in the photomultiplier window. The scintillation decay curve is exponential with a decay time  $\tau = 38 \pm 2$  ns. Slower components are not present or hidden in the background. For  $\text{LiLuSiO}_4:\text{Ce}^{3+}$  a comparable scintillation response time of 41 ns was measured [180].

When the  $\text{Ce}^{3+}$  ions are excited directly with 295 nm photons, exponential decay is observed as well (curve (b)) with  $\tau = 39 \pm 1$  ns, hence equal to that under gamma excitation. It is known that the radiative lifetime of the  $\text{Ce}^{3+}$  excited state depends on the crystal field at the ion site and that the decay time is typically 20 to 80 ns [92, 185]. For the present compounds this lifetime appears to determine the scintillation response time.

The fast component at  $t < 20$  ns must be ascribed to a quenching process. The component is absent in curve (a). X-rays can penetrate the phosphor grain whereas the UV photons excite relatively many  $\text{Ce}^{3+}$  ions near the surface. Therefore more  $\text{Ce}^{3+}$  ions on disturbed sites will be excited which probably decay nonradiatively.

The scintillation decay curve under alpha particle excitation was examined on a digital oscilloscope. It has a fast component with a decay time of several tens of ns and a slower component with a decay time of several tens of  $\mu\text{s}$ . The intensity of the latter is of the same order of magnitude as that of the fast component. To determine the absolute intensity of the fast component we measured a pulse height spectrum of scintillation pulses produced by alpha particles. A reference measurement was done with the  $\text{BaF}_2$  powder. The (fast) light output per alpha particle absorbed

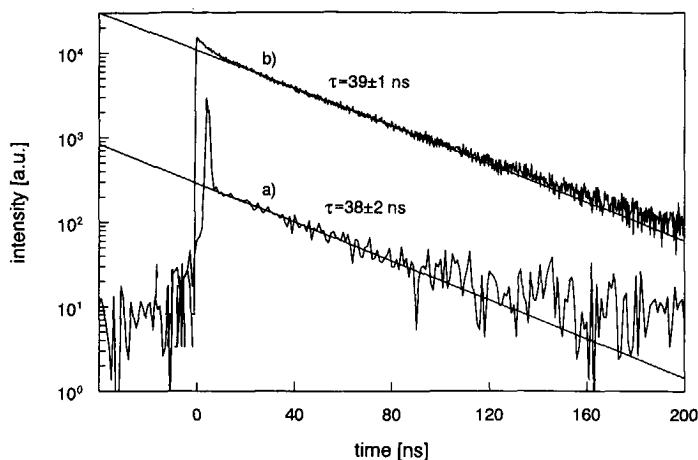


**Figure 5.8:** The scintillation decay curve of LiYSiO<sub>4</sub>:Ce<sup>3+</sup> excited with (a) <sup>60</sup>Co gamma rays and (b) 295 nm synchrotron photons. For curve (a) the resolution is determined by the TDC channel width: 1 ns/channel. For curve (b) it is determined by the width of the exciting pulses: 1 ns FWHM. The drawn lines are fits of the decay curves to determine the decay times. For the fit procedure a time range was selected at which the decay behaviour is purely exponential.

in LiYSiO<sub>4</sub>:Ce<sup>3+</sup> is a factor 0.4 relative to that of BaF<sub>2</sub>. So the light yield of a LiYSiO<sub>4</sub>:Ce<sup>3+</sup> single crystal is about  $2 \cdot 10^3$  photons per MeV of absorbed alpha particle energy. Hence, a good estimate for the light yield per absorbed thermal neutron is  $1 \cdot 10^4$  photons.

### 5.3.2 Optical stimulation

Curve (c) in figure 5.6 is the stimulation spectrum for LiYSiO<sub>4</sub>:Ce<sup>3+</sup>, recorded after irradiation with 23 keV X-rays. It consists of a broad structureless band that has a maximum, if any, at a wavelength shorter than 450 nm. The photostimulated luminescence (PSL) spectrum corresponds with the Ce<sup>3+</sup> emission band of figure 5.6. No other emission was detected. This indicates that optically stimulated detrapping of charge gives rise to electron-hole recombination on Ce<sup>3+</sup>. Similar stimulation band and emission bands were observed for LiLuSiO<sub>4</sub>:Ce<sup>3+</sup>. In LiLuSiO<sub>4</sub>:Ce<sup>3+</sup>,Tb<sup>3+</sup> only recombination luminescence of Ce<sup>3+</sup> whereas the Tb<sup>3+</sup> activated sample shows under photostimulation a line emission which is due to the <sup>5</sup>D<sub>4</sub> - <sup>7</sup>F<sub>J</sub> transitions of Tb<sup>3+</sup>.

Next the total amount of photostimulable centres after a known exposure to X-rays, alpha particles or neutrons was determined. As mentioned, stimulating photons with a wavelength of 515 nm were used. Considering the stimulation spectrum, photons with a shorter wavelength do stimulate the phosphor more efficiently but the discrimination between these photons and the photons emitted becomes more difficult. Figure 5.9(a) shows the total number of photons emitted

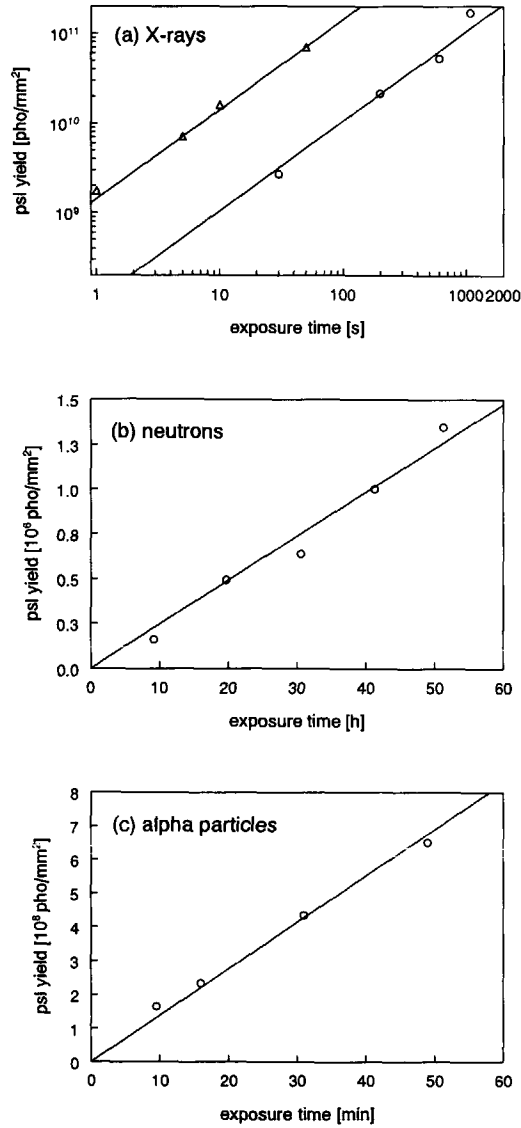


**Figure 5.9:** Number of photons emitted due to photostimulation as a function of the exposure time (prior to stimulation) to (a) 23 keV X-rays, (b) 48 meV neutrons and (c) 4.17 MeV alpha particles.  $\circ = \text{LiYSiO}_4:\text{Ce}^{3+}$ ,  $\Delta = \text{BaFBr:Eu}^{2+}$ . The radiation sources are specified in the text.

**Table 5.2:** The PSL yield and stimulation energy (SE) of the LiYSiO<sub>4</sub> and LiLuSiO<sub>4</sub> storage phosphors compared to the BaFBr:Eu<sup>2+</sup> reference sample. The PSL yield is defined as the number of photons emitted by photostimulation per radiation quantum or particle incident on the sample. For X-rays the conversion efficiency (CE) and for comparison the scintillation light (SL) yield are also given. The SE is given relative to BaFBr:Eu<sup>2+</sup>. The radiation types used were 23 keV X-rays, 48 meV neutrons or 4.17 MeV alpha particles. See the text for further details.

	X-rays			neutrons	alphas	SE relative
	PSL yield	CE	SL yield	PSL yield	PSL yield	
	pho/X-ray <sub>inc</sub>	[pJ/mm <sup>2</sup> /mR]	pho/MeV <sub>abs</sub>	pho/neut <sub>inc</sub>	pho/alpha <sub>inc</sub>	
LiYSiO <sub>4</sub> :Ce <sup>3+</sup>	2	0.09	1·10 <sup>4</sup>	0.5	2·10 <sup>2</sup>	20
LiLuSiO <sub>4</sub> :Ce <sup>3+</sup>	0.07	0.003	3·10 <sup>4</sup>	-	-	6
LiLuSiO <sub>4</sub> :Ce <sup>3+</sup> ,Tb <sup>3+</sup>	7	0.3	7·10 <sup>3</sup>	-	-	9
LiLuSiO <sub>4</sub> :Tb <sup>3+</sup>	1	0.06	-	-	-	21
BaFBr:Eu <sup>2+</sup>	3·10 <sup>1</sup>	1	-	-	-	1

during stimulation as a function of the sample exposure time to 23 keV X-rays. The measurements were performed with the LiYSiO<sub>4</sub>:Ce<sup>3+</sup> sample and the reference sample. The lines are fits to the data points and satisfy the equation  $y = a \cdot x$ . The fits make clear that both samples exhibit a response that is proportional with the exposure time (in the time range measured) and thus with the amount of energy absorbed. Similar measurements have been carried out upon irradiation of the LiYSiO<sub>4</sub>:Ce<sup>3+</sup> sample with thermalised neutrons, see figure 5.9(b), and alpha particles (figure 5.9(c)). Lines were fitted through the data points again to make clear that the response of the LiYSiO<sub>4</sub>:Ce<sup>3+</sup> sample is proportional with the exposure time when the sample is exposed to thermal neutrons or alpha particles.

In table 5.2 the results for PSL yield per type of radiation are presented. The numbers are obtained using the slopes of the lines in figure 5.9 and the specifications of the setup and radiation sources given in the previous section.

First the PSL yields for X-rays will be discussed and compared with that of the BaFBr:Eu<sup>2+</sup> reference sample. According to table 5.2 the yield of the reference sample is a factor of 15 larger than that of LiYSiO<sub>4</sub>:Ce<sup>3+</sup> and even a factor of 400 larger than that of the LiLuSiO<sub>4</sub>:Ce<sup>3+</sup> sample. The PSL yield is determined by (a) the X-ray stopping power of the samples, reflected by the dose depth profiles of figure 5.4, and (b) the efficiency in converting ionisation energy in photostimulable centres. Since the dose depth profiles of BaFBr:Eu<sup>2+</sup> and LiYSiO<sub>4</sub>:Ce<sup>3+</sup> are very similar the difference in their PSL yield is only caused by (b). The stopping power of the LiLuSiO<sub>4</sub> samples is considerably better. Thus their efficiency in converting ionisations relative to BaFBr:Eu<sup>2+</sup> is worse than their relative PSL yield.

The LiLuSiO<sub>4</sub>:Ce<sup>3+</sup>,Tb<sup>3+</sup> and LiLuSiO<sub>4</sub>:Tb<sup>3+</sup> samples give a higher PSL yield than the Ce<sup>3+</sup> activated sample. The former even 0.25 times that of BaFBr:Eu<sup>2+</sup>. For the samples that

emit via  $\text{Ce}^{3+}$  also the scintillation light (SL) yields are added to table 5.2. The  $\text{LiLuSiO}_4:\text{Ce}^{3+}$  sample showing the highest SL yield of  $3 \cdot 10^4$  photons per MeV has the lowest PSL yield. For  $\text{LiLuSiO}_4:\text{Ce}^{3+}, \text{Tb}^{3+}$  the situation is reverse. Apparently the two yields are correlated and their ratio strongly depends on the concentration of dopant and co-dopant.

For X-ray storage phosphors it is more common to use the conversion efficiency (CE) instead of the PSL yield, see chapter 3. The CE values have been calculated using the results for the PSL yield and are listed in the third column.

Only for  $\text{LiYSiO}_4:\text{Ce}^{3+}$  the PSL yield has been measured for neutrons and alpha particles. In the next section will be explained why the PSL yield for alphas was measured and how the results should be interpreted.

Another quantity characterising a storage phosphor is the stimulation energy (SE, see chapter 3). The SE of the silicates were determined at 514 nm relative to that of  $\text{BaFBr}:\text{Eu}^{2+}$ . The results are given in the last column of table 5.2. The SEs are found to be higher than that of  $\text{BaFBr}:\text{Eu}^{2+}$  and they vary also from sample to sample. This indicates that the traps that are optically stimulated are different from sample to sample.

### 5.3.3 Discussion

First the accuracy of the measurement results will be discussed. Next the relation between the PSL yield for X-rays, alphas and neutron will be clarified. Then the results for the PSL yield will be interpreted for application.

The method of measuring scintillation light yield on powder layers and extrapolating the result to single crystals is not very accurate. The probability that a created photon can escape the layer in the direction of the PMT are determined by the scattering length and the absorption length of the photons in the powder which in turn depend on the grain size and morphology, the refraction index, and on the presence of surface defects on the grains [186]. These parameters vary from sample to sample. Therefore the errors in the SL values in column 4 of table 5.2 are thought to be of the order of 50%. A measurement on one sample can be reproduced with an accuracy better than 90%.

For the  $\text{BaFBr}:\text{Eu}^{2+}$  reference sample a CE value of  $1 \text{ pJ/mm}^2/\text{mR}$  was found. In the literature, higher CE values of  $2 \text{ pJ/mm}^2/\text{mR}$  [112],  $12 \text{ pJ/mm}^2/\text{mR}$  [187] and even  $50 \text{ pJ/mm}^2/\text{mR}$  [109] are reported for  $\text{BaFBr}:\text{Eu}^{2+}$ , all determined at a stimulation wavelength of 633 nm.

There are several explanations possible for the observed differences and the fact that the CE found by us is rather low. At first, the way a sample is prepared largely influences its CE and therefore the variations are most probably due to the use of different preparation methods.

Other contributions could be the large errors in the determined exposure rates of the X-ray tubes used, and different X-ray energies applied. The CE depends by definition on the energy of the incident X-rays [108]. For 1 mR of 50 keV X-rays the photon flux is about 9 times larger than for 1 mR of 23 keV X-rays. Of course the photoelectric absorption coefficient of  $\text{BaFBr}:\text{Eu}^{2+}$  decreases (by a factor of 2.5) when going from 23 to 50 keV X-rays, but this is for a large part



compensated by the factor 2 more photostimulable centres created per X-ray absorbed.

It is not expected that the different stimulation wavelength used (515 nm instead of 633 nm) the CE values much. According to Schipper *et al.* [187] the CEs for BaFBr:Eu<sup>2+</sup> upon 488 nm and 515 nm stimulation light are equal.

To compare the PSL yields of LiYSiO<sub>4</sub>:Ce<sup>3+</sup> for X-rays, alphas, and neutrons, the dose depth profiles have to be considered per radiation type, see figure 5.5. These profiles are important because of the limited penetration depth of the stimulating and emitted photons in the pill.

It is reasonable to assume that the penetration depth of the stimulating photons is larger than that of the alpha particles. This implies that the PSL yield per *incident* alpha particle equals the yield per *absorbed* particle. A PSL yield of  $5 \cdot 10^1$  photons per MeV of absorbed alpha particle energy follows.

If a neutron is absorbed by a <sup>6</sup>Li atom, energy is deposited by the 2.05 MeV alpha particle and a 2.73 MeV triton in the crystal. It will be assumed that the PSL yield per unit of absorbed energy from these reaction products equals the PSL yield per unit of absorbed energy from a 4.17 MeV alpha particle. This assumption is based on the following argument. From scintillators it is known that the light output per unit of radiation energy absorbed depends on the type of radiation. The light output is usually higher for gamma-rays and X-rays than for ionising charged particles heavier than electrons, and for charged particles the light output increases with decreasing energy deposition density per unit path length of the incident ion [188, 189]. The quenching effects that are presumed to be responsible for this trend probably also influence the number of free charge carriers to be trapped and thus the PSL yield. But in the present case, the energy deposition density of 4.17 MeV alpha particles will not differ much from the density generated by the 2.05 MeV alpha particle and a 2.73 MeV triton. So the influence on the PSL yield will be limited.

Using this assumption the PSL yield after neutron irradiation is also  $5 \cdot 10^1$  photons per MeV of absorbed energy or  $2 \cdot 10^2$  photons per absorbed neutron. On the other hand, it can be calculated with equation (3.1) that the ratio between the number of neutrons incident on the sample and the number of neutrons absorbed amounts to  $2.4 \cdot 10^4$  per  $\mu\text{m}$  of sample layer. Furthermore, a PSL yield of 0.5 photons per incident neutron was determined (table 5.1). The latter two values do match the first if effectively only the stimuable energy stored in the first 60  $\mu\text{m}$  below the sample surface was read out. Deeper layers were not stimulated.

If this readout profile is compared to the dose depth profile of the X-rays it follows that about 20% of the photostimulable centres created by the X-rays can be stimulated. This means that the experimentally determined PSL yield of 2 emitted photons per incident X-ray corresponds with about  $4 \cdot 10^2$  photons per MeV of absorbed X-ray energy. This number is a factor of 10 higher than that for alphas and neutrons. However, taking into account the quenching effect discussed before, it is acceptable.

Are these numbers promising from the application point of view? The PSL yield of LiYSiO<sub>4</sub>:Ce<sup>3+</sup> powder for thermal neutrons is inferior to the yield of the BaFBr:Eu<sup>2+</sup>·Gd<sub>2</sub>O<sub>3</sub> system. The latter emits typically  $10^2$  photons per incident 25 meV neutron [190], making it much more appropriate to be used in an powder layered imaging plate. However, the PSL yield of LiYSiO<sub>4</sub>:Ce<sup>3+</sup>

upon thermal neutron irradiation can be largely improved if we consider a single crystal that is transparent for both the stimulation and emission light. The yield of such a crystal will be higher because all stimuable energy stored can be read out. Obviously, also its thickness can be larger than that of the pressed pill. A PSL yield for such a crystal can be predicted using the previously estimated PSL yield of  $2 \cdot 10^2$  photons per absorbed 48 meV neutron. It follows that a 1 mm thick single crystal ( $\mu = 0.78 \text{ cm}^{-1}$  for 25 meV neutrons) has a PSL yield of about 15 photons per incident thermal neutron. If the crystal would be 96%  $^6\text{Li}$  enriched ( $\mu = 10.7 \text{ cm}^{-1}$  or absorption probability 66%) the yield would be  $1 \cdot 10^2$  photons per incident thermal neutron.

As indicated in chapter 2 the quantity which expresses the imaging quality of a thermal neutron image plate is the DQE. It depends on the PSL yield of the storage phosphor used. In chapter 7 it is demonstrated that the yield found here is high enough for the DQE to become independent of the PSL yield, such that  $\text{DQE} \approx A$ , with  $A$  the neutron absorption probability. Hence, for a 1 mm thick crystal the DQE would be about 66%.

This result seems encouraging. However, a problem is the high stimulation energy, which

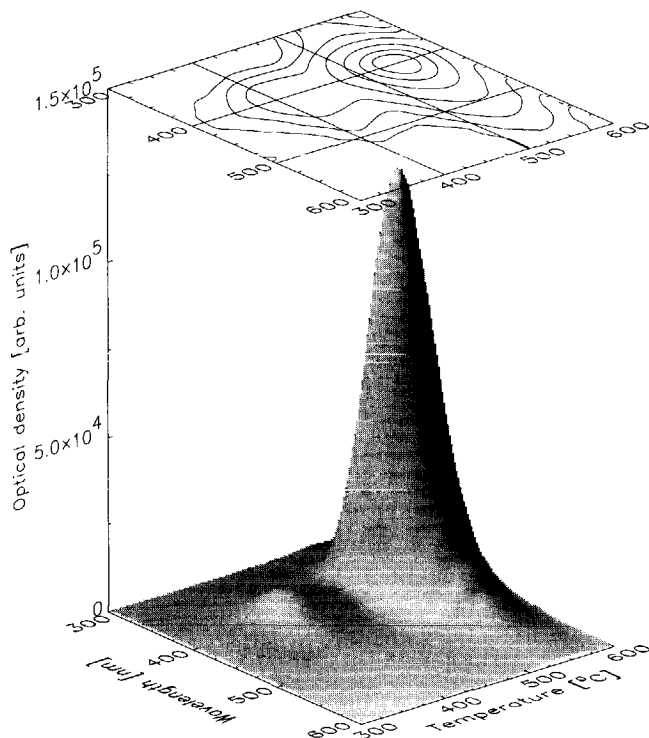


**Figure 5.10:** The TL intensity of  $\text{LiYSiO}_4:\text{Ce}^{3+}$  as a function of emission wavelength and temperature recorded after exposure to gamma rays from a  $^{60}\text{Co}$  source. Heating rate 1 K/s.

complicates the actual stimulation of all stimuable centres. Figure 5.3 shows that in our experiment the readout time of an irradiated  $\text{LiYSiO}_4:\text{Ce}^{3+}$  sample was quite long. Of course, it will be shortened by orders of magnitude when applying an  $\text{Ar}^+$  laser operating at 515 nm instead of the 'low' intensity lamp employed in the experiment. Still, the 20 times larger stimulation energy of  $\text{LiYSiO}_4:\text{Ce}^{3+}$  compared to  $\text{BaFBr}:\text{Eu}^{2+}$  implies relatively long readout times and a less favourable signal to noise ratio. Noise contributions other than statistical noise are neglected when calculating the DQE. This is realistic for  $\text{BaFBr}:\text{Eu}^{2+}$  [10] but probably not for  $\text{LiYSiO}_4:\text{Ce}^{3+}$ .

## 5.4 Thermoluminescence

### 5.4.1 Results

With TL experiments information about the mechanism of trapping and recombination is obtained. A set of measurement results is described that will be further interpreted in the next section.

Figure 5.10 shows the TL emission spectrum for  $\text{LiYSiO}_4:\text{Ce}^{3+}$  that was recorded after gamma ray irradiation. Like in the optically stimulated emission spectrum, only the  $\text{Ce}^{3+}$  emission band is observed.

In figure 5.11 the TL spectra recorded after exposure to gamma rays, X-rays, UV light, and alpha particles are compared. The dose the sample received differed by less than a factor of 2 for one irradiation type compared to the other. All spectra consist of 4 peaks of which peak 3 is most prominent. The spectra are normalised on this peak. Relative shifts of the spectra along the horizontal axis, most clearly observed for peak 3, are due to a varying temperature retardation of the sample compared to the thermocouple registering the temperature during the experiment.

The intensity ratio of the four peaks depends slightly on the type of radiation used. The intensity of peak 1 and 2 relative to peak 3 differs. Also at peak 4 differences can be observed. The intensity of peak 1 and 2 is highest for alpha radiation, then for X-rays and gamma rays and it is lowest for 254 nm photons. At peak 4 the situation is reversed. Not depicted is the neutron induced TL curve which is similar to the alpha curve. The differences in peak intensities must be due to the different densities of the ionisation tracks created by absorbed radiation. The density is highest for alpha particles and neutrons and lowest for UV photons.

In the inset of figure 5.11 the TL spectra of  $\text{LiYSiO}_4:\text{Ce}^{3+}$ ,  $\text{LiLuSiO}_4:\text{Ce}^{3+}$ ,  $\text{LiLuSiO}_4:\text{Ce}^{3+},\text{Tb}^{3+}$  and  $\text{LiLuSiO}_4:\text{Tb}^{3+}$  are compared. The samples were exposed to the same amount of gamma radiation. The spectra of the  $\text{LiLuSiO}_4$  samples look different from that of  $\text{LiYSiO}_4:\text{Ce}^{3+}$  and rather complicated. They all show structure just above and below 450 K. It is clear that the activator ions affect the number and the type of traps to a large extent. The latter is consistent with the SEs varying considerably.

For  $\text{LiYSiO}_4:\text{Ce}^{3+}$  the saturation of trap filling process was studied. This was done by measuring the TL as a function of the exposure time to a Hg lamp. By means of an interference filter

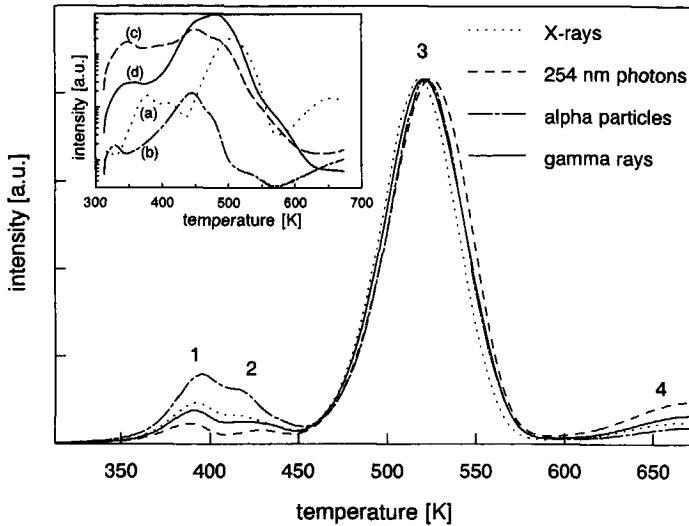


**Figure 5.11:** TL glow curves of  $\text{LiYSiO}_4:\text{Ce}^{3+}$  after exposure to respectively 23 keV X-rays,  $\approx 1.25$  MeV gamma-rays ( $^{60}\text{Co}$  source), 254 nm photons and 4.17 MeV alpha particles. Heating rate 1 K/s. Inset: TL spectra of (a)  $\text{LiYSiO}_4:\text{Ce}^{3+}$ , (b)  $\text{LiLuSiO}_4:\text{Ce}^{3+}$ , (c)  $\text{LiLuSiO}_4:\text{Tb}^{3+}$  and (d)  $\text{LiLuSiO}_4:\text{Ce}^{3+}, \text{Tb}^{3+}$  recorded after the samples received a gamma ray dose of 3 Gy. Heating rate 1 K/s.

the characteristic 254 nm line was selected. In figure 5.12 the maxima of peak 1, 2, and 3 are plotted as a function of the exposure time. Below 300 s the peak maxima are proportional with the exposure time. At longer times saturation takes place. The saturation of all TL peaks starts at the same exposure time.

Another important observation in this experiment was that the peak positions  $T_m$  did not change over at least three orders of magnitude starting from the lowest detectable exposure. This indicates that the recombination process follows first-order kinetics [191]. A TL glow curve governed by first-order kinetics in the recombination has typical asymmetrical line shape. The expected line shape is not consistent with the shape of the most dominant peak 3. However, with figure 5.13 it is demonstrated that peak 3 is not connected with a collection of completely identical traps.

Figure 5.13 shows glow curves recorded after X-ray irradiation and an optical bleaching treatment. The bleaching occurred by exposing the irradiated sample to the Hg lamp in combination with a glass filter that has a cut-off wavelength of 420 nm. Curve (a) is the reference curve, recorded after irradiation only. Curve (b) and (c) were recorded after bleaching during 10 and 45 min. respectively. The effect of the bleaching is that peak 1,2 as well as 3 decrease in intensity. Furthermore it can be clearly observed that peak 3 does not only decrease in intensity but also

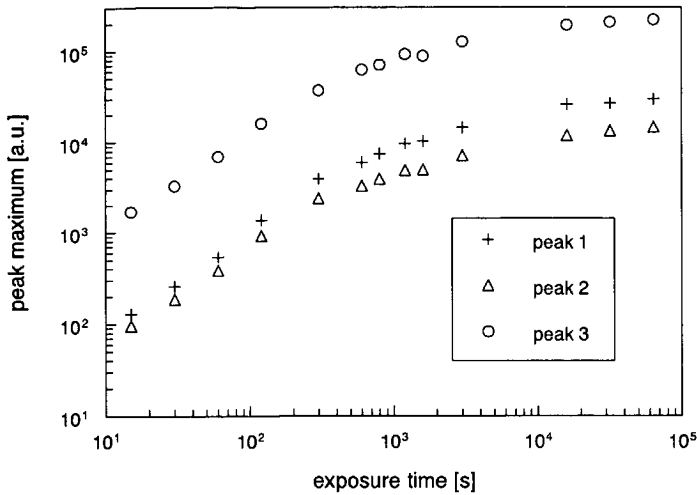


**Figure 5.12:** Maxima of peak 1, 2 and 3 of the TL glow curve of  $\text{LiYSiO}_4:\text{Ce}^{3+}$  as a function of the exposure time to a Hg lamp in combination with a interference filter to select the 254 nm line.

changes in shape. Its maximum shift to higher  $T$  and it adopts the asymmetrical shape typical for first-order kinetics. The geometry factor  $\mu_g$  of peak 3 of curve (c),  $\mu_g$  defined as  $\delta/\omega$  with  $\omega$  the full width at half height and  $\delta$  the width at half height on the high temperature side, amounts to 0.43. This is very close to the value of 0.42 for a peak governed by first-order kinetics. So at least a part of the recombination responsible for luminescence under peak 3 follows first-order kinetics. Since  $T_m$  does not shift as a function of dose it is well possible that the peak is a composition of several first-order peaks connected with traps that differ only slightly in depth. A more detailed analysis of the peak shape requires, prior to the analysis, a correction for the temperature dependent quenching of the  $\text{Ce}^{3+}$  luminescence.

From figure 5.13 is also concluded that the trapping centres involved in the TL can also be emptied optically. On the other hand the PSL signal has disappeared after recording the TL signal which shows that the photostimulable centres can also be emptied thermally. Together this strongly suggests that the trapping centres giving rise to TL are identical to those giving rise to PSL.

In figure 5.14 the so-called TL excitation spectrum is depicted. The data points were obtained as follows. The sample was illuminated with UV photons from a deuterium lamp at various wavelengths for a fixed time. Next a TL glow curve was recorded which was integrated over the whole temperature range. The integral number was corrected for the wavelength dependent intensity of the lamp. The threshold for trap filling is found around 300 nm.

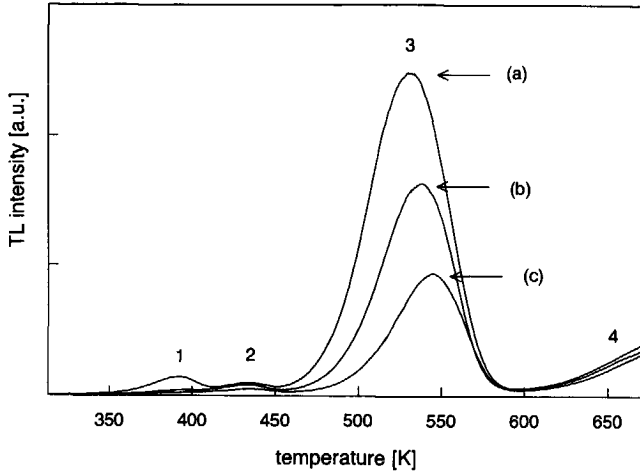


**Figure 5.13:** TL glow curves of  $\text{LiYSiO}_4:\text{Ce}^{3+}$  recorded after illumination with a Hg lamp for 1 min. followed by illumination with the Hg lamp in combination with a 420 nm cut-off filter for (a) 0 min., (b) 10 min. and (c) 45 min.

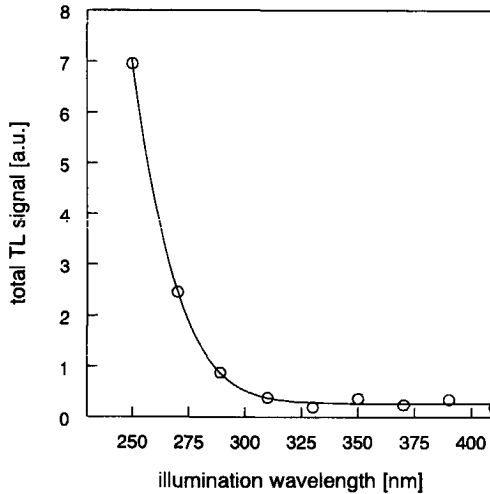


**Figure 5.14:** The total TL intensity of  $\text{LiYSiO}_4:\text{Ce}^{3+}$  as a function of the wavelength of the photons the sample was illuminated with. The line is drawn to guide the eye.

### 5.4.2 Discussion

Figure 5.12 shows that the structure of the TL spectrum does not change up to saturation. Such a behaviour can be expected when the electrons to be trapped stayed previously in the conduction

band (or the holes in the valence band) and the probability to be trapped by trap type  $i$  corresponding with a TL peak  $i$  depends only on the concentration  $N_i$  of traps and not on a trapping rate  $\Gamma_i$ .

According to the experiments with different radiation types (figure 5.11) this is not completely true. With an increasing ionisation density peak 4 becomes less pronounced compared to peak 1 and 2. Apparently,  $\Gamma_4$  is higher than  $\Gamma_1$  and  $\Gamma_2$ . With an high ionisation density all 'peak 4' traps become locally filled and consequently more free charge carriers are forced to choose 'peak 1' or 'peak 2' traps.

The results of figure 5.12 must be explained differently. It is possible that the traps do not become saturated at all but instead the *source* at which electron-hole pairs are created under 254 nm absorption is exhausted. This source corresponds with a centre absorbing photons up to 300 nm ( $\equiv 4.1$  eV) (figure 5.14). After absorption, the electron is separated from the hole and trapping can take place. An energy of 4.1 eV is insufficient to induce transitions across the forbidden gap. Hence an electronic level within the forbidden gap must be involved, belonging to an impurity or defect. After absorption only one charge carrier (electron or hole) can become delocalised. The other one must stay in the direct vicinity of the impurity/defect centre.

An obvious candidate for this centre is the  $\text{Ce}^{3+}$  activator ion, capturing either an electron becoming  $\text{Ce}^{2+}$  or being ionised becoming  $\text{Ce}^{4+}$ . As far as is known to the author, the formation of  $\text{Ce}^{2+}$  has only shown to be possible in  $\text{MF}_2:\text{Ce}^{3+}$  ( $\text{M}=\text{Ca}, \text{Sr}, \text{Ba}$ ; note  $\text{Ce}^{3+}$  replaces a divalent cation) after a chemical reduction treatment [192]. Even then it appears to be metastable. The ionisation of trivalent Ce has been demonstrated to occur in several materials, in particular when it forms a redox couple with another cation, like in  $\text{CaS}:\text{Ce}^{3+}, \text{Sm}^{3+}$  [193],  $\text{MgS}:\text{Ce}^{3+}, \text{Sm}^{3+}$  [119] and  $\text{Rb}_2\text{KInF}_6:\text{Ce}^{3+}$  ( $2\text{Ce}^{4+} + \text{In}^+$ ) [194]. It must be noted however, that the stability of  $\text{Ce}^{4+}$  is only (indirectly) proved in the latter material.

In the present case there are two indications that are consistent with the mechanism of the hole trapped on  $\text{Ce}^{3+}$  and the recombination occurring at this site after the electron has been released from its (unknown) trap: i) The TL and PSL emission spectra showed solely  $\text{Ce}^{3+}$  emission. ii) Only 3 excitation bands of  $\text{Ce}^{3+}$  were identified whereas 5 are expected. The explanation could be that the 2 remaining are located in the conduction band. This is in agreement with the observation that trap filling becomes possible when the  $\text{Ce}^{3+}$  excitation spectrum vanishes (compare figure 5.6 with figure 5.14). A similar model is proposed by Yen *et al.* for  $\text{Lu}_2\text{SiO}_5:\text{Ce}^{3+}$  [195].

Further verification of this simple model could be obtained by replacing  $\text{Ce}^{3+}$  by  $\text{Pr}^{3+}$  or  $\text{Tb}^{3+}$  and comparing the TL excitation spectra in the range 175-350 nm. Other centres that can show absorption in the UV range are for instance oxygen vacancies binding one or two electrons [196].

Several observations indicate that recombination is governed by first-order kinetics. First-order recombination via the conduction band requires that once the electron is liberated from its trap, recombination with a hole is much more probable than retrapping [191]. Suppose that  $\text{Ce}^{3+}$  is indeed responsible for absorption of the UV photons. Then figure 5.6 shows that radiative recombination is improbable. First-order recombination is still possible if the  $\text{Ce}^{4+}$  ion is spatially

correlated to the electron trap and tunneling takes place [191].

## 5.5 Summary and Conclusion

The scintillation and storage properties of  $\text{Ce}^{3+}$  doped  $\text{LiYSiO}_4$  and  $\text{LiLuSiO}_4$  powder samples have been studied. Upon X-ray excitation  $\text{LiYSiO}_4:\text{Ce}^{3+}$  exhibits spontaneous  $\text{Ce}^{3+}$  luminescence at 405 nm. The light yield per absorbed unit of X-ray energy is almost equal to that of a  $\text{BaF}_2$  powder reference sample. If the same applies to a  $\text{LiYSiO}_4:\text{Ce}^{3+}$  and a  $\text{BaF}_2$  single crystal the scintillation light yield of the latter is  $1 \cdot 10^4$  photons per MeV of absorbed X-ray energy. The light output per absorbed alpha particle is a factor 0.4 relative to that of the reference sample meaning that the light output for a single crystal would be  $2 \cdot 10^3$  photons per MeV of absorbed alpha particle energy and  $1 \cdot 10^4$  photons per absorbed neutron.

The gamma-induced scintillation decay curve contains a  $\tau = 38$  ns component, which corresponds with the lifetime of the  $\text{Ce}^{3+}$  5d excited state in this compound. For excitation with alpha particles a fast component with a  $\tau$  of several tens of ns is observed together with a slow component with a  $\tau$  of tens of  $\mu\text{s}$ . From the measurement it can not be concluded whether this slow component is also present in scintillations produced by gamma quanta. Combined with the Stokes shift of  $3600 \text{ cm}^{-1}$ , the application of a  $\text{LiYSiO}_4:\text{Ce}^{3+}$  single crystal as a fast thermal neutron scintillator is promising.

After irradiation with X-rays, alpha particles or thermal neutrons, the sample shows  $\text{Ce}^{3+}$  luminescence when thermally or optically stimulated. The optical stimulation spectrum shows a broad band with a maximum below 450 nm. The PSL yield for 23 keV X-rays is a factor of 15 less than the yield of a commercial  $\text{BaFBr}:\text{Eu}^{2+}$  sample. The PSL yield of the sample after 48 meV neutron irradiation is 0.5 photon per incident neutron, which is much less than the yield of  $\text{BaFBr}:\text{Eu}^{2+}$  mixed with  $\text{Gd}_2\text{O}_3$ . But the yield is estimated to increase with a factor of 200 when a 1 mm thick single crystal of  $\text{LiYSiO}_4:\text{Ce}^{3+}$  containing 96% enriched  $^6\text{Li}$  would be used instead of a powder layer. An image plate consisting of such a crystal will have a DQE of  $\sim 66\%$ , provided that only statistical noise is relevant. An important problem is the high stimulation energy being factor of 20 higher than that of the  $\text{BaFBr}:\text{Eu}^{2+}$  sample at 515 nm.

The optical properties of  $\text{Ce}^{3+}$  in  $\text{LiLuSiO}_4$  are very similar. Experiments on the  $\text{LiLuSiO}_4$  doped with  $\text{Ce}^{3+}$ ,  $\text{Tb}^{3+}$  or both, have learned that the PSL yield, the SE and the scintillation light yield depend strongly on the presence of rare-earth impurities and probably also other imperfections in the material. It is illustrative that the  $\text{LiLuSiO}_4:\text{Ce}^{3+}$  sample has the highest SL yield of  $3 \cdot 10^4$  pho/MeV whereas its PSL yield is low. On the other hand the  $\text{LiLuSiO}_4:\text{Ce}^{3+}, \text{Tb}^{3+}$  has the high X-ray PSL yield of 0.25 times that of  $\text{BaFBr}:\text{Eu}^{2+}$  whereas its SL yield is only  $7 \cdot 10^3$  pho/MeV.

Finally, TL experiments showed that under UV illumination ( $\leq 300$  nm) the same traps are filled as under irradiation with high energy particles or quanta. The centre responsible for the UV absorption could be  $\text{Ce}^{3+}$  implying that the hole is trapped near or on  $\text{Ce}^{3+}$ . Recombination is governed by first-order kinetics.



## 6

## Photoluminescence, scintillation and thermoluminescence in several $\text{Ce}^{3+}$ or $\text{Eu}^{2+}$ activated borates

### 6.1 Introduction

Borates generally exhibit a number of properties that make them attractive for use in optical systems. These properties include radiation hardness, moderate crystal-growth temperatures and, in particular for boron-oxygen rich networks, a stiff and covalent structure. The latter accounts for a limited Stokes shift of  $\text{Ce}^{3+}$  and consequently weak non-radiative losses.

In this chapter luminescence properties and the scintillation light yield of a group of  $\text{Ce}^{3+}$  activated borate compounds is discussed, thus examining their potential to be used as a thermal neutron scintillator. Also their thermoluminescence (TL) intensity has been measured after X-ray irradiation. The latter was done regarding the application of thermal neutron image plates.

The borates under consideration are

- the orthoborates  $\text{YBO}_3:\text{Ce}^{3+}$ ,  $\text{GdBO}_3:\text{Ce}^{3+}$  and  $\text{Li}_6\text{Y}(\text{BO}_3)_3:\text{Ce}^{3+}$ .
- the metaborates  $\text{LaB}_3\text{O}_6:\text{Ce}^{3+}$  and  $\text{GdB}_3\text{O}_6:\text{Ce}^{3+}$ .
- the compounds  $\text{LaMgB}_5\text{O}_{10}:\text{Ce}^{3+}$  and  $\text{YMgB}_5\text{O}_{10}:\text{Ce}^{3+}$  (denoted at present as the pentaborates).
- the compounds  $\text{CaLaB}_7\text{O}_{13}:\text{Ce}^{3+}$  and  $\text{CaLaB}_7\text{O}_{13}:\text{Eu}^{2+}$  (denoted as the heptaborates).
- the oxyorthoborates  $\text{CaYOBO}_3:\text{Eu}^{2+}$  and  $\text{Ca}_4\text{YO}(\text{BO}_3)_3:\text{Ce}^{3+}$ .

Of all compounds powder samples were synthesised. Table 6.1 lists the weight fraction of boron atoms  $W_B$  and the  $Z_{eff}$  of these compounds.

**Table 6.1:** The weight fraction of boron atoms  $W_B$  and the  $Z_{eff}$  of the borates under consideration.

compounds	$W_B(\%)$	$Z_{eff}$
YBO <sub>3</sub>	7.3	34
GdBO <sub>3</sub>	5.0	59
Li <sub>6</sub> Y(BO <sub>3</sub> ) <sub>3</sub>	11	29
LaB <sub>3</sub> O <sub>6</sub>	12	48
GdB <sub>3</sub> O <sub>6</sub>	11	55
LaMgB <sub>5</sub> O <sub>10</sub>	14	44
YMgB <sub>5</sub> O <sub>10</sub>	16	28
CaLaB <sub>7</sub> O <sub>13</sub>	16	42
CaYOBO <sub>3</sub>	5.3	32
Ca <sub>4</sub> YO(BO <sub>3</sub> ) <sub>3</sub> :Ce <sup>3+</sup>	7.3	27

The compounds Li<sub>6</sub>Ln(BO<sub>3</sub>)<sub>3</sub>, LnB<sub>3</sub>O<sub>6</sub> and LnMgB<sub>5</sub>O<sub>10</sub> (Ln = lanthanide or Y) are known because of the one-dimensional character of the interaction between the Ln ions. This has led to extensive luminescence studies (see respectively [169, 197–199], [200–202], [203, 204]) for lamp phosphor and plasma display panel applications. The interaction could also play role in the scintillation process.

The Gd compounds selected are less interesting from the application point of view, because the thermal neutrons will be captured by Gd isotopes instead of <sup>10</sup>B. This will give rise to a low light output with a large variance and will complicate the discrimination against ambient gamma rays.

Two samples are doped with Eu<sup>2+</sup>. Their scintillation response time will never be shorter than the decay time of Eu<sup>2+</sup> in its 4f<sup>6</sup>5d state, which is about 0.8 μs.

## 6.2 Experimental

### 6.2.1 Sample preparation

The samples were synthesized by means of solid state reactions. In table 6.2 the preparation methods for the different compounds are given. The purity of the reactants was 99.99% for the Ln<sub>2</sub>O<sub>3</sub> (Ln= the lanthanides including Y), > 98.5% for CeCl<sub>3</sub> and > 99.5% for the others. Prior to the reaction stoichiometric amounts of the reactants were mixed, but in case of YBO<sub>3</sub>:Ce<sup>3+</sup>, GdBO<sub>3</sub>:Ce<sup>3+</sup>, GdB<sub>3</sub>O<sub>6</sub>:Ce<sup>3+</sup>, LaMgB<sub>5</sub>O<sub>10</sub>:Ce<sup>3+</sup>, and YMgB<sub>5</sub>O<sub>10</sub>:Ce<sup>3+</sup> a small excess (5-10%) of H<sub>3</sub>BO<sub>3</sub> was used. The mixing was carried out either 'dry', with help of a mortar or ball mill, or 'wet'. In case of LnBO<sub>3</sub> (Ln = Y, Gd) and GdB<sub>3</sub>O<sub>6</sub>:Ce<sup>3+</sup> the latter meant that Ln<sub>2</sub>O<sub>3</sub> was dissolved in concentrated HCl and CeCl<sub>3</sub> and H<sub>3</sub>BO<sub>3</sub> in distilled water and that these solutions

**Table 6.2:** Specifications of the preparation method of the compounds. In the consecutive rows are given the compounds and their activator concentrations, the starting materials used in the solid state reaction, the method of mixing these materials (see text for details), and the firing steps with the surrounding atmosphere used.

compound	reactants	mixing	firing/atmosphere
$\text{Ln}_{1-x}\text{Ce}_x\text{BO}_3$ (Ln=Y,Gd) ( $x = 0.01$ )	$\text{H}_3\text{BO}_3$ , $\text{Ln}_2\text{O}_3$ , $\text{CeCl}_3 \cdot 7\text{H}_2\text{O}$	wet	3 h 1000 °C air 2 h 500 °C 90%Ar/10%H <sub>2</sub>
$\text{Li}_6\text{Y}_{(1-x)}\text{Ce}_x(\text{BO}_3)_3$ ( $x = 0.01$ )	$\text{H}_3\text{BO}_3$ , $\text{Y}_2\text{O}_3$ , $\text{Li}_2\text{CO}_3$ , $\text{CeO}_2$	dry	15 h 650 °C air 20 h 650 °C 99%Ar/1%H <sub>2</sub>
$\text{Gd}_{(1-x)}\text{Ce}_x\text{B}_3\text{O}_6$ ( $x = 0.01$ )	$\text{H}_3\text{BO}_3$ , $\text{Gd}_2\text{O}_3$ , $\text{CeCl}_3 \cdot 7\text{H}_2\text{O}$	wet	2 h 900 °C air 2 h 500 °C 90%Ar/10%H <sub>2</sub>
$\text{La}_{(1-x)}\text{Ce}_x\text{B}_3\text{O}_6$ ( $x = 0.1, 0.01, 0.005,$ 0.001, 0.0005)	$\text{H}_3\text{BO}_3$ , $\text{La}_2\text{O}_3$ , $\text{CeO}_2$	dry	2 h 850 °C air 2.5 h 90%Ar/10%H <sub>2</sub> 2.5 h 90%Ar/10%H <sub>2</sub>
$\text{La}_{(1-x)}\text{Ce}_x\text{MgB}_5\text{O}_{10}$ ( $x = 0.1, 0.01, 0.005,$ 0.001, 0.0005)	$\text{H}_3\text{BO}_3$ , $\text{La}_2\text{O}_3$ , $\text{CeO}_2$ , $\text{MgCO}_3^a$	dry	2 h 850 °C air 15 h 1020 °C 90%Ar/10%H <sub>2</sub> 10 h 1005 °C 90%Ar/10%H <sub>2</sub>
$\text{Y}_{(1-x)}\text{Ce}_x\text{MgB}_5\text{O}_{10}$ ( $x = 0.1, 0.01, 0.005,$ 0.001, 0.0005)	$\text{H}_3\text{BO}_3$ , $\text{Y}_2\text{O}_3$ , $\text{CeO}_2$ , $\text{MgCO}_3^a$	dry	2 h 850 °C air 4 h 995 °C 90%Ar/10%H <sub>2</sub> 3 h 995 °C 90%Ar/10%H <sub>2</sub>
$\text{Ca}_{(1-x)}\text{LaEu}_x\text{B}_7\text{O}_{13}$ $\text{CaLa}_{(1-x)}\text{Ce}_x\text{B}_7\text{O}_{13}$ ( $x = 0.01$ )	$\text{H}_3\text{BO}_3$ , $\text{La}_2\text{O}_3$ , $\text{CaCO}_3$ , $\text{CeO}_2$ or $\text{Eu}_2\text{O}_3$	wet	6 h 200 °C air 12 h 950 °C 99%Ar/1%H <sub>2</sub>
$\text{Ca}_{(1-x)}\text{YEu}_x\text{OBO}_3$ (1) ( $x = 0.01$ )	$\text{H}_3\text{BO}_3$ , $\text{Y}_2\text{O}_3$ , $\text{CaCO}_3$ , $\text{Eu}_2\text{O}_3$	dry	20 h 950 °C air 24 h 1400 °C air 24+40 h 1000 °C 99%Ar/1%H <sub>2</sub>
$\text{Ca}_{(1-x)}\text{YEu}_x\text{OBO}_3$ (2) ( $x = 0.01$ )	$\text{H}_3\text{BO}_3$ , $\text{Y}_2\text{O}_3$ , $\text{CaCO}_3$ , $\text{Eu}_2\text{O}_3$	wet	15 h 1000 °C 99%Ar/1%H <sub>2</sub> 20 h 1000 °C
$\text{Ca}_4\text{Y}_{(1-x)}\text{Ce}_x\text{O}(\text{BO}_3)_3$ ( $x = 0.01$ )	$\text{H}_3\text{BO}_3$ , $\text{Y}_2\text{O}_3$ , $\text{CaCO}_3$ , $\text{CeO}_2$	dry	15 h 950 °C air 20 h 1350 °C air 20 h 1000 °C 99%Ar/1%H <sub>2</sub>

<sup>a</sup>more properly:  $4\text{MgCO}_3 \cdot \text{Mg}(\text{OH})_2 \cdot 5\text{H}_2\text{O}$

were mixed. In case of  $\text{CaYBO}_3:\text{Eu}^{2+}$ ,  $\text{CaLaB}_7\text{O}_{13}:\text{Eu}^{2+}$  and  $\text{CaLaB}_7\text{O}_{13}:\text{Ce}^{3+}$  this meant that all reactants were dissolved in concentrated nitric acid.

The firing procedure consisted mostly of two stages of one or more heating steps: the first stage in an air atmosphere and the second stage in a reducing atmosphere in order to reduce the  $\text{Ce}^{4+}$  or  $\text{Eu}^{3+}$  activator ions. Between every firing step the samples were ground.

The structure of all samples was checked by X-ray diffraction using Cu or Co  $K_\alpha$  radiation. For most samples the spectrum matched those reported in literature. However, in  $\text{La}_{(1-x)}\text{Ce}_x\text{B}_3\text{O}_6$  some  $\text{LaBO}_3$  was detected, with a concentration of less than 5% for the lower  $x$  values. For the samples with  $x = 0.01$  and  $x = 0.1$  the concentration  $\text{LaBO}_3$  was, unfortunately, much higher. It was estimated to be  $\leq 30\%$ . In  $\text{LaMgB}_5\text{O}_{10}:\text{Ce}^{3+}$  some  $\text{LaBO}_3$  with a concentration of less than 5% and also some  $\text{LaB}_3\text{O}_6$  is found with a concentration of less than 10%. In  $\text{YMgB}_5\text{O}_{10}:\text{Ce}^{3+}$  some  $\text{YBO}_3$  could be observed with a concentration of less than 10%. Neither variation of the  $\text{H}_3\text{BO}_3$  excess nor prolonging of the firing time could enhance the purity of these samples.

## 6.2.2 Luminescence and light yield measurements

The photoluminescence studies were performed with an IBH model 5000U spectrophotometer described in chapter 5. Excitation measurements in the VUV range were carried out with the synchrotron at Daresbury Laboratory, United Kingdom. Excitation spectra were corrected for the wavelength dependent excitation intensity. Emission spectra were corrected for the sensitivity of the system. The X-ray induced emission measurements were recorded with a setup described by Dorenbos *et al.* [142]. Powder layers of typically 100  $\mu\text{m}$  were measured in transmission. The scintillation light yields were obtained from these measurements as described in chapter 5. TL glow curves were recorded with a setup described in [205]. From all samples a pill of 50 mg was pressed and exposed to a certain dose of gamma irradiation of a  $^{60}\text{Co}$  source. The total TL signal was compared with that of a pill of the commercially available reference material of  $\text{BaFBr}:\text{Eu}^{2+}$  (company Agfa-Gevaert, Belgium).

## 6.3 Results

### 6.3.1 Excitation/emission measurements

At first the excitation and emission spectra of  $\text{Ce}^{3+}$  or  $\text{Eu}^{2+}$  in the compounds will be discussed. The isostructural orthoborates  $\text{YBO}_3:\text{Ce}^{3+}$  and  $\text{GdBO}_3:\text{Ce}^{3+}$  are not discussed because their luminescence properties are well-known [206].

#### $\text{Li}_6\text{Y}(\text{BO}_3)_3:\text{Ce}^{3+}$

The structure of  $\text{Li}_6\text{Y}(\text{BO}_3)_3:\text{Ce}^{3+}$  has been unravelled by Abdullaev *et al.* [207]. The symmetry at the Ln ion site is C1 (distorted cube). The measured excitation and emission spectra of  $\text{Ce}^{3+}$  in

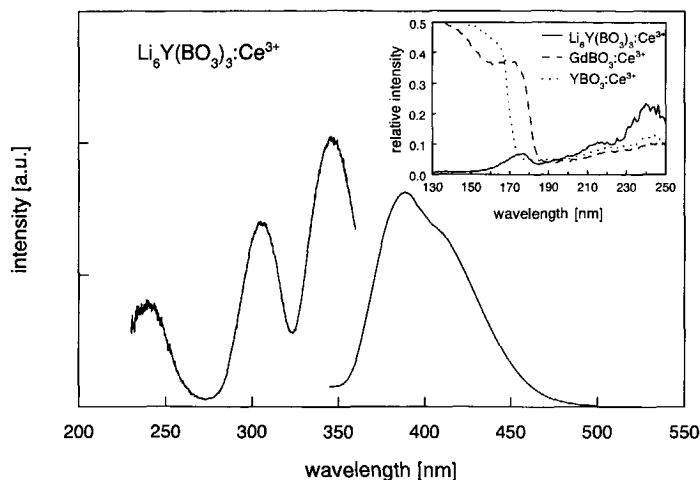


**Figure 6.1:** Excitation spectrum ( $\lambda_{em} = 390$  nm) and emission spectrum ( $\lambda_{ex} = 305$  nm) of  $\text{Li}_6\text{Y}_{0.99}\text{Ce}_{0.01}(\text{BO}_3)_3$ . Inset: Excitation spectra recorded in the (V)UV range of  $\text{Li}_6\text{Y}_{0.99}\text{Ce}_{0.01}(\text{BO}_3)_3$ ,  $\text{Y}_{0.99}\text{Ce}_{0.01}\text{BO}_3$  and  $\text{Gd}_{0.99}\text{Ce}_{0.01}\text{BO}_3$  ( $\lambda_{em} = 390$  nm), all relative to the excitation spectrum of sodium salicylate (NaSal) ( $\lambda_{em} = 410$  nm).

$\text{Li}_6\text{Y}(\text{BO}_3)_3$  are depicted in figure 6.1.

They look very similar to those of  $\text{Li}_6\text{Gd}(\text{BO}_3)_3:\text{Ce}^{3+}$  [169]. The excitation spectrum shows three bands at 345 nm, 305 nm and 240 nm respectively. The inset of figure 6.1 shows the excitation spectrum of  $\text{Li}_6\text{Y}(\text{BO}_3)_3:\text{Ce}^{3+}$  in the (V)UV range, together with that of the other orthoborates,  $\text{YBO}_3:\text{Ce}^{3+}$  and  $\text{GdBO}_3:\text{Ce}^{3+}$ . Two more bands found in this range, located around 217 and 176 nm. The 176 nm band must be attributed band to band transitions followed by a recombination on  $\text{Ce}^{3+}$ . Contrary to  $\text{YBO}_3:\text{Ce}^{3+}$  and  $\text{GdBO}_3:\text{Ce}^{3+}$ , the efficiency of this process drops again below 176 nm in  $\text{Li}_6\text{Y}(\text{BO}_3)_3:\text{Ce}^{3+}$ . This must be due to the increasing kinetic energy of electron-hole pairs created. Larger separations become possible between electron and hole, resulting in migration losses before formation of excitons or the subsequent trapping of electrons and holes on  $\text{Ce}^{3+}$  takes place. These losses are much higher than in  $\text{YBO}_3:\text{Ce}^{3+}$  and  $\text{GdBO}_3:\text{Ce}^{3+}$ .

The bands at longer wavelengths correspond with transitions to the components of the  $\text{Ce}^{3+}$  5d configuration which is splitted due to the crystal field. Because of the distorted cubic field two e-like orbitals can be expected at relatively low energy which are separated from the  $t_2$ -like orbitals at higher energies. Hence the two bands at 355 and 305 nm can be ascribed to transitions to e-like orbitals, being well separated (in terms of energy) from the other bands at 240 and 217 nm which represent the transitions to  $t_2$ -like states. Apparently the third  $t_2$ -orbital is energetically so close to the other two that it can not be resolved at RT. Since its energy level must be located at least  $40,000\text{ cm}^{-1}$  ( $\equiv 258$  nm) above the ground state it can be concluded that the average 5d-

$4f(^2F_{5/2})$  separation amounts to more than  $38,000\text{ cm}^{-1}$ . According to Blasse [206] this number is quite large for  $\text{Ce}^{3+}$  in an oxide system.

The emission spectrum of  $\text{Li}_6\text{Y}(\text{BO}_3)_3:\text{Ce}^{3+}$  was also measured upon 355 nm laser excitation at 77 K. Then two emission maxima can clearly be distinguished at 388 and 419 nm. The splitting of  $1900\text{ cm}^{-1}$  is in good agreement with the splitting between the  $^2F_{5/2}$  ground state and the  $^2F_{7/2}$  state of  $\text{Ce}^{3+}$  due to the spin-orbit coupling.

### **$\text{GdB}_3\text{O}_6:\text{Ce}^{3+}$ , $\text{LaB}_3\text{O}_6:\text{Ce}^{3+}$ , $\text{LaMgB}_5\text{O}_{10}:\text{Ce}^{3+}$ and $\text{YMgB}_5\text{O}_{10}:\text{Ce}^{3+}$**

These phosphors show similar optical properties of  $\text{Ce}^{3+}$ .  $\text{GdB}_3\text{O}_6$  and  $\text{LaB}_3\text{O}_6$  are isostructural. The structure has been described by Abdullaev *et al.* [208]. That of  $\text{LaMgB}_5\text{O}_{10}$  is described by Saubat *et al.* [209], and Saakes *et al.* [210] have reported  $\text{YMgB}_5\text{O}_{10}$  to be isostructural with it. In all compounds the Ln (Ln=La,Gd) ions occupy a site coordinated by 10 oxygens with C2 symmetry in the metaborates and C1 symmetry in the pentaborates.

The efficient luminescence of  $\text{Ce}^{3+}$  in  $\text{LaB}_3\text{O}_6:\text{Ce}^{3+}$ ,  $\text{GdB}_3\text{O}_6:\text{Ce}^{3+}$  and  $\text{LaMgB}_5\text{O}_{10}:\text{Ce}^{3+}$  has been reported before [200, 203, 211]. In all materials the emission band is located between 290 nm and 330 nm which is remarkably short for an oxide compound. The excitation spectra range from 200 to 275 nm and the fivefold splitting of the 5d state due to the low site symmetry can just be resolved at RT. These observations correspond with the spectra measured by us. The average  $5d-4f(^2F_{5/2})$  separation in terms of energy is for  $\text{LaB}_3\text{O}_6:\text{Ce}^{3+}$  more than  $43,000\text{ cm}^{-1}$  which is representative for these compounds and which is even considerably more than that for  $\text{Li}_6\text{Y}(\text{BO}_3)_3:\text{Ce}^{3+}$ . It is noted that in  $\text{LaPO}_4:\text{Ce}^{3+}$  this high number is found as well [212]. It can be concluded that this parameter covers a broad range for oxide systems.

In some  $\text{LaB}_3\text{O}_6:\text{Ce}^{3+}$  as well as in some  $\text{LaMgB}_5\text{O}_{10}:\text{Ce}^{3+}$  samples a weak additional emission at 355 nm and 376 nm has been observed which matches with the  $\text{Ce}^{3+}$  emission in  $\text{LaBO}_3$  [206].

The excitation and emission spectra of  $\text{Ce}^{3+}$  in  $\text{YMgB}_5\text{O}_{10}$  have not been reported before and are given in figure 6.2. In the excitation spectrum three maxima are present, respectively at 235 nm, 255 nm and 270 nm. It is very similar to the excitation spectrum of  $\text{LaMgB}_5\text{O}_{10}:\text{Ce}^{3+}$ , where the bands are located around 239 nm, 257 nm and 271 nm. The upper inset of figure 6.2 shows that two more bands are found peaking at 202 and 225 nm, again very close to the bands in  $\text{LaMgB}_5\text{O}_{10}:\text{Ce}^{3+}$ .

There is also a strong similarity between the emission spectra of these two materials. Like the 3 low energy excitation bands of  $\text{YMgB}_5\text{O}_{10}:\text{Ce}^{3+}$ , the emission band of  $\text{YMgB}_5\text{O}_{10}:\text{Ce}^{3+}$  is shifted by about 3 nm to the short wavelength side. Two weak emission bands were detected around 388 nm and 418 nm which correspond with the  $\text{Ce}^{3+}$  emission bands in  $\text{YBO}_3$ .

A difference is observed when exciting these materials in the VUV range (see inset). The spectrum of  $\text{YMgB}_5\text{O}_{10}:\text{Ce}^{3+}$  shows a weak  $\text{Ce}^{3+}$  emission when excited around 175 nm which can be due to creation of excitons but also to transitions to the  $\text{Ce}^{3+}$  6s states. At shorter wavelengths when band to band transitions become possible the luminescence is even weaker. In  $\text{LaMgB}_5\text{O}_{10}:\text{Ce}^{3+}$  however, the band around 175 nm is not observed (contrary to the observa-

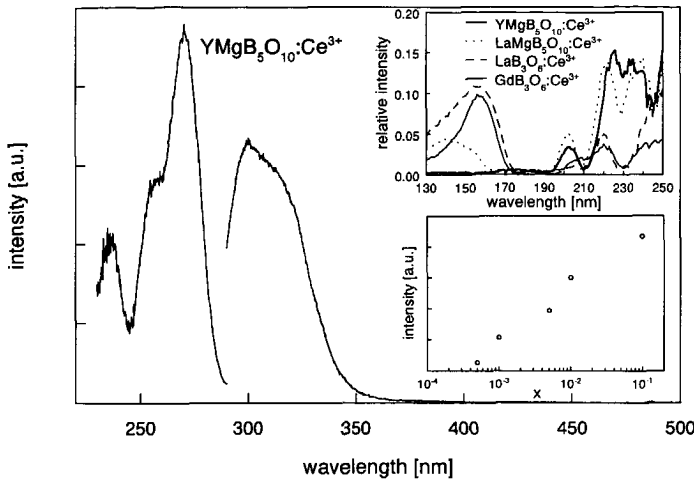


**Figure 6.2:** Excitation spectrum ( $\lambda_{em}=300$  nm) and emission spectrum ( $\lambda_{ex}=273$  nm) of  $Y_{0.99}Ce_{0.01}MgB_5O_{10}$ . Upper inset: Excitation spectra recorded in the (V)UV range of  $Y_{0.99}Ce_{0.01}MgB_5O_{10}$ ,  $La_{0.99}Ce_{0.01}MgB_5O_{10}$ ,  $La_{0.99}Ce_{0.01}B_3O_6$  and  $Gd_{0.99}Ce_{0.01}B_3O_6$  ( $\lambda_{em} = 310$  nm), all relative to the excitation spectrum of sodium salicylate (NaSal) ( $\lambda_{em} = 410$  nm). Lower inset: The relative luminescence intensity ( $\lambda_{ex} = 235$  nm) of  $Y_{(1-x)}Ce_xMgB_5O_{10}$  as a function of  $x$ .

tion of Saubat *et al.* [203] for  $La_{0.9}Ce_{0.1}MgB_5O_{10}$ , who distinguished two overlapping bands in this area). And in the  $LaMgB_5O_{10}:Ce^{3+}$  spectrum the luminescence intensity rises significantly under band to band excitations starting at 160 nm. Although the structure and the position of the  $Ce^{3+}$  4f energy levels relative to the 5d levels is almost the same in  $YMgB_5O_{10}:Ce^{3+}$  and  $LaMgB_5O_{10}:Ce^{3+}$ , the transfer of host lattice excitations to  $Ce^{3+}$  is not.

In the metaborates and the pentaborates  $Ce^{3+}$  dopant concentrations of tens of percents can be realised [203]. In the lower inset of figure 6.2 the luminescence intensity of  $Y_{(1-x)}Ce_xMgB_5O_{10}$  is plotted as a function of  $x$ , measured at  $\lambda_{ex}=235$  nm. The figure shows that the technical quantum efficiency increases with increasing  $x$ , which is to be expected since more exciting photons will be absorbed when the  $Ce^{3+}$  concentration increases. The effect of self-absorption is not visible at these values of  $x$ . The maximum intensity is expected not far beyond  $x = 0.1$ , being the optimal  $x$  value in in  $La_{(1-x)}Ce_xMgB_5O_{10}$  [203].

### **CaLaB<sub>7</sub>O<sub>13</sub>:Ce<sup>3+</sup> and CaLaB<sub>7</sub>O<sub>13</sub>:Eu<sup>2+</sup>**

The detailed structure of  $CaLaB_7O_{13}$  is not known in the literature but the X-ray powder diffraction data has been presented by Chen *et al.* [213].

The excitation and emission spectra of  $CaLaB_7O_{13}:Ce^{3+}$  are given in figure 6.3. Both show a

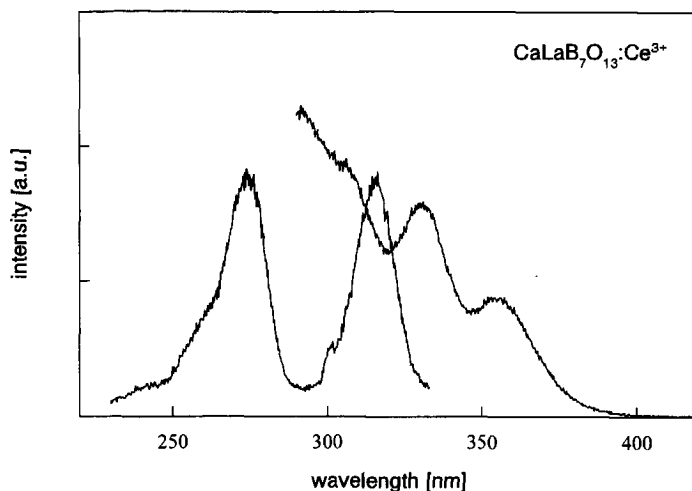


**Figure 6.3:** Excitation spectrum ( $\lambda_{em}=370$  nm) and emission spectrum ( $\lambda_{ex}=270$  nm) of  $Ce^{3+}$  in  $CaLaB_7O_{13}$ .

peculiar structure. In the emission spectrum measured at  $\lambda_{ex}=270$  nm four bands can be distinguished of which two pronounced ones at 330 nm and 354 nm and two less pronounced ones around 290 nm and 309 nm. The splitting between both pairs of bands amounts to about  $2000\text{ cm}^{-1}$  corresponding with the spin-orbit splitting of the  $Ce^{3+}$  ground state. The excitation spectrum measured at  $\lambda_{em}=370$  nm shows two relatively intense excitation bands at 273 and 316 nm. The one at 273 nm exhibits two shoulders at 242 nm and 259 nm and the band at 316 nm has a small shoulder at 301 nm. Alternatively, excitation at 305 nm results in the emission at 330 and 354 nm. Therefore it is concluded that the emission bands at 330 nm and 354 nm belong to one and the same  $Ce^{3+}$  site and the others to another. It is for example possible that  $Ce^{3+}$  ions occupy both  $La^{3+}$  and  $Ca^{2+}$  sites. More should be known about the structure to verify this hypothesis.

In  $CaLaB_7O_{13}:Eu^{2+}$  mainly  $Eu^{3+}$  luminescence was observed. Only under intense laser excitation (266 nm) the compound shows a weak broad band emission around 420 nm which can be attributed to a  $5d-4f$  transition in  $Eu^{2+}$ . It is not clear whether the reduction of  $Eu^{3+}$  during preparation has not been effective or  $Eu^{2+}$  does not show luminescence in this host.

#### **$Ca_4YO(BO_3)_3:Ce^{3+}$ and $CaYOBO_3:Eu^{2+}$**

The preparation and structure of the compound  $Ca_4YO(BO_3)_3:Ce^{3+}$  was reported by Norrestam *et al.* [214]. The structure consists of  $BO_3$  triangles and one oxygen ion which has no bond to boron. The  $Y^{3+}$  ions are in a distorted octahedral coordination of oxygens from which two do not belong to borate groups. The symmetry at the  $Y^{3+}$  site is  $C_s$ . The luminescence of  $Ce^{3+}$  in



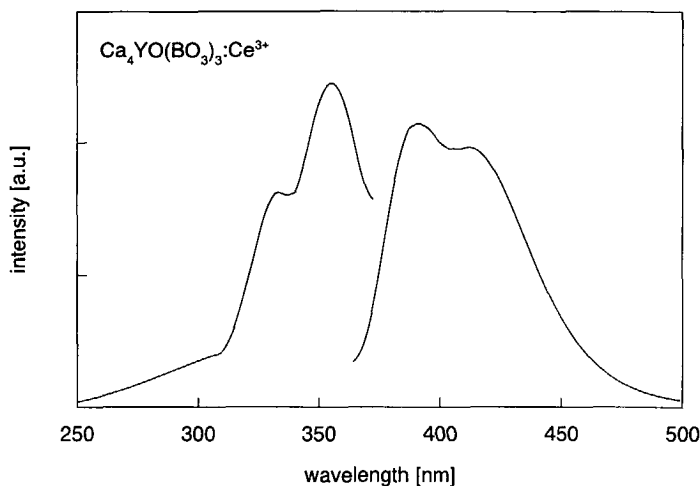


**Figure 6.4:** Excitation spectrum ( $\lambda_{em}=410$  nm) and emission spectrum ( $\lambda_{ex}=330$  nm) of  $Ce^{3+}$  in  $Ca_4YO(BO_3)_3$ .

this host is weak.

Figure 6.4 displays the excitation and emission spectra. The emission spectrum consists of two overlapping bands at 385 and 415 nm. A decomposition of the bands into two Gaussian shaped bands (on a  $cm^{-1}$  scale) yields an energy difference of  $1880\text{ cm}^{-1}$ . The excitation spectrum exhibits a band at 355 nm with a shoulder at 330 nm. A third, much less intense band is located around 300 nm. The strong decrease in the intensity of the excitation bands when going from longer to shorter wavelengths is an indication that the other 5d levels are located in the conduction bands which complicates their observation by means of an excitation measurement. Because of the weakness of the luminescence it can not be excluded that the luminescence is due to  $Ce^{3+}$  present in a second phase, which could not be detected by X-ray diffraction. Possible candidates of which the  $Ce^{3+}$  luminescence is known in the literature are  $Ca_3(BO_3)_2:Ce^{3+}$  [215] and  $YBO_3:Ce^{3+}$  [206]. However, in both cases the emission and/or excitation spectra do not match. It should be noted that  $Ce^{3+}$  does not luminesce in isostructural  $Ca_4GdO(BO_3)_3:Ce^{3+}$  [216].

The structure and luminescence of several trivalent rare earth ions (among them  $Ce^{3+}$ ) in the oxyorthoborate  $Ca_4YO(BO_3)_3$  has been reported by Blasse [217]. The quantum efficiency of  $Ce^{3+}$  appeared to be very low. As an alternative (thermo)luminescence of  $Eu^{2+}$  in this host was investigated. Upon 240 nm excitation the emission spectrum of  $CaYOBO_3:Eu^{2+}$  showed only the narrow lines in the red which are the typical  $Eu^{3+} {}^5D_0-{}^7F_J$  transitions. No  $Eu^{2+}$  luminescence is observed, even not under intense laser excitation at 266 or 355 nm. This means that either the  $Eu^{2+}$  luminescence is quenched or Eu is only present in the trivalent state. Considering the ionic radii of the ions involved:  $r(Eu^{2+})=1.09\text{ \AA}$ ,  $r(Eu^{3+})=0.95\text{ \AA}$ ,  $r(Y^{3+})=0.89\text{ \AA}$ ,  $r(Ca^{2+})=0.99\text{ \AA}$  [218]

it will be energetically favourable for Eu ions to occupy Y sites when they are in the trivalent state. However, in the reducing atmosphere applied,  $\text{Eu}^{2+}$  should be present and generally it is no problem for this ion to occupy the position of the smaller  $\text{Ca}^{2+}$  ion [120, 219]. Hence, it is thought that the quenching argument applies here.

### 6.3.2 X-ray induced emission and scintillation light yields

In table 6.3 the scintillation light yields are presented, determined by measuring the X-ray induced emission intensities. Also the maxima of the emission bands are given. For nearly all samples they correspond with the emission maxima measured upon direct excitation of  $\text{Ce}^{3+}$ . The exception is  $\text{GdB}_3\text{O}_6:\text{Ce}^{3+}$ , that showed mainly emission at 311 nm upon X-ray excitation, which is due to the  ${}^6\text{P}_{7/2}-{}^8\text{S}_{7/2}$  transition in  $\text{Gd}^{3+}$ . The amplitude of the  $\text{Ce}^{3+}$  emission is at least two orders of magnitude lower. Contrary to  $\text{LaB}_3\text{O}_6:\text{Ce}^{3+}$ , energy transfer from  $\text{Ce}^{3+}$  to  $\text{Gd}^{3+}$  is possible, with a rate equal to the radiative decay rate [200].

The scintillation light yields of the orthoborates  $\text{LaBO}_3:\text{Ce}^{3+}$ ,  $\text{ScBO}_3:\text{Ce}^{3+}$  and  $\text{YAl}_3\text{B}_4\text{O}_{12}:\text{Ce}^{3+}$  are added to table 6.3 although they were not directly measured. However, it was possible to estimate the light yield as follows: Blasse *et al.* [206] have reported the cathode ray efficiencies of these compounds together with that of  $\text{YBO}_3:\text{Ce}^{3+}$ . The cathode ray efficiencies, measured at 20 kV, were reported to be 2% for  $\text{YBO}_3:\text{Ce}^{3+}$ ,  $\text{ScBO}_3:\text{Ce}^{3+}$  and  $\text{YAl}_3\text{B}_4\text{O}_{12}:\text{Ce}^{3+}$  and 0.2% for  $\text{LaBO}_3:\text{Ce}^{3+}$ . This corresponds with a scintillation light yield of 6500 pho/MeV which is in reasonable agreement with the yield of 10,000 pho/MeV measured by us. Our assumption is that the relation between the cathode ray efficiencies holds for the scintillation efficiencies under X-ray excitation. Hence, in order to obtain the scintillation light yield for, say,  $\text{ScBO}_3:\text{Ce}^{3+}$  the measured scintillation light yield for  $\text{YBO}_3:\text{Ce}^{3+}$  is multiplied with the ratio of the cathode ray efficiency of  $\text{ScBO}_3:\text{Ce}^{3+}$  and  $\text{YBO}_3:\text{Ce}^{3+}$ . It should be noted that the decay time of

$\text{LaBO}_3:\text{Ce}^{3+}$ ,  $\text{YBO}_3:\text{Ce}^{3+}$ ,  $\text{ScBO}_3:\text{Ce}^{3+}$  and  $\text{YAl}_3\text{B}_4\text{O}_{12}:\text{Ce}^{3+}$  upon cathode ray excitation is between 25 and 60 ns [167] corresponding with the decay time of the 5d-4f transition in  $\text{Ce}^{3+}$ .

The light yield of a  $\text{Li}_6\text{Gd}(\text{BO}_3)_3:\text{Ce}^{3+}$  crystal is measured by Czirr [220]. He has also measured the light yield of a  $\text{Li}_6\text{Y}(\text{BO}_3)_3:\text{Ce}^{3+}$  powder sample relative to that of  $\text{Li}_6\text{Gd}(\text{BO}_3)_3:\text{Ce}^{3+}$ , from which a yield of 3000 photons per MeV (pho/MeV) for  $\text{Li}_6\text{Y}(\text{BO}_3)_3:\text{Ce}^{3+}$  follows. This number is higher than that determined by us (1200 pho/MeV), which illustrates the limited accuracy of the measurements on powder samples. The substantially higher light yield of  $\text{Li}_6\text{Gd}(\text{BO}_3)_3:\text{Ce}^{3+}$  compared to that of  $\text{Li}_6\text{Y}(\text{BO}_3)_3:\text{Ce}^{3+}$  must be explained by the efficient charge transport that is possible over the one-dimensional chains of  $\text{Gd}^{3+}$  ions, mentioned in section 6.1. If this mechanism plays a role the higher yield should be attended with an increase of the scintillation decay time when going from  $\text{Li}_6\text{Y}(\text{BO}_3)_3:\text{Ce}^{3+}$  to  $\text{Li}_6\text{Gd}(\text{BO}_3)_3:\text{Ce}^{3+}$ . This is confirmed by the measurements of Czirr, who finds 100 ns for  $\text{Li}_6\text{Y}(\text{BO}_3)_3:\text{Ce}^{3+}$  and components of 200 ns and 700 ns for  $\text{Li}_6\text{Gd}(\text{BO}_3)_3:\text{Ce}^{3+}$ .

Table 6.3 shows that the orthoborates, that is, the compounds that contain isolated triangular  $(\text{BO}_3)^{3-}$  groups, are generally more efficient in the scintillation process than the meta-, penta-

**Table 6.3:** Scintillation light (SL) yield and the thermoluminescence (TL) yield of the borate powder samples. The scintillation light yield, defined as the number of photons emitted per MeV of absorbed X-ray energy, is determined relative to that of a BaF<sub>2</sub> reference sample. The TL yield, defined as the total number of photons emitted during the recording of a glow curve per unit of absorbed gamma ray dose, is determined relative to that of a BaFBr:Eu<sup>2+</sup> reference sample. References in column 2 refer to earlier reports on Ce<sup>3+</sup> photoluminescence properties. References in column 3 refer to earlier reports on either cathode ray luminescence intensity or scintillation light yield.

compound		$\lambda_{em}$	SL yield	TL yield
BaF <sub>2</sub>		300	1	
BaFBr:Eu <sup>2+</sup>		390		1
YBO <sub>3</sub> :Ce <sup>3+</sup>	(~1%)	390,415	[217] 0.9	0.01
GdBO <sub>3</sub> :Ce <sup>3+</sup>	(~1%)	385,415	0.9	0.01
LaBO <sub>3</sub> :Ce <sup>3+</sup>	(~1%)	355,380	[217] 0.09	[206]
ScBO <sub>3</sub> :Ce <sup>3+</sup>	(~1%)	385,420	[217] 0.9	[206]
YAl <sub>3</sub> B <sub>4</sub> O <sub>12</sub> :Ce <sup>3+</sup>	(~1%)	344,367	[206] 0.9	[206]
Li <sub>6</sub> Y(BO <sub>3</sub> ) <sub>3</sub> :Ce <sup>3+</sup>	(1%)	388,419	0.1-0.3	< 0.001
Li <sub>6</sub> Gd(BO <sub>3</sub> ) <sub>3</sub> :Ce <sup>3+</sup>	(~1%)	385,415	[169] 1.3	[220]
GdB <sub>3</sub> O <sub>6</sub> :Ce <sup>3+</sup>	(1%)	311,(305,325)	0.02	< 0.001
LaB <sub>3</sub> O <sub>6</sub> :Ce <sup>3+</sup>	(0.05%)	300,320	[200] 0.7	< 0.001
LaB <sub>3</sub> O <sub>6</sub> :Ce <sup>3+</sup>	(0.5%)	300,320	[200] 0.16	< 0.001
LaMgB <sub>5</sub> O <sub>10</sub> :Ce <sup>3+</sup>	(0.05%)	300,317	[203] 0.12	< 0.001
LaMgB <sub>5</sub> O <sub>10</sub> :Ce <sup>3+</sup>	(0.5%)	300,317	[203] 0.03	< 0.001
YMgB <sub>5</sub> O <sub>10</sub> :Ce <sup>3+</sup>	(0.05%)	305 (RT)	0.03	< 0.001
YMgB <sub>5</sub> O <sub>10</sub> :Ce <sup>3+</sup>	(0.5%)	305 (RT)	0.03	< 0.001
CaLaB <sub>7</sub> O <sub>13</sub> :Ce <sup>3+</sup>	(1%)	291,309,330,360	0.02	< 0.001
CaLaB <sub>7</sub> O <sub>13</sub> :Eu <sup>2+</sup>	(1%)	no Eu <sup>2+</sup>		-
CaYOBO <sub>3</sub> :Eu <sup>2+</sup>	(1%)	no Eu <sup>2+</sup>		-
Ca <sub>4</sub> YO(BO <sub>3</sub> ) <sub>3</sub> :Ce <sup>3+</sup>	(1%)	390,420 (weak)	0.01	< 0.001

and heptaborates (with the exception of LaBO<sub>3</sub>:Ce<sup>3+</sup>). Furthermore it is noted that a relatively high scintillation light yield is coupled with a high luminescence intensity under 150 nm excitation. The latter is illustrated by the insets of figure 6.1 and figure 6.2.

Regarding all light yields given in table 6.3 it can be concluded that Li<sub>6</sub>Gd(BO<sub>3</sub>)<sub>3</sub>:Ce<sup>3+</sup> is the most efficient scintillator among the borates. However, its decay time is longer than those of the orthoborates [167], of which most have a light yield that is some 10,000 pho/MeV. Particularly interesting is YAlB<sub>4</sub>O<sub>12</sub> having the lowest  $Z_{eff}$  (28) and the highest  $W_B$  (12%) of the orthoborates.

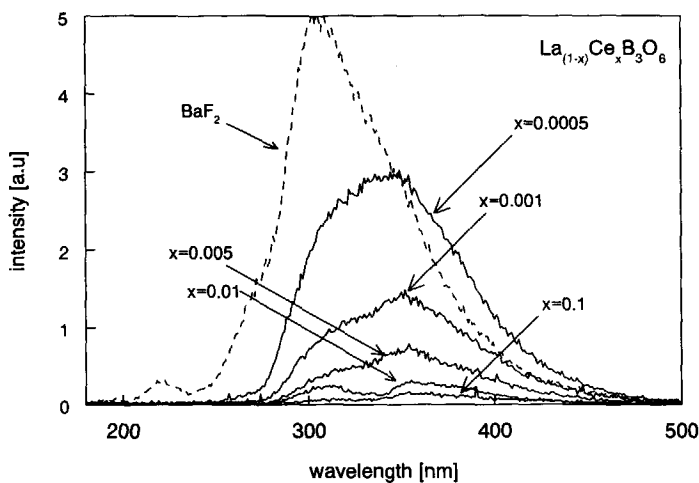


**Figure 6.5:** X-ray induced emission spectra of  $\text{La}_{(1-x)}\text{Ce}_x\text{B}_3\text{O}_6$  for different values of  $x$ . For comparison the spectrum of a  $\text{BaF}_2$  reference sample is also given. The spectra are not corrected for the sensitivity of the system.

For the meta and pentaborates, allowing high  $\text{Ce}^{3+}$  dopant concentrations, the X-ray induced luminescence as a function of the  $\text{Ce}^{3+}$  concentration was studied. In figure 6.5, X-ray excited emission spectra of  $\text{LaB}_3\text{O}_6:\text{Ce}^{3+}$  are depicted for different values of  $x$ . For  $x = 0.1$  the emission is negligible. For  $x=0.01$  two bands are visible: one that corresponds with the emission under photoexcitation ( $\lambda < 340$  nm) and one that corresponds with the  $\text{Ce}^{3+}$ -emission in the second phase,  $\text{LaBO}_3$  ( $\lambda > 340$  nm). For lower values of  $x$  the emission intensity increases further and for  $x = 0.0005$  one broad emission band remains, that peaks around 343 nm. Because this sample turned out to be single phase according to photoluminescence as well as X-ray diffraction analysis, it can be excluded that the broad band is a composite band similar to that shown for  $x = 0.01$ . The possibility of a host lattice emission remains, although the origin is unknown and should be studied further. In  $\text{La}_{(1-x)}\text{Ce}_x\text{MgB}_5\text{O}_{10}$  a similar band is observed for  $x = 0.0005$ , but the intensity is lower. For higher  $\text{Ce}^{3+}$  concentrations a weak emission band around 310 nm appears, corresponding with the photoluminescence band. In isostructural  $\text{Y}_{(1-x)}\text{Ce}_x\text{MgB}_5\text{O}_{10}$  the emission is very weak and the host lattice emission is not observed. This indicates that the emission is connected with the  $\text{La}^{3+}$  ions.

### 6.3.3 Thermoluminescence

As indicated in the last column of table 6.3, none of the samples shows strong TL when compared to  $\text{BaFBr}:\text{Eu}^{2+}$ . Also the effect of the introduction of extra impurities on the TL was examined. For this purpose samples of  $\text{La}_{(1-x-y)}\text{Ce}_x\text{R}_y\text{B}_3\text{O}_6$  with  $\text{R} = \text{Na}, \text{Ca}, \text{Sm}$  or  $\text{Zr}$ ;  $x = 0.001, y =$

0.001 were prepared. Note that all co-dopants have a slightly smaller ionic radius than  $\text{La}^{3+}$  when they take on their preferred valence. Also  $\text{Y}_{(1-x-y)}\text{Ce}_x\text{Sm}_y\text{BO}_3$  ( $x = 0.01; y = 0.01$ ) was synthesized. None of the co-dopants induced a significant enhancement of the TL intensity.

## 6.4 Discussion

The results summarised in table 6.3 show two peculiarities to be discussed below. At first, the weak luminescence of  $\text{Ce}^{3+}$  in  $\text{Ca}_4\text{YO}(\text{BO}_3)_3:\text{Ce}^{3+}$ . Secondly, the emission wavelength of  $\text{Ce}^{3+}$  in the meta and pentaborates is substantially shorter than in the orthoborates.

First the  $\text{Ce}^{3+}$  luminescence in  $\text{Ca}_4\text{YO}(\text{BO}_3)_3:\text{Ce}^{3+}$  is discussed. From the literature it is known that  $\text{Ce}^{3+}$  does not luminesce in  $\text{Ca}_4\text{GdO}(\text{BO}_3)_3:\text{Ce}^{3+}$  [216] and only weak luminescence is observed in  $\text{SrLa}_2\text{OBeO}_4:\text{Ce}^{3+}$  [221].  $\text{SrLaOBO}_3:\text{Ce}^{3+}$  luminesces around 450 nm but it is partly quenched at RT [222]. All these compounds have in common that one of the oxygen neighbours of  $\text{Ce}^{3+}$  is not coordinated to  $\text{B}^{3+}$  (or  $\text{Be}^{2+}$ ).

Dirksen *et al.* [216] suppose for  $\text{Ca}_4\text{GdO}(\text{BO}_3)_3:\text{Ce}^{3+}$  that this oxygen has a more covalent binding with  $\text{Ce}^{3+}$  than the other oxygens. As a consequence the  $\text{Ce}^{3+}$  5d excited state is located close to the conduction band and the situation becomes comparable with the lack of  $\text{Ce}^{3+}$  luminescence in other covalent systems like  $\text{Y}_2\text{O}_3:\text{Ce}^{3+}$  or  $\text{La}_2\text{O}_3:\text{Ce}^{3+}$ . The lack of luminescence in these systems has been ascribed to photoionisation of  $\text{Ce}^{3+}$ . The same explanation could be used for the other oxyorthoborates.

The second problem seems more complicated. The short wavelength emission in the meta and pentaborates was recognised before. Srivastava *et al.* [223] state that there is a relation between the high coordination number of  $\text{Ce}^{3+}$  in  $\text{LaMgB}_5\text{O}_{10}:\text{Ce}^{3+}$  and the low crystal field strength. The low field strength in turn should be responsible for the high position of the lowest 5d level. Saubat *et al.* [203] suppose that due to the strong covalency of the boron-oxygen bond both the crystal field splitting of the 5d orbitals and the nephelauxetic effect are reduced. The nephelauxetic effect will be explained below.

More quantitative explanations are not found in literature. This is understandable since the problem of describing the states of the 5d configuration of  $\text{Ce}^{3+}$  placed in a host matrix, is very complex. At present it will only be discussed whether the short emission wavelength is correlated with the atomic distances  $R_i$  between Ce and its ligands  $i$ .

Let us consider three borates where  $\text{Ce}^{3+}$  is positioned at an isovalent La site, that is  $\text{LaMgB}_5\text{O}_{10}:\text{Ce}^{3+}$ ,  $\text{LaB}_3\text{O}_6:\text{Ce}^{3+}$  and  $\text{LaBO}_3:\text{Ce}^{3+}$ . For the former two borates the emission wavelength is short whereas the emission of the latter is 'normal' for oxide systems. In table 6.4 structural data concerning the  $\text{Ce}^{3+}$  site in the different hosts is presented together with the spectroscopic properties of  $\text{Ce}^{3+}$ .

In column 2-5 of the structural data is listed. It is shown that the sites do not differ very much. In all cases the  $\text{Ce}^{3+}$  ions are surrounded by 9 to 10 oxygens in a low-symmetry arrangement. Also the average distance of the ligands to  $\text{Ce}^{3+}$  is about the same. We will return to column 5

**Table 6.4:** Comparison of the Ce sites in three lanthanum borates and the effect on the position of the 5d levels. Presented are the number of oxygen anions coordinating  $Ce^{3+}$  (crd.), the  $Ce^{3+}$  site symmetry, the average distance  $\bar{R}_i$  between the oxygens and the central ion, the sum  $\sum_i 1/R_i^6$  (see text), the position of the excitonic absorption band in the excitation spectrum (which is an indication for the width of the bandgap), the Stokes shift ( $\Delta S$ ), the barycentre of the 5d level with respect to the  $4f(2F_{5/2})$  ground level  $\overline{\Delta(5d-4f)}$ , and the splitting of the 5d levels  $\Delta(5d)$ . The structural data concerning  $LaBO_3:Ce^{3+}$ ,  $LaB_3O_6:Ce^{3+}$  and  $LaMgB_5O_{10}:Ce^{3+}$  are obtained from references [224], [208] and [209] respectively. Values for  $\overline{\Delta(4f-5d)}$  of  $LaBO_3:Ce^{3+}$  and  $LaB_3O_6:Ce^{3+}$  were derived from low  $T$  VUV excitation spectra presented in [211]. For  $LaMgB_5O_{10}:Ce^{3+}$  the measurements presented in figure 6.2 were used.

compound	crd.	sym.	$\bar{R}_i$ [Å]	$\sum_i 1/R_i^6$ [ $10^{-2} \text{ Å}^{-6}$ ]	$E_{excit.}$ [eV]	$\Delta S$ [eV]	$\overline{\Delta(4f-5d)}$ [eV]	$\Delta(5d)$ [eV]
$LaB_3O_6:Ce^{3+}$	10	$C_2$	2.61	3.31	7.6	0.46	5.24	1.45
$LaMgB_5O_{10}:Ce^{3+}$	10	$C_1$	2.59	3.32	7.3	0.43	5.28	1.60
$LaBO_3:Ce^{3+}$	9	$C_s$	2.59	3.26	7.05	0.30	4.93	2.02

below.

The next column gives a measure of the width of the band gaps. They are not exactly known but as an alternative we have given the position of the excitonic bands in the  $Ce^{3+}$  excitation spectrum. Also the Stokes shifts ( $\Delta S$ ) are compared. They differ at most 0.16 eV. The  $\Delta S$  of  $LaMgB_5O_{10}:Ce^{3+}$  and  $LaB_3O_6:Ce^{3+}$  is even larger than that of  $LaBO_3:Ce^{3+}$  and thus it can not explain the difference in emission wavelength.

In column 8 the average energy difference between the states of the 5d configuration and the  $4f(2F_{5/2})$  ground state is given. This parameter is denoted by  $\overline{\Delta(5d-4f)}$ . Here a significant effect is visible: For  $LaB_3O_6:Ce^{3+}$  and  $LaMgB_5O_{10}:Ce^{3+}$   $\overline{\Delta(5d-4f)}$  is larger than in the orthoborate. For the free  $Ce^{3+}$  ion  $\overline{\Delta(5d-4f)}$  amounts to  $51,230 \text{ cm}^{-1}$  ( $\cong 6.35 \text{ eV}$ ) [227]. The phenomenon of reduction of  $\overline{\Delta(5d-4f)}$  when the free ion is placed in a lattice environment is a result of the so-called nephelauxetic effect [225]. The reduction can be expressed as:

$$\Delta = \overline{\Delta(5d-4f)}_{freeion} - \overline{\Delta(5d-4f)}_{lattice} \quad (6.1)$$

where  $\overline{\Delta(5d-4f)}_{lattice}$  is  $\overline{\Delta(5d-4f)}$  for the  $Ce^{3+}$  ion placed in the lattice environment. With table 6.4 it is found that  $\Delta$  for  $LaMgB_5O_{10}:Ce^{3+}$  and  $LaB_3O_6:Ce^{3+}$  is 77% of  $\Delta$  for  $LaBO_3:Ce^{3+}$ .

The other part of the difference in emission wavelengths follows from the last column where the crystal field splitting  $\Delta(5d)$  is given. The splitting in  $LaB_3O_6:Ce^{3+}$  and  $LaMgB_5O_{10}:Ce^{3+}$  is 70-80% of that in  $LaBO_3:Ce^{3+}$ .

So, both the nephelauxetic effect and the crystal field splitting play a role. Aull and Jensen

[226] have tried to express the nephelauxetic effect in  $\text{Ce}^{3+}$  in term of ligand distances  $R_i$ . They argue that it is predominantly determined by two components which both originate from the interaction with the  $\text{Ce}^{3+}$  ligands, in this case the oxygen ions. The first component is due to covalency. Its contribution to  $\Delta(5d-4f)$  is proportional with  $\exp[-R_i/R_o]$  where  $R_o$  is typically several tenths of Å [226]. The second component is due to the 'correlated crystal field effect'. Its contribution to  $\Delta(5d-4f)$  is in first approximation equal to  $1/(R_i)^6$  [226].

The parameterisation of Aull and Jenssen illustrates that the dependence of  $\Delta(5d-4f)$  on the  $R_i$  is probably strong. Therefore the information about  $\bar{R}_i$  given in column 3 of table 6.4 is insufficient to reveal a possible correlation between the  $R_i$ s and  $\Delta(5d-4f)$ . As an alternative the sum  $\sum_i 1/R_i^6$  for the three borates has been calculated. The results are given in column 4 of table 6.4. The sum for  $\text{LaB}_3\text{O}_6:\text{Ce}^{3+}$  and  $\text{LaMgB}_5\text{O}_{10}:\text{Ce}^{3+}$  deviates only 2% from that of  $\text{LaBO}_3:\text{Ce}^{3+}$ . Hence, a correlation is still not found.

Perhaps the dependence of  $\Delta(5d-4f)$  and the crystal field splitting on  $R_i$  is more indirect. It is speculated that a more indirect dependence is found when the boron-oxygen bonds are important as proposed by Saubat *et al.* [209]. The borons being small and in the trivalent state are in competition with the  $\text{Ce}^{3+}$  ion in attracting the outer oxygen electrons. In the meta- and pentaborate boron-oxygen ratio is 1:1 whereas in the orthoborate it is 1:3. So the competition of the borons in the former two is considerably larger.

Considering this speculation it is not surprising that the oxide system with the largest  $\Delta(5d-4f)$  (and thus the smallest  $\Delta$ ) known from literature is  $\text{LaP}_5\text{O}_{14}:\text{Ce}^{3+}$  :  $\Delta(5d-4f) = 5.6$  eV [228].

## 6.5 Summary and Conclusion

For a group of  $\text{Ce}^{3+}$  activated borates we have discussed the  $\text{Ce}^{3+}$  luminescence properties and the scintillation light yield. In the oxyorthoborate  $\text{Ca}_4\text{GdO}(\text{BO}_3)_3:\text{Ce}^{3+}$  the  $\text{Ce}^{3+}$  shows inefficient luminescence or no luminescence at all and thus also the scintillation light yield is negligible. In  $\text{CaLaB}_7\text{O}_{13}:\text{Ce}^{3+}$  four  $\text{Ce}^{3+}$  emission bands are observed which suggests that there are two sites available for  $\text{Ce}^{3+}$ . However, the scintillation light yield is low.

When intrinsically exciting the  $\text{Ce}^{3+}$  dopant ions in the metaborates  $\text{LaB}_3\text{O}_6:\text{Ce}^{3+}$  and  $\text{GdB}_3\text{O}_6:\text{Ce}^{3+}$  and the pentaborates  $\text{LaMgB}_5\text{O}_{10}:\text{Ce}^{3+}$  and  $\text{YMgB}_5\text{O}_{10}:\text{Ce}^{3+}$  very efficient luminescence can be observed but their scintillation light yield is still low: max. 1800 pho/MeV for  $\text{LaB}_3\text{O}_6:\text{Ce}^{3+}$  and only some 250 pho/MeV for the others. For very low  $\text{Ce}^{3+}$  concentrations a broad luminescence band is observed in  $\text{LaB}_3\text{O}_6:\text{Ce}^{3+}$  and  $\text{LaMgB}_5\text{O}_{10}:\text{Ce}^{3+}$  whose nature is unknown. Due to this host lattice scintillation the light yield of  $\text{La}_{(1-x)}\text{Ce}_x\text{B}_3\text{O}_6$  ( $x = 0.0005$ ) is about 8000 pho/MeV. This yield is promising enough to study the decay time of this scintillation.

No correlation is found between the remarkably short emission wavelength of  $\text{Ce}^{3+}$  in the meta and pentaborates on one hand and the distances between  $\text{Ce}^{3+}$  and its ligands in these compounds on the other hand.

The orthoborates show also an efficient luminescence upon direct excitation of  $\text{Ce}^{3+}$  and the

scintillation light yield is in the order of 10,000 pho/MeV, with the exception of  $\text{LaBO}_3:\text{Ce}^{3+}$  (1000 pho/MeV) and  $\text{Li}_6\text{Y}(\text{BO}_3)_3:\text{Ce}^{3+}$  (2200 pho/MeV). The compound  $\text{Li}_6\text{Gd}(\text{BO}_3)_3:\text{Ce}^{3+}$  examined by Czirr appears to have the highest light yield of 14,000 pho/MeV. Czirr proposes to solve 'the Gd problem' by using depleted Gd. However, a drawback is the scintillation decay time with components of 200 and 700 ns.

The orthoborate with the highest potential to be used as a thermal neutron scintillator is probably  $\text{YAl}_3\text{B}_4\text{O}_{12}:\text{Ce}^{3+}$ . It combines a rather high scintillation light yield with a scintillation decay time of 30 ns and has a  $Z_{eff}$  of 28 and a boron weight fraction of 12%. These numbers are promising enough to investigate the scintillation response to thermal neutrons or alpha particles in the future.

Also the TL intensity of the  $\text{Ce}^{3+}$  activated borates was measured per unit dose of gamma radiation and compared with the intensity of the storage phosphor  $\text{BaFBr}:\text{Eu}^{2+}$ . None of the samples showed an intensity larger than 1% of that of  $\text{BaFBr}:\text{Eu}^{2+}$ .

Finally, some  $\text{Eu}^{2+}$  activated borates were considered. Photoluminescence of  $\text{Eu}^{2+}$  was not observed in  $\text{CaYOBO}_3:\text{Eu}^{2+}$  and in  $\text{CaLaB}_7\text{O}_{13}:\text{Eu}^{2+}$  it was extremely weak. Hence no TL could be measured. None of the samples studied has a potential as thermal neutron storage phosphor.



## 7

## The feasibility of the storage phosphors $M_2B_5O_9X:Eu^{2+}$ (M=Ca,Sr,Ba; X=Cl,Br) in thermal neutron image plates

### 7.1 Introduction

In chapter 2 the concept of the current thermal neutron image plate (IP) was described. It consists of a powder mixture of the BaFBr:Eu<sup>2+</sup> storage phosphor material and Gd<sub>2</sub>O<sub>3</sub> as a neutron absorber. From the secondary energy released by Gd isotopes in the form of gamma rays or conversion electrons (see table 2.1) less than 100 keV is absorbed in the BaFBr:Eu<sup>2+</sup> grains. The rest escapes from the plate.

The performance of such IP has been presented by different groups [6, 61, 63] and has been further optimised [64, 66]. Satisfying results have been achieved with respect to the linearity of the sensitivity and the dynamic range. Combined with the DQE and the spatial resolution this system has a unique performance compared to alternative detectors. Yet, the latter two parameters still allow for improvement. The most profound limitation is the high gamma sensitivity, caused by the presence of high Z elements like Gd and Ba.

Probably the DQE and the gamma insensitivity can be improved by using a different neutron absorbing material. As indicated in chapter 3, <sup>10</sup>B is the only candidate. According to table 2.1 much more ionisation energy is present after this <sup>10</sup>B(n,α) reaction than after the (n,γ) reactions in Gd, at least 25 times as much. The problem of the <sup>10</sup>B(n,α) reaction is the limited range of the reaction products. This prohibits that a considerable fraction of the reaction energy is absorbed in the BaFBr:Eu<sup>2+</sup> powder grains. A better alternative is therefore the use of a different storage phosphor, one that contains a large number of boron atoms per unit of mass by itself.

Even then it can not be stated a priori that the presence of 25 times more ionisation energy means automatically 25 times more energy available for storage. The possible quenching effect mentioned in chapter 3 must be taken into account. So, it is to be expected that the number of electrons and holes available for trapping is less than the factor of 25 higher for <sup>10</sup>B.

How does the DQE of an IP based on Boron (IP-B) compare to the IP based on Gadolinium currently used (IP-Gd)? In this chapter we will try to answer this question by a simple theoretical analysis. This analysis will be supported by Monte Carlo simulations of the energy deposition processes in both types of image plates.

Next, we will present the experimentally determined storage properties of the boron containing phosphors with the chemical formula  $M_2B_5O_9X:Eu^{2+}$  ( $M=Ca, Sr, Ba$ ;  $X=Cl, Br$ ) and discuss their feasibility. Haloborates are attractive thermal neutron storage phosphor candidates (see table 3.4). There are two arguments to study these haloborates in particular. At first, it has been shown by Meijerink *et al.* [229] that one of them,  $Ba_2B_5O_9Br:Eu^{2+}$ , is an X-ray storage phosphor with a sensitivity comparable with that of  $BaFBr:Eu^{2+}$ . Secondly, the weight fraction of boron atoms  $W_B$  is rather high: 9.8% for  $Ba_2B_5O_9Br:Eu^{2+}$  up to 17% in  $Ca_2B_5O_9Cl:Eu^{2+}$ . The  $Z_{eff}$  of these materials vary between 15.2 for  $Ca_2B_5O_9Cl$  and 48.0 for  $Ba_2B_5O_9Cl$ . The preparation and structure of the chloroborates as well as the efficient blue  $Eu^{2+}$  luminescence in these matrices have been reported by Peters *et al.* [127]. Later Fouassier *et al.* [230]. have presented the structure of the bromoborates.

## 7.2 The DQE of a thermal neutron image plate

In order to derive a general expression for the DQE of an IP equation (2.2) is taken as a starting point. The DQE of the haloborates and the  $BaFBr:Eu^{2+} \cdot Gd_2O_3$  system are going to be compared. Hence it is not necessary to involve possible effects of limited resolution. So the DQE will be derived at zero spatial frequency (see equation (2.4)) and it is supposed that no correlations between neighbouring pixels exist. The number of incident neutrons per pixel  $N_i$  is assumed to be distributed according to Poisson's law, so  $v_i$  equals  $1 / \langle N_i \rangle$ .

The generation of  $S_o$ , in casu a number of photoelectrons in the PMT, is a cascade of probability processes from the absorption of a neutron till the conversion from photons to photoelectrons. Each stage  $n$  will have its contribution to the statistical noise and can be expressed in an individual  $v_n$ . The  $v_n$  add up to  $v_o$  according to (see e.g. [231]):

$$v_o = v_1 + \frac{v_2}{\langle s_1 \rangle} + \dots + \frac{v_m}{\langle s_1 \rangle \cdot \langle s_2 \rangle \dots \langle s_{m-1} \rangle} \quad (7.1)$$

where  $\langle s_n \rangle$  represents the average signal after stage  $n$ . In case of a neutron IP we find for  $v_o$ :

$$v_o = \frac{1 + v_{N_{eh}}}{\langle N_i \rangle A} + \frac{1 - \eta_t \eta_{pe}}{\langle N_i \rangle A \langle N_{eh} \rangle \eta_t \eta_{pe}} \quad (7.2)$$

where  $A$  is the absorption probability of the neutrons in the phosphor layer,  $\langle N_{eh} \rangle$  is the average number of created electron-hole pairs per neutron absorbed,  $\eta_t$  is the probability of an electron-hole pair to form a photostimulable trap and  $\eta_{pe}$  is the probability that during the stimulation process the trap is stimulated and eventually yields a photoelectron. In table 7.1 the  $v_n$ s are given for each stage in the cascade.

**Table 7.1:** The relative variances for each stage in the generation of an output signal by a neutron image plate.

description stage	distribution type	relative variance
incident neutrons	Poisson	$v_1 = 1 / \langle N_i \rangle$
absorption of neutrons	Binomial	$v_2 = (1 - A)/A$
creation of e-h pairs	system dependent	$v_3 = v_{N_{eh}}$
filling of stimuable traps	Binomial	$v_4 = (1 - \eta_t)/\eta_t$
generation of photoelectrons	Binomial	$v_5 = (1 - \eta_{pe})/\eta_{pe}$

The generation of photoelectrons is in fact a cascade process in itself. But according to equation (7.1)  $v_4$  can be expressed in the product  $\eta_{pe}$  of the success probabilities of the individual stages if the number of successes is distributed binomially for each stage. If the success probability for each stage were close to 1, viz. the conversion process is efficient to such a degree that almost all energy deposited in the IP is converted into photoelectrons, the variance found with (7.2) would be too large. It would be necessary to introduce a Fano  $F$  factor smaller than 1 to correct for this [13]. For the present case the assumption is that the conversion process has considerable losses and thus  $F = 1$ . That this definitely true will become clear later.

Of course, the probability for a trap to be stimulated and the photon to escape depends on the distance  $z$  to the phosphor layer surface i.e. the depth. So  $\eta_{pe}$  must be an average over  $z$  according to:

$$\eta_{pe} \propto \frac{\int_0^d D(z) P_{stim}(z) P_{esc}(z) dz}{\int_0^d D(z) dz} \quad (7.3)$$

where  $D(z)$  is the dose profile of the neutrons in the phosphor layer of a pixel,  $P_{stim}(z)$  is the probability of stimulating a trap and  $P_{esc}(z)$  is the probability of a photon to escape at the side of the photon detector. A theoretical description of  $P_{stim}(z)$  and  $P_{esc}(z)$  is given by Thoms [232].

Because in (7.2) the product  $A \langle N_{eh} \rangle \eta_t \eta_{pe}$  is the average number of photoelectrons created per incident neutron,  $\langle N_{phe} \rangle$ , we arrive with (2.2) at the following expression for the DQE:

$$DQE = \frac{A \langle N_{phe} \rangle}{\langle N_{phe} \rangle (1 + v_{N_{eh}}) + A(1 - \eta_t \eta_{pe})} \quad (7.4)$$

It should be noted that only statistical noise contributions are taken into account, and not any detector noise like non-uniformity of pixels or PMT dark current. The effect of non-uniformity for commercially available plates is known to be about 1%. The effect of the dark current depends on the pixel readout time and will particularly be important at low neutron doses. But since this noise originates from the readout system and not from the IP it can be omitted in the comparison of the two different image plates.

In order to calculate the DQE, values for  $A$ ,  $\langle N_{phe} \rangle$  and  $v_{N_{eh}}$  have to be known. Since

these values are strongly dependent on the neutron converter material used we will continue by treating the two types of image plates separately.

### 7.2.1 Image plate based on $BaFBr:Eu^{2+} \cdot Gd_2O_3$ (IP-Gd)

First, we will determine  $A$ . In practice it is possible to obtain a grain filling factor of 0.7 [66]. Hence, 70% of the IP volume can be occupied with  $BaFBr:Eu^{2+}$  or  $Gd_2O_3$  grains and the rest is filled with organic binder material. The volume fraction of  $Gd_2O_3$  grains in the total volume at which the IP has its optimal sensitivity, is experimentally determined to be 21% for a plate

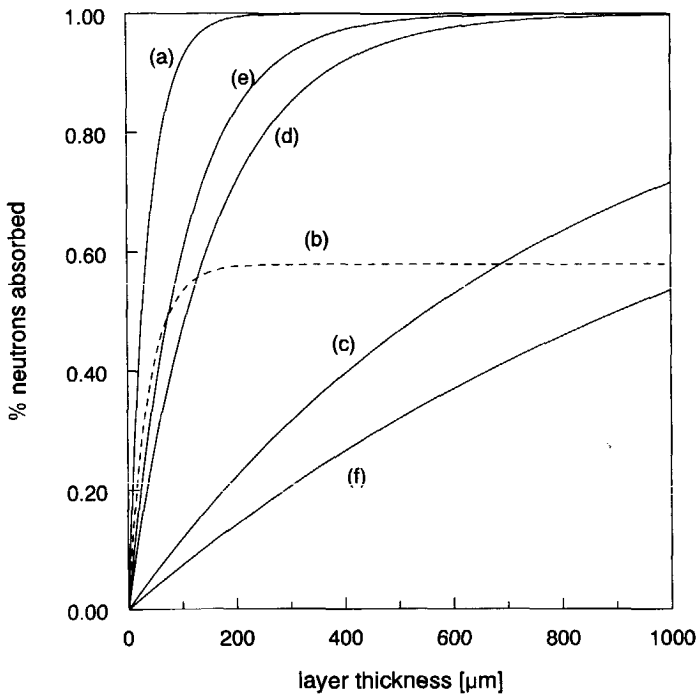


**Figure 7.1:** The calculated thermal (25 meV) neutron absorption probabilities  $A$  as a function of the powder layer thickness for (a) the  $BaFBr:Eu^{2+} \cdot Gd_2O_3$  image plate with a grain filling factor of 0.7 and a volume fraction of  $Gd_2O_3$  grains of 0.21. (b) similar situation as (a) but with  $A$  defined as the joint probability that a neutron is absorbed and some energy is stored. (c) a  $Sr_2B_5O_9Br:Eu^{2+}$  powder layer with a grain filling factor of 0.7, (d) similar to (c) but with 100% enriched  $^{10}B$ , (e) a  $Sr_2B_5O_9Br:Eu^{2+}$  single crystal containing 100% enriched  $^{10}B$ , (f) a  $Sr_2B_5O_9Br:Eu^{2+}$  pill and 48 meV instead 25 meV neutrons, corresponding with the experimental conditions.

thickness of  $150 \mu\text{m}$  [66]. For such a configuration using natural Gd the linear absorption coefficient is  $26 \text{ mm}^{-1}$ . Figure 7.1, curve (a), shows the neutron absorption probability as a function of the layer thickness. Almost 100% absorption is already obtained with a  $150 \mu\text{m}$  thick layer. As is shown in figure 7.1 and will be discussed later, it is practically impossible to obtain such an efficient absorption with an IP-B. Hence, at first glance, this strongly favours the choice of an IP-Gd.

According to equation (7.4) the DQE depends also on the variance of the number of e-h pairs created in the phosphor grains,  $\nu_{N_{eh}}$ . This variance is in the first place determined by the variance of the energy  $E$  that is absorbed in the phosphor grains,  $\nu_E$ , and secondly by the variance of the number of created e-h pairs for a given energy  $E$ , which is symbolised by  $\nu_{N_{eh}(E)}$ . The latter process is usually assumed to follow Poisson's law, hence  $\nu_{N_{eh}(E)}$  equals  $1/\langle N_{eh}(E) \rangle$ . Because  $E$  will be several tens of keV,  $N_{eh}$  is expected to be large which means that the main contribution to  $\nu_{N_{eh}}$  will come from  $\nu_E$ .

For determination of  $\nu_E$  it is necessary to know which part of the released energy is deposited in the BaFBr:Eu<sup>2+</sup> grains and which part will be deposited in the Gd<sub>2</sub>O<sub>3</sub> grains or organic binder material. Besides that, the fluctuations in these numbers have to be known.

We have studied the energy deposition process by means of a Monte Carlo simulation using the code GEANT [182]. This code describes the interaction of ionising radiation with matter. In the present case the radiation consists of the reaction products of the Gd(n, $\gamma$ ) reaction. In section 2.2.4 these products and their energies were discussed in more detail.

The absorption probability of gamma quanta with an energy  $>200 \text{ keV}$  in the IP is very low. The reader is reminded that quanta with lower energies as well as conversion electrons are only emitted when the lowest excited states of the Gd nuclei are populated. In 19% of the Gd\* decay processes in <sup>nat</sup>Gd, the lowest excited states are not populated at all, meaning that the probability is 19% that after a neutron absorption the energy deposition in the phosphor is approximately zero. In the simulation such events are counted as a neutron absorption events but their energy deposition is not simulated and directly set to zero.

It is also recalled that if the lowest states do become populated, energy is not only released by means of gamma ray emission, but also emission of conversion electrons becomes highly probable (see figure 2.2 and text section 2.2.4). Depending on the atomic shell the conversion electron is ejected from, this process is followed by the emission of Auger electrons and/or characteristic X-ray fluorescence. The Auger electrons and X-rays are predominantly irrelevant in the total energy storage process. Either their energy is so low that they will hardly escape the Gd<sub>2</sub>O<sub>3</sub> grains, or their creation probability is so low that they can be neglected, or both. The energies and creation probabilities of the X-rays and Auger electrons are listed in [10]. In the simulation their contribution is set to zero. However, one exception is made. If a K-conversion electron is emitted in the transition from the lowest excited state (at 79.5 keV in <sup>157</sup>Gd and 89.0 keV in <sup>155</sup>Gd) to the ground state, a 42 keV K-shell X-ray is emitted with a probability of 93%.

Two histograms representing the distribution of X-rays, gamma rays and electrons created in the Gd(n, $\gamma$ ) reaction are given in figure 7.2. These are the distributions as used for the input

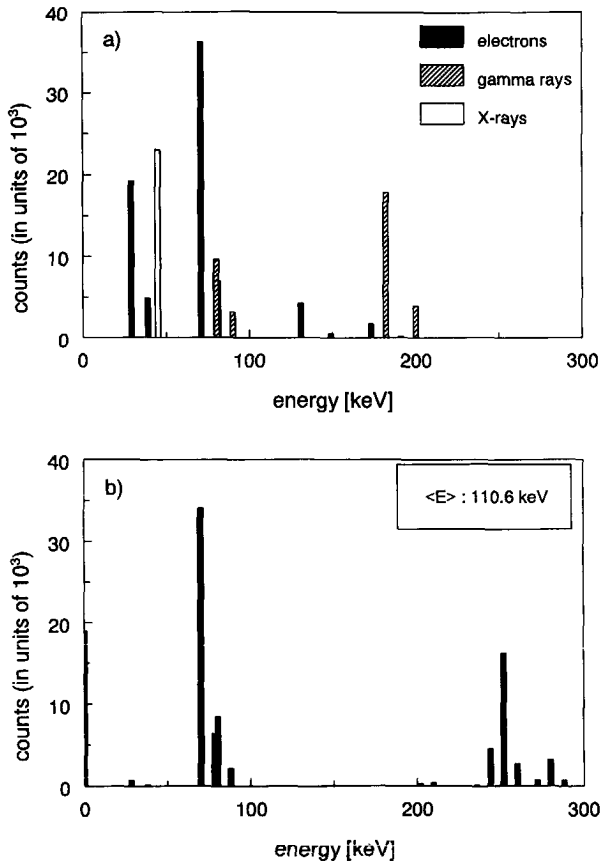


**Figure 7.2:** (a) The number and type of reaction products with their energies created upon the absorption of  $10^5$  neutrons in an image plate consisting of  $BaFBr:Eu^{2+}/^{nat}Gd_2O_3$ . (b) The distribution of the total energy available for the same case as (a). Only the reaction products that are involved in the simulation of the energy deposition process are taken into account (see text for details).

of the simulation. The high-energy gamma rays and the low-energy and/or low-intensity Auger electrons and X-rays mentioned above are not depicted. Figure 7.2(a) shows the number of the particles and quanta created per  $10^5$  absorbed neutrons. Particularly important are the K-conversion electrons emitted by  $^{157}Gd$  and  $^{155}Gd$  at 30 keV and 40 keV respectively, and the L-conversion electrons at 70 keV and 80 keV. Figure 7.2(b) shows the distribution of the total energy input per absorbed neutron, which is often an addition of energies of the different gamma rays, X-rays and electrons. To give an example of this we consider  $^{157}Gd$ : After neutron capture

and emission of the high-energy gamma rays, the second excited state can be populated, followed by a transition to the first excited state under emission of a 182 keV gamma ray and next a transition to the ground state can occur by emission of a 30 keV K-conversion electron. The latter can induce the emission of a 42 keV X-ray. Hence, for this example the total energy input is 254 keV.

In figure 7.2(b) the bar at  $E = 0$  represents the cases in which only high energetic gamma rays are emitted and thus the simulation energy input is zero. On the average 111 keV is available per absorbed neutron from which 10 keV X-ray energy, and 50 keV gamma energy.

Other important aspects of the simulation are the following: A small cubic cell was created with an edge of 30  $\mu\text{m}$ . At first BaFBr:Eu<sup>2+</sup> grains (density 5.2 g/cm<sup>3</sup>), which were modelled as ideal spheres with a diameter of 7  $\mu\text{m}$ , were placed one by one at random positions in the cell. If two grains by coincidence had physical overlap the overlapping volume was considered as being occupied by only one of these grains.

This process continued until the desired fraction of the total cell volume was occupied with BaFBr:Eu<sup>2+</sup>. Next, the same was performed with the Gd<sub>2</sub>O<sub>3</sub> grains (density 7.7 g/cm<sup>3</sup>), having a diameter of either 1 or 2  $\mu\text{m}$  (see results). Similar to the BaFBr:Eu<sup>2+</sup> grains, the Gd<sub>2</sub>O<sub>3</sub> grains were allowed to have mutual overlap, but overlap with the BaFBr:Eu<sup>2+</sup> grains was excluded. The volume ratio of Gd<sub>2</sub>O<sub>3</sub> grains and BaFBr:Eu<sup>2+</sup> grains is chosen such that the neutron capture probability of the IP is always 98%, and thus the ratio depends on the thickness of the IP. The grain filling factor was taken 0.7, as discussed before, the remaining 30% of the cell volume being filled with binder material. We have taken nitro-cellulose, (density 1,0 g/cm<sup>3</sup>) a well known binder material for lamp phosphors.

By using this filling method we obtain a random configuration of the three different substances. Also the shape and size of the powder grains varied, because of the allowed overlap between grains.

The plate dimensions were taken into account as follows: If secondary energy in the form of conversion electrons or gamma rays escaped from the small cell it was put back into the cell on the opposite side. In two dimensions this was allowed to happen an unlimited number of times, in the third dimension the thickness of the IP determined the limit. The probability of a neutron absorption event to occur at a certain location in the plate depends on the depth  $z$  of the location below the plate surface, according to the expected dose deposition function  $e^{-\mu z}$ .

The interaction of the conversion electrons with the surrounding medium is described by the continuous energy transfer due to ionisations and excitations whereas the generation of delta rays is not treated individually. Also multiple scattering of the electron is taken into account, as described with the Molière theory in GEANT [182]. For every calculation 10<sup>5</sup> absorption events were simulated.

We simulated various geometries which differ in plate thickness, Gd<sub>2</sub>O<sub>3</sub> grain size, and/or use of <sup>nat</sup>Gd or enriched <sup>157</sup>Gd. In figure 7.3 and figure 7.4 the results for two configurations are depicted. In figure 7.3 the plate thickness was chosen 150  $\mu\text{m}$ , the Gd<sub>2</sub>O<sub>3</sub> grain size was 2  $\mu\text{m}$  and volume occupation of Gd<sub>2</sub>O<sub>3</sub> was 21%, values that correspond with that of the optimised

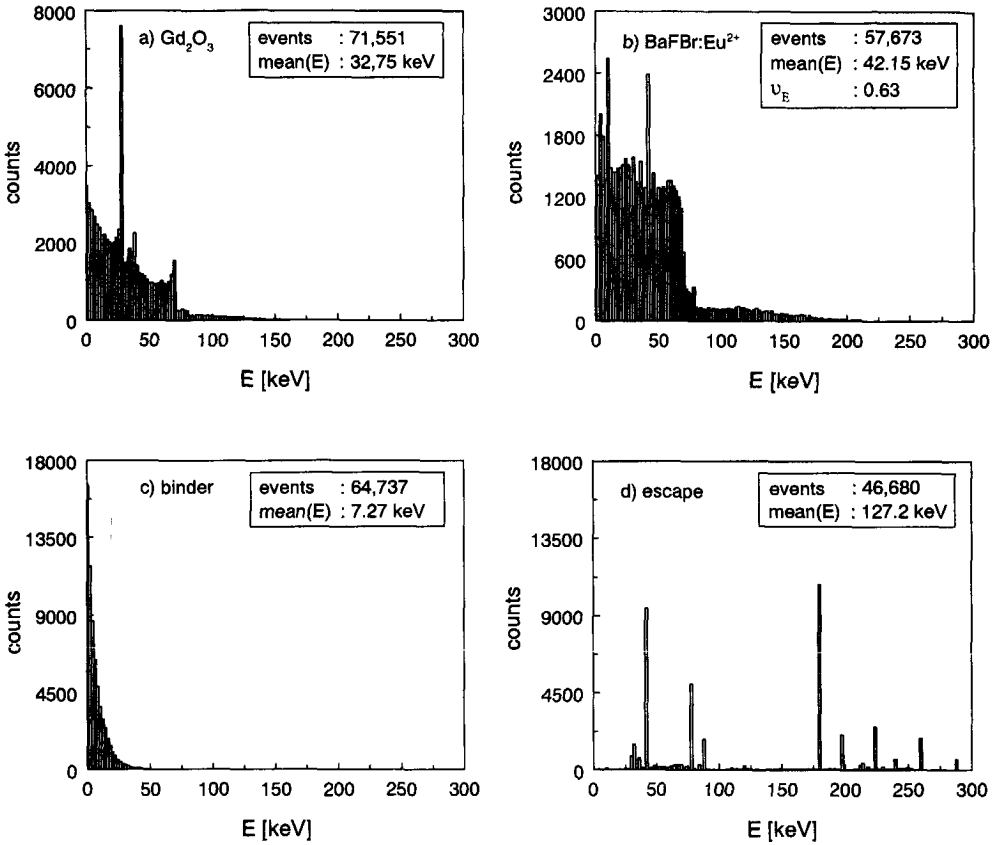


**Figure 7.3:** The simulated energy deposition distribution in an image plate based on  $BaFBr:Eu^{2+}/^{nat}Gd_2O_3$  after the absorption of  $10^5$  neutrons. The  $BaFBr:Eu^{2+}/Gd_2O_3$ /binder volume ratio amounts to 0.49/0.21/0.30. The  $BaFBr:Eu^{2+}$  grain size was taken  $7 \mu m$  and the  $Gd_2O_3$  grain size  $2 \mu m$ . The total deposition is split up into the part absorbed in (a) the  $Gd_2O_3$  grains, (b) the  $BaFBr:Eu^{2+}$  grains, (c) the binder material and (d) the part that escapes from the plate. For each diagram the number of events that contributed to the energy deposition is given as well as the mean energy  $\langle E \rangle$  deposited by these events. For the phosphor medium also the variance of  $E$ ,  $v_E$ , is given.

IP of Thoms *et al.* [66]. Figure 7.3(a) shows the energy deposition distribution in the  $Gd_2O_3$  grains, 3(b) that in the  $BaFBr:Eu^{2+}$  grains, 3(c) in the organic binder and figure 7.3(d) shows what escapes from the plate (where only the two lowest  $Gd^*$  excited states are considered). In 3(a) we see that a significant part of the energy is deposited in  $Gd_2O_3$ . According to the large peak in this spectrum, the 30 keV K-conversion electrons emitted from the K-shell have a 30%



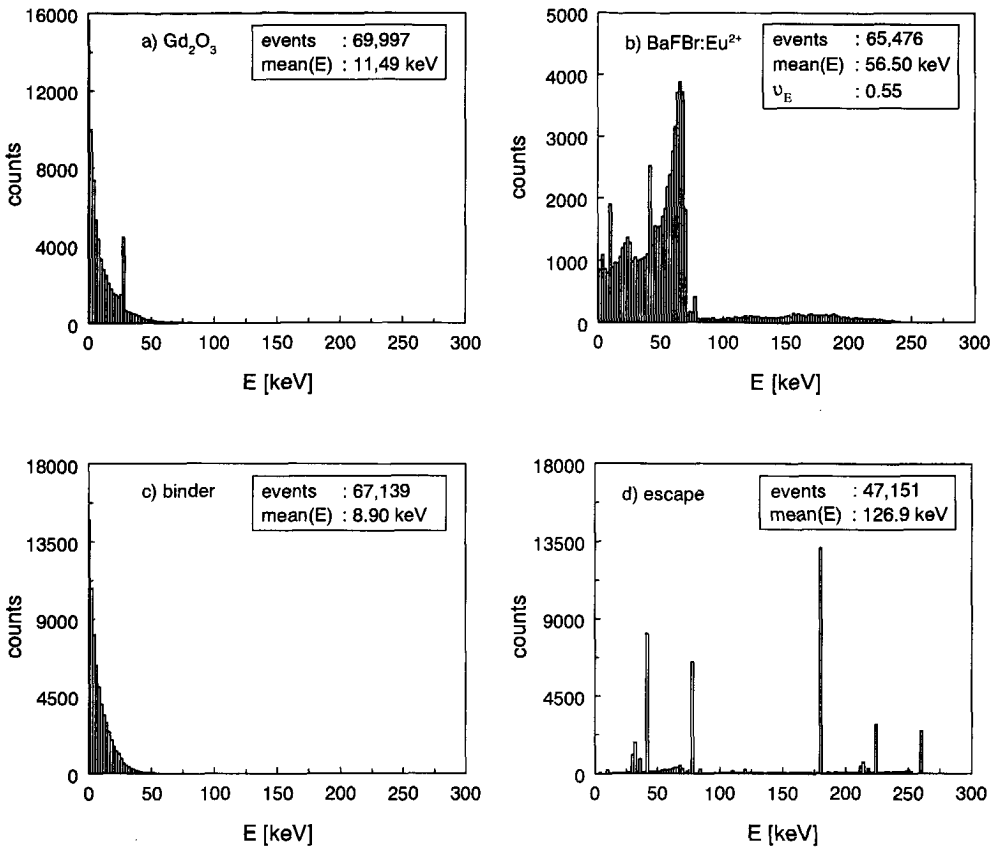


**Figure 7.4:** The simulated energy deposition distribution in an image plate based on BaFBr:Eu $^{2+}$ /90% enriched  $^{157}Gd_2O_3$  after the absorption of  $10^5$  neutrons. The BaFBr:Eu $^{2+}$ /Gd $_2O_3$ /binder volume ratio amounts to 0.66/0.04/0.30. The BaFBr:Eu $^{2+}$  grain size was taken  $7 \mu m$  and the Gd $_2O_3$  grain size  $2 \mu m$ . The total deposition is split up into the part absorbed in (a) the Gd $_2O_3$  grains, (b) the BaFBr:Eu $^{2+}$  grains, (c) the binder material and (d) the part that escapes from the plate. For each diagram the number of events that contributed to the energy deposition is given as well as the mean energy  $\langle E \rangle$  deposited by these events. For the phosphor medium also the variance of  $E$ ,  $v_E$ , is given.

chance to ionise only Gd $_2O_3$  material. Furthermore small peaks are visible at 40 keV and 70 keV corresponding with the energy of other conversion electrons.

The most important information is derived from figure 7.3(b). The sharp edge at 70 keV must be ascribed to the maximum energy that can be deposited by the 70 keV electrons in BaFBr:Eu $^{2+}$  grains, which are relatively numerous. The peak at 42 keV is due to the full absorption of

the characteristic K X-ray energy of Gd in a BaFBr:Eu<sup>2+</sup> grain, which can occur when the K-photoelectron and the full K-shell binding energy of the Ba atom (37 keV) are absorbed. The 11 keV peak consists of events of the same absorption process, where the K $\alpha$  X-ray of Ba escapes and is not absorbed in another BaFBr:Eu<sup>2+</sup> grain. The peak around 5 keV is due to events where either a K $\beta$  X-ray escapes or both the K $\alpha$  X-ray and an L X-ray.

It is remarkable that of all the neutrons absorbed 43% does not give rise to any excitation of the storage phosphor material. This means that in addition to the 20% which were set to an energy deposition of zero because only gamma rays with energies >200 keV are emitted, another 23% of the neutrons absorbed yields no energy storage at all. The other 57% of the events deposits a mean energy of 42 keV (figure 7.3(b)).

By taking the product of the number of events and  $\langle E \rangle$  for figure 7.3 (a)-(d) the amount of energy deposited per medium is obtained. We see that the relative energy deposition in BaFBr:Eu<sup>2+</sup>/Gd<sub>2</sub>O<sub>3</sub> /binder/air outside' is 0.22/0.21/0.04/0.53. So equal amounts of energy are deposited in BaFBr:Eu<sup>2+</sup> and Gd<sub>2</sub>O<sub>3</sub> whereas the volume ratio of these materials in the plate is 70/30. Hence, the amount of energy that will be deposited in BaFBr:Eu<sup>2+</sup> can not simply be estimated by multiplying the total amount of energy to be deposited with the volume fraction of BaFBr:Eu<sup>2+</sup> in the total powder volume. Furthermore, figure 7.3(d) learns that roughly 30% of the X-rays and 50% of the (low energy) gamma rays escapes from the plate without having any interaction.

If 90% enriched <sup>157</sup>Gd is used instead of <sup>nat</sup>Gd<sub>2</sub>O<sub>3</sub> the volume fraction Gd<sub>2</sub>O<sub>3</sub> in the plate can be reduced from 0.21 to 0.04. In this case better results are obtained, see figure 7.4. The number of events contributing to energy deposition in BaFBr:Eu<sup>2+</sup>, the mean energy deposited, as well as the relative variance of the latter have improved. Comparing figure 7.4(a) with 7.3(a) learns that the energy loss in Gd<sub>2</sub>O<sub>3</sub> has decreased considerably as could be expected. The fact that the 30 keV peak has only partly decreased means that in this case we are only looking at events for which the electrons stay in one and the same grain.

How can we determine the DQE from these results?

Assuming that  $\langle N_{phe} \rangle \gg A$  expression (7.4) can be rewritten as:

$$\lim_{\langle N_{phe} \rangle \rightarrow \infty} DQE = \frac{A}{(1 + \nu_{N_{eh}})} \quad (7.5)$$

It will be shown later that the DQE value determined with (7.5) is a good approximation. We have defined A as the probability that a neutron is absorbed. But 30% to 50% of these events appears to give no energy storage at all. It is therefore more convenient, to define for this case A<sub>s</sub>: the joint probability that firstly a neutron is captured and secondly some fraction of energy is deposited in the BaFBr:Eu<sup>2+</sup> phosphor. Hereafter this will be called a successful event. As stated before,  $\nu_{N_{eh}}$  is well approximated by  $\nu_E$ . We arrive at:

$$DQE = \frac{A_s}{1 + \nu_E} \quad (7.6)$$

where for the variance  $\nu_E$  no longer all absorption events should be considered, but only suc-

**Table 7.2:** Simulation results for the energy deposition process after neutron absorption in a BaFBr:Eu<sup>2+</sup>-Gd<sub>2</sub>O<sub>3</sub> image plate. The probability  $A_s$  that any energy deposition in the BaFBr:Eu<sup>2+</sup> grains takes place, the average energy  $\langle E \rangle$  deposited then, the variance  $\nu_E$  of  $E$  and the DQE are given for plates that differ in thickness, Gd<sub>2</sub>O<sub>3</sub> particle size and/or the Gd<sub>2</sub>O<sub>3</sub> volume fraction in the total volume. The results in the lower three rows were obtained by neglecting the energy deposition by the X-ray and/or gamma rays.

thickness [ $\mu\text{m}$ ]	Gd <sub>2</sub> O <sub>3</sub>	part.size [ $\mu\text{m}$ ]	$\gamma$ -rays	X-rays	BaFBr:Eu <sup>2+</sup> grains			DQE
					$A_s$	$\langle E \rangle$	$\nu_E$	$\lim_{N_{phe} \rightarrow \infty}$
300	10.5%	2	yes	yes	67%	55 keV	0.57	43%
150	21%	2	yes	yes	58%	42	0.63	35%
150	21%	1	yes	yes	61%	44	0.59	38%
150	4%, enrich.	2	yes	yes	65%	57	0.55	42%
150	21%	2	no	yes	54%	41	0.61	34%
150	21%	2	yes	no	53%	42	0.59	33%
150	21%	2	no	no	49%	41	0.59	31%

cessful events. The number of successful events out of  $10^5$  attempts is indicated in figure 7.3(b) and 4(b) and thus  $A_s$  is immediately determined. The desired  $\nu_E$  is also indicated in figure 7.3(b) and 4(b).

With equation (7.6) the DQE values were calculated for all cases simulated. The results are presented in table 7.2, together with the results for  $A_s$ ,  $\langle E \rangle$  and  $\nu_E$ .

Comparison of the results leads to the following conclusions: The DQE is rather strongly dependent on the phosphor/converter volume ratio, the latter being directly connected with the plate thickness in order to maintain the neutron absorption probability of 98%. A maximal DQE of 43% can be obtained by 'maximising' the plate thickness. Then the number of successful events as well as the variance are optimised. In practice the maximum thickness will also be determined by both the penetration depth of the laser light used to stimulate the phosphor and the stimulated light. The depth is typically 300  $\mu\text{m}$  for such grain sizes. Decreasing the Gd<sub>2</sub>O<sub>3</sub> particle size from 2 to 1  $\mu\text{m}$  only improves the DQE by 3%. Evidently, a high DQE of 42% is obtained when using 4 volume percent enriched <sup>157</sup>Gd<sub>2</sub>O<sub>3</sub>, due to both  $A_s$  and  $\nu_E$ . For this case the number of successful events amounts to 65% which is close to the probability of 70% that a conversion electron is created after the absorption of a neutron.

The geometries for which a DQE value of respectively 42% and 43% was calculated need a remark. At first, considering the price of enriched <sup>157</sup>Gd<sub>2</sub>O<sub>3</sub> the use of this material in a Gd-IP is in fact no realistic option. This case just marks the limit for the DQE of a Gd<sub>2</sub>O<sub>3</sub> based plate. For the other case at which the plate thickness amounts to 300  $\mu\text{m}$  it should be realised that  $\eta_{pe}$  from equation (7.3) can become so small that the assumption  $\langle N_{phe} \rangle \gg A$  is not valid anymore, meaning that the real DQE is smaller than 43%. We conclude therefore that the

maximum obtainable DQE for a Gd-IP will be 35%-40%.

In the lower three rows of table 7.2 results are shown for cases where either the generation of the 42 keV X-ray or the gamma rays or both was prohibited. With these cases it is made clear what the contributions of the X-ray and gamma rays to the total energy deposition is. Therefore the results should be compared with the case where the X-ray and gamma rays are taken into account and the other parameters are the same. We see that omitting the X-ray and gamma rays lowers  $A_s$  from 58% to 49%, but that the DQE decreases with only 4%. Furthermore it is found that the contribution of the X-ray to the DQE is small: respectively 2% and 1% on a total DQE of 35%.

What will  $N_{phe}$  be for an IP of 150  $\mu\text{m}$  with a  $Gd_2O_3$  grain size of 2  $\mu\text{m}$ ? Thoms *et al.* [234] have found that for X-ray irradiation on a  $BaFBr:Eu^{2+}$  crystal on the average 125 eV is needed to form a photostimulable centre. This is in rather good agreement with measurement results of Templer [235] who reports 162 eV per photostimulable centre for a Fuji image plate when using  $CuK\alpha$  radiation. Taking the most optimistic value of 125 eV and an average ionisation energy of 45 keV per neutron that causes any ionisations in the phosphor grains (which is about 60%, see table 7.2), the number of photostimulable centres per incident neutron will be 220. If 50% of these centres is stimulated, the collection efficiency of the optical system is 20% (which is realisable) and the quantum efficiency of the PMT 25%, then  $\langle N_{phe} \rangle$  is about 6. With (7.4) a DQE of 34% follows which is close to the value of 35% found with (7.5) and given in row 3 of table 7.2.

Let us compare the obtained results for the DQE with experimental values reported in the literature. Rausch *et al.* have reported DQE values of 18.2% [62], 23.6% [190] and recently 40% has been measured for very large pixel sizes (up to 40  $\text{mm}^2$ ) and a homogeneously irradiated area of  $12.8 \times 12.8 \text{ mm}^2$  using 2.44  $\text{\AA}$  (14 meV) neutrons [236]. The exact composition of the plates used in [62] and [190] is not known to us, but a 150  $\mu\text{m}$  thick plate with a  $BaFBr:Eu^{2+}/Gd_2O_3$  /binder volume ratio of 50.1/8.6/40.5 was used in [236]. The neutron absorption probability of such a plate is 86%. According to our simulation, with such a geometry  $A_s$  equals 0.54 and  $\nu_E$  is 0.58 from which a DQE of 34% follows, being somewhat less than the experimental result. Unfortunately, a DQE value for the optimised plate of Thoms *et al.* [66] has not been reported.

Finally, we will discuss the resolution of the IP-Gd and its influence on the DQE. As indicated before, the expression of the DQE is derived under the assumption that the detector creates no correlations between neighbouring pixels. This means that the pixels can not have unlimited small dimensions. It is well-known that the essential step in IP application is the readout procedure, due to scattering of photons at the powder grain edges. The resolution is therefore not less than 100-150  $\mu\text{m}$  (FWHM of the line spread function), dependent on the plate thickness and the grain sizes.

For a decent experimental determination of the DQE it is also necessary that the pixels dimensions are chosen large enough. If not, a too high DQE value will be found, as demonstrated by Rausch *et al.* [236]. They showed that for their 300  $\mu\text{m}$  thick plate the influence of pixel correlations on the DQE could be neglected when the pitch of the pixel is larger than several

mm.

Can a contribution to the pixel correlations be expected from the energy deposition process? The attenuation length of the X-ray is about  $250\ \mu\text{m}$  and that of the gamma rays is even larger.

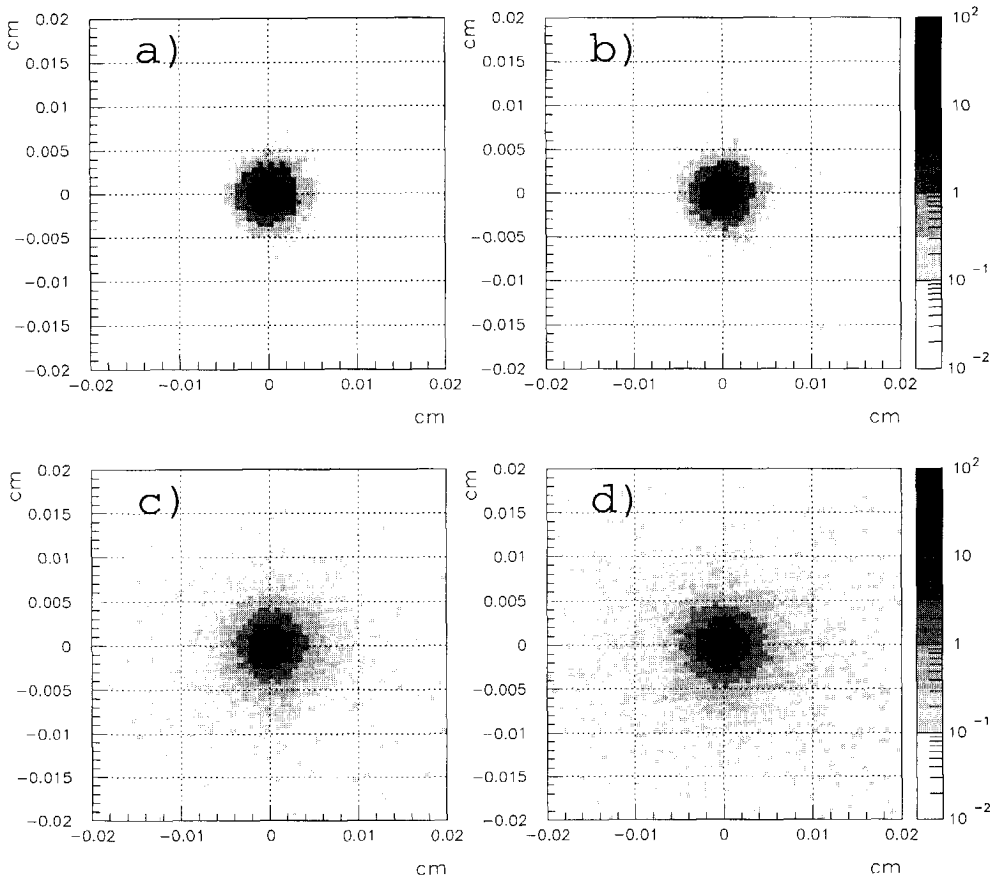


**Figure 7.5:** The energy deposition as a function of the distance to the location of the neutron absorption in an image plate based on  $\text{BaFBr:Eu}^{2+}\cdot\text{Gd}_2\text{O}_3$ . The 4 situations simulated are (a)  $150\ \mu\text{m}$  plate thickness,  $\text{BaFBr:Eu}^{2+}/\text{Gd}_2\text{O}_3/\text{binder}$  volume ratio of 0.49/0.21/0.3 and only energy deposition of conversion electrons is taken into account, (b) idem (a) but also deposition by the 42 keV X-ray, (c) idem (b) but also deposition by the gamma rays, (d) idem (c) but for a  $300\ \mu\text{m}$  plate with a  $\text{BaFBr:Eu}^{2+}/\text{Gd}_2\text{O}_3/\text{binder}$  volume ratio of 0.595/0.105/0.3.

According to GEANT the specific energy loss of a 70 keV conversion electron is 17 MeV/cm in BaFBr:Eu<sup>2+</sup>, 24 MeV/cm in Gd<sub>2</sub>O<sub>3</sub> and 5 MeV/cm in the binder. The maximum track length of such an electron is about 35 μm (measured along the track). Comparing this length with the resolution mentioned before and realising that the contribution of the X-ray and gamma rays to the DQE is small it is not to be expected that the energy deposition step will contribute significantly. However, the energy deposition as a function of the lateral coordinates (x,y) of the IP can easily be calculated utilising the simulation code. We have done this by simulation of 10<sup>5</sup> neutron absorptions at the coordinate (0,0). The results are depicted in figure 7.5.

Figure 7.5(a) shows the energy deposition due to the conversion electrons only, in a 150 μm thick plate. The FWHM of the energy deposition function is smaller than 40 μm as could be expected. In figure 7.5(b) also the X-ray was taken into account and in figure 7.5(c) both the X-ray and the gamma rays. The FWHM does not change much, but the low-level background at longer distances is clearly elevated. Still, at 60 μm from the centres the energy deposition is less than 0.01% from of maximum. Figure 7.5(d) shows the equivalent of 5(c) for a 300 μm thick plate. Clearly, by increasing the thickness it is mainly the long distance background that increases. When in figure 7.5(d) a pixel of 100×100 μm centred at (0,0) is defined and the energy deposited inside is integrated, it is found that this number is at least 100 times larger than the integral energy calculated for neighbouring pixels. This factor increases to about 1000 for pixels at a distance of 300 μm.

We conclude that the energy deposition step is not relevant for the resolution and pixel correlations. The X-ray and gamma rays cause some 'fog' in the image plate but the effect is limited. It should be noted that the high energy gammas were not taken into account.

### 7.2.2 Image plate based on a haloborate (IP-B)

For this case the variance  $v_E$  is less important which means that a simple expression for the DQE can be derived without approximations. Moreover it is not necessary to use  $A_s$ , since every absorption event will be a successful event, hence  $A_s = A$ . Again, we will determine a value for  $A$  first. As a representative of the haloborates we have chosen Sr<sub>2</sub>B<sub>5</sub>O<sub>9</sub>Br:Eu<sup>2+</sup> (density 3.55 g/cm<sup>3</sup>). The grain filling factor is assumed to be 70% again and the rest is filled with the binder material. For this composition the neutron absorption coefficient is 1.1 mm<sup>-1</sup>. This number can be enhanced by a factor of 5 by using 100% enriched <sup>10</sup>B. In figure 7.1, curve (c) and (d), the neutron absorption probability  $A$  is plotted as a function of the powder layer thickness containing natural and enriched boron respectively. These curves should not be compared with curve (a) but with curve (b), since curve (b) represents the probability of a successful event for a 150 μm thick plate (see row 3 table 7.2). The figure shows that it is necessary to use enriched boron. In that case the effective absorption probabilities of the two plate types do not differ much anymore. Note that another improvement of  $A$  for the Sr<sub>2</sub>B<sub>5</sub>O<sub>9</sub>Br:Eu<sup>2+</sup> IP can be attained by using a single crystal (curve (e)). Still, the dose depth profile of the Gd<sub>2</sub>O<sub>3</sub> based plate is favourable regarding the limited penetration of the stimulating photons.

Similar to case 1, we have calculated  $E$  and  $v_E$  by means of a Monte Carlo simulation with

GEANT. For the simulation a cubic cell was created with an edge of  $150\ \mu\text{m}$ . In fact the limited range of the  ${}^7\text{Li}$  and the  ${}^4\text{He}$  particle make the incorporation of the exact plate dimensions in the simulation irrelevant. For convenience, the cell filled with ideal spheres of phosphor material that were hexagonally close-packed. The inter phosphor-grain spaces were occupied with binder material. Of course such an ordered configuration is far from reality. But it seems reasonable to expect that the energy deposition distribution depends mainly on the grain filling factor rather than on the exact configuration and sizes of the grains. For the arrangement described the filling factor matches the required 70%.

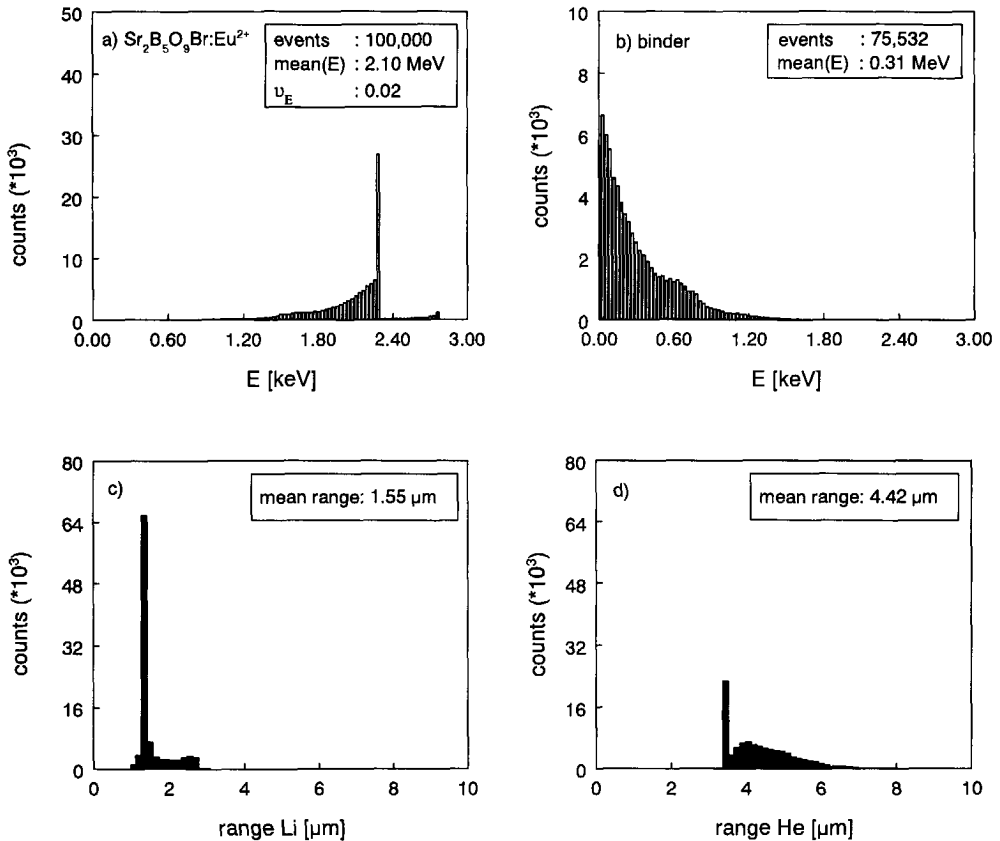


**Figure 7.6:** The simulated energy deposition distribution in an image plate based on  $\text{Sr}_2\text{B}_5\text{O}_9\text{Br}:\text{Eu}^{2+}$ . The grain filling factor is 0.7 and the grain size was taken  $7\ \mu\text{m}$  grains of the image plate. (a) The fraction deposited in the phosphor, (b) the fraction deposited in the binder. The figures (c) and (d) give the distribution of the ranges of the  ${}^7\text{Li}$  and  ${}^4\text{He}$  particle respectively.

At arbitrary locations in a central phosphor grain the reaction products with their appropriate energies were generated. The 480 keV gamma ray was neglected because its interaction probability in an IP of typically  $150 \mu\text{m}$  thickness is low. The possible effect of energy escape at the edges of the IP are also neglected with this method, because of the large cell dimensions.

A difficulty in calculating the energy loss of a heavy ion as it traverses a medium is the change in its charge due to electron-exchange processes with the atoms. The GEANT code therefore uses an effective charge which is parameterised according to the expression of Andersen and Ziegler [182]. Comparison of calculations with experimental data yielded deviations in the energy loss being less than 20% and deviations in the energy loss fluctuation being less than 30%.

Representative results of the calculations are depicted in figure 7.6. The grain size for this case was chosen  $7 \mu\text{m}$ . In figure 7.6(a) the distribution of the energy absorbed in the storage phosphor is plotted. The large peaks at 2.31 MeV and the small peak at 2.78 MeV reflect the events at which all energy is deposited in the grain that absorbed the neutron. Both peaks show a tail on the left side that represent events where part of the energy is lost in the binder material. On the average, 2.1 MeV is absorbed in the phosphor which is 90% of the reaction energy available. Figure 7.6(c) and (d) show the calculated distribution function of the  ${}^7\text{Li}$  and the  ${}^4\text{He}$  particles respectively. The average range of the  ${}^7\text{Li}$  particle of  $1.6 \mu\text{m}$  is so short that almost no particles escape from the grain at which they were created. The average range of the  ${}^4\text{He}$  particles amounts to  $4.5 \mu\text{m}$  with the consequence that more than 75% escapes its initial grain.

In reality a grain size distribution with a width of a few  $\mu\text{m}$  can be expected, which is even

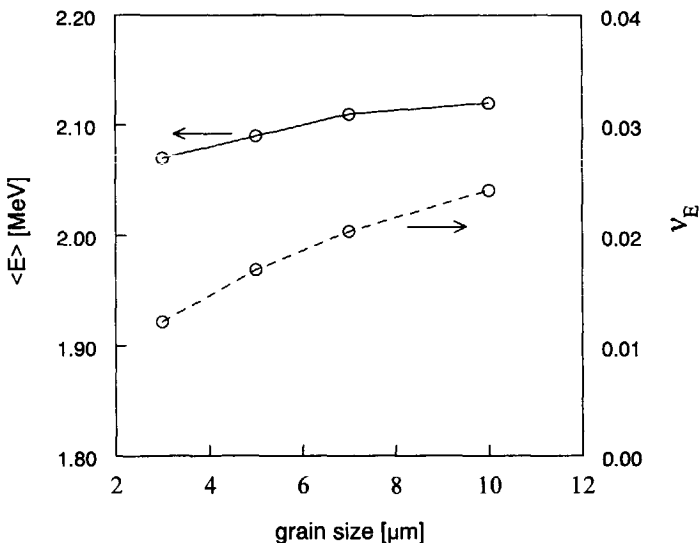


**Figure 7.7:** The average energy  $\langle E \rangle$  deposited in the  $\text{Sr}_2\text{B}_5\text{O}_9\text{Br:Eu}^{2+}$  grains and the variance  $v_E$  as a function of the grain size. The grain filling factor of the image plate is 0.7.



necessary to obtain the filling factor of 0.7. Therefore it is interesting to study the change of the results of figure 7.6(a) when changing the grain size. In figure 7.7 the calculated  $\langle E \rangle$  and  $\nu_E$  are plotted versus the grain size. For smaller grain sizes  $\langle E \rangle$  decreases slightly but the differences are negligible. Remarkable is that  $\nu_E$  becomes also smaller which is perhaps not according to the intuition. The explanation is that  $\langle E \rangle$  is mainly determined by the small peak at 2.78 MeV (see figure 7.6(a)). For smaller grains the peak is smeared out towards the average energy  $\langle E \rangle$ .

In conclusion it can be expected that for a realistic grain size distribution  $\nu_E$  will be less than 5% and that it will be predominantly determined by the filling factor. Regarding expression (7.4)  $\nu_E$  becomes relevant for the DQE when it is larger than 10%. Hence, as long as the filling factor is not much lower than 0.7,  $\nu_E$  can be neglected and  $\nu_{N_{eh}}$  can be approached by  $1/\langle N_{eh} \rangle$ . The DQE for an IP-B is then described with the simple expression:

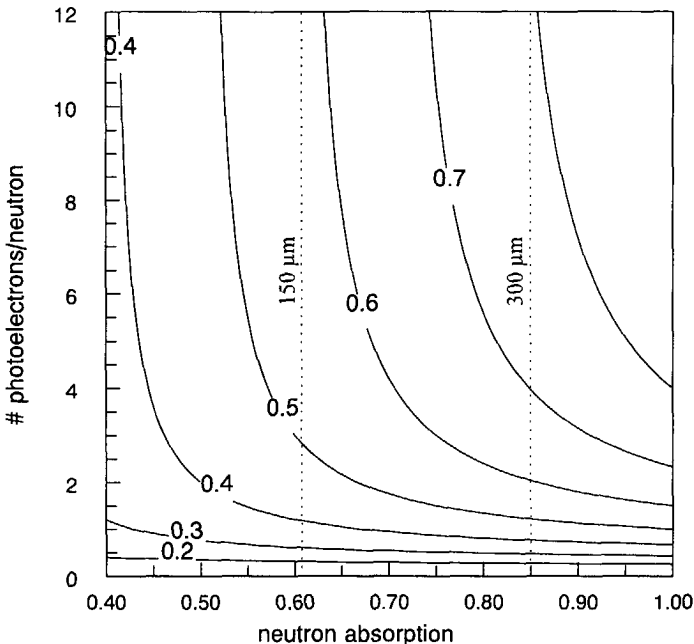


**Figure 7.8:** Contour plot of the DQE of a neutron image plate based on a 100% enriched  $^{10}\text{B}$  containing phosphor, as a function of the neutron absorption probability  $A$  and the average number of created photoelectrons per incident neutron,  $N_{phe}$ . The vertical broken lines mark the values for  $A$  of a  $\text{Sr}_2\text{B}_5\text{O}_9\text{Br}:\text{Eu}^{2+}$  plate with a thickness of  $150\ \mu\text{m}$  and  $300\ \mu\text{m}$  respectively and a grain filling factor of 0.7.

$$DQE = \frac{A \langle N_{phe} \rangle}{\langle N_{phe} \rangle + A} \quad (7.7)$$

Figure 7.8 is a contour plot of the DQE as a function of realistic values for  $A$  and  $\langle N_{phe} \rangle$ , which is based on equation (7.7). The vertical lines indicate the  $A$  values for plates with a thickness of 150  $\mu\text{m}$  and 300  $\mu\text{m}$  respectively and the filling factor of 0.7. It should be noted that equation (7.7) is not valid for an IP-Gd.

Taking the most optimistic DQE value of 40% for an IP-Gd, figure 7.8 makes clear which requirement should be put on a 150  $\mu\text{m}$  thick IP-B:  $\langle N_{phe} \rangle$  has to be larger than 1.3 for the DQE to be higher than 40%. In the limiting case of a high  $\langle N_{phe} \rangle$  a maximum DQE of 60% can be obtained for this plate. A further increase is possible by increasing the plate thickness, which should not go at the expense of  $\langle N_{phe} \rangle$ . A 300  $\mu\text{m}$  thick plate will have a DQE of 40% when  $\langle N_{phe} \rangle = 0.8$  and the maximum obtainable DQE is 85%.

In the next part the experimentally determined values for  $\langle N_{phe} \rangle$  for all haloborates studied will be presented. Also other results expressing the stimulation efficiency, dose response linearity, gamma sensitivity and fading characteristics of these compounds are given.

## 7.3 Experimental

### 7.3.1 Samples

The  $M_2B_5O_9X:Eu^{2+}$  ( $M=\text{Ca,Sr,Ba}$ ;  $X=\text{Cl,Br}$ ) powder samples were prepared as follows: appropriate amounts of  $MCO_3$ ,  $MX_2 \cdot 10H_2O$  (10% excess),  $Eu_2O_3$  and  $H_3BO_3$  (20% excess) were carefully mixed. The mixtures were fired in a reducing atmosphere (95% Ar + 5%  $H_2$ ) at 800-850  $^{\circ}\text{C}$ . For each of the six compounds, 3 versions were made, with firing times of 3, 6 and 9 hours respectively, the latter two with intermediate grinding. Each time the dopant concentration was 0.1%. All samples were checked by X-ray powder diffraction using  $CuK\alpha$  radiation. No impurity phases were found with this technique. The powder samples were pressed into pills of 50 mg as a part of the experimental procedure.

### 7.3.2 Irradiation facilities and optical measurements

The photoluminescence experiments were performed with an IBH model 5000U spectrophotometer that is described in chapter 5. Excitation spectra and photostimulation spectra are corrected for the wavelength dependent intensity of the lamp. Emission spectra are corrected for the wavelength dependent transmission of the system. The method of determination of conversion efficiencies (CE) and stimulation energies (SE) is also in chapter 5. To measure the response of the samples upon continuous stimulation the 632.8 nm line of a HeNe laser (Melles Griot 05-LHR-151) is applied. A diaphragm with a diameter of 1 mm is positioned in front of the sample

**Table 7.3:** Column 2: Wavelength of maximum emission intensity of the compounds  $M_2B_5O_9X:Eu^{2+}$  ( $M=Ca,Sr,Ba$ ;  $X=Cl,Br$ ) for excitation at 250 nm. The numbers between brackets are the maxima for the samples fired for 3 hours, which deviated. Column 3-5: The PSL yield per type of radiation expressed in emitted photons per incident quantum. Column 6: The stimulation energies (SE) at 623.8 nm. The stimulation energy of  $BaFBr:Eu^{2+}$  and its PSL yield under X-ray radiation are given as a reference.

compound	$\lambda_{em}$ [nm]	PSL yield			SE [mJ/mm <sup>2</sup> ]
		X-rays 48 keV	alphas 4.17 MeV	neutrons 1.3 Å	
$BaFBr:Eu^{2+}$	390	11			0.015
$Ca_2B_5O_9Cl:Eu^{2+}$	447(433)	0.009	100	6	0.8
$Sr_2B_5O_9Cl:Eu^{2+}$	423	0.08	50	4	0.8
$Ba_2B_5O_9Cl:Eu^{2+}$	413	0.09	30		2.5
$Ca_2B_5O_9Br:Eu^{2+}$	445(435)	0.05	140	14	0.5
$Sr_2B_5O_9Br:Eu^{2+}$	426	0.4	200	21	0.7
$Ba_2B_5O_9Br:Eu^{2+}$	414	0.1	36		5.0

to stimulate a well-defined surface area. The laser intensity at this surface is made homogeneous within 20% by means of a beam expander and amounts to 1.1 mW/mm<sup>2</sup>.

Irradiation with X-rays occurred with a tube with a tungsten anode that operated at 60 kV and 15 mA. A filter is used to obtain a Gaussian-like shaped spectrum around 48 keV. The exposure is registered on-line with a well-calibrated ionisation chamber. The sources used for irradiation with gamma rays, alpha particles as well as a description of the beam of thermalised neutrons can be found in chapter 5.

As a reference sample a Fuji image plate type IP-5 HR is used, comprising  $BaFBr:Eu^{2+}$  as phosphor material.

## 7.4 Results

The  $Eu^{2+}$  luminescence in the haloborates has been studied in detail by Meijerink et al. [237] who showed that there are two different crystallographic sites occupied by the  $Eu^{2+}$ . In table 7.3 column 2, the emission maxima measured at an excitation wavelength of 250 nm are given for all studied compounds.

The Ca compounds show a significantly broader emission band than the other compounds and the emission maximum is dependent on the firing time and also on the dopant concentration. This is probably due to the fact that the  $Eu^{2+}$  ions replace the smaller  $Ca^{2+}$  ions which might induce the creation of defects in the direct vicinity of these sites. We also excited at 495 nm to observe probable  $Eu^{3+}$  luminescence around 600 nm. The luminescence was observed but with

an intensity always less than 0.5% of the  $Eu^{2+}$  luminescence. The Ba containing samples show a small extra emission band around 380 nm that reveals the presence of a second phase. This is probably  $\alpha$ - $BaB_2O_4:Eu^{2+}$  which luminesces around 370 nm [238].

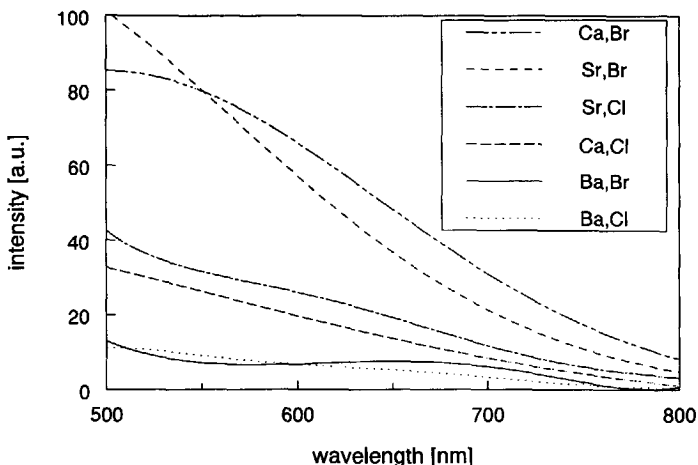


**Figure 7.9:** Stimulation spectra of the  $Eu^{2+}$  luminescence in the haloborates. The spectra were corrected for the wavelength dependent intensity of the xenon lamp.

When the samples are irradiated with gamma rays and then photostimulated at 633 nm, again the  $Eu^{2+}$  luminescence is observed. But the emission ascribed to  $BaB_2O_4:Eu^{2+}$  is lacking. Apparently the storage and/or recombination of electron-hole pairs in this compound is much less efficient. In figure 7.9 the photostimulation spectra are depicted of the samples that were prepared by means of firing for 6 hours. They were recorded after gamma ray irradiation for a fixed time. The almost structureless spectra show that stimulation at the HeNe laser wavelength (632.8 nm) is possible although not most efficient. The compounds  $Ca_2B_5O_9Br:Eu^{2+}$  and  $Sr_2B_5O_9Br:Eu^{2+}$  give the largest response to the stimulation. The samples prepared by firing for 3 hours showed without exception less response than their '6 hours' equivalents and are therefore not depicted. The difference with the '6 hours' samples varied between a factor of 2 for the Ba compounds to a factor of 35 for  $Ca_2B_5O_9Br:Eu^{2+}$ . An increase of the firing time to 9 hours does not result into an enhancement of the photostimulated luminescence signal compared with the '6 hours' samples. It is remarkable that for this series it is  $Ca_2B_5O_9Cl:Eu^{2+}$  that gives the highest PSL signal, whereas the response of the Ba compounds is still lowest.

For the samples that were fired for 6 hours we determined the number of photons emitted due to photostimulation after giving a known dose of X-rays, alpha particles or neutrons. As explained in chapter 5 this is done by continuous stimulation of the irradiated samples followed by integration of the measured signal. Figure 7.10 is the result of such a measurement

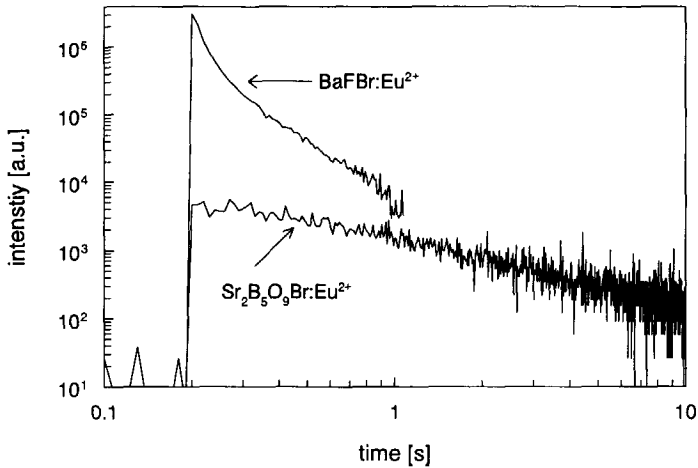


**Figure 7.10:** Measured luminescence intensity during HeNe laser stimulation of a  $\text{Sr}_2\text{B}_5\text{O}_9\text{Br}:\text{Eu}^{2+}$  sample and the  $\text{BaFBr}:\text{Eu}^{2+}$  reference sample after exposure to 1 R of 48 keV X-rays. It should be noted that the X-ray sensitivity of  $\text{BaFBr}:\text{Eu}^{2+}$  is higher than that of  $\text{Sr}_2\text{B}_5\text{O}_9\text{Br}:\text{Eu}^{2+}$  and that in the case of neutron irradiation the energy deposited in  $\text{Sr}_2\text{B}_5\text{O}_9\text{Br}:\text{Eu}^{2+}$  will be at least a factor of 40 higher.

for  $\text{Sr}_2\text{B}_5\text{O}_9\text{Br}:\text{Eu}^{2+}$  and the reference sample after an X-ray exposure of 1 R. When using neutrons the picture changes considerably in favour of  $\text{Sr}_2\text{B}_5\text{O}_9\text{Br}:\text{Eu}^{2+}$ . At first because the X-ray sensitivity of  $\text{BaFBr}:\text{Eu}^{2+}$  is higher than that of  $\text{Sr}_2\text{B}_5\text{O}_9\text{Br}:\text{Eu}^{2+}$  as will be discussed below. At second because of the difference in the amount of energy that is deposited per neutron. The PSL signal of  $\text{Sr}_2\text{B}_5\text{O}_9\text{Br}:\text{Eu}^{2+}$  decays more rapidly than that of  $\text{BaFBr}:\text{Eu}^{2+}$ , meaning that more laser energy is needed so stimulate the photon emission. This, together with the lower conversion efficiency for X-rays, makes that there is a large difference in the luminescence intensity during the first hundreds of ms of stimulation.

In table 7.3 column 3, the number of photons emitted due to stimulation is given per incident X-ray, alpha particle or thermal neutron. For the reference sample (which is not sensitive to neutrons) only the number per incident X-ray quantum is given. This number corresponds with a conversion efficiency of  $1.6 \text{ pJ}/(\text{mm}^2 \cdot \text{mR})$  which is comparable to values found in the literature [112, 187]. As is shown in the table, it is a factor of 28 higher than that of the best haloborate,  $\text{Sr}_2\text{B}_5\text{O}_9\text{Br}:\text{Eu}^{2+}$ . Differences in PSL yield can partly be attributed to differences in absorption probabilities for the X-rays. The results of the PSL yield upon alpha irradiation are a better indication for the response of these samples to neutrons. Contrary to irradiation with X-rays (where the photoelectric effect is the dominant absorption mechanism) there is a negligible difference in stopping power. This explains that the relation between the yields of the different compounds has changed in favour of the materials with the lower effective Z. Only for the most

promising materials the PSL yield has been determined for thermal neutrons. Compared to results in column 4, the yields are much lower because of the lower stopping power and the lower energy deposition per absorbed quantum. But one would expect the ratio between the yields for alphas and neutrons to be constant. However, varies between 10 and 17 and has a relative standard deviation of 45%. This deviation must be ascribed to experimental errors.

In column 6 of table 7.3 the stimulation energies of the haloborates and the  $BaFBr:Eu^{2+}$  sample are presented. The laser energy needed to stimulate the traps in the Ca and Sr haloborates is roughly a factor of 45 higher than that needed for  $BaFBr:Eu^{2+}$  (see also figure 7.10). For the Ba haloborates it is even much more. The stimulation energies are independent of the type of irradiation. In other words, the profile of the absorbed radiation dose in the pill does not affect the time dependence of the PSL under continuous laser stimulation.

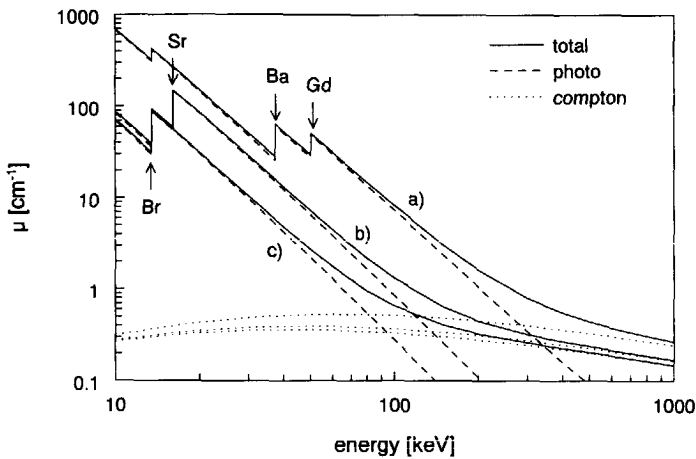


**Figure 7.11:** The linear photon attenuation coefficient  $\mu$  as a function of the photon energy for (a)  $BaFBr:Eu^{2+} \cdot Gd_2O_3$ , (b)  $Sr_2B_5O_9Br:Eu^{2+}$  and (c)  $Ca_2B_5O_9Br:Eu^{2+}$ .

The gamma sensitivity of the most efficient storage phosphors,  $Sr_2B_5O_9Br:Eu^{2+}$  and  $Ca_2B_5O_9Br:Eu^{2+}$  is calculated and presented in figure 7.11, together with that of  $BaFBr:Eu^{2+} \cdot Gd_2O_3$  (with a  $BaFBr:Eu^{2+} \cdot Gd_2O_3$  ratio of 70/30). The calculations were based on the photon cross sections as given by Hubbell [239]. Since we are only interested in how sensitivities relate, the single crystal densities were used, thus assuming equal packing densities of the powders. The sensitivities are expressed with the linear photon attenuation coefficient  $\mu$ . The separate contributions of the photo-effect and the Compton-effect are added with dashed lines. Comparing  $Sr_2B_5O_9Br:Eu^{2+}$  with  $BaFBr:Eu^{2+} \cdot Gd_2O_3$  shows that  $\mu$  is a factor of 1.5 (at  $E \geq 1$  MeV) to 8 (around 100 keV) lower for the former. These numbers are 1.5 and 20 respectively when taking  $Ca_2B_5O_9Br:Eu^{2+}$ .

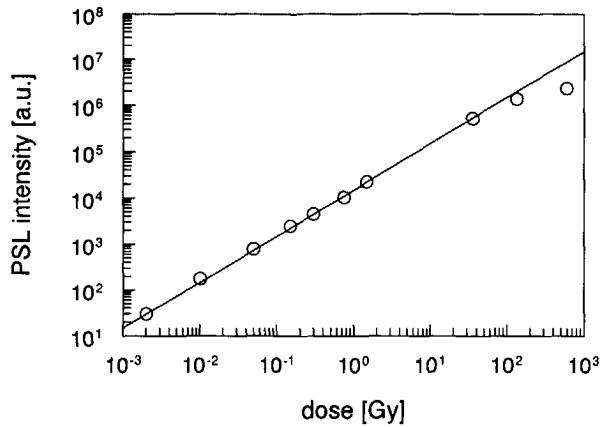


**Figure 7.12:** The PSL intensity of  $\text{Sr}_2\text{B}_5\text{O}_9\text{Br}:\text{Eu}^{2+}$  as a function of the X-ray dose.

The response of the  $\text{Sr}_2\text{B}_5\text{O}_9\text{Br}:\text{Eu}^{2+}$  phosphor is linear with the dose it received, as is shown in figure 7.12. The sample was irradiated with X-rays instead of neutrons. The dynamic range is at least 4 orders of magnitude. It can be expected that the response will be linear upon neutron irradiation as well.

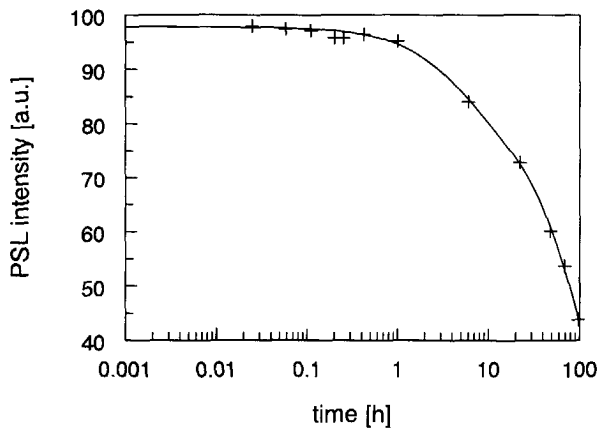


**Figure 7.13:** The PSL intensity of  $\text{Sr}_2\text{B}_5\text{O}_9\text{Br}:\text{Eu}^{2+}$  as a function of the time between irradiation and readout, measured at room temperature.

While reading out an IP it is important that the stored information does not fade away before readout. We have measured the effect of fading by irradiation of the  $\text{Sr}_2\text{B}_5\text{O}_9\text{Br}$  sample and

probing the PSL intensity with 633 nm photons at elapsed times. The PSL signal should not be affected by the probing photostimulation. Therefore the stimulation energy was minimised by using a  $\mu$ s flashlamp. In figure 7.13 the fading of the PSL signal is as a function of time is depicted, measured at room temperature. The measured values can be well fitted with two exponential functions as is shown, which suggests that two different charge traps contribute to the PSL at 633 nm. The fading takes place very slowly. After 8 hours the PSL signal is still 80% of its original.

## 7.5 Discussion

### DQE

In table 7.3 can be found that the most efficient samples,  $Ca_2B_5O_9Br:Eu^{2+}$  and  $Sr_2B_5O_9Br:Eu^{2+}$  show a PSL yield of 14 and 21 photons per incident neutron respectively. If we assume a realisable photon collection efficiency of 20% and a PMT quantum efficiency of 25%, the  $N_{phe}$ s are 0.7 and 1. These values are rather close to the  $N_{phe}$  of 1.3 necessary for a 150  $\mu$ m thick IP-B to obtain a DQE of 40%. Two important remarks should be added:

- 1) In the experiment we used 48 meV neutrons and the samples contain natural boron. Curve (f) of figure 7.1 gives the  $A$  valid in the experiment. In the first 300  $\mu$ m only 20% of the neutrons is absorbed which has definitely affected the results for the  $N_{phe}$ . As it is difficult to introduce a correction factor we will not do so.
- 2) It is not probable that the DQE of the  $Gd_2O_3$  based plate will be improved significantly. Because of the large variance  $\nu_{N_{phe}}$  it does not make sense to improve the conversion efficiency of the  $BaFBr:Eu^{2+}$  phosphor. However, an improvement in the conversion efficiency of  $Sr_2B_5O_9Br:Eu^{2+}$  or  $Ca_2B_5O_9Br:Eu^{2+}$  will directly lead to an improvement of the DQE as could be seen in figure 7.8. It is known that the conversion efficiency strongly depends on the preparation conditions of a material. This probably explains the fact that Meijerink *et al.* [229] have found a conversion efficiency for  $Ba_2B_5O_9Br:Eu^{2+}$  upon X-rays of 1  $\mu$ J/mm<sup>2</sup>/mR which is at least a factor of 60 higher than the efficiency measure by us.

### Stimulation energy

The stimulation energy of  $Sr_2B_5O_9Br:Eu^{2+}$  and  $Ca_2B_5O_9Br:Eu^{2+}$  is a factor of 30 larger than that of  $BaFBr:Eu^{2+}$ . This means that more time is required to read out the irradiated plate, which leads to a smaller signal to noise ratio, in particular for pixels that absorbed a few neutrons. Again, it is remarkable that Meijerink *et al.* has found a stimulation efficiency of less than 100  $\mu$ J/mm<sup>2</sup> for  $Ba_2B_5O_9Br:Eu^{2+}$  [229].

### Resolution

Because of the limited range of the  $^7Li$  and the  $^4He$  particle the resolution of a  $Sr_2B_5O_9Br:Eu^{2+}$  or  $Ca_2B_5O_9Br:Eu^{2+}$  based plate will be fully determined by the readout procedure. Furthermore, long distance correlations due to the numerous gamma rays and X-rays emitted by  $Gd^*$  will be absent. If a high resolution is a stringent requirement the use of a single crystal can be considered.



Then, the neutron absorption probability will also increase as indicated by curve (f) of figure 7.1.

## 7.6 Summary and Conclusion

In this chapter a study on an alternative image plate for the detection of thermal neutrons is presented. The plate should consist of a powder layer of one of the compounds  $M_2B_5O_9X:Eu^{2+}$  ( $M=Ca, Sr, Ba$ ;  $X=Cl, Br$ ) and a binder material. This plate, which we call IP-B is compared with the type of plate that is currently used and which we call IP-Gd. The IP-Gd consists of a layer of mixed  $BaFBr:Eu^{2+}$  and  $Gd_2O_3$  powder in a binder. In particular the DQE of both plate types is considered. The DQE depends on the neutron absorption probability  $A$ , the number of photoelectrons created per incident neutron  $N_{phe}$  and on the relative variance of  $N_{phe}$ ,  $\nu_{N_{phe}}$ .

It is found that under the condition that highly enriched  $^{10}B$  is used, the *effective*  $A$ s of both plate types do not differ much. This is partly due to the fact that more than 30% of the neutrons absorbed by  $^{155}Gd$  or  $^{157}Gd$  do not yield any energy deposition in the  $BaFBr:Eu^{2+}$  powder grains. If a neutron does induce energy deposition it amounts typically 45 keV whereas the energy deposited in a haloborate material will be about 2.1 MeV. Still,  $N_{phe}$  of the  $Gd_2O_3$  based plate is larger because of the much higher conversion efficiency of  $BaFBr:Eu^{2+}$ .

The essential difference between a IP-Gd and the IP-B is the variance in the number of photoelectrons  $\nu_{N_{phe}}$ . This difference is directly connected with the difference in the neutron capture reactions (see table 2.1). By taking these reactions as a starting point we have studied the energy deposition in the two plate types by means of a Monte Carlo simulation. It follows that the relative variance of the energy deposition  $\nu_E$  in the IP-Gd is between 0.55 and 0.63 (depending on the exact geometry of the plate), thus completely determining  $\nu_{N_{phe}}$ . This implies that the DQE can be at most 35%-40%.

Simulations with the haloborate representative  $Sr_2B_5O_9Br:Eu^{2+}$  show that for this case  $\nu_E$  substantially smaller. For a comparison with the IP-Gd the reader is referred to figures 3(b) and 6(b). It is found that  $\nu_E$  is less than 0.03 when the grain filling factor is 0.7. Therefore  $\nu_E$  and as a consequence  $\nu_{N_{phe}}$  can be neglected in the calculation of the DQE. This implies that, contrary to the IP-Gd, the theoretical maximum of the DQE is not limited by  $\nu_{N_{phe}}$ . It also implies that for a 150  $\mu m$  thick IP-B plate with 100% enriched  $^{10}B$ , the  $N_{phe}$  has to be only 1.3 to obtain a DQE value of 40%, the maximum for the IP-Gd.

The theoretical maximum for the DQE of an IP-B is limited by  $A$ . This parameter is directly dependent on the plate thickness, the phosphor material and the filling factor. For a  $Sr_2B_5O_9Br:Eu^{2+}$  based plate and a filling factor of 0.7 the maximum DQE is 60% when the thickness is 150  $\mu m$  and 85% when the thickness is 300  $\mu m$ .

Values for  $N_{phe}$  have also been determined experimentally for all haloborates. The highest values were found for  $Sr_2B_5O_9Br:Eu^{2+}$  and  $Ca_2B_5O_9Br:Eu^{2+}$ :  $N_{phe} = 1$  and  $N_{phe} = 0.7$  respectively. It should be noted that 48 meV neutrons were employed and that only 20% of them is absorbed in the first 300  $\mu m$  of the pressed powder layer. If 25 meV neutrons and 100% enriched  $^{10}B$  were

used, the fraction absorbed (in 300  $\mu\text{m}$ ) would be more than 80%. Then the values found for  $N_{phe}$  would have been higher. It seems therefore that a DQE higher than 40% can be achieved.

The experiments have shown as well that the response of  $Sr_2B_5O_9Br:Eu^{2+}$  on radiation is linear with the dose and that fading of the information goes sufficiently slowly. It has also been demonstrated that the gamma sensitivity of  $Sr_2B_5O_9Br:Eu^{2+}$  and  $Ca_2B_5O_9Br:Eu^{2+}$  is significantly lower than that of  $BaFBr:Eu^{2+}\cdot Gd_2O_3$ . Besides, a high resolution can be obtained as the range of capture reaction products is limited and there are no gamma rays and X-rays causing 'fog' in the image. At present, an important disadvantage of  $Ca_2B_5O_9Br:Eu^{2+}$  and  $Sr_2B_5O_9Br:Eu^{2+}$  is the stimulation energy that is considerably larger than that of  $BaFBr:Eu^{2+}$ .

In conclusion,  $Sr_2B_5O_9Br:Eu^{2+}$  or  $Ca_2B_5O_9Br:Eu^{2+}$  have a high potential to replace the  $BaFBr:Eu^{2+}\cdot Gd_2O_3$  system. It is therefore necessary to study the relation between the sample preparation conditions and both the stimulation energy and conversion efficiency in more detail. According to other results on these compounds reported in literature considerable improvement can be envisaged.

## 8

# On the trapping and recombination of charge carriers in $\text{Sr}_2\text{B}_5\text{O}_9\text{Br}:\text{Eu}^{2+}$

## 8.1 Introduction

In the previous chapter the possibility of employing  $\text{M}_2\text{B}_5\text{O}_9\text{X}:\text{Eu}^{2+}$  ( $\text{M}=\text{Ca},\text{Sr},\text{Ba}$ ;  $\text{X}=\text{Cl},\text{Br}$ ) as an alternative thermal neutron storage phosphor for the  $\text{BaFBr}:\text{Eu}^{2+}\cdot\text{Gd}_2\text{O}_3$  mixture has been discussed. In this chapter experiments providing information about the physical mechanisms responsible for the trapping and detrapping of charge carriers, the nature of the traps, and the recombination luminescence will be presented and interpreted. In particular the role of the Eu activator ions is studied. The focus is on  $\text{Sr}_2\text{B}_5\text{O}_9\text{Br}:\text{Eu}^{2+}$ , the compound with the highest efficiency of creating optically stimulable centres after a neutron capture. The efficient luminescence of this compound was first reported by Peters *et al.* [127] and later the structure and luminescence properties were discussed in more detail by several authors [230, 237, 238, 240].

In figure 8.1(a) the unit cell of  $\text{Sr}_2\text{B}_5\text{O}_9\text{Br}$  is given. The  $\text{Sr}^{2+}$  and  $\text{Br}^-$  ions are located in tunnels formed by a  $(\text{B}_5\text{O}_9)_\infty$  network extending along the *c*-axis. The B-O bonds have a covalent character whereas the binding between the other ions and their binding with the network is more ionic. There are two different sites available for the  $\text{Eu}^{2+}$  ions to substitute a  $\text{Sr}^{2+}$  ion, which are both occupied [237]. One of the sites is shown in figure 8.1(b). At both sites, the  $\text{Eu}^{2+}$  ion will be coordinated by seven  $\text{O}^{2-}$  ions and two  $\text{Br}^-$  ions. The interatomic distances of the sites differ slightly.

The presentation of experimental results is structured as follows. By means of photoluminescence measurements the characteristic luminescence of the Eu dopant ions is studied and explained. A theoretical calculation determines the position of the  $\text{Eu}^{2+}$  ground state relative to the valence band. The latter result is used to understand the role of the  $\text{Eu}^{2+}$  ions in the trapping of charge carriers.

Next, the radiation-induced absorption and optical stimulation bands are presented. Also thermoluminescence (TL) glow curves were recorded after irradiation. Extra attention is paid

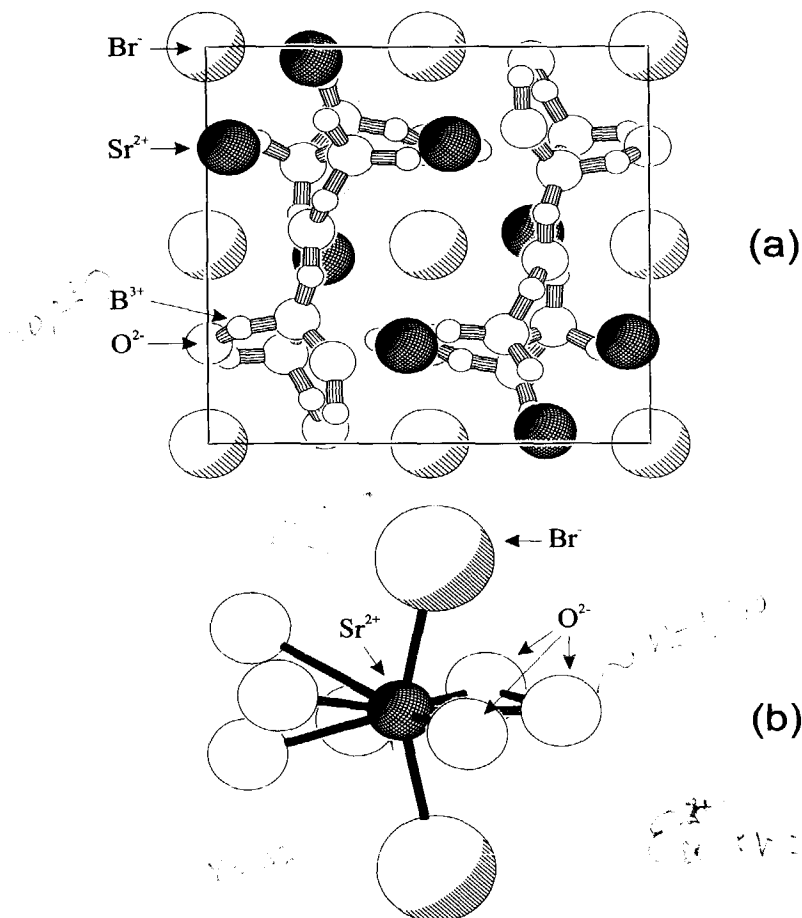


**Figure 8.1:** (a) Projection of a unit cell of  $\text{Sr}_2\text{B}_5\text{O}_9\text{Br}$ . For clarity the relative size of the oxygen ions is chosen smaller than in reality. (b) One of the two  $\text{Sr}^{2+}$  sites. The relative size of the ionic species is in agreement with reality.

to the TL after UV illumination. The effect of irradiation is also studied by EPR. All these experiments provide information about the charge traps.

Then combined scintillation and TL measurements are discussed. From these is determined which part of the free electrons and holes recombines promptly and which part gets trapped. Finally, isothermal luminescence decay curves, recorded after irradiation at various temperatures, are presented. They reflect the mechanism of recombination.

## 8.2 Methods of experiments and calculations

### 8.2.1 Samples

For the experiments several  $\text{Sr}_{2(1-x)}\text{Eu}_{2x}\text{B}_5\text{O}_9\text{Br}$  samples were prepared and studied:

Series A: 2 samples;  $x = 0.001$ , firing time: 3 hours and 6 hours, the latter with intermediate grinding, in a 95%Ar, 5% $\text{H}_2$  atmosphere. Series B: 2 samples;  $x = 0.01$  and 0.001 and a firing time of 9 hours in a 95%Ar, 5% $\text{H}_2$  atmosphere. Series C: 5 samples;  $x = 0.01, 0.005, 0.002, 0.001, 0.0005$ . Firing time 6 hours in a  $\text{N}_2$  atmosphere.

All samples that were fired for 6 or 9 hours were once ground intermediately. More details about the preparation were given in chapter 7. For comparison the TL intensity of a commercially used material BaFBr:Eu<sup>2+</sup> prepared at Agfa-Gevaert, Belgium is also measured (see figure 8.7).

### 8.2.2 Irradiation facilities

X-ray irradiation occurred with an X-ray tube with a Cu anode operated at 35 kV and 25 mA. If higher irradiation dose rates were required, gamma radiation of a well-calibrated <sup>60</sup>Co source was employed. As far as is noticed during experiment, there is no difference in the storage of free charges generated by gamma ray or X-ray absorption. The X-ray tube has been calibrated by comparing its intensity with that of another well-calibrated tube using dosimetric materials. This calibration is particularly important for the results presented in figure 8.15, presenting the TL photon yield per unit of absorbed radiation energy. Since an accurate calibration of a tube with respect to the emitted energy per unit of time is difficult, the TL photon yield was determined with the <sup>60</sup>Co source as well. The difference was 40%. It is concluded that the numbers given in table 8.1 can be wrong by at most a factor of 2.

UV illumination occurred with a deuterium lamp with a well-known emission spectrum combined with a monochromator. Thus it was possible to correct for the wavelength dependent intensity of the lamp, as was necessary to obtain the data points belonging to curve (a) of figure 8.9. During irradiation with shorter wavelength photons the sample room was held at vacuum. Intense UV irradiation up to saturation of the sample was performed with the 254 nm line of a Hg lamp. UV irradiation at low T occurred in an  $\text{N}_2$  atmosphere to prohibit condensation of  $\text{H}_2\text{O}$  on the sample.

### 8.2.3 Excitation, emission and stimulation measurements

Photoluminescence spectra in the visible region and emission intensities under continuous laser stimulation are recorded with an IBH 5000 photospectrometer with a xenon lamp as a light source described in chapter 5. Excitation spectra in the UV region (170-300 nm) were measured in vacuum by means of the deuterium lamp in combination with an ARC VM502 monochromator and a Philips XP2254 PMT. The VUV excitation measurements were performed at the synchrotron

of Daresbury Laboratory, United Kingdom. Excitation spectra and photostimulation spectra are corrected for the wavelength dependent intensity of the lamp. Emission spectra are corrected for the wavelength dependent transmission of the system.

Diffuse reflection measurements were performed with a diode array UV/VIS spectrophotometer (HP 8452A) equipped with a 95 mm diameter Spectralon Integrating Sphere (RSA-HP-84-UV) with an externally mounted xenon light source allowing measurements in the 300-800 nm wavelength range. Large area samples were compared with a calibrated 99% diffuse reflectance standard.

### 8.2.4 TL and EPR measurements

TL glow curves were recorded with a modified and improved Harshaw 2000 reader with automated, microprocessor controlled readout described elsewhere [205]. This setup is calibrated such that an estimate of the absolute number of photons emitted by a sample can be obtained. The error in this estimation is about 50%. The TL emission spectra were recorded with a home-built facility [241] with a spectral resolution of 6 nm. They were subsequently corrected for the wavelength dependent response of the system.

EPR measurements were carried out at the Laboratory of Applied Chemistry of the Solid State belonging to the ENSCP (Paris) at temperatures of 120 K and RT. Use was made of a Bruker ESP300e spectrometer equipped with a variable temperature accessory from Oxford Instruments. The microwave frequency was measured with a Systron Donner frequency counter.

### 8.2.5 Theoretical calculations

The position of the  $\text{Eu}^{2+}$  ground state in  $\text{Sr}_2\text{B}_5\text{O}_9\text{Br}:\text{Eu}^{2+}$  relative to the valence and conduction band has been determined by means of a theoretical calculation. The crystal was modelled as a cluster of ions with the  $\text{Sr}^{2+}$  ion as a centre. This cluster is embedded in an array of point charges which give the right Madelung potential at the sites of the cluster. The cluster was chosen to consist of the Sr ion surrounded by all ions within 3.2 Å. So we have one  $\text{Sr}^{2+}$  ion, three  $\text{B}^{3+}$  ions, seven  $\text{O}^{2-}$  ions and two  $\text{Br}^-$  ions. The ions are occupied using the ion models based on Hartree-Fock theory. The electrons occupy gaussian type orbitals which are determined by an optimisation method. The package used is the Gaussian94 of Carnegie Mellon University [242]. The orbital energies give a good estimate of the positioning of the core, valence and to a lesser extent also of the conduction band. The orbital basis sets were partly copied from tables published by Stevens *et al.* [243] and also from those of Huzinaga *et al.* [244]. In order to obtain the position of the levels of the  $\text{Eu}^{2+}$  ion, in particular those of the  $4f^7$  configuration, new calculations were done with  $\text{Sr}^{2+}$  replaced by  $\text{Eu}^{2+}$ . The basis set for this ion was taken from lanthanide tables published by Cundari *et al.* [245]. These basis sets consist of the 1s, 2s and 2p states of  $\text{B}^{3+}$ , the 2s and 2p states of  $\text{O}^{2-}$ , the 4s and 4p states of  $\text{Br}^-$  and finally the 5s and 5p states of  $\text{Sr}^{2+}$ . For  $\text{Eu}^{2+}$  a set for the 4f, 5s, 5p, and 5d orbitals was taken. The rest of

the electron core is represented by an effective core potential (ECP). Non-occupied parts of the basis sets are chosen in such a way that an estimate can be made of the bottom of the conduction band (diffuse components). The positioning process of levels, particularly the 4f levels of  $\text{Eu}^{2+}$ , is not trivial. Because of correlation effects (a missing part in the Hartree-Fock calculations) the orbitals obtained by the minimalisation procedure are only approximations to the real excitation energies. So one has to correct these energies to account for this effect. It was chosen to use the experimental ionisation energies of the free ion as a reference for the calculated values. For  $\text{Eu}^{2+}$  the tables published by Martin *et al.* [227] were used. The correction amounts to about 1.5 eV. For a more detailed description of a similar calculation see e.g. [246]. It should be noted that calculating the energy levels of the  $4f^65d$  configuration of the  $\text{Eu}^{2+}$  excited state is much more complicated because of the strong interaction of the state with the crystal field. Since the crystal field can not be calculated accurately enough, such a calculation has not been performed.

## 8.3 Results

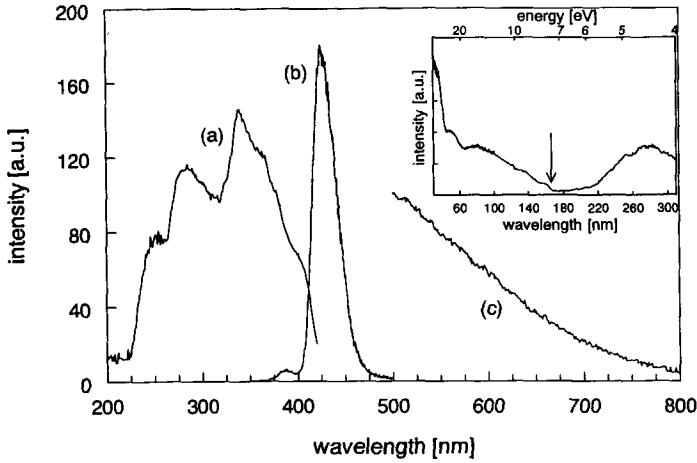
### 8.3.1 Spectroscopic properties of the Eu dopant ions

Figure 8.2 shows the excitation (a) and emission (b) spectra of  $\text{Eu}^{2+}$  in  $\text{Sr}_{2(1-x)}\text{Eu}_{2x}\text{B}_5\text{O}_9\text{Br}$  ( $x = 0.001$ ), recorded at room temperature. Its maximum is located at 426 nm. The emission is ascribed to the  $4f^65d \rightarrow 4f^7$  ( ${}^8\text{S}_{7/2}$ ) transition on  $\text{Eu}^{2+}$ .

Because of the low point symmetry at the  $\text{Eu}^{2+}$  site the  $4f^6({}^7\text{F}_j)5d$  states are expected to be fivefold splitted by the crystal field. However, the observation of this splitting is obscured by effects of exchange interaction between the 4f electrons and the 5d electron [237] and Fano-antiresonance [247].

The inset of figure 8.2 shows the excitation spectrum of  $\text{Eu}^{2+}$  in the VUV region. At 168 nm (7.4 eV, see arrow) interband transitions in the host lattice followed by capture of the electron and hole by a  $\text{Eu}^{2+}$  ion become possible. At 65 nm a stepwise increase of the luminescence intensity is observed that can be ascribed to the process of electron multiplication [248].

To understand the role of the  $\text{Eu}^{2+}$  ions in the trapping and recombination of charge, the positions of the  $\text{Eu}^{2+}$   $4f^7$  ( ${}^8\text{S}_{7/2}$ ) ground state and the observed excited states relative to the valence and conduction band should be known. The position of the  $\text{Eu}^{2+}$  ground state and that of the valence and conduction band were calculated with the cluster calculation described before. The errors in the calculated results are believed to be less than 1 eV. In figure 8.3 the energy levels of  $\text{Sr}_2\text{B}_5\text{O}_9\text{Br}:\text{Eu}^{2+}$  based on the experimental and calculated results are sketched. The upper valence band consists of Br(4p) states. The bottom of the conduction band comprises B(2s) as well as Sr(5s) states. The calculated band gap of 8.5 eV is typical for alkaline earth halides. However, it is more than the 7.4 eV threshold that was determined from experiment. To explain the difference not only the error in the calculation must be considered. Experiment can not distinguish real band-to-band transitions from transitions accompanied with formation of (impurity) bound excitons. The latter will occur at somewhat lower photon energies. According



**Figure 8.2:** Excitation spectrum (curve a) recorded at  $\lambda_{em} = 440$  nm, emission spectrum (curve b) recorded at  $\lambda_{ex} = 250$  nm and photostimulation spectrum (curve c) recorded at  $\lambda_{em} = 430$  nm of  $\text{Sr}_{2(1-x)}\text{Eu}_{2x}\text{B}_5\text{O}_9\text{Br}$  ( $x = 0.001$ ), all measured at 300 K. The excitation and photostimulation spectrum are corrected for the wavelength dependent xenon lamp intensity. Inset: VUV excitation spectrum, corrected for the wavelength dependent synchrotron intensity.

to the calculation, the  $\text{Eu}^{2+}$  ground state is positioned at the top of the valence band. Taking the calculation error into account it must be located close to the top of the valence band.

In figure 8.4 an emission spectrum recorded at  $\lambda_{ex} = 465$  nm is shown (solid line). A complex of narrow lines can be observed around 590 nm, 620 nm, and 700 nm. Similar emission lines have been observed in many  $\text{Eu}^{3+}$  activated host lattices (see e.g. [249–251]).

Each emission line is identified. Radiative transitions can occur from the  $^5\text{D}_0$  excited state to the  $^7\text{F}_j$  manifold. Radiative decay of the higher excited  $^5\text{D}_0$  states with  $J = 1, 2, 3$  is also possible but this process competes with nonradiative decay to the  $^5\text{D}_0$  state. In borates the latter is relatively efficient because of the presence of high frequency phonons [116]. This explains that all emission lines originate from the  $^5\text{D}_0$  state. Transitions between  $4f^n$  states are expected to occur by a magnetic dipole process. According to the selection rules the only allowed transition is the  $^5\text{D}_0 \rightarrow ^7\text{F}_1$  transition. This transition is observed but it is less intense than others. As was demonstrated by Blasse [249], a lack of inversion symmetry at the  $\text{Eu}^{3+}$  ion site results into a small mixing of opposite parity  $4f^{n-1}5d$  states into the  $4f^n$  states. This gives rise to the addition of a small electric dipole moment to the transition. Then Judd-Ofelt theory states that for rare-earth ions with an even number of electrons transitions from  $J = 0 \rightarrow \text{odd } J'$  are weak and those from  $J = 0 \rightarrow J' = 2, 4, 6$  are strong [116]. This is the case in figure 8.4 and illustrates the low symmetry around  $\text{Eu}^{3+}$ . The transition to the state with  $J' = 6$  is expected around 816 nm and thus outside the region of measurement.



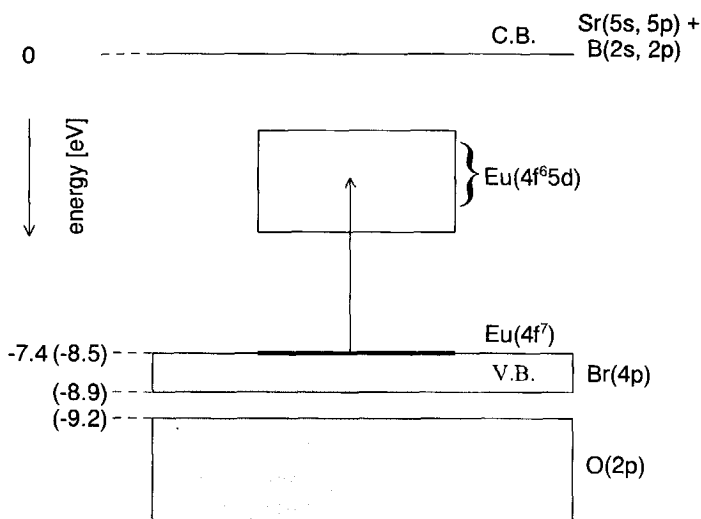


**Figure 8.3:** Sketch of the band structure of  $\text{Sr}_2\text{B}_5\text{O}_9\text{Br}:\text{Eu}^{2+}$  and the energy levels of  $\text{Eu}^{2+}$  relative to the bands for  $\text{Eu}^{2+}$  in its ground state. The numbers between brackets denote the location of energy levels relative to the bottom of the conduction band, according to the cluster calculation. The other number is based on the excitation measurements (figure 2). The position of the band comprising the  $\text{Eu}^{2+}(4f^65d)$  excited states is also derived from figure 2.

The other two curves depicted in figure 8.4 are excitation spectra recorded at  $\lambda_{em} = 615$  nm. One curve shows narrow peaks representing excitations within the  $4f^6$  configuration of  $\text{Eu}^{3+}$ . Below 300 nm a broad band appears that peaks around 215 nm. Its intensity increases with increasing activator concentration. Such a broad band has been observed in more  $\text{Eu}^{3+}$  activated oxides and fluorides in the UV and VUV range [252–254] and is ascribed to a charge transfer (CT) mechanism where an electron is transferred from an anion ligand to the  $\text{Eu}^{3+}$  ion. The energy released when the electron and hole recombine again is used to excite  $\text{Eu}^{3+}$  resulting in  $\text{Eu}^{3+}$  luminescence. The experimental observation that excitation in this band gives rise to  $\text{Eu}^{3+}$  luminescence confirms that such a mechanism is taking place in  $\text{Sr}_2\text{B}_5\text{O}_9\text{Br}:\text{Eu}^{2+}$ . It is not clear whether the bromine or oxygen ligands are involved in the CT. Both in oxides and bromides CT has been observed in the wavelength region 200–300 nm [253, 255].

It is noted that the integral intensity of the  $\text{Eu}^{3+}$  emission lines is about a factor of  $10^4$  less than that of the  $\text{Eu}^{2+}$  emission band as will be shown later in figure 8.11.

### 8.3.2 Radiation induced absorption and stimulation bands

When the samples are exposed to radiation and then photostimulated, only  $\text{Eu}^{2+}$  emission is observed. The sensitivity of this measurement is too low to detect possible weak  $\text{Eu}^{3+}$  emis-

sion shown before (figure 8.4). Curve (c) in figure 8.2 shows the photostimulation spectrum of  $\text{Sr}_{2(1-x)}\text{Eu}_{2x}\text{B}_5\text{O}_9\text{Br}$  ( $x = 0.001$ ) after the sample has received a dose of 250 Gy by means of irradiation with  $^{60}\text{Co}$  gamma rays. It was recorded at  $\lambda_{em} = 430$  nm which matches the  $\text{Eu}^{2+}$  emission band.

The stimulation spectrum is quite structureless and it is not clear whether it reaches a maximum below 500 nm. Because of the necessary separation between stimulating and emitted photons it is not possible to measure the stimulation spectrum at shorter wavelengths.

By carrying out optical reflection measurements on powder, it is possible to study absorption bands and hence also stimulation bands over a broader wavelength region. Figure 8.5 shows two curves which are both the difference between reflection spectra recorded prior to and after irradiation. The difference between these spectra must be due to absorption bands that are induced by radiation. The gamma radiation doses were 1 kGy (curve (a)) and 10 kGy (curve (b)). High radiation doses need to be applied, because of the low sensitivity of this measurement technique.

In both curves three bands are visible: two broad bands around 375 nm and 660 nm respectively and a relatively narrow band located at 426 nm. The broad absorption band at 660 nm is the one that is of most interest for practical application. It could be the 1s-2p absorption band of  $\text{F}(\text{Br}^-)$  centres. In absorption spectra of other storage phosphors in which bromine vacancies act as electron traps, viz.  $\text{BaFBr}:\text{Eu}^{2+}$ ,  $\text{RbBr}:\text{Tl}^+$  [110, 256], and also  $\text{Ba}_2\text{B}_5\text{O}_9\text{Br}:\text{Eu}^{2+}$  [172],

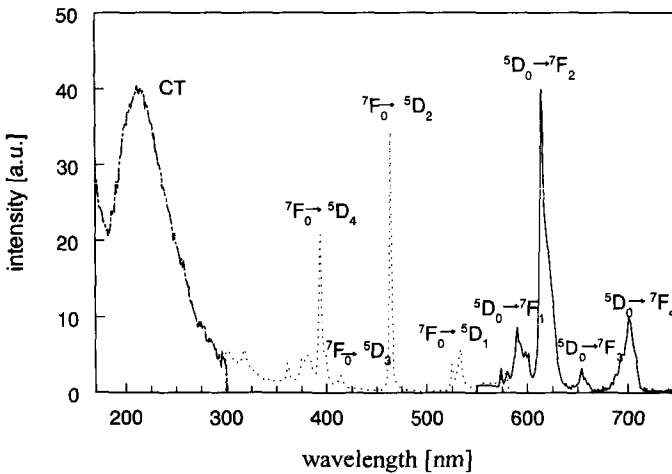


**Figure 8.4:** Excitation and emission spectra of  $\text{Eu}^{3+}$  in  $\text{Sr}_2\text{B}_5\text{O}_9\text{Br}:\text{Eu}^{2+}$ . Solid line: emission recorded at  $\lambda_{ex} = 465$  nm and corrected for the wavelength dependent sensitivity of the detection system. Dotted line: excitation spectrum recorded with a xenon lamp at  $\lambda_{em} = 615$  nm, not corrected for the lamp intensity. Broken line: Excitation spectrum recorded with a deuterium lamp at  $\lambda_{em} = 615$  nm, corrected for the lamp intensity.

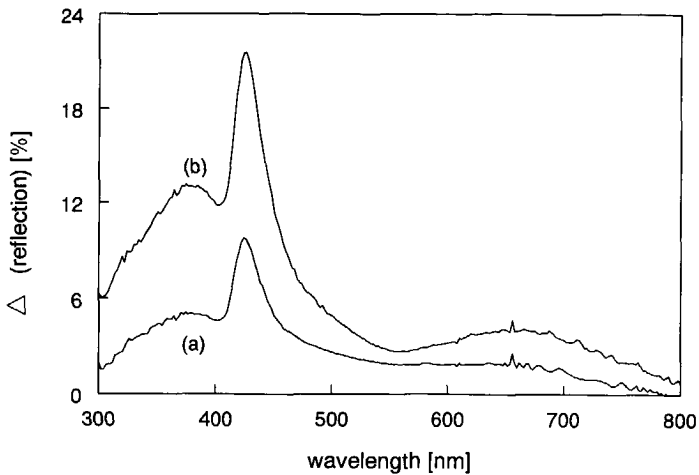


**Figure 8.5:** Reflection spectrum of  $\text{Sr}_{2(1-x)}\text{Eu}_{2x}\text{B}_5\text{O}_9\text{Br}$  ( $x = 0.001$ ) recorded prior to irradiation minus the reflection spectrum recorded after irradiation with  $^{60}\text{Co}$  gamma rays. The dose applied was 1 kGy for curve (a) and 10 kGy for curve (b).

a similar band is observed in the 600-700 nm region. In first approximation the position of the F-centre absorption band is determined by the lattice spacing (see e.g. [257]) which is not much different in  $\text{Sr}_2\text{B}_5\text{O}_9\text{Br}:\text{Eu}^{2+}$  (see also equation (3.8)).

The origin of the band at 375 nm is unknown. A very similar radiation induced absorption band (with respect to position and FWHM) was observed in the storage phosphor  $\text{Ba}_5\text{SiO}_4\text{Br}_6:\text{Eu}^{2+}$  [258]. The band located at 426 nm is an experimental artefact due to  $\text{Eu}^{2+}$  fluorescence. When a glass filter is used in the experiment that cuts off the incident photons below 400 nm which are able to excite the  $\text{Eu}^{2+}$  ions, the 426 nm peak is absent.

The structure between 500 nm and 800 nm differs from the stimulation spectrum (curve (c) figure 8.2). It seems that in the stimulation spectrum the 660 nm band is more hidden under the 375 nm band. The reason for this is not clear.

### 8.3.3 TL and its relation to photostimulated luminescence (PSL)

Recombination of trapped charge carriers can also be stimulated thermally. The TL emission spectrum appears to be equal to the  $\text{Eu}^{2+}$  emission (curve (b) figure 8.2) spectrum. Hence, recombination of detrapped charge occurs on  $\text{Eu}^{2+}$ , like in the PSL process.

The TL was studied as a function of the Eu dopant concentration. Equal weights of different samples were exposed to equal amounts of  $^{60}\text{Co}$  gamma radiation. Next, TL glow curves were recorded, presented in figure 8.6. For all dopant concentrations four peaks are observed at about 350 K, 405 K, 480 K, and 610 K. Hereafter these peaks will be numbered 1,2,3 and 4 respectively

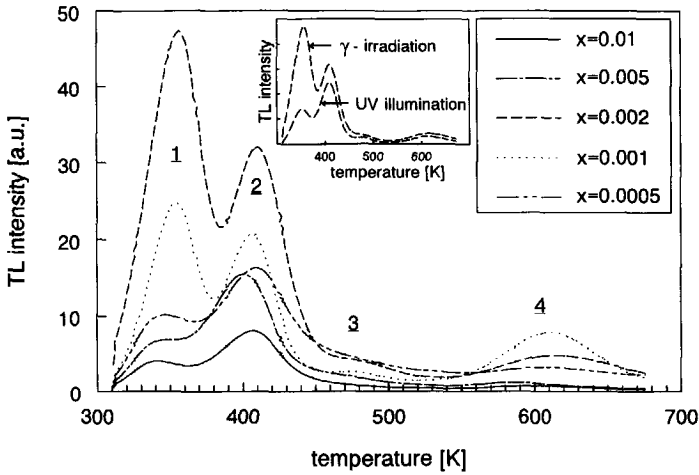


**Figure 8.6:** TL glow curves of  $\text{Sr}_{2(1-x)}\text{Eu}_{2x}\text{B}_5\text{O}_9\text{Br}$  (C series) with various values of  $x$ , after a fixed sample weight received a dose of 15 Gy by irradiation with  $^{60}\text{Co}$  gamma rays. Heating rate 1 K/s. Inset: comparison of the TL glow curves recorded after gamma irradiation and UV illumination for  $x = 0.002$ .

as denoted in figure 8.6. So it appears that at least four different trap species are present. The exact position of the maximum of the peaks varies somewhat with the concentrations. Also the height of the peaks relative to the other peaks varies from sample to sample. Most striking is that the height of the peaks (the TL intensity) depends strongly on the dopant concentration and a maximum is reached at  $x = 0.002$ .

For a fixed dopant concentration  $x = 0.001$  we have varied the conditions of preparation, in particular the firing time. Similar TL measurements were performed, which are depicted in figure 8.7, together with a TL spectrum of optimised  $\text{BaFBr}:\text{Eu}^{2+}$ . This figure shows that the firing time during preparation determines the TL intensity. The optimal efficiency is obtained for a 6 hour firing time with intermediate grinding. Firing for a longer time reduces the efficiency again. The use of a slightly reducing or neutral atmosphere does not affect the type of traps that are created as can be concluded when comparing curve (a), (c) and (d). It is not understood why curve (b) has a somewhat deviating structure. A comparison with the result for optimised  $\text{BaFBr}:\text{Eu}^{2+}$  (curve (e)) shows that the integral TL signal of the samples fired for 6 hours is about an order of magnitude smaller than that of optimised  $\text{BaFBr}:\text{Eu}^{2+}$ .

The TL peaks are related to PSL as illustrated with the following experiment. TL glow curves of two  $\text{Sr}_{2(1-x)}\text{Eu}_{2x}\text{B}_5\text{O}_9\text{Br}$  ( $x = 0.001$ ) samples that received a fixed radiation dose were recorded. Next, the samples received the same radiation dose, but before recording the TL glow curve the samples were optically bleached with a HeNe laser beam for 100 s. The curves are compared in figure 8.8. Due to the optical stimulation the intensity of all TL peaks has decreased.

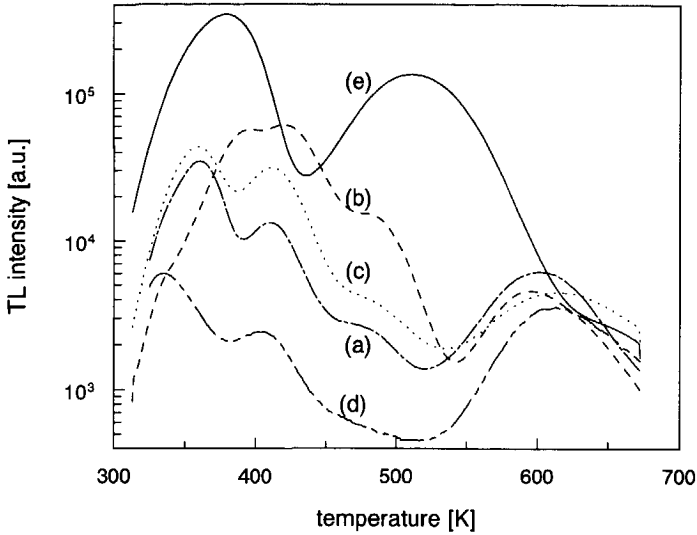


**Figure 8.7:** TL glow curves of  $\text{Sr}_{2(1-x)}\text{Eu}_2\text{xB}_5\text{O}_9\text{Br}$  ( $x = 0.001$ ) samples prepared with different firing times (curve (a)-(d)) and a comparison with the TL curve of optimised  $\text{BaFBr:Eu}^{2+}$  (curve (e)), after a fixed sample weight received a dose of 15 Gy by irradiation with  $^{60}\text{Co}$  gamma rays. Firing time sample curve (a): 3 hours, curve (b),(c): 6 hours, curve (d): 9 hours, all in a reducing atmosphere except sample (c): neutral atmosphere. Thermal heating rate 1 K/s.

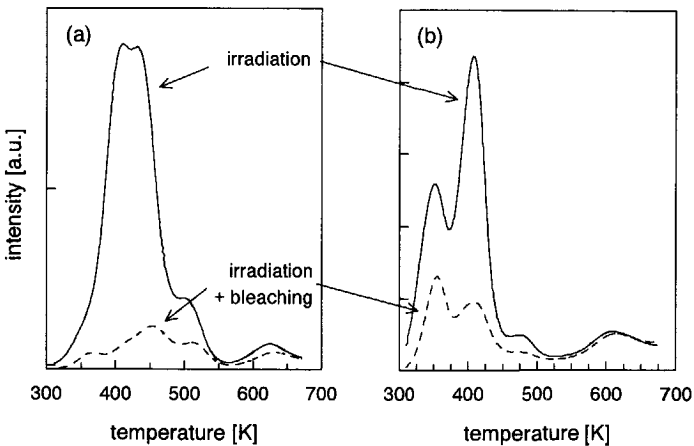


**Figure 8.8:** Effect of bleaching with a HeNe laser on the TL of two  $\text{Sr}_{2(1-x)}\text{Eu}_2\text{xB}_5\text{O}_9\text{Br}$  samples with  $x = 0.001$ . (a) sample from series A. (b) sample from series C.

But the traps connected to the peak 2 are emptied most efficiently, whereas the concentration of the deepest trapped charges does hardly decrease.

### 8.3.4 Filling of traps by illumination with UV light

TL glow curves have also been measured on samples which were illumination with UV light. The curve of  $\text{Sr}_{2(1-x)}\text{Eu}_{2x}\text{B}_5\text{O}_9\text{Br}$  ( $x = 0.002$ ) is given in the inset of figure 8.6. It appears that the same traps are filled as under X-ray or gamma irradiation. The only difference in the glow curves is that for the samples with a high TL signal ( $x = 0.001, 0.002$ ) the ratio between the intensities of peak 1 and 2 is smaller.

An explanation for the UV-induced TL could be that electrons are 'lifted' from deeper traps to traps which are shallow enough to enable thermal stimulation in the temperature range of the experiments. However, there is no difference between the UV-induced TL signal of a sample that was never exposed to radiation before, and one that was. So, traps that were filled prior to illumination do not play a role.

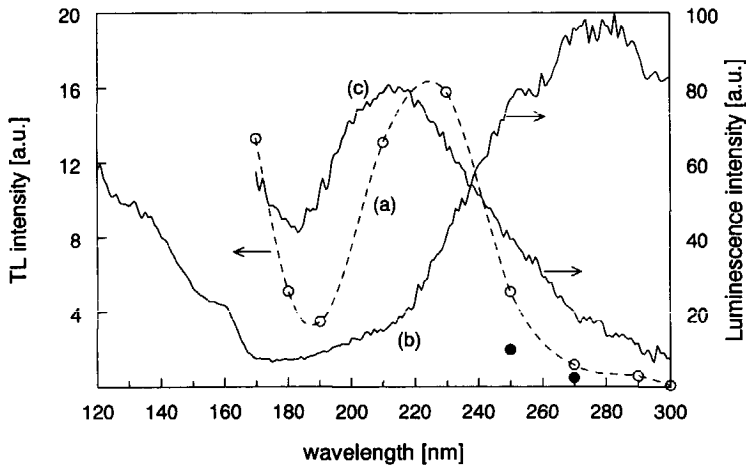


**Figure 8.9:** (a) The total TL signal of UV illuminated  $\text{Sr}_{2(1-x)}\text{Eu}_{2x}\text{B}_5\text{O}_9\text{Br}$  ( $x = 0.001$ ) as a function of the wavelength of the UV light. Open circles: illuminated at 300 K. Closed circles: illuminated at 200 K. The lines connecting the points are drawn to guide the eye. (b) Part of the  $\text{Eu}^{2+}$  excitation spectrum from the inset of figure 1. (c) The charge transfer band from the  $\text{Eu}^{3+}$  excitation spectrum.

In another experiment, TL glow curves were recorded after illumination of  $\text{Sr}_{2(1-x)}\text{Eu}_{2x}\text{B}_5\text{O}_9\text{Br}$  ( $x = 0.001$ ) with UV photons, using various photon wavelengths. For every glow curve the TL curve was integrated over the entire temperature range and plotted versus

the illumination wavelength. Thus a spectrum is obtained that could be called the TL excitation spectrum, see figure 8.9. The threshold for excitation is located around 300 nm. At shorter photon wavelengths there is a band with a maximum around 225 nm (5.5 eV). The efficiency increases again below 180 nm.

For comparison, part of the  $\text{Eu}^{2+}$  excitation spectrum of figure 8.2 is added, as well as the charge transfer band that was observed in the  $\text{Eu}^{3+}$  excitation spectrum of figure 8.4. The latter shows similarity with the TL excitation spectrum, although the maximum of the CT band is located somewhat more towards shorter wavelengths.

Also a correlation with the  $\text{Eu}^{2+}$  excitation spectrum is possible. The TL excitation band at 225 nm starts to rise at the short wavelength side of the  $\text{Eu}^{2+} 4f^7-4f^65d$  excitation band and reaches a maximum in the flank of this band. Such a correlation can be expected when two processes are possible after  $\text{Eu}^{2+}$  excitation. The first is radiative decay. The second is a ionisation process with the condition that ionisation is energetically only possible if  $\text{Eu}^{2+}$  is in a higher excited  $4f^65d$  state.

The TL response was also measured after UV illumination at 200 K, see figure 8.9. Unfortunately, illumination at this temperature could technically be realised at only two illumination wavelengths. The dependence of the trap filling on the temperature is clear: At 200 K the TL signal is reduced by a factor 2.5.

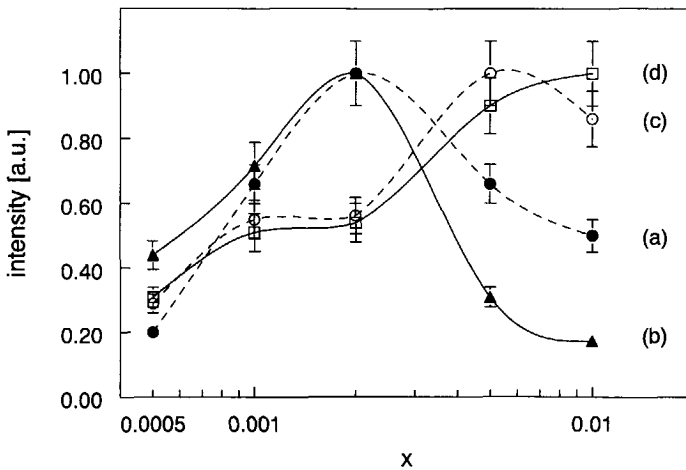


**Figure 8.10:** Dependence of the intensity of the  $\text{Eu}^{2+}$  TL, SL and PL signal on the nominal dopant concentration  $x$  in the samples  $\text{Sr}_{2(1-x)}\text{Eu}_{2x}\text{B}_5\text{O}_9\text{Br}$ . (a) The total TL signal after UV illumination, (b) the total TL signal after gamma irradiation, (c) the SL signal under continuous X-ray irradiation, (d) the PL signal under continuous  $\lambda_{ex} = 350$  nm excitation. The maximum TL, SL and PL signals were normalised to 1 and the other data points are multiplied with the same normalisation factor.

In figure 8.10 (data points belonging to curve (a)) the integral TL signal is plotted for 5 samples with different dopant concentrations (series C) that were exposed to the same UV photon intensity for a fixed time. On the x-axis the nominal Eu concentration is given. Curve (a) should be compared with curve (b), which is obtained similarly with the difference that gamma radiation is used instead of UV (in fact the measurements of figure 8.6 are used). Both curves peak at  $x = 0.002$  but also an important difference can be observed. Curve (a) is relatively higher at higher x-values than curve (b) and relatively lower at lower values of x. This observation can be understood by considering the dependence of curve (a) and (b) on x, starting with curve (a).

The intensity of the integral TL signal generated after UV illumination,  $S_{TL_{uv}}(x)$ , is a product of following terms:

$$S_{TL_{uv}}(x) \propto P_{a_{uv}}(x) \cdot P_{t_{uv}}(x) \cdot P_{r_{uv}}(x) \quad (8.1)$$

where  $P_{a_{uv}}(x)$  is the probability of absorption of an incident UV photon,  $P_{t_{uv}}(x)$  is the probability that the absorption is followed by trapping of electron and hole, and  $P_{r_{uv}}(x)$  is the probability of radiative recombination due to thermal stimulation. All terms may depend on the dopant concentration x.

When a gamma ray is incident on the sample, the probability that it is absorbed and next creates a certain number of electron-hole pairs, does not depend on x. Hence, for  $S_{TL_{\gamma}}$  can be written:

$$S_{TL_{\gamma}}(x) \propto P_{\gamma}(x) \cdot P_{r_{\gamma}}(x) \quad (8.2)$$

with analogues definitions for  $P_{\gamma}(x)$  and  $P_{r_{\gamma}}(x)$  as given above. Obviously,  $P_{r_{\gamma}}(x) = P_{r_{uv}}(x)$ . Perhaps,  $P_{\gamma}(x) \neq P_{t_{uv}}(x)$ , but it can be supposed that both depend similarly on x. Therefore it is probable that the difference between curve (a) and (b) is caused by  $P_{a_{uv}}(x)$ . This strongly suggests that under UV illumination, photons are absorbed by the  $\text{Eu}^{2+}$  or  $\text{Eu}^{3+}$  ions. Then, electron/hole trapping can take place.

If  $\text{Eu}^{2+}$  photoionisation is the initial process in the trapping of charge under UV illumination, one expects that the concentration of  $\text{Eu}^{2+}$  ions,  $[\text{Eu}^{2+}]$ , decreases during irradiation and the concentration of  $\text{Eu}^{3+}$  ions,  $[\text{Eu}^{3+}]$ , increases. This must be accompanied with a change in the intensity of the characteristic luminescence. Since the TL spectra of UV irradiated and X-ray/gamma ray irradiated samples are similar, the same should be observed after gamma irradiation. Figure 8.11 shows the luminescence of  $\text{Sr}_{2(1-x)}\text{Eu}_{2x}\text{B}_5\text{O}_9\text{Br}$  ( $x = 0.001$  in 11(a),  $x = 0.01$  in 11(b)) before and after high-dose irradiation (500 Gy) when excited at 395 nm. At this wavelength both  $\text{Eu}^{2+}$  and  $\text{Eu}^{3+}$  ions can be excited. It is clearly observed that the  $\text{Eu}^{2+}$  luminescence around 426 nm has decreased after the irradiation. A similar observation was already done by Pu *et al.* [240]. However, a shift in the emission band as reported by them was not observed. The decrease amounts to 30% for  $x = 0.01$  and 50% for  $x = 0.001$ .

$\text{Eu}^{3+}$  luminescence is observed around 590 nm and 610 nm, being most intense for  $x = 0.01$ . This luminescence is about 4 orders of magnitude less intense than the  $\text{Eu}^{2+}$  luminescence. The



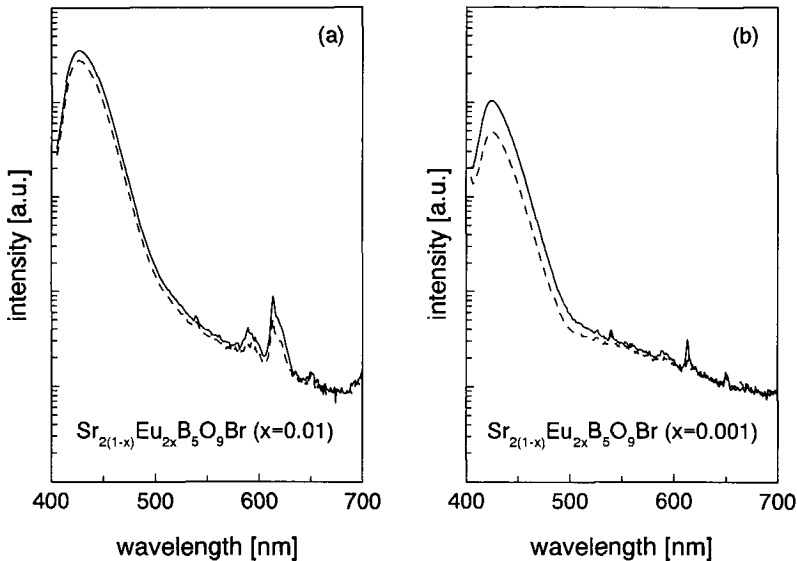


**Figure 8.11:**  $\text{Eu}^{2+}$  and  $\text{Eu}^{3+}$  emission measurement recorded at  $\lambda_{ex} = 395$  nm for (a)  $\text{Sr}_{2(1-x)}\text{Eu}_{2x}\text{B}_5\text{O}_9\text{Br}$ ,  $x = 0.01$  and (b)  $\text{Sr}_{2(1-x)}\text{Eu}_{2x}\text{B}_5\text{O}_9\text{Br}$ ,  $x = 0.001$ . The solid curves are recorded before gamma irradiation and the broken curves after irradiation. The irradiation dose amounted 500 Gy.

decrease of the  $\text{Eu}^{2+}$  luminescence intensity is definitely not accompanied by an increase of the  $\text{Eu}^{3+}$  luminescence intensity. In fact, the latter has decreased as well. For  $x = 0.001$  the decrease is more pronounced than for  $x = 0.01$ , similar to the change in the  $\text{Eu}^{2+}$  luminescence. The same decrease is observed after intense illumination with UV light, in particular when the illumination time is so long that the TL response reaches a maximum. For discussion, see section 8.4.

### 8.3.5 EPR measurements

In figure 8.12 EPR measurements are presented on  $\text{Sr}_{2(1-x)}\text{Eu}_{2x}\text{B}_5\text{O}_9\text{Br}$  for various values of  $x$ . In the upper part the EPR is recorded before gamma irradiation whereas in the lower part the same is done after irradiation. Before irradiation resonances are observed in a wide range below 3000 Gauss, with an intensity that increases with the dopant concentration. These signals must be due to either  $\text{Eu}^{2+}$  or  $\text{Eu}^{3+}$ . From the  ${}^7\text{F}_0$  ground state of  $\text{Eu}^{3+}$  no signal is to be expected because  $J = 0$ . From paramagnetic  $\text{Eu}^{2+}$  we can expect a strong signal though. Since it is an S-state ion, the spin-orbit coupling is usually small. Hence, often very small values of  $\delta g$  are found [259],  $\delta g$  denoting the shift of the effective  $g$  from  $g_e$  (2.0023). In our case the main  $g$ -values are located between 2.4 and 5.4 and thus the shifts are substantial. The reason for this is

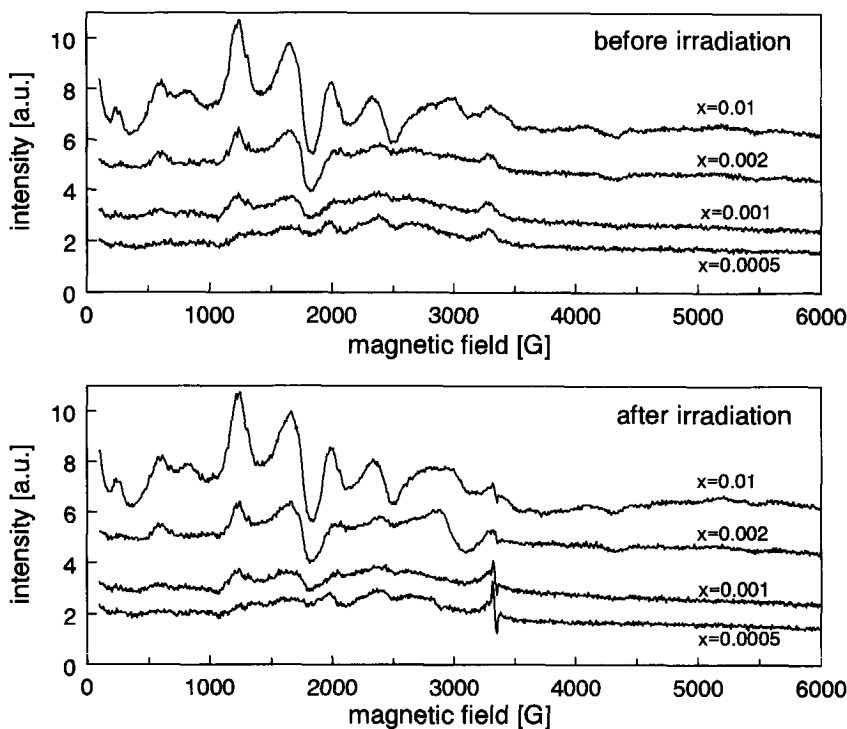


**Figure 8.12:** EPR spectra of  $\text{Sr}_{2(1-x)}\text{Eu}_x\text{B}_5\text{O}_9\text{Br}$  for various values of  $x$ , before and after gamma irradiation. The spectra were recorded at RT and the microwave frequency applied amounted 9.375 GHz with a power of 20 mW.

the very low symmetry at the  $\text{Eu}^{2+}$  site. It implies that in the spin Hamiltonian crystal field terms are at least as important as the Zeeman term and resonances within widely separated Kramers levels giving high  $g$ -values are possible [260].

An 'empty cavity' measurement (measurement without a sample mounted) proves that the small band around 3300 Gauss is not due to the sample. Also the drop in the signal that is sometimes observed when going from 2800 to 3100 Gauss is due to an artefact.

Let us now consider the effect of irradiation. Important is that no change is observed in the signal due to  $\text{Eu}^{2+}$ . But an extra resonance appears around 3325 Gauss corresponding with  $g \approx 2$ . The extra signal is strongest at the lowest dopant concentrations and smallest for the sample with  $x = 0.002$ , being the one with the largest TL signal. In figure 8.13 it is depicted in more detail. First of all, the signal shows no hyperfine structure although splittings smaller than some 10 Gauss can not be resolved. Secondly the structure of the signal indicates anisotropy at the defect site.

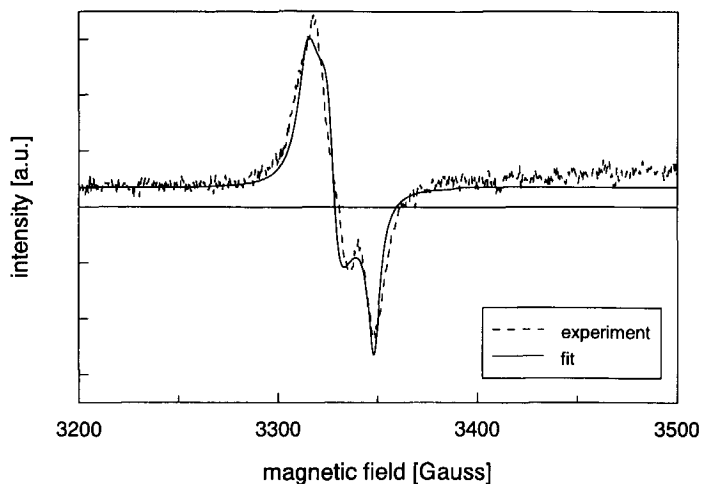


**Figure 8.13:** Detailed picture of the radiation induced EPR signal. See caption figure 8.12 for experimental conditions. Also shown is a fit of the measurement curve based on Lorentzian functions to obtain the  $g$ -values (see text).

A fit based on Lorentzian functions is also shown in the figure. This fit yields the values  $g_1 = 2.021(2)$ ,  $g_2 = 2.013(2)$ , and  $g_3 = 2.001(2)$  with the error in the last digit indicated between brackets. The widths at half height are respectively 7, 6, and 4 Gauss. The labels 1,2,3 are used instead of  $x,y,z$  because the orientation of the defect with respect to the magnetic field is unknown. Because of the predominantly positive  $g$ -shift the signal is attributed to a trapped hole.

Based on these measurements, carried out with powder samples, an unequivocal identification of the trap is impossible. But the lack of hyperfine interaction with its surroundings, and its anisotropy are typical for localised oxygen type centres [261]. The sequence  $g_x, g_y > g_e, g_z \leq g_e$  is particularly found for  $O^-$  centres (an 'isolated' oxygen that has trapped a hole) [261]. Considering the structure of  $Sr_2B_5O_9Br$  (figure 1) all oxygens are part of  $BO_3$  triangles or  $BO_4$  tetrahedra [238]. These oxygens are strongly bound to boron. Therefore trapped holes on these centres would result in hyperfine structure due to interaction with the  $^{11}B$  ( $I = 3/2$ ) isotope. It is possible that it is masked by the total linewidth since the four-line hyperfine structure can take up less than 40 Gauss in borates and boracites [262, 263]. In the other case, lack of hyperfine structure can only be expected when the  $O^{2-}$  is located on a  $Br^-$  site where the hole can be locally trapped. Both suppositions are in agreement with the observation that the defect concentration is highest at low dopant concentrations (figure 8.12) which suggests that the hole trap is not connected with the Eu dopants but with the host lattice (including its impurities). Lowering the temperature to 120 K yields no additional EPR signals. The decrease of the EPR intensity between  $x = 0.0005$  and  $x = 0.002$  must imply that the presence of Eu ions introduces a competing destination channel for the free holes, which could be the capture by a new type of hole

trap.

In figure 8.14 the relative intensity of EPR signal around  $g = 2$  is depicted for  $\text{Sr}_{2(1-x)}\text{Eu}_{2x}\text{B}_5\text{O}_9\text{Br}$  ( $x = 0.001$ ), as a function of the number of TL peaks that is thermally cleaned prior to the measurement. On the x-axis the peak numbers are indicated, which correspond with the numbers given in figure 8.6. When peak 1 of the TL spectrum is cleaned, the EPR signal vanishes only partly. The shape of the signal and the  $g$  values show no change. Removing the second TL peak has no impact on the EPR. The signal vanishes almost entirely when peak 3 is cleaned. Hence the EPR signal must be connected with peak 3, which thus represents a hole trap. Since part of the EPR vanishes when cleaning peak 1 it can be concluded that peak 1 is connected with the release of electrons. Part of these electrons recombines with the trapped holes responsible for the EPR signal.

### 8.3.6 Photon yield of X-ray induced scintillation and thermoluminescence

From the integral of a TL glow curve the total number of TL photons emitted per unit of energy absorbed in the sample has been determined. This provides information about the number of charge carriers trapped. Before integrating the glow curve, a correction was made for the quenching of the  $\text{Eu}^{2+}$  luminescence at higher temperatures which was already observed for the alkaline chloroborates [127]. This occurred as follows. For  $\text{Sr}_{2(1-x)}\text{Eu}_{2x}\text{B}_5\text{O}_9\text{Br}$  ( $x = 0.001$ ) glow curves were measured for a fixed dose at a varying heating rates. The higher this rate, the more the position of the TL peak maxima,  $T_m$ , shift to higher temperatures [264]. By plotting

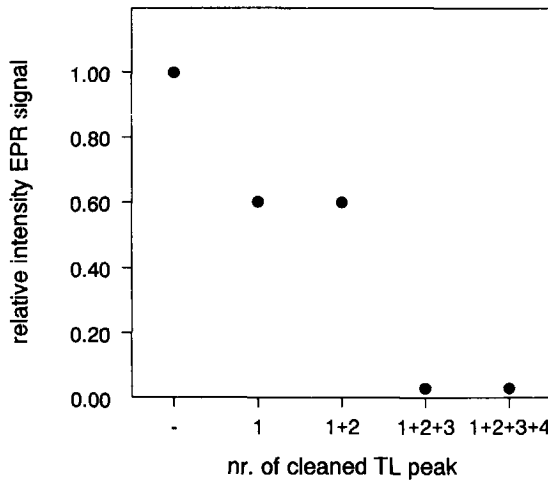


**Figure 8.14:** Relative intensity of the radiation induced EPR signal, measured as a function of the number of TL peaks that is thermally cleaned prior to EPR. The TL peak numbers indicated on the x-axis correspond with the numbers indicated in figure 6.

the content of each peak as a function of  $T_m$  a good impression is obtained of the luminescence quenching over the whole temperature range which can be used for correction. It appears that the quantum efficiency at  $T = 480$  K is 50% of the value below 350 K, which is close to the result for  $\text{Sr}_2\text{B}_5\text{O}_9\text{Cl:Eu}$  [127]. The inset of figure 8.15 shows a typical TL glow curve, before and after correction.

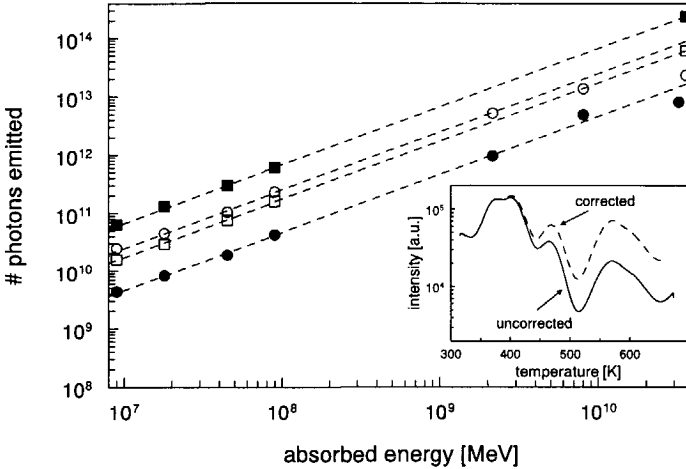


**Figure 8.15:** Total number of photons emitted by TL (circles) and scintillation (squares) as a function of the X-ray energy absorbed in 4 mg samples of  $\text{Sr}_2(1-x)\text{Eu}_x\text{B}_5\text{O}_9\text{Br}$ . Open squares/circles:  $x = 0.001$ . Closed:  $x = 0.01$ . Broken lines:  $y = a \cdot x$  type fits of the points below  $10^{10}$  MeV. Inset: TL curve before (solid line) and after the correction for the temperature quenching.

For two  $\text{Sr}_2(1-x)\text{Eu}_x\text{B}_5\text{O}_9\text{Br}$  samples ( $x = 0.001$  and  $x = 0.01$ ) the corrected and integrated TL signal was measured as a function of the X-ray irradiation time. The result is shown in figure 8.15. Also plotted is the total number of photons that is emitted due to scintillation during the irradiation, measured as described in section 5.2.2. The results are fitted with a  $y = a \cdot x$  function. The points belonging to the longest irradiation times are omitted in the fitting process. The coefficients  $a$  represent the number of photons emitted in scintillation (SL) or during thermal stimulation per MeV of absorbed energy and are presented in table 8.1 as  $N_{SL}$  and  $N_{TL}$  respectively.

From figure 8.15 and table 8.1 is concluded:

- (1) Up to energies of  $10^9$  MeV the integral TL and SL are proportional to the amount of energy absorbed.
- (2) For TL a saturation effect becomes visible above  $2 \cdot 10^9$  MeV of absorbed energy for  $x = 0.001$  and above  $8 \cdot 10^9$  MeV for  $x = 0.01$ . The SL retains its proportionality.

**Table 8.1:** The total number of photons emitted spontaneously,  $N_{SL}$ , and after thermal stimulation,  $N_{TL}$ , per MeV of absorbed energy in  $\text{Sr}_{2(1-x)}\text{Eu}_{2x}\text{B}_5\text{O}_9\text{Br}$  with  $x = 0.01$  (series A) and 0.001 (series B).

	$N_{SL} [\text{MeV}^{-1}]$	$N_{TL} [\text{MeV}^{-1}]$
$x = 0.001$	$1.7 \cdot 10^3$	$2.5 \cdot 10^3$
$x = 0.01$	$6.7 \cdot 10^3$	$0.5 \cdot 10^3$

(3) From the saturation level the minimal number of thermally stimuable traps available per mole of sample material can be determined. Taking the asymptotic value of  $4 \cdot 10^{13}$  photons emitted during TL by 4 mg of  $\text{Sr}_{2(1-x)}\text{Eu}_{2x}\text{B}_5\text{O}_9\text{Br}$  (see figure 8.15, for  $x = 0.001$ ), the number of available traps amounts to  $4.5 \cdot 10^{18}$  per mole  $\text{Sr}_2\text{B}_5\text{O}_9\text{Br}$  or 1 per 250 Eu activator ions. Upon illumination with 254 nm light the saturation level of the trap filling is studied as well. It appears that the maximal TL response amounts to 20% of that from a sample saturated under X-ray irradiation.

(4) In wide bandgap materials roughly one electron-hole pair is created per  $2.5 \cdot E_g$  of energy absorbed, with  $E_g$  the energy of the forbidden gap [265]. Hence, the bandgap being about 8 eV (figure 8.3), roughly 50,000 electron-hole pairs are created per MeV. Table 8.1 shows that  $N_{SL}$  and  $N_{TL}$  amount typically to several thousands of photons per MeV. Apparently, about 90% of the electrons and holes eventually recombine nonradiatively. Hence,

$$N_{NR} \gg N_{SL}, N_{TL}. \quad (8.3)$$

where  $N_{NR}$  is the number of nonradiatively recombining electron-hole pairs.

The dependence of the photon yields  $N_{SL}$  and  $N_{TL}$  on the dopant concentration  $x$  is given in figure 8.10.  $N_{SL}$  (curve (c)) increases with  $x$  and reaches a maximum around  $x = 0.005$ . Also given in figure 8.10 is the photoluminescence intensity (PL) at  $\lambda_{ex} = 350$  nm, at which the  $\text{Eu}^{2+}$  ions are directly excited (curve (d)). It shows that the  $N_{SL}$  depends similarly on  $x$  as the PL signal.

The increase of the PL signal with  $x$  can be attributed to the increasing probability that a photon incident on the powder sample is absorbed by a  $\text{Eu}^{2+}$  ion. The increase of the SL signal with  $x$  can be attributed to the increasing probability that the free carriers created are trapped by a  $\text{Eu}^{2+}$  ion (followed by radiative recombination).

The same probability will play a role in the dependence of  $N_{TL}$  on  $x$  (see curve (b)) since recombination on  $\text{Eu}^{2+}$  is also the last stage of TL. But apparently another more dominant but unknown mechanism determines that  $N_{TL}$  decreases at  $x > 0.002$ . Prompt recombination and trapping of free charge carriers are competing processes. Therefore one could suppose that there exists an anti-correlation between  $N_{SL}$  and  $N_{TL}$  at  $x > 0.002$ : more electron-hole pairs recombining promptly means that less get trapped and thus  $N_{TL}$  decreases.

However, this supposition is inconsistent with (8.3). According to this inequality the number of electrons and holes that gets trapped is almost independent of the number that recombines

promptly. The supposition is also inconsistent with the observation that  $N_{SL}$  does not change when saturation of the TL signal occurs (see item (2)).

### 8.3.7 Time dependence of the recombination luminescence

In this section the time dependence of thermally and optically stimulated luminescence after irradiation is discussed, providing information on the mechanism of recombination. The thermal stimulation experiments were carried out as follows. First a  $\text{Sr}_2\text{B}_5\text{O}_9\text{Br}:\text{Eu}^{2+}$  sample was illuminated with UV light. Next, the sample was heated to a specific temperature and kept at this temperature for 400 s during which the decay of the isothermal luminescence intensity was recorded. After this, a TL glow curve was measured to study the effect of the heating treatment. Isothermal luminescence was recorded at temperatures between 305 and 411 K, comprising the temperature range of the first two TL peaks (see figure 8.6).

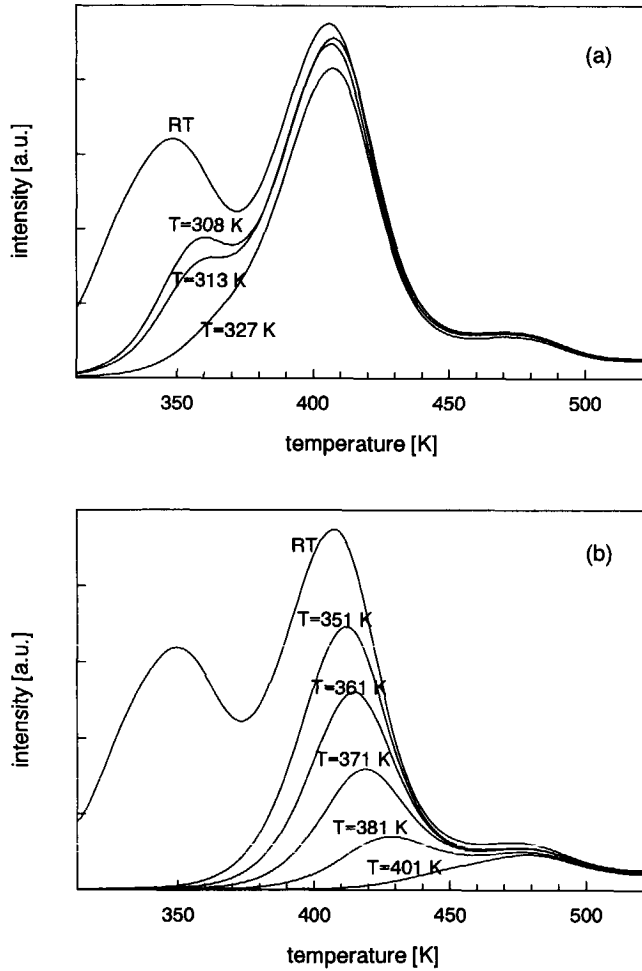
The results are depicted in the figures 8.16 and 8.17. Figure 8.16(a) shows the glow curves recorded after a low temperature heating treatment, at temperatures lower than 350 K. The treatment has mainly cleaned peak 1. Figure 8.16(b) shows the glow curves recorded after a relatively high temperature heating treatment. Here isothermal luminescence was accompanied with the cleaning of peak 2. In both (a) and (b) is observed that when peak 1 or 2 is partly cleaned, its maximum shifts to higher temperature. Similar shifts, although less pronounced, can be observed after the optical bleaching experiments shown in figure 8.8. They could be a manifestation of second-order (or higher) kinetics in the recombination. When the recombination mechanism follows higher than first-order kinetics the maximum  $T_m$  of a TL peak is a function of the number of initially filled traps [266]. To check this possibility, the TL glow curve as a function of the dose, that is, the number of initially filled traps has been measured. Over at least three orders of magnitude (starting from a minimal detectable dose) *no* shift in  $T_m$  occurs and moreover no change in the glow curve shape at all. A  $T_m$  that is independent of dose applies only for first-order kinetics [266]. In addition, peak 2 becomes more asymmetrical when further cleaned (figure 8.16(b)). First-order kinetics gives rise to asymmetrical TL peaks [266].

Figure 8.17 shows the isothermal luminescence decay curves recorded at the different temperatures. They are plotted as the reciprocal intensity  $I^{-1}$  versus  $t$  (after the normalisation  $I(0) = 1$ ). Up to 313 K  $I^{-1}(t)$  shows a perfectly linear behaviour, at higher temperatures it is supralinear. At the initial stage of the  $T = 361$  K curve the fast cleaning of peak 1 can be observed, followed by the slower cleaning of peak 2. The same initial effect is visible at  $T = 371$  K.

According to a fit procedure  $I(t)$  can be well-described with Becquerel's empirical decay law:

$$I(t) = \frac{1}{1 + at^p} \quad (8.4)$$

with parameters  $a$  and  $p$ . The initial part of the curves with  $T = 361, 371$  and  $381$  K was omitted in the fitting procedure. The parameter  $a$  depends on experimental conditions like radiation dose



**Figure 8.16:** TL glow curves of  $\text{Sr}_{2(1-x)}\text{Eu}_{2x}\text{B}_5\text{O}_9\text{Br}$  ( $x = 0.002$ ) recorded after illumination of the sample with 254 nm light and a heating period of 400 s at a constant temperature  $T$ .  $T$  is indicated for every curve. (a): low  $T$  heating, cleaning the peak at 350 K. (b): higher  $T$  heating, cleaning the peak at 405 K. For comparison the glow curve of a sample that has not been heated (RT) is also given.

and temperature and is not considered here. The results for the fit parameters  $p$  are given in table 8.2.

When cleaning peak 1,  $p$  becomes slightly higher than 1 with increasing temperature and reaches a maximum at  $T = 327$  keV. In case of peak 2 this effect is much stronger. A maximum



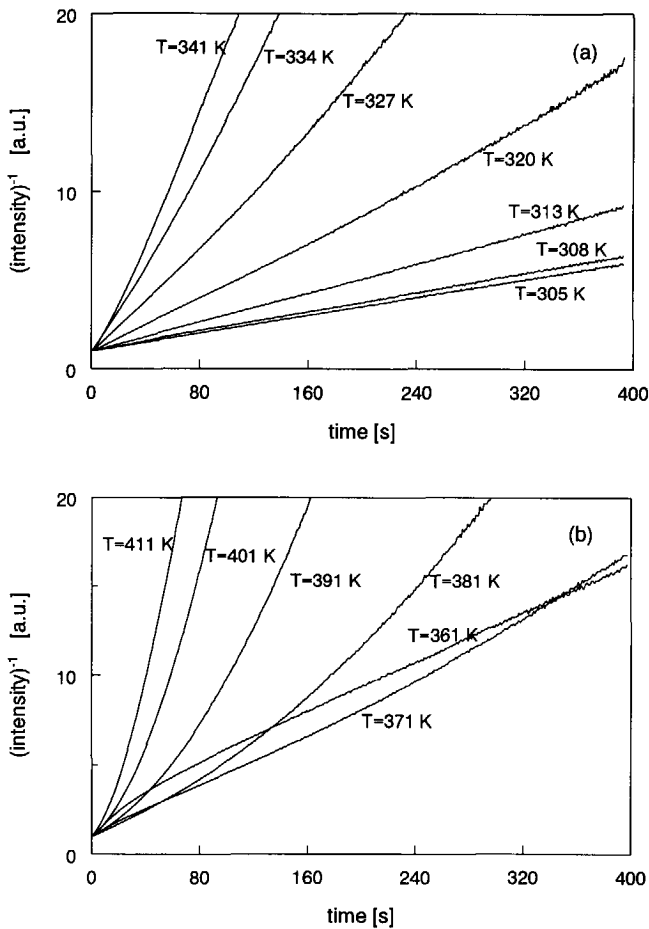


**Figure 8.17:** Isothermal luminescence of  $\text{Sr}_{2(1-x)}\text{Eu}_{2x}\text{B}_5\text{O}_9\text{Br}$  ( $x = 0.002$ ) recorded as a function of time at different temperatures  $T$  after illumination of the sample with 254 nm light.

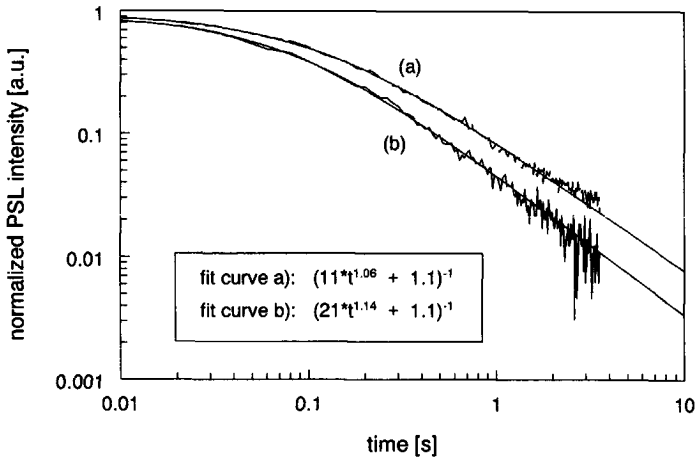
of 1.69 is found at  $T = 391$  K after which  $p$  decreases again.

Figure 8.18 shows the  $\text{Eu}^{2+}$  luminescence decay curve of an irradiated  $\text{Sr}_2\text{B}_5\text{O}_9\text{Br}:\text{Eu}^{2+}$  sample under continuous optical stimulation with a HeNe laser. Curve (a) shows the result for an X-ray irradiated sample. According to the curve fit to the decay shows a Becquerel type behaviour with the power  $p \approx 1$ .

The penetration of the X-rays in the pressed pill is such that stimulated luminescence can also originate from pill layers deep below surface where the laser intensity is weak. Contributions from these layers could affect the time dependence of the luminescence and thus cause

**Table 8.2:** The results for the fitting parameter  $p$  of the function  $1/(1 + at^p)$  used to fit the decay curves depicted in figure 8.15.

peak 1	$p$	peak 2	$p$
T=305 K	1.00	T=361 K	1.03
T=308 K	0.98	T=371 K	1.30
T=313 K	1.01	T=381 K	1.56
T=320 K	1.07	T=391 K	1.69
T=327 K	1.14	T=401 K	1.59
T=334 K	1.15	T=411 K	1.50
T=341 K	1.14		



**Figure 8.18:** Photostimulated luminescence intensity as a function of time recorded at  $\lambda_{em} = 430$  nm upon continuous stimulation with a HeNe laser. Curve (a): after irradiation with X-rays. Curve (b): after irradiation with alpha particles. The intensities are normalised to 1 at  $t = 0$ .

an experimental artefact. One does not encounter this problem when the sample is irradiated with alpha particles. These have a penetration depth of only several  $\mu\text{m}$ . In such a thin layer the laser intensity can be assumed to be homogeneous. Therefore also the optically stimulated luminescence of a sample irradiated with 4.17 MeV alpha particles was recorded, see curve (b). It appears that curves (a) and (b) do not differ essentially. The difference in  $p$  for curve (a) and (b) can be ascribed to experimental errors.

## 8.4 Discussion

### 8.4.1 Role of the $\text{Eu}^{2+}$ and $\text{Eu}^{3+}$ ions

The TL emission measurements demonstrate that the  $\text{Eu}^{2+}$  ions are the main recombination centres. There are also indications that  $\text{Eu}^{2+}$  or  $\text{Eu}^{3+}$  ions do trap charge carriers themselves, or introduce stable charge traps in their vicinity. A first indication is that the EPR measurements show a dependence of the distribution of charge traps on the Eu dopant concentration  $x$ . Secondly, it was shown that upon UV illumination traps can be filled (figure 8.9). The UV photon energy is definitely not sufficient to cause a band-to-band transition and thus create a free electron and hole. From figure 8.10 (comparison of curve (a) and (b), see section 8.3.4) it was concluded that it is probable that the UV photons are first absorbed by  $\text{Eu}^{2+}$  or  $\text{Eu}^{3+}$ , somehow followed by separation of electron from hole.

Only one charge carrier type (electron or hole) can become delocalised after absorption of a UV photon. Hence, if the UV photons are first absorbed by  $\text{Eu}^{2+}$  or  $\text{Eu}^{3+}$ , it follows that the other charge carrier type *must* be trapped in the direct vicinity of the  $\text{Eu}^{2+}$  or  $\text{Eu}^{3+}$  ion or on the ion itself.

The question remains, how the absorption of the UV photon by the Eu ion can give rise to the electron-hole separation and charge trapping. Two simple models are discussed.

#### *Model 1: Ionisation of $\text{Eu}^{2+}$*

This model was already briefly discussed in section 8.3.4. The 5d electron can escape from the UV-excited  $\text{Eu}^{2+}$  ion. This is imaginable if the higher excited states are located very close to, or even in the conduction band. In the literature the existence of this mechanism has been reported in various compounds. Aguirre de Cárcer *et al.* [268] show that in  $\text{Eu}^{2+}$  doped NaCl, KCl, KBr and KI photoconductivity excitation spectrum overlaps the high energy side of the  $\text{Eu}^{2+}$  excitation spectrum. According to them it is improbable that  $\text{Eu}^{3+}$  (CT) plays a role since its luminescence is very weak after high dose irradiation. Coincidence with the photoconductivity spectra has also been observed by Fuller *et al.* [269] and Pedrini *et al.* [270] for  $\text{SrF}_2:\text{Eu}^{2+}, \text{Sm}^{3+}$  and  $\text{CaF}_2:\text{Eu}^{2+}$ . In  $\text{SrF}_2:\text{Eu}^{2+}, \text{Sm}^{3+}$  more intense  $\text{Eu}^{3+}$  luminescence has been detected after UV illumination. A decrease of the  $\text{Eu}^{2+}$  EPR signal has been reported by Title *et al.* [271] after blue light illumination of  $\text{SrS}:\text{Eu}, \text{Sm}$ .

The location of  $\text{Eu}^{2+}$  excited states in or close to the conduction band is inconsistent with the low position of the  $\text{Eu}^{2+}$  ground state according to the theoretical calculations. This problem could be solved by supposing that the electron does not escape via the conduction band but via tunnelling.

In either case the model predicts that due to storage of charge,

- (1) the  $\text{Eu}^{2+}$  concentration decreases and the  $\text{Eu}^{3+}$  increases.
- (2) Under X-ray/gamma ray irradiation holes are trapped by  $\text{Eu}^{2+}$  ions (since the TL spectra are similar after UV or X-ray/gamma irradiation).
- (3) All TL peaks are due to the release of electrons from the traps and recombination with  $\text{Eu}^{3+}$

ions.

Figure 8.11 shows that prediction (1) is not observed experimentally. The question is however, whether the concentration changes should have been observed. If the concentration of  $\text{Eu}^{3+}$  ions relative to that of  $\text{Eu}^{2+}$  ions were known, the relative increase of  $\text{Eu}^{3+}$  luminescence could be predicted by the relative decrease of  $\text{Eu}^{2+}$  luminescence.

The  $[\text{Eu}^{3+}]/[\text{Eu}^{2+}]$  ratio in the samples can be estimated from figure 11 as follows. At 395 nm, both  $\text{Eu}^{2+}$  and  $\text{Eu}^{3+}$  excitation is possible (figure 8.2 + figure 8.4). Excitation of  $\text{Eu}^{2+}$  by the dipole allowed transitions and  $\text{Eu}^{3+}$  excitation by the  ${}^7\text{F}_0 \rightarrow {}^5\text{D}_2$  transition.

The latter is a forced dipole allowed transition (see section 8.3.1). According to figure 8.4 its effective oscillation strength is about 10 times higher than the magnetic dipole allowed  ${}^7\text{F}_0 \rightarrow {}^5\text{D}_1$  transition. From a magnetic dipole allowed transition it is known that its oscillation strength is typically  $10^{-5}$  times that of a pure electric dipole transition [116]. Using this it follows that the ratio between the oscillation strengths of the dipole allowed  $\text{Eu}^{2+}$  transition and the forced dipole allowed  $\text{Eu}^{3+}$  transition at 395 nm is roughly  $1:10^{-4}$ . This is the same ratio as found for the  $\text{Eu}^{2+}$  and  $\text{Eu}^{3+}$  emission intensity at  $\lambda_{\text{ex}} = 395$  nm (figure 8.11). Hence, the  $\text{Eu}^{2+}$  and  $\text{Eu}^{3+}$  concentrations in the samples can be of the same order of magnitude. It is noted that Sun *et al.* found an  $[\text{Eu}^{2+}]/[\text{Eu}^{3+}]$  ratio of  $\approx 1$  for  $\text{BaFBr}:\text{Eu}^{2+}$  that was prepared in a  $\text{N}_2/10\%\text{H}_2$  atmosphere [272].

From the experimental results of figure 8.15 followed that the  $\text{Sr}_{2(1-x)}\text{Eu}_{2x}\text{B}_5\text{O}_9\text{Br}$  ( $x = 0.001$ ) sample receiving a saturating dose of 500 Gy yields 1 thermally stimulated photon per 250 Eu dopant ions. So at least 1 electron-hole pair was trapped per 250 Eu dopant ions. If  $\text{Eu}^{2+}$  is the main hole trap minimal 1 on 250 Eu ions has been converted from the divalent into the trivalent state. Such a change in  $[\text{Eu}^{2+}]$  can not be detected in the experiment of figure 8.11. If  $[\text{Eu}^{2+}]/[\text{Eu}^{3+}] \approx 1$  the change in  $[\text{Eu}^{3+}]$  can not be detected either.

In conclusion, the experiment of figure 8.11 provides no absolute evidence to reject prediction (1) and thus discard the model of ionisation of  $\text{Eu}^{2+}$ . It is shown that the real  $[\text{Eu}^{3+}]$  is easily underestimated. The decrease in both the  $\text{Eu}^{2+}$  and  $\text{Eu}^{3+}$  luminescence intensity observed can be explained with the appearance of the absorption band around 375 nm depicted in figure 8.5. The 395 nm photons meant to excite the  $\text{Eu}^{2+}/\text{Eu}^{3+}$  ions can be absorbed elsewhere after irradiation. Similarly there is no experimental evidence for prediction (2). However, in the literature no convincing report can be found for  $\text{Eu}^{2+}$  activator ions capturing free holes in alkaline earth compounds. Takahashi [100] reports an increase of the  $\text{Eu}^{3+}$  luminescence combined with decrease of the  $\text{Eu}^{2+}$  luminescence in  $\text{BaFBr}:\text{Eu}^{2+}$  after intense radiation with 3.7 eV photons and extrapolates this to the situation of irradiation with X-rays. However, Hangleiter *et al.* [101] and Koschnick *et al.* [273] identified other hole traps after X-ray irradiation of  $\text{BaFBr}:\text{Eu}^{2+}$ , while no change was observed in the EPR signal of  $\text{Eu}^{2+}$ . This indicates that  $\text{Eu}^{2+}$  is at least not the prominent hole centre. Other authors have also tried to observe formation of  $\text{Eu}^{3+}$  centres in alkaline earth compounds under X-ray irradiation, with negative result [105].

Finally prediction (3) is considered. From the EPR experiments (figure 8.13) follows that at least one of the TL peaks corresponds with a hole trap. This is in disagreement with the model of

$\text{Eu}^{2+} \rightarrow \text{Eu}^{3+}$  conversion.

In conclusion, model 1 can not be excluded as an explanation, but it can not be the only mechanism being active.

*Model 2: CT between  $\text{Eu}^{3+}$  and its ligands*

Considering figure 8.9 it is tempting to identify the TL excitation band around 225 nm as the  $\text{Eu}^{3+}$  CT band and attribute the shift of the maximum to an experimental problem. This model is considered more plausible than model 1.

The possibility of charge trapping upon UV induced CT is not well-known. However, the literature provides some striking examples and shows also that  $\text{Eu}^{3+}$  can function as an electron trap under X-ray/gamma irradiation. Vrabel *et al.* [274] have demonstrated the increase of the  $\text{Eu}^{2+}$  EPR signal in  $\text{CdF}_2:\text{Eu}^{2+}$  after UV illumination and Catlow *et al.* [275] have observed an increase of the  $\text{Eu}^{2+}$  luminescence after X-ray irradiation. Dhopte *et al.* have observed a combined increase of the  $\text{Eu}^{2+}$  luminescence and decrease of the  $\text{Eu}^{3+}$  luminescence intensity due to gamma irradiation in both  $\text{CaSO}_4:\text{Eu}^{2+}$  [276] and  $\text{CaF}_2:\text{Eu}^{2+}$  [277]. Especially interesting is a paper of Forest *et al.* [278] on  $\text{La}_2\text{O}_2\text{S}:\text{Eu}^{3+}$ . Their TL excitation spectrum does not only show overlap with the  $\text{Eu}^{3+}$  CT band but even some of the narrow lines corresponding with the  $4f^6$  interconfigurational transitions are visible. This nicely demonstrates the excited  $\text{Eu}^{3+}$  ion as a precursor for storage. It also proves that storage is even possible when  $\text{Eu}^{3+}$  is in an excited state with a very local character. According to the authors transfer to the CT state is possible with help of phonons.

The appearance of the narrow lines in the TL excitation spectrum has also been checked for  $\text{Sr}_2\text{B}_5\text{O}_9\text{Br}:\text{Eu}^{2+}$ , in particular for the intense  ${}^7\text{F}_0 \rightarrow {}^5\text{D}_4$  line at 395 nm. No TL signal was detected. This is not surprising since the CT band in  $\text{Sr}_2\text{B}_5\text{O}_9\text{Br}:\text{Eu}^{2+}$  is located at substantially higher photon energies than in  $\text{La}_2\text{O}_2\text{S}:\text{Eu}^{3+}$  (5.5 eV versus 3.5 eV) which makes transfer from the  $\text{Eu}^{3+}$  excited state to the CT state less probable.

For understanding the step between the CT state and the storage of charge, the CT state itself should be considered. The electron that was transferred from the ligand, resides in the vicinity of  $\text{Eu}^{3+}$ . However, it is not on a 4f orbital since it is supposed that there exists a considerable Frank-Condon shift between the CT state and the 4f states [279]. A transition from the CT state to an excited state of  $\text{Eu}^{3+}$  is possible, giving rise to the  $\text{Eu}^{3+}$  luminescence. But like already proposed by others [278,280], one can imagine that there is a second channel of relaxation. The hole moves away and gets trapped elsewhere. It should be realised that a  $\text{Eu}^{3+}$  ion on a  $\text{Sr}^{2+}$  site requires charge compensation. The charge compensator might simultaneously function as a hole trap. The removal of the hole is followed by self-trapping of the electron close to, or even on  $\text{Eu}^{3+}$ . The probability of this process to occur relative to the other, should increase with temperature in the range 200-300 K (figure 8.9).

The question rises how optically or thermally stimulated recombination can result in  $\text{Eu}^{2+}$  luminescence. More should be known about the trapping centres and about the recombination mechanism.

### 8.4.2 Nature of the traps

The TL measurements show that at least 4 different trap species are involved in the PSL process (figure 8.6 + figure 8.8), but optical/EPR measurements provide insufficient information to identify them. Because the defects connected with TL peaks 1 and 2 are 'silent' in the EPR measurements (a) they are not paramagnetic or (b) the relaxation time from the upper Zeeman level is too short or (c) a complex of hyperfine interactions broaden the signal to a large extent.

Item (b) and/or (c) can be responsible for the lack of an EPR signal from  $\text{F}(\text{Br}^-)$  centres. Measuring down to 4 K combined with an increase of the microwave power could perhaps reveal them. Schipper *et al.* [258] report the same negative result for  $\text{Ba}_5\text{SiO}_4\text{Br}_6$  and  $\text{Ba}_5\text{SiO}_4\text{Br}_6:\text{Eu}^{2+}$  where according to optical measurements  $\text{F}(\text{Br}^-)$  centres should be present. The oscillation strength of the 1s-2p transition is known to be high. Still, the absorption band which is expected in the red region of the stimulation spectrum (figure 8.2) and the reflection spectrum is overshadowed by the absorption band around 375 nm which indicates that the concentration of defects responsible for the latter is considerably larger.

The radiation induced EPR signal in  $\text{Sr}_{2(1-x)}\text{Eu}_{2x}\text{B}_5\text{O}_9\text{Br}$  is ascribed to an oxygen centre, probably an  $\text{O}^-$  ion (an  $\text{O}^{2-}$  ion which has trapped a hole) on a  $\text{Br}^-$  vacancy. The EPR signal is lowest for  $x = 0.002$ , at which the TL signal is highest. This indicates that at  $x = 0.002$  the competition of another hole trap not giving an EPR signal is highest. The  $\text{O}^{2-}$  ion is a logical charge compensator for the  $\text{Eu}^{3+}$  ions and thus one would expect an increase of these hole traps with an increasing  $\text{Eu}^{2+}/\text{Eu}^{3+}$  concentration. This is in disagreement with the EPR measurements.

### 8.4.3 Recombination

As mentioned, the TL measurements show signatures of a first-order recombination mechanism. Two models can give rise to first-order kinetics. In the first, the liberated electron (or hole) arrives in a non-localised state of the conduction band (valence band) and recombination must be far more probable than retrapping [266]. In the second, there are only pairs of spatially correlated electron and hole traps. Recombination occurs via tunnelling and thus is a local process [266, 267].

Suppose that there is only one trap type with depth or activation energy  $E$ . Then first-order recombination gives rise to an exponential isothermal decay curve. This is in disagreement with the Becquerel type decay curves of figure 8.17. Hence, they must be the result of a more complicated mechanism. It is not tried to derive a model to explain these functions exactly because sophistication of the model will always yield the desired result. However, two relatively simple models should be mentioned which are reported in literature and use first-order kinetics as a starting point.

Randall and Wilkins [281] have extended the first-order kinetics model by considering a distribution of traps  $N(E)$  where  $E$  is the activation energy. Then  $I(t)$  is obtained by integrating over the exponential decay function connected with the group of traps with activation energy

between  $E$  and  $E + dE$ :

$$I(t) \propto \int_0^{\infty} N(E) \exp[-E/kt] \exp[-se^{-E/kt}t] dE \quad (8.5)$$

where  $s$  is the so-called frequency factor. It is shown that if  $N(E)=\text{constant}$  (uniform distribution function) a decay like in (8.4) with  $p = 1$  is obtained and if  $N(E) \propto \exp[-\alpha E]$  then  $p = 1 + \alpha kT$  with  $\alpha$  a constant and thus  $p$  becomes temperature dependent.

Another extension to simple first-order kinetics has been proposed by Avouris *et al.* [282]. They assumed tunnelling recombination within electron and hole trap pairs and not  $E$  was taken as a distribution variable but instead the tunnelling distance  $R$ , which determines the recombination rate  $W(R)$ . Then  $I(t)$  is obtained by integrating over the exponential decay function connected with the group of pairs with tunnelling distance between  $R$  and  $R + dR$ :

$$I(t) \propto \int_0^{\infty} N(R)W(R) \exp[-W \cdot t] dR \quad (8.6)$$

with  $N(R)$  the distribution of trap pairs. When for  $W(R)$  is taken

$$W(R) = W_0 \exp[-2R/a] \quad (8.7)$$

with  $a$  the effective radius of the overlap of the wave functions of begin and end state and a uniform distribution  $N(R)$ , again a  $t^{-1}$  decay is obtained.

The TL glow curves (figure 8.6) show that the peak maxima vary from sample to sample (also at very low heating rates). For individual samples it was observed that the maxima shift upon optical bleaching whereas they are independent of the dose. These are indications that one peak consists of traps with slightly different trap depths  $E$  or recombination rates  $W(R)$ . A model of this kind is a good approach of what takes place in  $\text{Sr}_2\text{B}_5\text{O}_9\text{Br}:\text{Eu}^{2+}$ . The dependence of the power  $p$  on  $T$  (table 8.1) that applies for TL peak 2 shows that the reality is probably even more complicated.

## 8.5 Summary and Outlook

The mechanism of trap filling and recombination and the nature of the traps have been studied in a collection of samples with the formula  $\text{Sr}_{2(1-x)}\text{Eu}_{2x}\text{B}_5\text{O}_9\text{Br}$ . Although most samples were prepared in a reducing atmosphere not only  $\text{Eu}^{2+}$  but also weak  $\text{Eu}^{3+}$  luminescence was detected. The position of the  $\text{Eu}^{2+}$  ground state was calculated with respect to the conduction band. The result shows that direct photoionisation with 5 eV photons is improbable. The  $\text{Eu}^{3+}$  excitation spectrum comprises a charge transfer (CT) band in the UV range.

Next to the possibility of direct (non-)radiative recombination of free charge carriers created during irradiation, the samples are rather efficient in storing them in stable traps. About 10% of the free charge carriers created contributes to luminescence via scintillation (SL) or TL. Per MeV of absorbed radiation this corresponds with several thousands of photons emitted, both for TL and SL, dependent on the dopant concentration  $x$  (see table 8.1).

Recombination luminescence is observed under optical or thermal stimulation. In both cases only  $\text{Eu}^{2+}$  luminescence is detected. The photostimulation spectrum shows a structureless band between 500 and 800 nm. According to reflection measurements a broad radiation induced absorption band at 375 nm and a smaller band around 660 nm contribute to the photostimulation spectrum. The defects responsible for the former are unknown, the latter is thought to be due to  $\text{F}(\text{Br}^-)$  centres.

Almost all samples show four distinguishable peaks in the TL glow curve recorded after irradiation. The three peaks located below 500 K vanish under optical stimulation. The TL intensity is strongly dependent on  $x$  and reaches a maximum at  $x = 0.002$ . By UV illumination the same peaks appear although the first peak is significantly less intense. The TL excitation spectrum shows a band located around 225 nm which almost coincides with the measured  $\text{Eu}^{2+}$  CT band. The TL response recorded after illuminating in this band increases with temperature (between 200-300 K) and it depends also on  $x$ . The dependence on  $x$  differs from that upon gamma irradiation in the sense that there is a stronger positive correlation between the TL signal and  $x$ . This supports the idea that trap filling under UV illumination starts with the electron-hole pair creation at  $\text{Eu}^{2+}$  or  $\text{Eu}^{3+}$ . Since it is impossible that both the electron and hole become decollated after absorption of a UV photon, at least one of them must be trapped at the Eu ion or in its vicinity.

To distinguish between the role of  $\text{Eu}^{2+}$  and  $\text{Eu}^{3+}$  ions and observe a possible conversion from one to the other due to irradiation, the characteristic luminescence intensity of both was measured prior to and after intense gamma ray or UV irradiation. Unexpectedly, both the  $\text{Eu}^{2+}$  and the  $\text{Eu}^{3+}$  luminescence intensity decreased. It was pointed out that, although the  $\text{Eu}^{3+}$  luminescence was 4 orders of magnitude weaker it is possible that  $[\text{Eu}^{3+}]$  is of the same order of magnitude as  $[\text{Eu}^{2+}]$ . Also it was found that heavy irradiation causes one trapped e-h pair on every 250 Eu ions. This explains that it is impossible to observe a relative change of the  $\text{Eu}^{2+}/\text{Eu}^{3+}$  luminescence intensity.

It is considered most plausible that the  $\text{Eu}^{3+}$  ions are essential in the trapping stage under any type of irradiation and in the first stage of electron-hole pair creation under UV illumination in particular. At first because the band in the TL excitation spectrum matches almost the  $\text{Eu}^{3+}$  CT band, which should be combined with the fact that the same traps are filled under UV as under X-ray or gamma irradiation. At second because it is more probable that  $\text{Eu}^{3+}$  can trap free electron in its vicinity (after X-ray/gamma irradiation) than that  $\text{Eu}^{2+}$  traps a free hole.

EPR measurements (between 120-300 K) and a correlation study with TL have shown that one of the TL peaks is due to a trapped hole, probably on an oxygen centre. No change in the  $\text{Eu}^{2+}$  EPR signal was observed after irradiation and also a signal due to  $\text{F}(\text{Br}^-)$  centres is not detected.

The time dependence of recombination luminescence follows a power law of the type  $(1 + at^p)^{-1}$  with the power  $p$  close to 1 (but for one TL peak dependent on  $T$ ). This applies to both thermal and optical stimulation and deviates from the exponential behaviour to be expected for first-order recombination. However, TL glow curves show features of first-order recombination.



It has been pointed out that both observations can be unified by assuming a more complex model where each TL peak reflects a group of traps with slightly varying depth or varying tunnelling distance to the recombination centre.

Finally, it may have become clear that the physics of trapping and recombination in  $\text{Sr}_2\text{B}_5\text{O}_9\text{Br}:\text{Eu}^{2+}$  is complex and not easy to reveal. However, it is thought that, based on the knowledge obtained in this study, still considerable progress can be made with the following experiments:

- Exciting the  $\text{Eu}^{2+}$  and  $\text{Eu}^{3+}$  ions with a flash lamp and monitoring the luminescence decay time as a function of the excitation wavelength. At wavelengths where trap filling is possible (figure 8.9) one might see a quenching of the luminescence.
- EPR measurements down to LHeT which might reveal more trap species.
- Preparation of a set of identical samples with the atmosphere during firing as the only parameter. The atmosphere should vary in several steps between purely oxidising (air) via neutral ( $\text{N}_2$ ) to a purely reducing one (100%  $\text{H}_2$ ). Next the ratio  $[\text{Eu}^{2+}]/[\text{Eu}^{3+}]$  should be determined by means of Mössbauer spectroscopy. When this method is successful in creating samples that are 'only' activated with  $\text{Eu}^{2+}$  or  $\text{Eu}^{3+}$  in the extreme cases it is interesting to compare the TL glow curves and it should be possible to monitor radiation induced valence changes of the activator by means of EPR and optical techniques.
- Preparation of samples with a varying excess/shortage of bromide as well as preparation of undoped samples for comparison of the TL glow curves and EPR signals.

## Summary

There are several reasons to search for better inorganic crystalline scintillator and storage phosphor materials for the detection of thermal neutrons. One is that neutrons are scarce and expensive, necessitating efficient use. High detection efficiencies and, in some cases, the coverage of large solid angles contribute to this efficiency and are directly related to the materials used. Another reason is that the European Spallation Source (ESS) is planned for the future. At this neutron facility more intense neutron beams will be produced which requires higher count rates (pulse pair resolution) of the detectors. Thirdly, at some experiments a very low gamma sensitivity is required, or a very high spatial resolution. These wishes can not always be fulfilled with the scintillator or storage phosphor materials currently available.

In **chapter 2** the current neutron detection technology is reviewed. It is explained that scintillators belong to the class of *counting detectors* which register each neutron capture event individually. The properties of today's most important scintillators,  ${}^6\text{LiF/ZnS:Ag}^+$  and  ${}^6\text{Li}$  loaded silicate glass are compared with each other and with those of other counting systems like gas detectors. The qualities of both scintillators are their low parallax, flexible geometry and their low cost. The spatial and pulse pair resolution, gamma sensitivity and detector background of  ${}^6\text{LiF/ZnS:Ag}^+$  screens are comparable to those of some gas detectors.  ${}^6\text{Li}$  loaded glass scintillators have a higher pulse pair resolution and show high detection efficiencies even for thin layers. The spatial resolution is comparable with that of gas detectors but the number of background and gamma induced counts is higher. No scintillator combines a high light yield ( $>10,000$  photons/neutron, to obtain a high spatial resolution) with a short decay time ( $<100$  ns, to obtain a high pulse pair resolution) and a low intrinsic background.

Storage phosphors are used in image plates (IPs). The thermal neutron IPs currently used consist of a powder mixture of the X-ray storage phosphor  $\text{BaFBr:Eu}^{2+}$  and  $\text{Gd}_2\text{O}_3$  as a neutron absorber. IPs belong to the class of *integrating detectors*. Integrating detectors add up more detection events before giving an output signal. Other important integrating detectors are film based systems and CCD based detectors. Compared to films, IPs have a much higher dynamic range and easy readout. Compared to CCDs they show a higher resolution which is independent of the detector area. The challenges for improvement are the gamma insensitivity and *Detective Quantum Efficiency* (DQE) of the IP although the latter is already higher than of the other systems. The DQE is a quantity that can express the efficiency of detecting neutrons for both

integrating and counting detectors.

Subsequently the requirements for scintillators and IPs are translated into material requirements in **chapter 3**. Scintillator materials worth examining should be selected from the group of Li or B containing compounds. Fast scintillation can be expected from materials doped with one of the rare-earth ions  $\text{Ce}^{3+}$ ,  $\text{Pr}^{3+}$  or  $\text{Nd}^{3+}$ , which should act as the luminescent ion. Even more interesting are materials which combine rare-earth luminescence with core-valence luminescence.

For storage phosphors the selection is restricted to B containing compounds. Most efficient conversion of ionisations into appropriate photostimulable centres can be expected from the small group of haloborates. Doping of the haloborates with one of the cations  $\text{Ce}^{3+}$ ,  $\text{Eu}^{2+}$ ,  $\text{Tl}^{+}$  or  $\text{In}^{+}$  should provide a possibility for fast (photostimulated) luminescence.

In **chapter 4** the scintillation properties of a  $\text{LiBaF}_3$  single crystal are presented. The measurement techniques to characterise a scintillator are explained. The light yield of  $\text{LiBaF}_3$  amounts to 3500 photons per neutron. The energy resolution for the  ${}^6\text{Li}(n,\alpha)$  reaction is about 14%.  $\text{LiBaF}_3$  exhibits core-valence luminescence with a decay time of 0.8 ns and self-trapped-exciton luminescence with a decay time of 6  $\mu\text{s}$ . The former does *not* show up under thermal neutron irradiation, whereas both give a response under gamma irradiation. This offers a unique opportunity for pulse shape discrimination between thermal neutron and gamma-ray induced events. The discrimination method is simple and effective. The gamma sensitivity could be reduced to a value of at most  $5.7 \cdot 10^{-7}$  and probably it is even much lower. Incorporation of  $\text{Ce}^{3+}$  in this lattice is under study.

The scintillation properties of two other Li containing materials,  $\text{LiLnSiO}_4:\text{Ce}^{3+}$  ( $\text{Ln} = \text{Y}, \text{Lu}$ ), are discussed in **chapter 5**. Also the storage properties of these powders are studied and the measurement techniques to characterise a storage phosphor are explained. The light yield of a  $\text{LiYSiO}_4:\text{Ce}^{3+}$  single crystal is estimated at  $1 \cdot 10^4$  photons per MeV of absorbed X-ray energy and the same light yield is expected per neutron absorbed. The gamma-induced scintillation decay curve contains a  $\tau = 38$  ns component. For excitation with alpha particles an additional  $\mu\text{s}$  component is observed.

$\text{LiYSiO}_4:\text{Ce}^{3+}$  is also a rather good storage phosphor. The optical stimulation spectrum shows a broad band with a maximum below 450 nm. The photostimulated luminescence (PSL) yield for 23 keV X-rays is a factor of 15 less than the yield of a commercial  $\text{BaFBr}:\text{Eu}^{2+}$  sample. The PSL yield of the sample after 48 meV neutron irradiation is 0.5 photon per incident neutron. This yield is estimated to increase with a factor of 200 when a 1 mm thick single crystal of  $\text{LiYSiO}_4:\text{Ce}^{3+}$  containing 96% enriched  ${}^6\text{Li}$  would be used instead of a powder layer. An important problem is the high stimulation energy (SE) being a factor of 20 higher than that of the  $\text{BaFBr}:\text{Eu}^{2+}$  sample at 515 nm.

The optical properties of  $\text{Ce}^{3+}$  in  $\text{LiLuSiO}_4$  are very similar. Experiments on the  $\text{LiLuSiO}_4$  doped with  $\text{Ce}^{3+}$ ,  $\text{Tb}^{3+}$  or both, have learned that the PSL yield, the stimulation energy (SE) as well as the scintillation light (SL) yield depend strongly on the presence of rare-earth impuri-

ties and probably also other imperfections in the material. The  $\text{LiLuSiO}_4:\text{Ce}^{3+}$  sample exhibits the highest SL yield of  $3 \cdot 10^4$  pho/MeV whereas its PSL yield is low. On the other hand the  $\text{LiLuSiO}_4:\text{Ce}^{3+}, \text{Tb}^{3+}$  has the high X-ray PSL yield of 0.25 times that of  $\text{BaFBr}:\text{Eu}^{2+}$  whereas its SL yield is low. Future studies on these materials should be aimed at the relation between (co-)dopant concentrations/preparation conditions and the SL and PSL yield. Also the growth of single crystals should be investigated.

The luminescence and scintillation in a group of  $\text{Ce}^{3+}$  activated orthoborates, metaborates, pentaborates, heptaborates and oxyorthoborates is discussed in **chapter 6**. The SL yield of most orthoborates is of the order of  $10^4$  photons per MeV of X-ray energy. Most interesting for further study is the orthoborate  $\text{YAl}_3\text{B}_4\text{O}_{12}:\text{Ce}^{3+}$ , having a short scintillation decay time of 30 ns and a favourable effective atomic number and boron weight fraction.

The SL yield of the other borates is generally lower. And exception is  $\text{LaB}_3\text{O}_6:\text{Ce}^{3+}$  which shows host lattice luminescence being prominent at low  $\text{Ce}^{3+}$  concentrations. None of these samples shows intense thermally stimulated luminescence, that is, an intensity higher than 0.01 times that of  $\text{BaFBr}:\text{Eu}^{2+}$ . Thus the storage properties are not worth a more detailed study. The luminescence in the  $\text{Eu}^{2+}$  activated borates  $\text{CaYOBO}_3$  and  $\text{Ca}_4\text{YO}(\text{BO}_3)_3$  appeared weak or absent.

In the discussion of this chapter the remarkably short wavelength of the  $\text{Ce}^{3+}$  emission materials like  $\text{LaMgB}_5\text{O}_{10}:\text{Ce}^{3+}$  and  $\text{LaB}_3\text{O}_6:\text{Ce}^{3+}$  is considered. A possible relation with the structural data concerning the  $\text{Ce}^{3+}$  site in these hosts is sought, but not found.

The last two chapters deal purely with storage phosphors. In **chapter 7** an alternative thermal neutron IP concept is proposed. The plate should consist of a powder layer of  $\text{M}_2\text{B}_5\text{O}_9\text{X}:\text{Eu}^{2+}$  ( $\text{M}=\text{Ca}, \text{Sr}, \text{Ba}$ ;  $\text{X}=\text{Cl}, \text{Br}$ ) in a binder material. This plate, referred to as IP-B, is compared with the plate concept currently used, referred to as IP-Gd. In particular the DQE of both plates is considered. The theory dictates that the DQE depends on the absorption probability  $A$ , the number of photoelectrons created per incident neutron  $N_{phe}$ , and on the relative variance of  $N_{phe}$ ,  $\nu_{N_{phe}}$ .

The essential difference between a IP-Gd and the IP-B is the variance in the number of photoelectrons  $\nu_{N_{phe}}$ . This difference is directly connected with the difference in the neutron capture reactions. By taking these reactions as a starting point the energy deposition in the two plate types by means of a Monte Carlo simulation was studied. It follows that  $\nu_{N_{phe}}$  for IP-Gd is much larger than in the IP-B. It limits the DQE to a maximum of 35%-40%. The DQE of the IP-B is not limited by  $\nu_{N_{phe}}$ . This implies that for a  $150 \mu\text{m}$  thick IP-B plate with 99% enriched  $^{10}\text{B}$ ,  $N_{phe}$  has to be only 1.3 to obtain a DQE value of 40%, the maximum for the IP-Gd. The theoretical maximum for the DQE of the IP-B is 60% when the thickness is  $150 \mu\text{m}$  and 85% when the thickness is  $300 \mu\text{m}$ , provided a grain filling factor of 0.7.

Values for  $N_{phe}$  have also been determined experimentally for all haloborates. The highest values were found for  $\text{Sr}_2\text{B}_5\text{O}_9\text{Br}:\text{Eu}^{2+}$  and  $\text{Ca}_2\text{B}_5\text{O}_9\text{Br}:\text{Eu}^{2+}$ :  $N_{phe} = 1$  and  $N_{phe} = 0.7$  respectively. These values found should be much higher if 99% enriched  $^{10}\text{B}$  was used. It seems there-

fore that a DQE > 40% can be achieved. In conclusion,  $\text{Sr}_2\text{B}_5\text{O}_9\text{Br}:\text{Eu}^{2+}$  or  $\text{Ca}_2\text{B}_5\text{O}_9\text{Br}:\text{Eu}^{2+}$  have a high potential to replace the  $\text{BaFBr}:\text{Eu}^{2+} \cdot \text{Gd}_2\text{O}_3$  system.

In **chapter 8** one of the haloborates,  $\text{Sr}_2\text{B}_5\text{O}_9\text{Br}:\text{Eu}^{2+}$ , is studied on a more fundamental level. Results of photoluminescence, photostimulated luminescence, thermoluminescence and EPR experiments are presented which provide information about the nature of the charge traps and the recombination mechanisms. In all  $\text{Sr}_2\text{B}_5\text{O}_9\text{Br}:\text{Eu}^{2+}$  samples weak  $\text{Eu}^{3+}$  luminescence is observed, next to the strong  $\text{Eu}^{2+}$  luminescence. Under UV illumination the same traps are filled as under X-ray irradiation. The thermoluminescence excitation spectrum shows a remarkable similarity with the charge transfer band of  $\text{Eu}^{3+}$ . This observation, and others, suggests that the  $\text{Eu}^{3+}$  ions are essential in the trapping stage. It also suggests that under UV illumination the absorption of the photons and the creation of electron-hole pairs, occurring prior to storage, takes place at the  $\text{Eu}^{3+}$  ions.

EPR measurements (between 120-300 K) show a radiation-induced signal which can probably be attributed to an  $\text{O}_{\text{Br}^-}^-$  centre (an  $\text{O}_{\text{Br}^-}^{2-}$  centre having trapped a hole). According to the TL glow curves more trap species should be present. No change in the  $\text{Eu}^{2+}$  EPR signal was observed after irradiation and also a signal due to  $\text{F}(\text{Br}^-)$  centres is not detected.

The isothermal luminescence decay curves (recorded after irradiation) follow a power law of the type  $(1 + at^p)^{-1}$ . The power  $p$  is close to 1 but depends on the temperature. The luminescence decay curve recorded under continuous optical stimulation follows the same law with  $p \approx 1$ . On the other hand, TL glow curves show features of a first-order recombination process. First-order recombination must give rise to an exponential luminescence decay curve. Both observations can be unified by assuming a more complex model where each TL peak reflects a group of traps with slightly varying depth or varying tunneling distance to the recombination centre.

## Bibliography

- [1] A.D. Taylor, *Physica B* **213&214** (1995) 1037.
- [2] M. Sonoda, M. Takano, J. Miyahara, H. Kato, *Radiology* **148** (1983) 833.
- [3] G. Bushnell-Wye, J.L. Finney, J.D. Wicks, *Nucl. Instr. Meth. B* **97** (1995) 557.
- [4] Y. Kudo, S. Kojima, K.-Y. Liu, S. Kawado, T. Ishikawa, K. Hirano, *Rev. Sci. Instrum.* **66**(9) (1995) 4487.
- [5] D. Villers, C. Fougnyes, L. Paternostre, C. Beumier, M. Dosiere, *Nucl. Instr. Meth. B* **97** (1995) 265.
- [6] Ch. Rausch, T. Bücherl, R. Gähler, H. v. Seggern, A. Winnacker, *SPIE* **1737** (1992) 255.
- [7] P.J. Leblans, Agfa-Gevaert Belgium, personal correspondence.
- [8] P. Convert, J.B. Forsyth (eds.), *Position-sensitive Detection of Thermal Neutrons* (Academic Press, London, 1983).
- [9] G.W. Fraser, *Proc. SPIE* **12339** (1995) 287.
- [10] C.R. Rausch, *Detektoren für thermische Neutronen mit hoher Ortsauflösung*, thesis, ch. 2-4, (TU München, 1996).
- [11] R.K. Crawford, *Proc. SPIE* **1737** (1992) 210.
- [12] J. Baruchel, J.L. Hodeau, M.S. Lehmann, J.R. Regnard, C. Schlenker (eds.), *Neutron and Synchrotron Radiation for Condensed Matter Studies* (Springer-Verlag, New York, 1993)
- [13] G.F. Knoll, *Radiation Detection and Measurement*, 2<sup>nd</sup> edition (Wiley, New York, 1989).
- [14] A. Bäcklin, G. Hedin, B. Fogelberg, M. Saraceno, R.C. Greenwood, C.W. Reich, H.R. Koch, H.A. Baader, H.D. Breitig, O.W.B. Schult, K. Schreckenbach, T. von Egidy, W. Mampe, *Nucl. Phys. A* **380** (1982) 189.

- [15] R.C. Greenwood, C.W. Reich, H.A. Baader, H.R. Koch, H.D. Breitig, O.W.B. Schult, B. Fogelberg, A. Bäcklin, W. Mampe, T. von Egidy, K. Schreckenbach, *Nucl. Phys. A* **304** (1978) 327.
- [16] B. Gebauer, Ch. Schulz, Th. Wilpert, S.F. Biagi, *Nucl. Instr. Meth. A* **409** (1998) 56.
- [17] C. Mori, T. Haga, A. Uritani, *Nucl. Instr. Meth. A* **310** (1991) 437.
- [18] A. Rose, *J. Soc. Motion Picture Engrs.* **47** (1946) 273.
- [19] J.C. Dainty, R. Shaw, *Image Science* (Academic Press, London, 1974).
- [20] W. Hillen, U. Schiebel, T. Zaengel, *Med. Phys.* **14**(5) (1987) 744.
- [21] A.W. Hewat, in: *Position-sensitive Detection of Thermal Neutrons*, paper 25, eds.: P. Convert, J.B. Forsyth (Academic Press, London, 1983).
- [22] P. Convert, D. Fruchart, D. Roudaut, P. Wolfers, in: *Position-sensitive Detection of Thermal Neutrons*, paper 23, eds.: P. Convert, J.B. Forsyth (Academic Press, London, 1983).
- [23] R. Lewis, *Synchrotron Rad.* **1** (1994) 43.
- [24] A. Oed, *Nucl. Instr. Meth. A* **263** (1988) 351.
- [25] A. Oed, P. Convert, M. Berneron, H. Junk, C. Budtz-Jorgensen, M.M. Madsen, P. Jonasson, H.W. Schopper, *Nucl. Instr. Meth. A* **284** (1989) 223.
- [26] A. Angelini, R. Bellazini, A. Brez, M.M. Massai, R. Rafo, G. Spandre, M.A. Spezziga, *Nucl. Instr. Meth. A* **335** (1993) 69.
- [27] *Scintillation Detectors*, catalogue, Crismatec (1991).
- [28] R.J. Ginther, J.H. Schulman, *IRE Trans. Nucl. Sci.* **NS-5** (1958).
- [29] R.J. Ginther, J.H. Schulman, *IRE Trans. Nucl. Sci.* **NS-7**, no. 2&3 (1960) 28.
- [30] L.M. Bollinger, G.E. Thomas, R.J. Ginther, *Nucl. Instr. Meth.* **17** (1962) 97.
- [31] D.G. Anderson, *J. Elec. Control* **7** (1959) 463.
- [32] A.R. Spowart, *Nucl. Instr. Meth.* **135** (1976) 441.
- [33] A.R. Spowart, *Nucl. Instr. Meth.* **140** (1977) 19.
- [34] E.J. Fairly, A.R. Spowart, *Nucl. Instr. Meth.* **150** (1978) 159.
- [35] A.R. Spowart, in: *Position-sensitive Detection of Thermal Neutrons*, paper 7, eds.: P. Convert, J.B. Forsyth (Academic Press, London, 1983).

- [36] A.R. Spowart, *IEEE Trans. Nucl. Sci.* **NS-31**, no.1 (1984).
- [37] R. Hofstadter, J.A. McIntyre, H. Roderick, H.I. West, *Phys. Rev.* **82** (1951) 749.
- [38] J. Schenck, *Nature* **171** (1953) 518.
- [39] R. Kurz, J. Schelten, in: *Position-sensitive Detection of Thermal Neutrons*, paper 11, eds.: P. Convert, J.B. Forsyth (Academic Press, London, 1983).
- [40] K.H. Sun, P.R. Malmberg, F.A. Pecjak, *Phys. Rev.* **95** (1954) 600.
- [41] J.B. Birks, *The Theory and Practice of Scintillation Counting*, 2<sup>nd</sup> edition (Pergamon Press, Oxford, 1967).
- [42] *Scintillation Materials*, catalogue, Nuclear Enterprises Ltd. (1990).
- [43] N.J. Rhodes, M.W. Johnson, in: Proc. Int. Conf. on Inorg. Scintillators and their Applications SCINT95, Aug 28 - Sept 1 1995, Delft, The Netherlands, eds.: P. Dorenbos, C.W.E. van Eijk, (Delft University Press, Delft, 1996) 73.
- [44] P.L. Reeder, *Nucl. Instr. Meth. A* **340** (1994) 371.
- [45] J.T. Lindsay, J.D. Jones, C.W. Kauffman, B. van Pelt, *Nucl. Instr. Meth. A* **242** (1986) 525.
- [46] H. Nguyen Ngoc, J. Jeanjean, J. Jacobé, P. Mine, *Nucl. Instr. Meth.* **188** (1981) 677.
- [47] P.L. Davidson, H. Wroe, in: *Position-sensitive Detection of Thermal Neutrons*, paper 8, eds.: P. Convert, J.B. Forsyth (Academic Press, London, 1983).
- [48] M.G. Strauss, R. Brenner, F.J. Lynch, C.B. Morgan, *IEEE Trans. Nucl. Sci.* **NS-28**, no.1, (1981) 800.
- [49] R. Kurz, J. Schelten, *Nucl. Instr. Meth. A* **273** (1988) 273.
- [50] M. Heiderich, R. Reinartz, R. Kurz, J. Schelten, *Nucl. Instr. Meth. A* **305** (1991) 423.
- [51] J.B. Forsyth, R.T. Lawrence, C.C. Wilson, *Nucl. Instr. Meth. A* **273** (1988) 741.
- [52] M.G. Strauss, R. Brenner, H.P. Chou, A.J. Schultz, C.T. Roche, in: *Position-sensitive Detection of Thermal Neutrons*, paper 9, eds.: P. Convert, J.B. Forsyth (Academic Press, London, 1983).
- [53] R.A. Schrack, *Nucl. Instr. Meth. A* **222** (1984) 499.
- [54] V. Dangendorf, A. Demian, H. Friedrich, V. Wagner, A. Akkerman, A. Breskin, R. Chech-  
nik, A. Gibrekhterman, *Nucl. Instr. Meth. A* **350** (1994) 503.



- [55] G.W. Fraser, J.F. Pearson, O.S. Al-Horayess, W.B. Feller, L.M. Cook, Proc. SPIE **1737** (1992) 298.
- [56] J. Schelten, R. Reinartz, R. Engels, M. Balzhäuser, J. Lauter, W Schäfer, K.D. Müller, Nucl. Instr. Meth. A **389** (1997) 447.
- [57] C. Petrillo, F. Sacchetti, O. Toker, N.J. Rhodes, J. Neutron Res. **4** (1996) 65.
- [58] Y. Kumashiro, K. Kudo, Y. Okada, T. Koshiro, J. Less-Common Met. **143** (1988) 71.
- [59] E.O. Wollan, G.G. Shull, M.C. Marney, Phys. Rev. **73** (1948) 527.
- [60] D. Hohlwein, in: *Position-sensitive Detection of Thermal Neutrons*, paper 34, eds.: P. Convert, J.B. Forsyth (Academic Press, London, 1983).
- [61] C. Wilkinson, A. Gabriel, M.S. Lehmann, T. Zemb, F. Né, Proc. SPIE **1737** (1992) 324.
- [62] T. Bücherl, C. Rausch, H. von Seggern, Nucl. Instr. Meth. A **333** (1993) 502.
- [63] N. Niimura, Y. Karasawa, I. Tanaka, J. Miyahara, K. Takahashi, H. Saito, S. Koizumi, M. Hidaka, Nucl. Instr. Meth. A **349** (1994) 521.
- [64] Y. Karasawa, N. Niimura, I. Tanaka, J. Miyahara, K. Takahashi, H. Saito, A. Tsuruno, M. Matsubayashi, Physica B **213&214** (1995) 978.
- [65] J. Hofmann, C. Rausch, Nucl. Instr. Meth. A **355** (1995) 494.
- [66] M. Thoms, M.S. Lehmann, C. Wilkinson, Nucl. Instr. Meth. A **384** (1997) 457.
- [67] H. von Seggern, in: Proc. Workshop on Neutron Image Plates, Feb. 22-23, 1996, Brookhaven, USA, to be published.
- [68] C. Wilkinson, personal correspondence.
- [69] R.K. Crawford, in: Proc. Workshop on Neutron Image Plates, Feb. 22-23, 1996, Brookhaven, USA, to be published.
- [70] M. Lehmann, in: Proc. Workshop on Neutron Image Plates, Feb. 22-23, 1996, Brookhaven, USA, to be published.
- [71] N. Niimura, in: Proc. Workshop on Neutron Image Plates, Feb. 22-23, 1996, Brookhaven, USA, to be published.
- [72] P.N. Chernyshov, A.A. Sumbatyan, V.Ya. Kezerashvili, S.P. Gaevoi, V.M. Gataulin, V.A. Turnov, Instr. Exp. Techn. **29** (1986) 1297.
- [73] M.W. Johnson, Rutherford Appleton Laboratory report no. RAL-92-040 (1992).

- [74] U. Kilgus, R. Kotthaus, E. Lange, Nucl. Instr. Meth. A **297** (1990) 425.
- [75] G. Bertolini, A.M. del Turco, G. Restelli, Nucl. Instr. Meth. **7** (1960) 350.
- [76] T.R. Ophel, Nucl. Instr. Meth. **3** (1958) 45.
- [77] P.A. Rodnyi, *Physical Processes in Inorganic Scintillators* (CRC Press, Boca Raton, 1997).
- [78] A.L. Boonstra, N. Brummund, H. Lohner, A. Raschke, A. Stiens, L.B. Venema, H.W. Wildschut, TAPS internal report 11, KVI Groningen, The Netherlands (1990).
- [79] M.J. Knitel, unpublished result.
- [80] M. Moszynski, T. Ludziejewski, D. Wolski, W. Klamra, L.O. Norlin, Nucl. Instr. Meth. A **345** (1994) 461.
- [81] D.W. Anderson, *Absorption of Ionizing Radiation* (University Park Press, Baltimore, 1984).
- [82] R. Visser, *Energy Transfer in Fluoride Scintillators*, thesis (Delft University of Technology).
- [83] J. Menefee, C.F. Swinchart, E.E. O'Dell, IEEE Trans. Nucl. Sci. **NS-13** (1966) 720.
- [84] E. Rutherford, J. Chadwick, C.D. Ellis, *Radiations from Radioactive Sources* (University Press, Cambridge, 1930).
- [85] H. Yamada, A. Suzuki, Y. Uchida, M. Yoshida, H. Yamamoto, J. Electrochem. Soc. **136**(9) (1989) 2713.
- [86] C.W.E. van Eijk, J. Lumin. **60&61** (1994) 936.
- [87] I.N. Ogorodnikov, A.V. Kruzhalov, V.Yu. Ivanov, Sov. Phys. Sol. Stat. **34** (1992) 1053.
- [88] S. Kubota, S. Sakuragi, S. Hashimoto, J. Ruan, Nucl. Instr. Meth. A **268** (1988) 275.
- [89] V.V. Averkiev, I.M. Bolesta, I.M. Kravchuk, A.B. Lyskovich, V.K. Lyapidevskii, V.A. Prorvich, Ukr. Fiz. Zh. **25** (1980) 1392.
- [90] D.J. Ehrlich, P.F. Moulton, R.M. Osgood, Optics Letters **5**(8) (1980) 339.
- [91] S. Yokono, T. Abe, T. Hoshina, J. Lumin. **24&25** (1981) 309.
- [92] C.W.E. van Eijk, Proc. SPIE **2706** (1996) 158.
- [93] S. Schweizer, P. Willems, P.J.R. Leblans, L. Struye, J.-M. Spaeth, J. Appl. Phys. **79**(8) (1996) 4157.
- [94] K. Machida, G. Adachi, J. Shiokawa, J. Lumin. **21** (1979) 101.

- [95] Y. Abe, K. Onisawa, Y.A. Ono, M. Hanazono, *Jpn. J. Appl. Phys.* **29** (1990) 305.
- [96] H. von Seggern, *Cryst. Latt. Def. and Amorph. Mat.* **18** (1989) 399.
- [97] M. Yuste, L. Taurel, M. Rahmani, D. Lemoyne, *J. Phys. Chem. Sol.* **37** (1976) 961.
- [98] M. Thoms, H. von Seggern, A. Winnacker, *Phys. Rev. B* **44** (1991) 9240.
- [99] J.M. Spaeth, Th. Hangleiter, F.K. Koschnick, Th. Pawlik, *Rad. Eff. and Def. in Sol.* **135** (1995) 1.
- [100] K. Takahashi, K. Kohda, J. Miyahara, *J. Lumin.* **31&32** (1984) 266.
- [101] T. Hangleiter, F.K. Koschnick, J.-M. Spaeth, R.H.D. Nutall, R.S. Eachus, *J. Phys. Cond. Mat.* **2** (1990) 6837.
- [102] F.K. Koschnick, J.-M. Spaeth, R.S. Eachus, W.G. McDugle, R.H.D. Nutall, *Phys. Rev. Lett.* **67**(25) (1991) 3571.
- [103] H. von Seggern, T. Voigt, W. Knüpfner, G. Lange, *J. Appl. Phys.* **64**(3) (1988) 1405.
- [104] T.J. Bastow, S.N. Stuart, W.G. McDugle, R.S. Eachus, J.-M. Spaeth, *J. Phys. Cond. Mat.* **6** (1994) 8633.
- [105] M.K. Crawford, L.H. Brixner, *J. Lumin.* **48&49** (1991) 37.
- [106] N. Itoh, *Advance in Physics*, **31**(5) (1982) 491.
- [107] A. Harrison, M.T. Harrison, G.P. Keogh, R.H. Templer A.S. Wills, *Phys. Rev. B* **53**(9) (1996) 5039.
- [108] A. Kalnins, I. Plavina and A. Tale, *Nucl. Instr. Meth. B* **84** (1994) 95.
- [109] T. Pawlik, J.-M. Spaeth, in: *Proc. Int. Conf. on Inorg. Scintillators and their Applications SCINT95, Aug 28 - Sept 1 1995, Delft, The Netherlands*, eds.: P. Dorenbos, C.W.E. van Eijk, (Delft University Press, Delft, 1996) 392.
- [110] H. von Seggern, A. Meijerink, T. Voigt, A. Winnacker, *J. Appl. Phys.* **66**(9) (1989) 4418.
- [111] L.E. Trinkler, M.F. Trinkler, A.I. Popov, *Phys. Stat. Sol. B* **180** (1993) K31.
- [112] A. Meijerink, G. Blasse, L. Struye, *Mat. Chem. Phys.* **21** (1989) 261.
- [113] M. Nikl, R. Morlotti, C. Magro, R. Bracco, *J. Appl. Phys.* **79**(6) (1996) 2853.
- [114] W.J. Schipper, J.J. Hamelink, E.M. Langeveld, G. Blasse, *J. Phys. D: Appl. Phys.* **26** (1993) 1.

- [115] W.B. Fowler, *Physics of Color Centers* (Academic Press, New York, 1968).
- [116] B. Henderson, G.F. Imbusch, *Optical Spectroscopy of Inorganic Solids* (Clarendon Press, Oxford, 1989).
- [117] A.R. Lakshmanan, *Phys. Stat. Sol. A* **153** (1996) 3.
- [118] W.J. Schipper, *Luminescence and Storage Mechanism of New X-ray Storage Phosphors*, thesis (Utrecht University, 1993).
- [119] K. Chakrabarti, V.K. Mathur, J.F. Rhodes, R.J. Abbundi, *J. Appl. Phys.* **64**(3) (1988) 1363.
- [120] Y. Tamura, A. Shibukawa, *Jpn. J. Appl. Phys.* **32** (1993) 3187.
- [121] F. Urbach, D. Pearlman, H. Hemmendinger, *J. Opt. Soc. Am.* **36** (1946) 372.
- [122] W.J. Schipper, G. Blasse, P. Leblans, *Chem. Mater.* **6**(10) (1994) 1784.
- [123] R. Visser, P. Dorenbos, C.W.E. van Eijk, A. Meijerink, G. Blasse, H.W. den Hartog, *J. Phys. Cond. Mat.* **5** (1993) 1659.
- [124] J.W.M. Verwey, G.J. Dirksen, G. Blasse, *J. Phys. Chem. Sol.* **53**(3) (1992) 367.
- [125] S. Asano, N. Yamashita, T. Ohnishi, *Phys. Stat. Sol. B* **99** (1980) 661.
- [126] D. van der Voort, I. de Maat-Gersdorf, G. Blasse. *Eur. J. Sol. Stat. Inorg. Chem.* **29** (1992) 1029.
- [127] T.E. Peters, J. Baglio, *J. Inorg. Nucl. Chem.* **32** (1970) 1089.
- [128] A. Levasseur, C. Fouassier, *C.R. Acad. Sc. Paris*, 272, série C (1971) 80.
- [129] Z. Zak, F. Hanic, *Acta Cryst. B* **32** (1976) 1784.
- [130] J.G. Fletcher, F.P. Glasser, R. Alan-Howie, *Acta Cryst. C* **47** (1991) 12.
- [131] T. Alekel, D.A. Keszler, *Acta Cryst. C* **48** (1992) 1382.
- [132] D.M. Chackraburty, *Acta Cryst. C* **10** (1957) 199.
- [133] D.A. Keszler, A. Akella, K.I. Schaffers, T. Alekel, *Proc. Materials Research Society* **329** 15. (Materials Research Society, Pittsburgh, 1994).
- [134] W.J. Schipper, G. Blasse, *J. Alloys Comp.* **203** (1994) 267.
- [135] T. Alekel, D.A. Keszler, *J. Sol. Stat. Chem.* **106** (1993) 310.
- [136] X. Liu, Y. Zhang, Z. Wang, S. Lu, *J. Lumin.* **40&41** (1988) 885.

- [137] D. van der Voort, G. Blasse, *J. Phys. Chem. Sol.* **52**(9) (1991) 1149.
- [138] T.A. Bither, H.S. Young, *J. Sol. Stat. Chem.* **10** (1974) 302.
- [139] A.A. Brovkin, L.V. Nikishova, *Kristallografiya* **20** (1975) 415.
- [140] A. Levasseur, C. Fouassier, P. Hagenmuller, *Mat. Res. Bull.* **6** (1971) 15.
- [141] C.E. Messer, *J. Sol. Stat. Chem.* **2** (1970) 144.
- [142] P. Dorenbos, J.T.M. de Haas, R. Visser, C.W.E. van Eijk, R.W. Hollander, *IEEE Trans. Nucl. Sci.* **40**(4) (1993) 424.
- [143] L.M. Bollinger, G.E. Thomas, *Rev. Sci. Instr.* **32** (1961) 1044.
- [144] W.W. Moses, *Nucl. Instr. Meth. A* **336** (1993) 253.
- [145] M. Laval, M. Moszynski, R. Allemand, E. Cormoreche, P. Guinet, R. Odru, J. Vacher, *Nucl. Instr. Meth. A* **206** (1983) 169.
- [146] E.N. Mel'chakov, M.A. Petrova, I.G. Podkolzina, P.A. Rodnyi, M.A. Terekhin, *Opt. Spectrosc. USSR* **69**(4) (1990) 481.
- [147] R.T. Williams, M.N. Kabler, W. Hayes, J.P. Scott, *Phys. Rev. B* **14** (1976) 725.
- [148] P.A. Rodnyi, M.A. Terekhin, E.N. Mel'chakov, *J. Lumin.* **47** (1991) 281.
- [149] J. Jansons, Z. Rachko, J. Valbis, J. Andriessen, P. Dorenbos, C.W.E. van Eijk, in: *Proc. 12<sup>th</sup> Conf. Defects in Insulating Materials 2*, eds.: O. Kanert and J.-M. Spaeth, (World Scientific, Singapore, 1992) 1256.
- [150] Y.M. Alexandrov, V.N. Makhov, P.A. Rodnyi, T.I. Syreishchikova, M.N. Yakimenko, *Sov. Phys. Sol. Stat.* **26** (1984) 1734.
- [151] J. Jansons, Z. Rachko, J. Valbis, J. Andriessen, P. Dorenbos, C.W.E. van Eijk, N.M. Khaidukov, *J. Phys. Condens. Matter* **5** (1993) 1589.
- [152] C.M. Combes, P. Dorenbos, C.W.E. van Eijk, *J. Lumin.* **72-74** (1997) 753.
- [153] P. Lecoq, M. Schussler, M. Schneegans, *Nucl. Instr. Meth. A* **315** (1992) 337.
- [154] K. Wisshak, personal correspondence.
- [155] S. Kubota, M. Suzuki, J. Ruan, *Nucl. Instr. Meth. A* **242** (1986) 291.
- [156] C. Coceva, *Nucl. Instr. Meth. A* **21** (1963) 63.
- [157] J. Schelten, R. Kurz, I. Naday, W. Schäfer, *Nucl. Instr. Meth. A* **205** (1983) 319.

- [158] S. Usuda, S. Sakurai, K. Yasuda, Nucl. Instr. Meth. A **388** (1997) 193.
- [159] K. Wisshak, F. Käppeler, Nucl. Instr. Meth. **227** (1984) 91.
- [160] C.M. Combes, P. Dorenbos, J. Andriessen, C.W.E. van Eijk, J.Y. Gesland, N. Korolev, in: Proc. Int. Conf. on Inorg. Scintillators and their Applications SCINT97, Sept. 22-25, Shanghai, eds.: Z.W. Yin, P.J. Li, X.Q. Feng, Z.L. Xue, (CAS Press, Shanghai, 1997) 322.
- [161] M. Itoh, S. Hashimoto, S. Sakuragi, S. Kubota, Sol. Stat. Comm. **65**(6) (1988) 523.
- [162] M.A. Terekhin, A.N. Vasil'ev, M. Kamada, E. Nakamura, S. Kubota, Phys. Rev. B **52**(5) (1995) 3117.
- [163] C.M. Combes, M.J. Knitel, R.W. Hollander, P. Dorenbos, C.W.E. van Eijk, in: Proc. Int. Conf. on Inorg. Scintillators and their Applications SCINT97, Sept. 22-25, Shanghai, eds.: Z.W. Yin, P.J. Li, X.Q. Feng, Z.L. Xue, (CAS Press, Shanghai, 1997) 349.
- [164] I. Tale, P. Kulis, U. Rogulis, V. Tale, J. Trokss, A. Veispals, M. Barboza-Flores, H.-J. Fitting, J. Lumin. **72-74** (1997) 722.
- [165] A.H. Gomes de Mesquita, A. Bril, Mat. Res. Bull. **4** (1969) 643.
- [166] I.A. Bondar, A.A. Kolpakova, L.Ya. Markovskii, A.N. Sokolov, L.E. Tarasova, N.A. Toropov, Trans. Sov. Phys. - Doklady **33** (1969) 1057.
- [167] A. Bril, G. Blasse, J.A. de Poorter, J. Electrochem. Soc. **117**(3) (1970) 346.
- [168] M.J.J. Lammers, G. Blasse, J. Electrochem. Soc. **34**(8) (1987) 2068.
- [169] H.S. Kiliaan, F.P. van Herwijnen, G. Blasse, Mat. Chem. Phys. **18** (1987) 351.
- [170] H. Suzuki, T.A. Tombrello, C.L. Melcher, J.S. Schweitzer, Nucl. Instr. Meth. A **320** (1992) 263.
- [171] J. Lin, Q. Su, J. Mater. Chem. **5**(8) (1995) 1151.
- [172] A. Meijerink, W.J. Schipper, G. Blasse, J. Phys. D: Appl. Phys **24** (1991) 997.
- [173] D. Meiss, W. Wischert, S. Kemmler-Sack, Mat. Chem. Phys. **38** (1994) 191.
- [174] P. Dorenbos, C.W.E. van Eijk, A.J.J. Bos, C.L. Melcher, J. Phys. B: Condens. Matter **6** (1994) 4167.
- [175] R. Visser, C.L. Melcher, J.S. Schweitzer, IEEE Trans. Nucl. Sci. **41**(4) (1994) 691.
- [176] G. Blasse, J. de Vries, J. Inorg. Nucl. Chem. **29** (1967) 1541.
- [177] Y.V. Nikolskii, Doklady Akademii Nauk SSSR (1976) 230. In Russian.

- [178] R.W.G. Wyckoff, *Crystal Structures* Vol. 3 (Interscience, New York, 1965).
- [179] G. Blasse, A. Bril, J. Inorg. Nucl. Chem. **29** (1967) 2231.
- [180] J.C. van 't Spijker, P. Dorenbos, C.W.E. van Eijk, A.G. Avanesov, P.I. Bykovskii, in: Proc. Int. Conf. on Inorg. Scintillators and their Applications SCINT97, Sept. 22-25, Shanghai, eds.: Z.W. Yin, P.J. Li, X.Q. Feng, Z.L. Xue, (CAS Press, Shanghai, 1997) 326.
- [181] K. Takahashi, personal correspondence.
- [182] GEANT (GEometry ANd Tracking), Detector Description and Simulation Tool, CERN-CN division, CERN Program Library Long Writeup W5013.
- [183] K. Meijvogel, internal report no. IRI-131-96-004 (1996).
- [184] R. Atrata, P. Schauer, Jiří Kvapil, Josef Kvapil, Scanning **5** (1983) 91.
- [185] T. Hoshina, J. Phys. Soc. Japan, **48**(4) (1980).
- [186] R. Raue, A.T. Vink, T. Welker, Philips Tech. Rev. **44**(11/12) (1989) 335.
- [187] W. Schipper, Z.A.E.P. Vroon, G. Blasse, Th. Schleid, G. Meyer, Mater. Chem. Phys. **30** (1991) 43.
- [188] K. Michaelian, A. Menchaca-Rocha, E. Belmont-Moreno, Nucl. Instr. Meth. A **356** (1995) 297.
- [189] K. Michaelian, A. Menchaca-Rocha, Phys. Rev. B **49**(22) (1994) 15551.
- [190] J. Hoffmann, C. Rausch, Nucl. Instr. Meth. A **355** (1995) 494.
- [191] S.W.S. McKeever, *Thermoluminescence of Solids*, (Cambridge University Press, 1985).
- [192] C. Pedrini, P.O. Pagost, C. Madej, D.S. McClure, J. Phys. **42** (1981) 323.
- [193] K. Chakrabarti, V.K. Mathur, L.A. Thomas, R.J. Abbundi, J. Appl. Phys. **65**(5) (1989) 2021.
- [194] J.P. Chaminade, A. Garcia, T. Gaewdang, M. Pouchard, J. Grannec, B. Jacquier, Rad. Eff. Def. Sol. **135** (1995) 137.
- [195] W.M. Yen, J. Choi, S.A. Basun, M. Raukas, U. Happek, in: Proc. Int. Conf. on Inorg. Scintillators and their Applications SCINT97, Sept. 22-25, Shanghai, eds.: Z.W. Yin, P.J. Li, X.Q. Feng, Z.L. Xue, (CAS Press, Shanghai, 1997) 289.
- [196] F. Agullo-Lopez, C.R.A. Catlow, P.D. Townsend, *Point Defect in Materials* (Academic Press, London, 1988).

- [197] C.T. Garapon, B. Jacquier, J.P. Chaminade, C. Fouassier, *J. Lumin.* **34** (1985) 211.
- [198] J. Mascetti, C. Fouassier, P. Hagenmuller, *J. Sol. Stat. Chem.* **50** (1983) 204.
- [199] J. Hölsa, M. Leskelä, *J. Lumin.* **48&49** (1991) 497.
- [200] H. Zhiran, G. Blasse, *Mat. Chem. Phys.* **12** (1985) 257.
- [201] Z. Pei, G. Blasse, *J. Sol. Stat. Chem.* **110** (1994) 399.
- [202] A. Mayolet, W. Zhang, P. Martin, B. Chassigneux, J.C. Krupa, *J. Electrochem. Soc.* **143**(1) (1996) 330.
- [203] B. Saubat, C. Fouassier, P. Hagenmuller, *Mat. Res. Bull.* **16** (1981) 193.
- [204] M. Leskelä, M. Saakes, G. Blasse, *Mat. Res. Bull.* **19** (1984) 151.
- [205] M.H. van Wijngaarden, J. Plaisier, A.J.J. Bos, *Radiat. Prot. Dosim.* **11** (1985) 179.
- [206] G. Blasse, A. Bril, *J. Chem. Phys.* **47** (1967) 5139.
- [207] G.K. Abdullaev, K.S. Mamedov, P.F. Rza-Zade, S.A. Guseinova, G.G. Dzararov, *Russ. J. Inorg. Chem.* **22** (1977) 1765.
- [208] G.K. Abdullaev, Kh.S. Mamedov, G.G. Dzhafarov, *Sov. Phys. Crystallogr.* **26** (1981) 473.
- [209] B. Saubat, M. Vlasse, C. Fouassier, *J. Sol. Stat. Chem.* **34** (1980) 271.
- [210] M. Saakes, M. Leskelä, G. Blasse, *Mat. Res. Bull.* **19** (1984) 83.
- [211] A. Mayolet, *Etude des Processus d'Absorption et de Transfert d'Energie au sein de Matériaux Inorganiques Luminescents dans le Domaine UV et VUV*, thesis, (University of Paris XII, Orsay, 1995).
- [212] M.V. Hoffman, *J. Electrochem. Soc.* **118**(9) (1971) 1508.
- [213] R. Chen, J. Huang, L. Lu, Y. Xu, *Mat. Res. Bull.* **23** (1988) 1699.
- [214] R. Norrestam, M. Nygren, J.-O. Bovin, *Chem. Mater.* **4** (1992) 737.
- [215] D. van der Voort, J.M.E. de Rijk, R. van Doorn, G. Blasse, *Mat. Chem. Phys.* **31** (1992) 333.
- [216] G.J. Dirksen, G. Blasse, *J. Alloys Comp.* **191** (1993) 121.
- [217] G. Blasse, *J. Inorg. Nucl. Chem.* **31** (1969) 1519. *Book reviewed at 07-358 6-989 C=10.42*
- [218] R.C. Weast, M.J. Astle (eds.), *Handbook of Chemistry and Physics* 60th edition (CRC Press, Boca Raton, 1979).



- [219] T. Kobayasi, S. Mroczkowski, J.F. Owen *J. Lumin.* **21** (1980) 247.
- [220] J.B. Czirr, Internal Report Photogenics Inc. PGI-97-1.
- [221] G. Blasse, G.J. Dirksen, *J. Electrochem. Soc.* **136**(5) (1989) 1550.
- [222] H. Zhiran, G. Blasse, *J. Sol. Stat. Chem.* **55** (1984) 23.
- [223] A.M. Srivastava, D.A. Doughty, W.W. Beers, *J. Electrochem. Soc.* **143**(12) (1996) 4113.
- [224] G.K. Abdullaev, *Azerbaidzhanskii Khimicheskii Zhurnal* (1976) 117.
- [225] H.L. Schäffer, C.K. Jörgensen, *J. Inorg. Nucl. Chem.* **8** (1958) 149.
- [226] B.F. Aull, H.P. Jenssen, *Phys. Rev. B* **34**(10) (1986) 6640.
- [227] W.C. Martin, R. Zalubas, L. Hagan (eds.), *Atomic Energy Levels - The Rare-Earth Elements* National Standard Reference Data Series 60, (U.S. Government Printing Office, Washington D.C., 1978).
- [228] W. Lenth, *4f Übergangswahrscheinlichkeiten und interionische Wechselwirkungen in Lasermaterialien aus reinen Seltenen Erd-Verbindungen*, thesis, ch. 3 (Hamburg University, 1993).
- [229] A. Meijerink, G. Blasse, *J. Phys. D: Appl. Phys.* **24** (1991) 626.
- [230] C. Fouassier, A. Lévassieur, P. Hagenmuller, *J. Sol. Stat. Chem.* **3** (1971) 206.
- [231] E. Breitenberger, *Progress in Nucl. Phys.* **4** (1955) 56.
- [232] M. Thoms, *Appl. Opt.* **35** (19) (1996).
- [233] C.R. Rausch, *Detektoren für thermische Neutronen mit hoher Ortsauflösung*, thesis, (TU München, 1996).
- [234] M. Thoms, H. von Seggern, *J. Appl. Phys.* **75**(9) (1991) 4658.
- [235] R.H. Templer, *Nucl. Instr. Meth. A* **300** (1991) 357.
- [236] C. Rausch, J. Hofmann, M. Thoms, H.v. Seggern, in: *Proc. Workshop on Neutron Image Plates*, Feb. 22-23, 1996, Brookhaven, USA, to be published.
- [237] A. Meijerink, G. Blasse, *J. Lumin.* **43** (1989) 283.
- [238] K.-I. Machida, G.-Y. Adachi, N. Yasuoka, N. Kasai, J. Shiokawa, *Inorg. Chem.* **19** (1980) 3807.
- [239] J.H. Hubbell, *Int. J. Appl. Radiat. Isotope* **33** (1982) 1269.

- [240] Z. Pu, M. Su, S. Ruan, *Mat. Res. Bull.* **30**(10) (1995) 1227.
- [241] T.M. Piters, W.H. Meulemans, A.J.J. Bos, *Rev. Sci. Instrum.* **64** (1993) 109.
- [242] Gaussian, Inc., Pittsburgh PA, U.S.A. (1995).
- [243] W.J. Stevens, M. Krauss, H. Basch, P.G. Jasien, *Can. J. Chem.* **70** (1992) 619.
- [244] S. Huzinaga, with J. Andzelm *et al.*, *Gaussian Basis Sets for Molecular Calculations* (Elsevier, Amsterdam, 1984).
- [245] Th.R. Cundari, W.J. Stevens, *J. Chem. Phys.* **98** (1993) 5555.
- [246] J. Andriessen, P. Dorenbos, C.W.E. van Eijk, *Mol. Phys.* **74**(3) (1991) 535.
- [247] A. Meijerink, G. Blasse, *Phys. Rev. B* **40**(10) (1989) 7288.
- [248] C. Pedrini, A.N. Belsky, A.N. Vasil'ev, D. Bouttet, C. Dujardin, B. Moine, P. Martin, M.J. Weber, *Mat. Res. Soc. Symp. Proc.* **348** (1994) 225.
- [249] G. Blasse, in: *Luminescence of Inorganic Solids*, Proc. of a Course on Luminesc. Inorg. Solids at the Int. School on Atomic and Mol. Spectr., June 15-30, 1977, Erice, Italy, ed: B. Di Bartolo (Plenum Press, New York, 1978).
- [250] J.A. Koningstein, *Phys. Rev.* **136A** (1964) 717.
- [251] J.D. Kingsley, J.S. Prener, *Phys. Rev.* **126** (1962) 458.
- [252] G. Blasse, *J. Sol. Stat. Chem.* **4** (1972) 52.
- [253] H.E. Hoefdraad, *J. Sol. Stat. Chem.* **15** (1975) 175.
- [254] A. Mayolet, J.C. Krupa, I. Gerard, P. Martin, *Mat. Chem. Phys.* **31** (1992) 107.
- [255] J.L. Ryan, C.K. Jørgensen, *J. Phys. Chem.* **70**(9) (1966).
- [256] D.M. de Leeuw, T. Kovats, S.P. Herko, *J. Electrochem. Soc.* **134** (1987) 491.
- [257] R. Dawson, D. Pooley, *Phys. Stat. Sol.* **35** (1969) 95.
- [258] W.J. Schipper, *Luminescence and Storage Mechanism of New X-ray Storage Phosphors*, thesis, ch. 6, (Utrecht University, 1993).
- [259] A. Abragam, B. Bleaney, *Electron Paramagnetic Resonance of Transition Ions* (Clarendon, Oxford, 1970)
- [260] C.M. Brodbeck, L.E. Iton, *J. Chem. Phys.* **83**(9) (1985) 4285.

- [261] A.S. Marfunin, *Spectroscopy, Luminescence and Radiation Centers in Minerals*, ch. 7, (Springer-Verlag, Berlin, 1979).
- [262] M. Haddad, G. Vignaud, R. Berger, A. Levasseur, *J. Phys. Chem. Sol.* **46**(9) (1985) 997.
- [263] A. Meijerink, *Luminescence of New X-ray Storage Phosphors*, thesis, ch. 8, (Utrecht University, 1990).
- [264] Y.S. Horowitz, *Thermoluminescence and Thermoluminescent Dosimetry Vol.1* (CRC Press, Boca Raton U.S.A., 1984).
- [265] P.A. Rodnyi, P. Dorenbos, C.W.E. van Eijk, *Phys. Stat. Sol. B* **187** (1995) 15.
- [266] R. Chen, Y. Kirsch, *Analysis of Thermally Stimulated Processes* (Pergamon Press, New York, 1981).
- [267] R.K. Bull, *J. Phys. D: Appl. Phys.* **22** (1989) 1375.
- [268] I. Aguirre de Cárcer, F. Cusso, F. Jaque, *Phys. Rev. B* **38**(15) (1988) 10812.
- [269] R.L. Fuller, D.S. McClure, *Phys. Rev. B* **43**(1) (1991) 27.
- [270] C. Pedrini, F. Rogemond, D.S. McClure, *J. Appl. Phys.* **59**(4) (1986) 1196.
- [271] R.S. Title, *Phys. Rev. Lett.* **3** (1959) 273.
- [272] X.-P. Sun, M.-Z. Su, *J. Lumin.* **40&41** (1988) 171.
- [273] F.K. Koschnick, J.-M. Spaeth, R.S. Eachus, *J. Phys. Condens. Mat.* **4** (1992) 8919.
- [274] M.J. Vrubel, H.A. Atwater, *J. Chem. Phys.* **48** (1968) 946.
- [275] C.R.A. Catlow, *J. Phys. C* **12** (1979) 969.
- [276] S.M. Dhopte, P.L. Muthal, V.K. Kondawar, S.V. Moharil, *J. Lumin.* **50** (1991) 187.
- [277] S.M. Dhopte, P.L. Muthal, V.K. Kondawar, S.V. Moharil, *J. Lumin.* **54** (1992) 95.
- [278] H. Forest, A. Cocco, H. Hersh, *J. Lumin.* **3** (1970) 25.
- [279] C.W. Struck, W.H. Fonger, *J. Lumin.* **1&2** (1970) 456.
- [280] M. Danilkin, *Interaction of Intrinsic and Impurity Defects in CaS:Eu Luminophors*, thesis, (University of Tartu, Estonia, 1997).
- [281] J.T. Randall, M.H.F. Wilkins, *Proc. Roy. Soc. (London)* **A184** (1945) 366.
- [282] P. Avouris, T.N. Morgan, *J. Chem. Phys.* **74**(8) (1981) 4347.

## List of Abbreviations

CCD	Charge Coupled Device
CD	Single Crystal Diffractometry
CE	Conversion Efficiency
CT	Charge Transfer
CVL	Core Valence Luminescence (also termed CL: Cross Luminescence)
DE	Detection Efficiency
DQE	Detective Quantum Efficiency
ECP	Effective Core Potential
EPR	Electron Paramagnetic Resonance
ESS	European Spallation Source
FWHM	Full Width at Half Maximum
GEANT	GEometry ANd Tracking
IP	Image Plate
IP-B	Image Plate comprising a Boron containing phosphor
IP-Gd	Image Plate comprising BaFBr:Eu <sup>2+</sup> ·Gd <sub>2</sub> O <sub>3</sub>
MCP	MicroChannel Plate
MTF	Modulation Transfer Function
MWPC	Multi-Wire Proportional Chamber
PD	Powder Diffractometry
PMT	Photo Multiplier Tube
PSL	PhotoStimulated Luminescence
RD	Radiography
RT	Room Temperature
Q-ADC	Charge Integrating Analogue-to-Digital Converter
QE	Quantum Efficiency
SANS	Small-Angle Neutron Scattering
SE	Stimulation Energy
SL	Scintillation Light
STE	Self-Trapped Exciton
TDC	Time-to-Digital Converter
TL	ThermoLuminescence
TOF	Time Of Flight

# Publications

## JOURNALS

- M.J.Knitel, J.T.M. de Haas, P. Dorenbos, C.W.E. van Eijk, *LiBaF<sub>3</sub>, as a thermal-neutron scintillator*, Rad. Meas. **24**(4) (1995) p. 361.
- M.J. Knitel, J.T.M. de Haas, P. Dorenbos, C.W.E. van Eijk, *LiBaF<sub>3</sub>, a scintillator for thermal neutron detection with optimal neutron-gamma discrimination*, J. Neutron Research **4** (1996) p. 117.
- M.J. Knitel, J.T.M. de Haas, P. Dorenbos, C.W.E. van Eijk, *LiBaF<sub>3</sub>, a scintillator for thermal neutron detection with optimal neutron-gamma discrimination*, Nucl. Instr. and Meth. A **374** (1996) p. 197.
- M.J. Knitel, P. Dorenbos, C.M. Combes, J. Andriessen, C.W.E. van Eijk, *Luminescence and storage properties of LiYSiO<sub>4</sub>:Ce<sup>3+</sup>*, J. Lumin. **69** (1996) p. 325.
- M.J. Knitel, P. Dorenbos, C.W.E. van Eijk, *Photostimulated luminescence and thermoluminescence properties of LiYSiO<sub>4</sub>:Ce<sup>3+</sup>*, J. Lumin. **72-74** (1997) p. 765.
- M.J. Knitel, P. Dorenbos, C.W.E. van Eijk, L.Berezovskaya, V. Dotsenko, *Trapping of charge carriers in Sr<sub>2</sub>B<sub>5</sub>O<sub>9</sub>Br:Eu<sup>2+</sup> under irradiation with UV light*, Rad. Meas. **29**(3-4) (1998) p. 327.
- M.J. Knitel, P. Dorenbos, C.W.E. van Eijk, L.Berezovskaya, V. Dotsenko, *The feasibility of boron containing phosphors in thermal neutron image plates, in particular the systems M<sub>2</sub>B<sub>5</sub>O<sub>9</sub>X:Eu<sup>2+</sup> (M=Ca,Sr,Ba; X=Cl,Br). Part I: Simulation of energy deposition*, Submitted to Nucl. Instr. and Meth.
- M.J. Knitel, P. Dorenbos, C.W.E. van Eijk, L.Berezovskaya, V. Dotsenko, *The feasibility of boron containing phosphors in thermal neutron image plates, in particular the systems M<sub>2</sub>B<sub>5</sub>O<sub>9</sub>X:Eu<sup>2+</sup> (M=Ca,Sr,Ba; X=Cl,Br). Part II: Experimental results*, Submitted to Nucl. Instr. and Meth.
- M.J. Knitel, B. Plasteig, X.E. Yu, P. Dorenbos, C.W.E. van Eijk, *Scintillation and thermoluminescence of some Ce<sup>3+</sup> and Eu<sup>2+</sup> activated borates*, to be published.

## CONFERENCE PROCEEDINGS

- M.J. Knitel, J.T.M. de Haas, P. Dorenbos, C.W.E. van Eijk, *LiBaF<sub>3</sub>, a scintillator for thermal neutron detection with optimal neutron-gamma discrimination*, in: the Proceedings of the International Conference on Inorganic Scintillators and their Applications, SCINT95, eds. P. Dorenbos and C.W.E van Eijk (Delft University Press, Delft, 1996) p. 81.
- M.J. Knitel, X.E. Yu, P. Dorenbos, C.W.E. van Eijk, *Scintillation properties of Ce<sup>3+</sup> doped LaB<sub>3</sub>O<sub>6</sub>:Ce<sup>3+</sup>, LaMgB<sub>5</sub>O<sub>10</sub>:Ce<sup>3+</sup> and YMgB<sub>5</sub>O<sub>10</sub>:Ce<sup>3+</sup> for detection of thermal neutrons*, in: the Proceedings of the International Conference on Inorganic Scintillators and their Applications, SCINT97, eds. Z.W. Yin, P.J. Li, X.Q. Feng, Z.L. Xue (CAS Press, Shanghai, 1998) p. 318.
- M.J. Knitel, P. Dorenbos, C.W.E. van Eijk, L.Berezovskaya, V. Dotsenko, *Storage properties of the system M<sub>2</sub>B<sub>5</sub>O<sub>9</sub>X:Eu<sup>2+</sup> (M=Ca,Sr,Ba; X=Cl,Br)*, in: the Proceedings of the International Conference on Inorganic Scintillators and their Applications, SCINT97, eds.: Z.W. Yin, P.J. Li, X.Q. Feng, Z.L. Xue (CAS Press, Shanghai, 1998) p. 334.
- C.M. Combes, M.J.Knitel, R.W. Hollander, P. Dorenbos, C.W.E.van Eijk, *New thermal-neutron scintillators with n/gamma discrimination: K<sup>+</sup> or Rb<sup>+</sup> co-doped LiBaF<sub>3</sub>:Ce<sup>3+</sup>*, in: the Proceedings of the International Conference on Inorganic Scintillators and their Applications, SCINT97, eds. Z.W. Yin, P.J. Li, X.Q. Feng, Z.L. Xue (CAS Press, Shanghai, 1998) p. 349.

# Samenvatting

## Voor iedereen: het wat en waarom van dit onderzoek

Zonder opleiding in de natuurkunde komt de titel van dit proefschrift: *Nieuwe Anorganische Scintillatoren en Opslagfosforen voor de Detectie van Thermische Neutronen* u wellicht nogal moeilijk voor. Ik nodig u echter uit deze paragraaf eens door te lezen en ben er van overtuigd dat veel u duidelijk zal worden. Als leidraad gebruik ik de sleutelwoorden die in de titel voorkomen, waarbij ik achteraan begin.

*Neutronen* zijn deeltjes die zich normaalgesproken in de kernen van atomen bevinden. Neutronen kunnen onder bepaalde omstandigheden uit een kern vrijkomen. Bijvoorbeeld door radioactief verval, maar ook door beschieting van een kern met (andere) neutronen zoals gebeurt in een atoombom en in een kernreactor.

Bundels van vrije neutronen worden echter ook voor andere toepassingen gebruikt. Neutronen kunnen diep doordringen in allerlei materialen, nog veel dieper dan bijvoorbeeld röntgenstraling. Wanneer je een neutron een stuk materiaal instuurt, kan het er ergens anders weer uitkomen. De richting die het deeltje dan heeft, en soms ook de snelheid, zeggen iets over dat materiaal, bijvoorbeeld over de structuur ervan. Neutronen kun je dus zien als een mooi stuk gereedschap om materialen op microscopisch niveau te bestuderen.

De toevoeging *thermisch* in de titel, zegt iets over de snelheid waarmee de vrije neutronen door de ruimte bewegen. Het blijkt dat vooral thermische neutronen interessant zijn voor de studie van materialen.

Het is duidelijk dat we in ieder geval de richting van het neutron dat uit het materiaal kwam moeten kunnen bepalen. Met andere woorden, het uittredende neutron moet ergens buiten het materiaal *gedetecteerd* worden, zodanig dat de plaats van het deeltje nauwkeurig bekend wordt. Hoe kun je de onzichtbare neutronen nou detecteren? Neutronen kun je zien als een vorm van straling, net als röntgenstraling of gammastraling. Ook vrije elektronen zou je als een vorm van straling kunnen zien. Er zijn allerlei technieken om straling zichtbaar te maken. Eén van die technieken is, om de straling om te zetten in licht. Dit gebeurt bijvoorbeeld in een televisie: Een bundel elektronen wordt van achteren op het TV-scherf geschoten. De elektronen worden geabsorbeerd in een poeder dat op het scherm is aangebracht. De energie die een elektron meebrengt wordt door het poeder omgezet in rood, groen of blauw licht.

Op soortgelijke wijze werken de neutrondetectoren waar ik aan heb gewerkt. Ieder lichtflitsje op het detectorscherm geeft de absorptie van een neutron aan. De plaats van ieder neutron wordt zo dus bekend. Het scherm kan poeder (kleine kristalletjes) bevatten maar kan ook bestaan uit een groot transparant kristal, vergelijkbaar met een glasplaat.

Wanneer het scherm *direct* oplicht wanneer een neutron wordt geabsorbeerd noemen we het oplichtend kristal een *scintillator*. Je hebt echter ook kristallen die na absorptie van een neutron niet direct oplichten. De energie die vrijkomt als een neutron wordt geabsorbeerd wordt eerst in het kristalrooster *opgeslagen*. Pas als ze na de blootstelling aan de neutronen met een laserbundel worden beschenen lichten deze kristallen alsnog op. Poeders die zich aldus gedragen worden *opslagfosforen* genoemd. Een opslagfosforscherm kan dus na het experiment met de neutronen uitgelezen worden, terwijl het licht van een scintillatorscherm tijdens het neutronenexperiment geregistreerd moet worden. Beiden hebben zo hun voordelen.

Tijdens het promotieonderzoek heb ik scintillatoren en opslagfosforen van verschillende chemische samenstelling bestudeerd en gekeken hoe effectief zij zijn in het omzetten van de neutronenstraling in licht. Op die manier heb ik bijgedragen aan de verbetering van deze detectoren, zodat ze effectiever zijn in het registreren van neutronen en in het onderscheid maken tussen neutronen en andere ongewilde straling. Hoe beter de detector, hoe minder neutronen er ongezien verloren gaan, zodat er minder neutronen nodig zijn om iets van een materiaal te weten te komen. Experimenten worden daardoor minder tijdrovend. Dit is belangrijk omdat er maar weinig plaatsen op de wereld zijn waar vrije neutronen voor wetenschappelijke doeleinden worden geproduceerd.

Een andere reden om te werken aan de verbetering van deze typen detectoren is dat er een nieuwe grote Europese neutronenfaciliteit gepland is, de zogenaamde European Spallation Source (ESS). De intense neutronenbundels die hier geproduceerd zullen worden stellen hogere eisen aan de detectoren dan tot nu toe het geval was.

## Voor de specialist: De resultaten in dit proefschrift

In **hoofdstuk 2** wordt de huidige technologie op het gebied van neutronendetectoren beschreven. Scintillatoren worden ingedeeld bij de klasse van tellende detectoren die iedere neutronenabsorptie afzonderlijk registreren. De eigenschappen van de meest belangrijke scintillatoren,  ${}^6\text{LiF/ZnS:Ag}^+$  en  ${}^6\text{Li}$  bevattend silikaatglas worden met elkaar en met andere tellende systemen zoals gasdetectoren vergeleken. De sterke punten van de scintillatoren zijn hun verwaasloosbare parallax, flexibele geometrie en relatief lage kosten. Het plaatsoplossend vermogen, de telsnelheid, en de gamma gevoeligheid van  ${}^6\text{Li}$  schermen zijn vergelijkbaar met de meeste gasgebaseerde systemen. Detectoren gebruikmakend van  ${}^6\text{Li}$  bevattend silikaatglas halen meestal hogere telsnelheid dan gasdetectoren en combineren dit met een hoog detectierendement. Het plaatsoplossend vermogen is vergelijkbaar met hetgeen met gasdetectoren gehaald kan worden. Een duidelijk nadeel vormen de relatief grote achtergrondbijdrage van de detector zelf alsmede de hoge gamma gevoeligheid. Er bestaat geen neutronsintillator die een hoge lichtopbrengst (>



10,000 fotonen/neutron om een hoog plaatsoplossend vermogen te verkrijgen) combineert met een korte vervaltijd ( $< 100$  ns om een hoge telsnelheid mogelijk te maken) en een lage intrinsieke achtergrond.

Opslagfosforen worden gebruikt in zogenaamde 'image plates' (IP's). De IP's voor thermische neutronen die momenteel gebruikt worden bevatten een poedermengsel van het bekende röntgenopslagfosfor  $\text{BaFBr:Eu}^{2+}$  en  $\text{Gd}_2\text{O}_3$  als neutronenabsorberend materiaal. IP's worden ingedeeld bij de klasse van integrerend detectoren. Integrerende detectoren tellen meerdere detectiegebeurtenissen op alvorens een uitgangssignaal te geven. Andere belangrijke integrerende detectoren zijn systemen gebaseerd op fotografisch film of op scintillator/CCD combinaties. Vergeleken met film hebben IP's een veel groter dynamisch bereik en zijn ze makkelijker uit te lezen. Vergeleken met CCD's vertonen ze vooralsnog een hoger plaatsoplossend vermogen, onafhankelijk van de grootte van het detectorscherm. De IP zou nog verbeterd kunnen worden op punten van gamma gevoeligheid en op de zogenaamde *Detective Quantum Efficiency* (DQE) van de IP, hoewel de laatste reeds hoger is dan die van de andere systemen. De DQE is een grootheid die de efficiëntie in het registreren van neutronen kan uitdrukken, zowel voor tellende als voor integrerende detectoren.

In **hoofdstuk 3** worden de eisen die aan de nieuwe, betere scintillatoren en opslagfosforen gesteld worden vertaald in eisen waaraan de te onderzoeken materialen sowieso moeten voldoen. De scintillatiematerialen die onderzocht kunnen worden moeten Li of B bevattende verbindingen zijn. Snelle scintillatie is mogelijk wanneer deze verbindingen gedoteerd worden met een van de zeldzame aardionen  $\text{Ce}^{3+}$ ,  $\text{Pr}^{3+}$  of  $\text{Nd}^{3+}$ . Dit moet dan fungeren als luminescerend centrum. Het meest aantrekkelijk zijn materialen die zeldzame aardluminescentie combineren met zogenaamde 'core-valence' luminescentie.

Wat betreft de opslagfosforen is de keuze beperkt tot B houdende verbindingen. De meest efficiënte conversie van ionisaties in centra die goed fotostimuleerbaar zijn kan worden verwacht van de kleine groep van haloboraten. Door deze te doteren met een van de kationen  $\text{Ce}^{3+}$ ,  $\text{Eu}^{2+}$ ,  $\text{Tl}^+$  of  $\text{In}^+$  bestaat er in principe een mogelijkheid voor voldoende snelle fotogestimuleerde luminescentie.

In **hoofdstuk 4** worden de scintillatie eigenschappen van een  $\text{LiBaF}_3$  éénkristal gepresenteerd. Eerst worden de meettechnieken om een scintillator te karakteriseren beschreven. De scintillatielichtopbrengst (SL opbrengst) van  $\text{LiBaF}_3$  bedraagt 3500 fotonen per geabsorbeerd neutron. De energieresolutie voor de  ${}^6\text{Li}(n,\alpha)$  reactieproducten bedraagt ongeveer 14%.  $\text{LiBaF}_3$  vertoont core-valence luminescentie met een vervaltijd van 0.8 ns en 'self-trapped-exciton' luminescentie met een vervaltijd van 6  $\mu\text{s}$ . Er wordt geen core-valence luminescentie waargenomen onder thermische neutronenexcitatie terwijl beide typen van luminescentie te zien zijn onder gamma excitatie. Dit biedt een unieke mogelijkheid tot pulsform discriminatie tussen scintillatiepulsens veroorzaakt door neutronen enerzijds en gamma's anderzijds. De gammagevoeligheid van dit kristal kan zo teruggebracht worden tot een waarde van hoogstens  $5.7 \cdot 10^{-7}$  en waar-

schijnlijk is ze zelfs veel lager. Dotering van  $\text{LiBaF}_3$  met  $\text{Ce}^{3+}$  wordt bestudeerd.

De scintillatie-eigenschappen van twee andere Li houdende materialen,  $\text{LiLnSiO}_4:\text{Ce}^{3+}$  ( $\text{Ln} = \text{Y, Lu}$ ) wordt besproken in **hoofdstuk 5**. Ook de opslageigenschappen van deze poeders is bestudeerd en de meettechnieken om een opslagfosfor te karakteriseren worden beschreven. De lichtopbrengst van een  $\text{LiYSiO}_4:\text{Ce}^{3+}$  éénkristal wordt geschat op  $1 \cdot 10^4$  fotonen per MeV geabsorbeerde röntgenenergie en dezelfde lichtopbrengst kan verwacht worden voor per geabsorbeerd neutron. De scintillatiepuls, gemeten onder gamma excitatie, bevat een  $\tau = 38$  ns component. Onder excitatie met alfa deeltjes wordt tevens een  $\mu\text{s}$  component waargenomen.

$\text{LiYSiO}_4:\text{Ce}^{3+}$  blijkt ook een vrij goede opslagfosfor te zijn. Het stimulatiespectrum vertoont een brede band met een maximum beneden de 450 nm. De fotogestimuleerde luminescentieopbrengst (PSL opbrengst) voor 23 keV röntgens is een factor 15 minder dan die van een commercieel verkrijgbaar  $\text{BaFBr}:\text{Eu}^{2+}$  sample. De PSL opbrengst voor 48 meV neutronen bedraagt 0.5 foton per invallend neutron. Volgens schatting neemt deze opbrengst met een factor 200 toe wanneer een 1 mm dik éénkristal  $\text{LiYSiO}_4:\text{Ce}^{3+}$ , dat 96% verrijkt  $^6\text{Li}$  bevat gebruikt zou worden in plaats van een poederlaag. Een belangrijk probleem is de hoge stimulatie energie (SE), die bij 515 nm een factor 20 hoger is dan die van  $\text{BaFBr}:\text{Eu}^{2+}$ .

De optische eigenschappen van  $\text{Ce}^{3+}$  in  $\text{LiLuSiO}_4:\text{Ce}^{3+}$  zijn zeer vergelijkbaar. Experimenten met  $\text{LiLuSiO}_4$  gedoteerd met  $\text{Ce}^{3+}$ ,  $\text{Tb}^{3+}$ , of allebei laten zien dat de PSL opbrengst, de SL opbrengst en de SE sterk afhankelijk zijn van de aanwezigheid van dotering en waarschijnlijk ook van andere onregelmatigheden in het kristalrooster. Het  $\text{LiLuSiO}_4:\text{Ce}^{3+}$  monster vertoont de hoogste lichtopbrengst van  $3 \cdot 10^4$  pho/MeV terwijl de PSL opbrengst laag is. Anderzijds heeft het  $\text{LiLuSiO}_4:\text{Ce}^{3+}, \text{Tb}^{3+}$  monster de hoogste PSL opbrengst (onder röntgenbestraling) die 0.25 keer die van  $\text{BaFBr}:\text{Eu}^{2+}$  bedraagt, terwijl de SL opbrengst laag is. Toekomstige studies zouden erop gericht moeten zijn om de relatie tussen dotering/bereidingswijze en de SL/PSL opbrengst te verhelderen. Ook de groei van éénkristallen zou onderzocht moeten worden.

De luminescentie en scintillatie in een groep van  $\text{Ce}^{3+}$  gedoteerde orthoboraten, metaboraten, pentaboraten, heptaboraten en oxyorthoboraten is het onderwerp van **hoofdstuk 6**. De SL opbrengst van de meeste orthoboraten is van de orde van  $10^4$  fotonen per MeV röntgenenergie. Het orthoboraat dat het meest in aanmerking komt voor verder onderzoek is  $\text{YAl}_3\text{B}_4\text{O}_{12}:\text{Ce}^{3+}$ , dat een scintillatie vervaltijd heeft van 30 ns en een gunstig effectief atoomnummer alsmede een hoge boron gewichtsfractie.

The SL opbrengst van de andere boraten is over het algemeen lager. Een uitzondering is  $\text{LaB}_3\text{O}_6:\text{Ce}^{3+}$  dat een dominante gastrooster luminescentie vertoont bij lage  $\text{Ce}^{3+}$  concentraties.

Geen enkel materiaal laat thermisch gestimuleerde luminescentie zien die qua intensiteit meer dan een factor 0.01 is van die van  $\text{BaFBr}:\text{Eu}^{2+}$ . De opslageigenschappen van deze boraten hoeven dus niet verder onderzocht te worden. De luminescentie in de  $\text{Eu}^{2+}$  gedoteerde boraten  $\text{CaYOBO}_3:\text{Eu}^{2+}$  en  $\text{Ca}_4\text{YO}(\text{BO}_3)_3:\text{Ce}^{3+}$  blijkt zwak te zijn.

In de discussie van dit hoofdstuk wordt onder meer de opmerkelijk kortgolvlige emissie van  $\text{Ce}^{3+}$  in de meta- en pentaboraten besproken. Er wordt gezocht naar een relatie met de geometrie

van de  $Ce^{3+}$  site, maar deze wordt niet gevonden.

De laatste twee hoofdstukken gaan uitsluitend over opslagfosforen. In **hoofdstuk 7** wordt een alternatief concept voor de thermische neutronen IP voorgesteld. De plaat moet een poederlaag van  $M_2B_5O_9X:Eu^{2+}$  ( $M=Ca, Sr, Ba$ ;  $X=Cl, Br$ ) in een bindend materiaal bevatten. Deze plaat, hier IP-B genoemd, wordt vergeleken met het huidige concept, hier IP-Gd genoemd. In het bijzonder wordt de DQE van beide platen beschouwd. De theorie geeft aan dat de DQE afhangt van de neutron absorptiewaarschijnlijkheid  $A$ , het aantal fotoelektronen  $N_{phe}$  dat per invallend neutron gecreëerd wordt, en van de variantie in dit aantal fotoelektronen,  $\nu_{N_{phe}}$ .

Het essentiële verschil tussen een IP-Gd en een IP-B is de waarde voor  $\nu_{N_{phe}}$ . Dit verschil is direct verbonden met het verschil in de neutronenvangstreacties. Met behulp van Monte Carlo simulaties is het energiedepositieproces in beide typen platen bestudeerd, waarbij reactieproducten van de invangsreacties als startpunt zijn genomen. Uit de simulaties blijkt dat  $\nu_{N_{phe}}$  voor de IP-Gd veel groter is dan voor de IP-B. Daardoor kan de DQE van een IP-Gd niet groter worden dan 35%-40%.

De DQE van een IP-B wordt nauwelijks gelimiteerd door  $\nu_{N_{phe}}$ . Dit impliceert dat voor een 150  $\mu m$  dikke IP-B plaat met 99% verrijkt  $^{10}B$  de waarde van  $N_{phe}$  'slechts' 1.3 hoeft te zijn om een DQE te verkrijgen van 40%, het maximum voor de IP-Gd. Het theoretische maximum voor de DQE van de IP-B bedraagt 60% voor een 150  $\mu m$  dikke plaat en 85% voor een 300  $\mu m$  dikke plaat, gegeven een vulfactor van de fosforkorrels van 70%.

De waarden voor  $N_{phe}$  zijn ook experimenteel bepaald voor alle genoemde haloboraten. De hoogste waarden werden gevonden voor  $Sr_2B_5O_9Br:Eu^{2+}$  en  $Ca_2B_5O_9Br:Eu^{2+}$ :  $N_{phe} = 1$  en  $N_{phe} = 0.7$ . De getallen zouden hoger zijn uitgevallen wanneer 99% verrijkt  $^{10}B$  zou zijn gebruikt. Daarom moeten DQE waarden  $> 40\%$  haalbaar zijn. Concluderend hebben  $Sr_2B_5O_9Br:Eu^{2+}$  en  $Ca_2B_5O_9Br:Eu^{2+}$  zeker potentieel om het  $BaFBr:Eu^{2+} \cdot Gd_2O_3$  mengsel te vervangen.

In **hoofdstuk 8** wordt één van deze boraten,  $Sr_2B_5O_9Br:Eu^{2+}$ , op meer fundamenteel niveau bestudeerd. Resultaten van fotoluminescentie, fotogestimuleerde luminescentie, thermoluminescentie en EPR experimenten worden gepresenteerd, Ze verschaffen informatie over de aard van de ladingsinvangscentra en de het mechanisme van recombinatie. In alle  $Sr_2B_5O_9Br:Eu^{2+}$  samples kan zwakke  $Eu^{3+}$  luminescentie waargenomen worden, naast de intense  $Eu^{2+}$  luminescentie. Onder UV belichting worden dezelfde invangstcentra gevuld als onder bestraling met röntgens. Het excitatiespectrum van de thermoluminescentie vertoont in het UV gebied een opmerkelijke gelijkenis met de 'charge transfer band' van  $Eu^{3+}$ . Deze waarneming, naast andere, suggereert dat  $Eu^{3+}$  ionen essentieel zijn in het stadium van ladingsopslag, ongeacht de gebruikte straling. Ook suggereert zij dat onder UV belichting de creatie van elektron-gat paren, als eerste stadium in het ladingsopslagproces, plaatsvindt op de  $Eu^{3+}$  ionen.

EPR metingen (tussen 120-300 K) laten een stralingsgeïnduceerd signaal zien dat waarschijnlijk toegeschreven kan worden aan  $O_{Br}^-$  centra ( $O_{Br}^{2-}$  centra die een gat hebben ingevangen). Volgens de TL gloeicurves moeten ook nog andere typen invangstcentra aanwezig zijn. Ook de  $Eu^{2+}$  ionen veroorzaken een EPR signaal maar de grootte ervan verandert niet door bestraling.

Een EPR signaal afkomstig van  $F(\text{Br}^-)$  centra is niet waargenomen.

De isotherme luminescentievervalcurves (de intensiteit van de luminescentie als functie van de tijd, opgenomen na bestraling bij een bepaalde, constante temperatuur) gedragen zich volgens een functie van het type  $(1 + at^p)^{-1}$ . De macht  $p$  ligt dichtbij 1 maar is afhankelijk van de temperatuur. Ook de luminescentie vervalcurve opgenomen onder continue optische stimulatie vertoont een dergelijk gedrag met  $p \approx 1$ . Anderzijds vertonen de TL gloeicurves duidelijke kenmerken van eerste orde recombinitie. Het eerste-orde recombinitiemodel voorspelt een exponentiële luminescentie vervalcurve. Beide waarnemingen kunnen verenigd worden in een complexer model waarin iedere TL gloeipiek een groep van invangstcentra vertegenwoordigt. De invangstcentra moeten dan onderling variërende waarden van hun potentiaalextrimum hebben of variërende tunneling afstanden tot het recombinitiecentrum.

## Nawoord

Promovendi zijn solisten. Zij dwalen door stille instituutsgangen en als zij daar onverhoopt iemand tegen het lijf lopen wenden zij schuw hun blik af. Zwijgend staren zij uren naar hun computerscherm. Daar zij met de rug naar u toegekeerd zitten, verraadts slechts het onregelmatige geluid van vingers die het toetsenbord beroeren, dat er gewerkt wordt.

In mijn geval is er per ongeluk toch een aanzienlijk aantal mensen dat een belangrijke bijdrage heeft geleverd aan de totstandkoming van dit proefschrift. Hen wil ik hier noemen en bedanken.

Mijn promotor Carel van Eijk voor zijn enthousiasme, optimisme en goede suggesties. Achter zijn drempelloze deur werd de vaak broodnodige structuur in mijn werk aangebracht. Mijn begeleider Pieter Dorenbos voor zijn kritische maar tegelijkertijd vriendschappelijke wijze van begeleiden. Veel goede ideeën en interpretaties zijn van hem afkomstig, al meen ik in de loop van de tijd wat van zijn denkwijze meegekregen te hebben.

Hans Andriessen dank ik voor de theoretische berekeningen, gepresenteerd in hoofdstuk 8, die hij voor me heeft uitgevoerd en voor de overdracht van een stukje van zijn grote kennis van de theorie der vaste stof. Ook Victor Bom heeft voor me zitten rekenen. De Monte-Carlo simulaties met het programma GEANT, gepresenteerd in hoofdstuk 7, komen van zijn hand. Victor: bedankt! Johan de Haas ben ik dank verschuldigd vanwege de vele technische - en software problemen die hij voor me heeft opgelost.

Olivier 'f..sorry' Guillot-Noël alsmede zijn collega's Danielle Simons en Bruno Viana dank ik voor het uitvoeren en mede interpreteren van de EPR metingen uit hoofdstuk 8. Olivier, only if you learn Dutch you will be able to translate the previous sentence for your French colleagues. The measurements at the synchrotron of Daresbury were carried out by Zhenya Melchakov. I am also grateful to Jan Jacobs, Benoit Plasteig, Irina Berezovskaya, Vladimir Dotsenko for preparation of some of the materials. When I was preparing the materials myself, I got considerable help from Yu Xianen and Ben Meester. Many thanks to both persons. Ben, sorry for the oven..... Other very useful suggestions came from Christian Rausch and Mihail Danilkin. Thank you for your interest.

Mijn kamergenoten Hans van 't (het?? ut??) Spijker en Cecile Combes creëerden samen een aangename kakafonie van achtergrondruis. Fijn ook, dat jullie minstens pretendeerden te luisteren wanneer ik even mijn mond niet kon houden. Het ga jullie goed in je verdere loopbaan. De afstudeerstudenten Martijn Engelsman en Bart Hommels bedank ik voor hun bijdrage aan de

metingen en het verbeteren van de meetopstelling. Ook de samenwerking met hen heb ik als zeer prettig ervaren.

Ook de andere ISO-leden hebben zeker bijgedragen aan de goede werksfeer, met name tijdens de zittingen aan tafel 2 van de kantine. Onder aanvoering van ene J. Dirker (voor niet ingewijden: de 'Jaap van der Scheur' van ISO) werd menig heftige discussie gevoerd en werd zin op aangename wijze afgewisseld met onzin. Jammer alleen, dat er nooit wat te lachen viel.....(!)

Verder wil ik nog een aantal niet-collega's noemen. De medewerkers van Van der Wegen/Kramer Artworks voor hun bijdrage aan de kaft. Mijn vrienden, jaarclubgenoten en (schoon)familie voor hun betrokkenheid en afleiding . Een aantal van hen wist gelukkig zeer goed waar ik het over had. In het bijzonder bedank ik mijn ouders. Voor hun medeleven en voor hun onvoorwaardelijke steun.

## Curriculum Vitae

De auteur van dit proefschrift werd geboren op 10 januari 1969 te Eindhoven. Aan het in diezelfde plaats gelegen Eckart College behaalde hij in 1987 het diploma ongedeelde VWO. Aansluitend begon hij de studie natuurkunde aan de toenmalige Rijksuniversiteit Utrecht met hoofdrichting experimentele natuurkunde. Het afstudeeronderzoek onder supervisie van Dr. H.A. Dijkerman werd verricht in de vakgroep atoom- en moleculfysica en betrof een bepaling van de polarisatietoestand van natrium atomen in een veld van meerdere laserbundels op grond van computersimulaties en experimenten. Daarna deed hij een onderzoeksstage in de vakgroep 'Quantumelectronics' van de State University of New York at Stony Brook. In augustus 1993 legde hij het doctoraal examen af en aan het einde van dat jaar begon hij zijn promotieonderzoek in dienst van de Nederlandse Organisatie voor Wetenschappelijk Onderzoek (NWO). Hij was werkzaam in de vakgroep Instrumentatie Stralingsonderzoek (ISO) van het Interfacultair Reactor Instituut (IRI), onderdeel van de Technische Universiteit Delft. De resultaten van dat onderzoek zijn vastgelegd in dit proefschrift. Zijn onderwijstaak vervulde hij door praktika natuurkunde voor eerste-, tweede- en derdejaars studenten natuurkunde of elektrotechniek te begeleiden.